UNIVERSITY OF THESSALY

SCHOOL OF ENGINEERING

DEPARTMENT OF MECHANICAL ENGINEERING

RAREFIED OSCILLATORY AND PULSATILE GAS FLOWS IN CAPILLARIES AND ENCLOSURES WITH APPLICATIONS IN VACUUM TECHNOLOGY AND MICROFLUIDICS

Alexandros Tsimpoukis

Diploma in Mechanical Engineering, Aristotle University of Thessaloniki, 2014

M.Sc. in Mechanical Engineering, University of Thessaly, 2015

Submitted in partial fulfillment of the requirements for the degree of Doctor of Philosophy in Mechanical Engineering at the University of Thessaly

Volos, 2020

The approval of the current dissertation by the Department of Mechanical Engineering of the University of Thessaly does not imply acceptance of the author's opinions (Law 5343/32 number 202 paragraph 2). Also, the views and opinions expressed herein do not necessarily reflect those of the European Commission.

Certified by the members of the Dissertation Committee:

1st member (Supervisor)	Prof. Dimitris Valougeorgis Professor in the Department of Mechanical Engineering University of Thessaly
2nd member	Prof. Nikos Andritsos Professor in the Department of Mechanical Engineering University of Thessaly
3rd member	Prof. Nikolaos Pelekasis Professor in the Department of Mechanical Engineering University of Thessaly
4th member	Prof. Vasilis Bontozoglou Professor in the Department of Mechanical Engineering University of Thessaly
5th member	Prof. Irina Martin Professor in the Department of Mechanical Engineering Aix-Marseille University
6th member	Prof. Silvia Lorenzani Associate Professor in the Department of Mathematics Politecnico di Milano
7th member	Prof. Yonghao Zhang Professor in the Department of Mechanical and Aerospace Engineering University of Strathclyde

ii

Dedicated to my family

Acknowledgements

At first, I would like to express my sincere gratitude to my supervisor Prof. Dimitris Valougeorgis for the continuous support of my PhD study and related research, for his patience, motivation, and immense knowledge. He helped me not only to flourish my scientific skills but also to develop a stronger personality. I am eternally grateful to him for trusting me and guiding me to the demanding field of rarefied gas dynamics.

Besides my supervisor, I would like to thank the rest of my thesis committee: Prof. Nikos Andritsos, Prof. Nikolaos Pelekasis, Prof. Vasilis Bontozoglou, Prof. Irina Martin, Assoc. Prof. Silvia Lorenzani and Prof. Yonghao Zhang, for reviewing my thesis. I really appreciate their effort to provide insightful comments.

I am also thankful to all my friends as well as my colleagues in the Laboratory of Transport Phenomena and Process Equipment. I would like to thank Dr. Steryios Naris for introducing me into the group as well as for its continuous assistance. Also, I would like to thank my friends Dr. Giorgos Tatsios and Mr. Nikolaos Vasileiadis as well as Mr. Makis Misdanitis and Dr. Guillermo Lopez-Quesada for the stimulating discussions, for sharing their knowledge with me, and for all the fun we have had in the last four years. Many thanks also to Dr. Christos Tantos and to Dr. John Lihnaropoulos.

I would also like to say a heartfelt thank you to Miss Eleni Chatzina who has been by my side throughout this PhD and without her support this journey would have been incomplete. Finally, I am eternally grateful to my parents, Thanasis and Maria and to my brother Christos for always believing in me and encouraging me to follow my dreams.

RAREFIED OSCILLATORY AND PULSATILE GAS FLOWS IN CAPILLARIES AND ENCLOSURES WITH APPLICATIONS IN VACUUM TECHNOLOGY AND MICROFLUIDICS

Alexandros Tsimpoukis

University of Thessaly, January 2020

Supervisor: Prof. D. Valougeorgis

Oscillatory rarefied gas flows are of main theoretical importance in fluid mechanics, revealing novel non-equilibrium transport phenomena, as well as of strong engineering interest in various technological fields, including microfluidics and vacuum technology. As in the case of viscous oscillatory flows, rarefied oscillatory gas flows are encountered in enclosures, driven by moving boundaries oscillating parallel or vertical to the main flow and in capillaries of various cross sections, driven by oscillating or pulsatile pressure or force gradients. Since in rarefied gas flows the classical Navier-Stokes-Fourier approach is not applicable, kinetic modeling and simulations, based on the computational solution of the Boltzmann equation or of reliable kinetic model equations via deterministic or stochastic schemes, have been implemented. Oscillatory gas flows are in the hydrodynamic regime, when both the mean free path and the oscillation frequency are much smaller than the characteristic length and the collision frequency respectively. When either of these restrictions is relaxed, the flow is classified as rarefied and may be in the transition or free molecular regimes depending on the time and space characteristic scales. Boundary driven rarefied oscillatory flows have attracted over the last two decades considerable attention. They may be present in resonating filters, sensors and actuators, as well as in systems enhancing acoustic transduction or achieving acoustic cloaking. Pressure or force driven rarefied oscillatory or pulsatile gas flows have attracted much less attention. They are also encountered in numerous typical and innovative applications in the transition and free molecular regimes, including pneumatic lines, electronic cooling, pulse tubes, enhanced heat and mass transfer devices, gas separation and mixing technologies and gas pumping systems.

In the present Ph.D. thesis oscillatory rarefied gas flows in various flow setups are considered in the whole range of gas rarefaction and oscillation frequencies. The investigation includes oscillatory and pulsatile fully-developed gas flow through circular

and rectangular channels, subject to oscillatory pressure gradients of small amplitude, as well as to oscillatory nonlinear fully-developed flow between parallel plates, subject to oscillatory forces of arbitrary amplitude. The investigation in capillaries also includes oscillatory fully-developed binary gas mixture flow between parallel plates driven by oscillatory pressure and molar fraction gradients. Furthermore, boundary driven flow in comb-type enclosures subject to vertical or lateral harmonic motion of the moving surface is investigated. The analysis is based, depending on the flow configuration on the deterministic solution of the BGK, Shakhov and McCormack kinetic models, as well as on the DSMC method. In all flow setups the effect of the flow and geometry parameters on the macroscopic distributions and overall quantities characterizing the flow is investigated, providing interesting theoretical and technological findings.

The oscillatory and pulsatile isothermal fully-developed rarefied gas flow in circular tubes and rectangular ducts respectively are simulated based on the linearized unsteady BGK kinetic model subject to Maxwell boundary conditions. Computational results for the amplitude, phase angle and time evolution of the velocity distribution, the flow rate, the mean wall shear stress, the acting inertial and viscous forces, the pumping power and the time average pumping power are provided, covering the whole range of gas rarefaction and oscillation parameters. The results are successfully validated with corresponding analytical or semi-analytical results in the slip and free molecular regimes for low and high oscillation frequencies, as well as with steady-state numerical results, which are reached faster as the flow becomes more rarefied. The amplitudes of the flow rate and the mean wall shear stress are always smaller than the corresponding steady ones. In general, as the frequency is increased the amplitude of the macroscopic quantities is decreased and their phase angle lag with respect to the pressure gradient is increased approaching asymptotically the limiting value of 90^0. The detailed computation of the inertia and viscous forces in terms of the gas rarefaction and oscillation parameters, clarifies when the flow consists of only one oscillating viscous region or of two regions, namely the inviscid piston flow in the core and the oscillating frictional Stokes layer at the wall with the velocity overshooting (Richardson effect). As the gas rarefaction is increased higher oscillation frequencies are needed to trigger these phenomena. In terms of the gas rarefaction, there is a non-monotonic behavior and the maximum flow rate amplitude may be observed at some intermediate value of the gas rarefaction parameter depending upon the oscillation parameter. The accommodation coefficient, characterizing the gas-surface interaction, has a significant effect on the amplitudes of the macroscopic quantities and a very weak one on their

vii

phases. The time average pumping power is increased as the oscillation frequency is reduced and its maximum value is one half of the corresponding steady one.

Next, the oscillatory nonlinear force driven fully-developed rarefied gas flow has been analyzed based on the DSMC method, as well as on the nonlinear BGK and Shakhov models, subject to diffuse boundary conditions. It has been found that even with large force amplitudes all macroscopic distributions have sinusoidal pattern with its fundamental frequency being the same with the driving frequency of the external force without the appearance of other harmonics, except of the axial heat flow where the nonlinearities are responsible for generating oscillatory motion containing several harmonics. Nonlinear effects are becoming more significant in highly rarefied flows with low oscillation frequencies. The DSMC flow rates have been compared with corresponding linear oscillatory ones, to find out that at small and moderate external forces, the agreement between nonlinear and linear flow rates is very good and always remains less than 10%, while at large external forces the deviation in the flow rate amplitude reaches about 25%. The bimodal shape of the temperature profile and nonconstant pressure profile, encountered in steady-state flows in the continuum limit, are also observed here and strongly depend on the gas rarefaction and oscillation parameters. The axial heat flow is the most affected macroscopic quantity by the amplitude of the external force. At large external forces and highly rarefied flows with low oscillation frequencies it exhibits a complex non-sinusoidal pattern containing several harmonics. The cycle-average pumping power is increased proportionally to the square of the external force amplitude and is smaller than the corresponding linear one following the same trend with the flow rates. In the case of nonisothermal plates, the space-average normal heat flow is not enhanced by increasing either the oscillation frequency or the force amplitude. The agreement between the DSMC and kinetic models is very good in flow rates and shear stresses but it deteriorates in heat flows.

The investigation in oscillatory capillary flows is concluded by examining the oscillatory pressure and molar fraction driven rarefied binary gas mixture flow between parallel plates, based on the McCormack model subject to diffuse boundary conditions. The presented results are for He–Xe, He-Ar and Ne–Ar with their molar fraction varying from zero to one. The output quantities include the macroscopic quantities of each species and of the mixture and they are successfully validated in various ways, including grid refinement, fulfillment of the derived force balance benchmark expression and systematic comparisons at limiting conditions, such as steady-state binary gas flow and oscillatory single gas flow. The flow rate, wall shear stress and pumping

viii

power of the oscillatory binary gas mixture flow have qualitative resemblance with the corresponding ones in oscillatory single gas flow, in terms of the gas rarefaction and oscillation parameters, but there are quantitative deviations particularly in the flow rates depending on the molar fraction and the mixture composition. As the molecular mass ratio of the heavy over the light species is increased, the mixture flow rate amplitude becomes larger and the phase angle becomes smaller than the corresponding ones of the single gas. The variation with respect to the molar fraction is non-monotonic, taking the maximum and minimum values for the amplitude and the phase angle respectively at intermediate values of the molar fraction. Concerning the species, it has been found that as the oscillation frequency is increased, although the flow rate amplitudes of both species are decreased, the relative difference between the flow rate amplitudes of the light and heavy species is increased. This behavior becomes more pronounced as the gas rarefaction is decreased, which is certainly not expected, since as it is well-known gas separation effects are decreased as the flow becomes less rarefied. This is due to inertia effects, which are increased with the oscillation frequency and they influence the flow rate amplitude of the heavy species much more than of the light one. This effect is further amplified as the flow becomes less rarefied, overcoming diffusion effects due to intermolecular collisions, provided that the oscillation frequency is sufficiently large. It has been confirmed that at high frequencies the flow rate amplitude ratio of the light over the heavy species, independent of the gas rarefaction parameter, tends to the molecular mass ratio of the heavy over the light species. Also, the phase lag of the flow rate of the heavy species are always larger than the corresponding one of the light one, while the velocity overshooting effect becomes more dominant as the molecular mass of the gas species is increased. The present results may be useful in the design and development of gas separation devises operating at moderate and high frequencies in the whole range of gas rarefaction applicable in various technological fields.

Turning next to boundary driven flows the classical oscillatory Couette flow and the two-dimensional oscillatory rarefied gas flow in comb-type structures driven by the vertical/lateral harmonic motion of the moving surface are investigated. The former one has been analyzed based on the linearized BGK kinetic model and it is considered mainly for benchmarking the developed complex kinetic codes. Excellent agreement between the present results and the available ones in the literature is observed. Also, a computationally efficient marching-type scheme is reported, with the real and imaginary parts of the kinetic formulation separately treated and solved. In

ix

addition, two parallelization strategies based on OpenMP and OpenACC directives are reported and a suitable speed-up is achieved without doing major modifications in the kinetic solver. Then, the developed validated parallel codes have been accordingly extended and adapted to all examined flow configurations. The time-dependent comb-type flow setup has been analyzed based on the linearized Shakhov kinetic model with diffuse boundary conditions. The vibrating part is the inner one, formatting complex flow patterns depending on the gas rarefaction and oscillation parameters, as well as on the comb dimensions. Computational results are presented mainly for the average normal pressure and shear stress at the moving walls. As the rarefaction parameter is increased the amplitudes of both quantities are initially reduced reaching some minimum values, then they slightly increase and oscillate and finally, they remain constant. The local minimums and maximums in the amplitudes correspond to certain anti-resonance and resonance states respectively, which may be implemented to control the system dissipation. The dimensions of the comb assembly affect the flow significantly at low oscillation frequencies. On the contrary, in the high frequency regime, the normal pressure and shear stress remain constant despite any change in comb dimensions. In these cases gas trapping is observed and the flow may be modeled as one-dimensional. The presented results may be useful in the development of the new generation acceleration sensors and resonators.

Overall, it may be stated that following specific kinetic formulation, modeling and simulations, various oscillatory flow setups have been considered in the whole range of gas rarefaction and oscillation frequency parameters. The investigation of oscillatory and pulsatile flows of single gases and binary gas mixtures in capillaries due to externally imposed small or large amplitude driving mechanisms, as well as of the oscillatory boundary driven comb assembly response, is novel and all corresponding results are reported for first time in the literature. It is hoped that the theoretical findings and the computational results reported here will support, at some extend, the detailed design and optimization of various technological devices.

Keywords: Rarefied gas dynamics, Vacuum technology, Microfluidics, Oscillatory flow, Pulsatile flow, Richardson effect, Nonlinear oscillatory flow, Oscillatory binary gas mixture flow, Gas separation, Comb drive assembly, Damping forces

Αραιοποιημένες ταλαντωτικές και παλμικές ροές αερίων σε αγωγούς και κοιλότητες με εφαρμογές στην τεχνολογία κενού και μικρορευστομηχανική

Αλέξανδρος Τσιμπούκης

Πανεπιστήμιο Θεσσαλίας, Ιανουάριος 2020

Επιβλέπων: Καθηγητής Δ. Βαλουγεώργης

Η θεωρητική σημασία των ταλαντωτικών αραιοποιημένων ροών αερίων για τον κλάδο της μηχανικής ρευστών είναι μεγάλη και εντοπίζεται στην ανακάλυψη καινοτόμων φαινομένων μεταφοράς εκτός θερμοδυναμικής ισορροπίας και στη σύνδεση με ενδιαφέρουσες εφαρμογές σε διάφορους τεχνολογικούς τομείς όπως η μικρορευστομηχανική και η τεχνολογία κενού. Όπως οι υδροδυναμικές ταλαντωτικές ροές, ομοίως οι ταλαντωτικές αραιοποιημένες ροές αερίων εμφανίζονται είτε σε οριοθετημένους χώρους με τοιχώματα που ταλαντώνονται παράλληλα ή κάθετα ως προς τη ροή είτε σε αγωγούς όπου η ροή δημιουργείται από ταλαντωτική ή παλμική διαφορά πίεσης ή δύναμης. Δεδομένου ότι η κλασσική προσέγγιση Navier-Stokes-Fourier δεν εφαρμόζεται στις αραιοποιημένες ροές αερίων, έχουν εφαρμοστεί κινητικές τεχνικές μοντελοποίησης και προσομοίωσης, οι οποίες βασίζονται στην υπολογιστική επίλυση είτε της εξίσωσης Boltzmann είτε αντίστοιχης εξίσωσης κατάλληλου κινητικού μοντέλου μέσω ντετερμινιστικών ή στοχαστικών σχημάτων. Οι ταλαντωτικές ροές αερίων βρίσκονται στο υδροδυναμικό όριο όταν και η μέση ελεύθερη διαδρομή των μορίων του αερίου είναι μικρότερη ενός χαρακτηριστικού μήκους, καθώς επίσης και όταν η συχνότητα ταλάντωσης είναι μικρότερη της συχνότητας των συγκρούσεων. Όταν μια από τις δύο προϋποθέσεις δεν ισχύει, τότε η ροή χαρακτηρίζεται ως αραιοποιημένη και ανάλογα με το μέγεθος του χαρακτηριστικού μήκους και του χρόνου, ενδέχεται να βρίσκεται στη περιοχή μετάβασης ή στην ελεύθερη μοριακή περιοχή. Οι αραιοποιημένες ταλαντωτικές ροές αερίων λόγω κίνησης τοιχώματος έχουν διερευνηθεί εκτενώς τα τελευταία είκοσι χρόνια. Οι αραιοποιημένες ταλαντωτικές ή παλμικές ροές αερίων λόγω διαφοράς πίεσης ή δύναμης δεν έχουν λάβει την αντίστοιχη προσοχή. Οι ροές αυτές εμφανίζονται σε πολλές κλασσικές αλλά και καινοτόμες εφαρμογές στη περιοχή μετάβασης και στην ελεύθερη μοριακή περιοχή όπως για παράδειγμα σε πνευματικές γραμμές, σε ψύξη ηλεκτρονικών συστημάτων, σε παλμικούς αγωγούς, σε συσκευές ενίσχυσης μεταφοράς μάζας και θερμότητας, σε τεχνολογίες διαχωρισμού και ανάμειξης αερίων και σε συστήματα άντλησης αερίων.

Στην παρούσα διδακτορική διατριβή, οι ταλαντωτικές αραιοποιημένες ροές αερίων διαφόρων διατάξεων ροής μελετώνται σε όλο το εύρος της αραιοποίησης του αερίου και των συχνοτήτων ταλάντωσης. Η μελέτη περιλαμβάνει ταλαντωτικές και παλμικές πλήρως-αναπτυγμένες ροές αερίων σε κυλινδρικούς και τετραγωνικούς αγωγούς, που υπόκεινται σε μικρές διαφορές του πλάτους της πίεσης, όπως επίσης και μη γραμμικές πλήρως-αναπτυγμένες ροές ανάμεσα από δύο παράλληλες πλάκες, που υπόκεινται σε ταλαντωτικές δυνάμεις μικρού ή μεγάλου πλάτους. Η μελέτη των αγωγών επίσης περιλαμβάνει και τη ταλαντωτική ροή μείγματος δύο αερίων ανάμεσα από δύο παράλληλες πλάκες λόγω ταλαντωτικής διαφοράς πίεσης ή συγκέντρωσης. Επιπλέον, διερευνάται η ταλαντωτική ροή σε διατάξεις comb είτε κάθετης είτε παράλληλης αρμονικής ταλάντωσης του κινούμενου τοιχώματος. Ανάλογα με τη διάταξη της ροής, η ανάλυση υιοθετεί είτε τη ντετερμινιστική επίλυση των κινητικών μοντέλων BGK, Shakhov και McCormack είτε τη μέθοδο DSMC. Για όλες τις ροές, μελετάται η επίδραση των παραμέτρων της ροής και της γεωμετρίας πάνω στις μακροσκοπικές κατανομές και στις συνολικές ποσότητες οι οποίες χαρακτηρίζουν την εκάστοτε ροή και οδηγούν σε ευρήματα με τεχνολογικό και θεωρητικό ενδιαφέρον.

Η ταλαντωτική ισοθερμοκρασιακή πλήρως-αναπτυγμένη αραιοποιημένη ροή αερίου σε κυλινδρικό αγωγό και η αντίστοιχη παλμική αραιοποιημένη ροή σε ορθογωνικό αγωγό προσομοιώνονται με βάση το γραμμικοποιημένο χρονομεταβαλλόμενο κινητικό μοντέλο BGK σύμφωνα με οριακές συνθήκες τύπου Maxwell. Δίνονται αριθμητικά αποτελέσματα για το πλάτος, τη διαφορά φάσης και τη χρονική εξέλιξη των ποσοτήτων της ταχύτητας, της παροχής, της μέσης διατμητικής τάσης στο τοίχωμα, των δυνάμεων της αδράνειας και του ιξώδους καθώς και της χρονικά μεταβαλλόμενης και μέσης ισχύς άντλησης. Το εύρος των αποτελεσμάτων καλύπτει όλο το εύρος των παραμέτρων αραιοποίησης και συχνότητας ταλάντωσης. Τα κινητικά αποτελέσματα επιβεβαιώνονται από αποτελέσματα αναλυτικών ή ημι-αναλυτικών λύσεων στη περιοχή ολίσθησης όπως και στην ελεύθερη μοριακή περιοχή, καθώς και με αντίστοιχα αριθμητικά αποτελέσματα μόνιμης ροής. Η μόνιμη ροή εμφανίζεται γρηγορότερα όταν το αέριο είναι πιο αραιό. Τα πλάτη της παροχής και της μέσης διατμητικής τάσης στο τοίχωμα είναι πάντα μικρότερα από τα αντίστοιχα μεγέθη της μόνιμης ροής. Γενικά, όταν αυξάνεται η συχνότητα, το πλάτος των μακροσκοπικών ποσοτήτων μειώνεται και η καθυστέρηση της διαφοράς φάσης τους σε σχέση με τη βαθμίδα πίεσης αυξάνεται και προσεγγίζει την οριακή τιμή των 90^0. Ο λεπτομερής υπολογισμός των δυνάμεων αδράνειας και ιξώδους σε σχέση με τις παραμέτρους αραιοποίησης και ταλάντωσης, αποσαφηνίζει πότε η ροή αποτελείται από ένα ή δύο μέρη ροής. Όταν υπάρχουν δύο μέρη ροής, η μία ροή στο κέντρο είναι ροή χωρίς ιξώδες ενώ η άλλη

xii

εμφανίζει οριακά στρώματα Stokes στα τοιχώματα που χαρακτηρίζονται από υψηλότερη ταχύτητα σε σχέση με το κέντρο της ροής (φαινόμενο Richardson). Όσο το αέριο γίνεται πιο αραιό, χρειάζονται υψηλότερες συχνότητες για να εμφανιστεί αυτό το φαινόμενο. Η συμπεριφορά της παροχής δεν είναι μονοτονική σε σχέση με τη παράμετρο της αραιοποίησης και το μέγιστο πλάτος της εμφανίζεται σε κάποια ενδιάμεση τιμή της παραμέτρου αραιοποίησης, η οποία εξαρτάται όμως και από την παράμετρο της ταλάντωσης. Ο συντελεστής των οριακών συνθηκών τύπου Maxwell, που χαρακτηρίζει την αλληλεπίδραση αερίου-τοιχώματος, επιδρά σημαντικά μόνο στα πλάτη των μακροσκοπικών ποσοτήτων ενώ η επίδραση του στη διαφορά φάσης τους είναι πολύ μικρή. Η μέση ισχύς άντλησης αυξάνεται όταν η συχνότητα ταλάντωσης μειώνεται και η μέγιστη τιμή της ισούται με τη μισή της αντίστοιχης ισχύς άντλησης μόνιμης ροής.

Στη συνέχεια, αναλύεται η μη γραμμική ταλαντωτική πλήρως αναπτυγμένη αραιοποιημένη ροή αερίου λόγω εξωτερικής δύναμης μέσω της μεθόδου DSMC καθώς και μέσω των μη γραμμικών μοντέλων BGK και Shakhov σε οριακές συνθήκες πλήρους διάχυσης. Παρατηρήθηκε πως η χρονική εξέλιξη σχεδόν όλων των ποσοτήτων παραμένει αρμονική και με συχνότητα ίδια με αυτή της δύναμης χωρίς να εμφανίζονται υψηλότερες αρμονικές λόγω των μεγάλων δυνάμεων. Η μόνη ποσότητα που εμφανίζει υψηλότερες αρμονικές είναι η μέση αξονική θερμορροή. Επίσης, η επίδραση των μη γραμμικών φαινομένων είναι εντονότερη σε υψηλά αραιοποιημένες ροές και χαμηλές συχνότητες ταλάντωσης. Τα αποτελέσματα με τη μέθοδο DSMC συγκρίνονται με αντίστοιχα αποτελέσματα της γραμμικής ταλαντωτικής ροής για μικρές δυνάμεις και η απόκλιση μεταξύ των δύο παραμένει μικρότερη του 10 %. Αντιθέτως, για μεγάλες δυνάμεις η απόκλιση αυξάνεται στο 25 %. Το διτροπικό σχήμα της κατανομής θερμοκρασίας και η μη συνεχής κατανομή της πίεσης, που έχουν ήδη μελετηθεί για μόνιμες ροές, παρατηρούνται και εδώ και επιπρόσθετα στη συγκεκριμένη περίπτωση εξαρτώνται από τη παράμετρο αραιοποίησης και τη παράμετρο ταλάντωσης. Η ποσότητα που επηρεάζεται περισσότερο από το πλάτος της εξωτερικής δύναμης είναι η μέση αξονική θερμορροή. Εμφανίζει μία σύνθετη μη-ημιτονοειδής κατανομή που περιέχει αρκετές αρμονικές στη περίπτωση που εφαρμόζονται μεγάλες εξωτερικές δυνάμεις, σε υψηλά αραιοποιημένες ροές και χαμηλές συχνότητες ταλάντωσης. Η μέση ισχύς άντλησης αυξάνεται αναλογικά με το τετράγωνο του πλάτους της εξωτερικής δύναμης και είναι μικρότερη από την αντίστοιχη γραμμική, ακολουθώντας πάντα την ίδια τάση με τις παροχές. Στην περίπτωση μη ισοθερμοκρασιακών πλακών, η μέση κάθετη θερμορροή δεν ενισχύεται με την αύξηση είτε της συχνότητας ταλάντωσης είτε του εύρους της δύναμης. Η μέθοδος DSMC και τα κινητικά μοντέλα συμπίπτουν στις παροχές και τις διατμητικές τάσεις αλλά όχι στη περίπτωση των θερμορροών.

Η μελέτη των ταλαντωτικών ροών σε αγωγούς ολοκληρώνεται με τη διερεύνηση της ταλαντωτικής αραιοποιημένης ροής μείγματος δύο αερίων λόγω διαφοράς πίεσης ή συγκέντρωσης ανάμεσα από δύο παράλληλες πλάκες. Η μοντελοποίηση γίνεται με το κινητικό μοντέλο McCormack σε οριακές συνθήκες πλήρους διάχυσης. Παρουσιάζονται αποτελέσματα για τα μείγματα Ήλιο-Ξένο, Ήλιο-Αργό και Νέον-Αργό των οποίων η συγκέντρωση κυμαίνεται από μηδέν έως ένα. Τα αποτελέσματα περιλαμβάνουν τις μακροσκοπικές ποσότητες κάθε αερίου και του μείγματος και επιβεβαιώνονται επιτυχώς με διάφορους τρόπους συμπεριλαμβανομένης της βελτίωσης του πλέγματος, της ικανοποίησης του ισοζυγίου δυνάμεων καθώς και μέσω συγκρίσεων σε οριακές καταστάσεις, π.χ. με αποτελέσματα της μόνιμης ροής μειγμάτων και με αποτελέσματα της ταλαντωτικής ροής μονοατομικού αερίου. Η παροχή, η διατμητική τάση στο τοίχωμα και η ισχύς άντλησης της ταλαντωτικής ροής του μείγματος αερίων μοιάζουν ποιοτικά με τις αντίστοιχες ποσότητες της ταλαντωτικής ροής ενός αερίου, όσον αφορά τις παραμέτρους αραιοποίησης και ταλάντωσης. Όμως, υπάρχουν και ποσοτικές διαφορές ιδιαίτερα στις παροχές οι οποίες εξαρτώνται από τη συγκέντρωση και τη σύνθεση του μείγματος. Όταν αυξάνεται ο λόγος μοριακής μάζας του βαρέος συστατικού ως προς το ελαφρύ, τότε το πλάτος της παροχής του μείγματος γίνεται μεγαλύτερο σε σχέση με το αντίστοιχο της ροής ενός μονοατομικού αερίου ενώ η διαφορά φάσης γίνεται μικρότερη. Η μεταβολή της παροχής σε σχέση με τη συγκέντρωση είναι μη μονοτονική ενώ το εύρος και η διαφορά φάσης της παροχής εμφανίζουν αντίστοιχα μέγιστες και ελάχιστες τιμές στις ενδιάμεσες τιμές της συγκέντρωσης. Όσον αφορά το κάθε συστατικό, έχει βρεθεί ότι καθώς αυξάνεται η συχνότητα ταλάντωσης, παρόλο που τα πλάτη της παροχής αμφοτέρων των συστατικών μειώνονται, η σχετική διαφορά μεταξύ των παροχών των συστατικών αυξάνεται. Αυτό το φαινόμενο γίνεται πιο έντονο καθώς το αέριο γίνεται πιο πυκνό, κάτι που σίγουρα δεν είναι αναμενόμενο, αφού είναι γνωστό πως τα φαινόμενα διαχωρισμού ενός αερίου μειώνονται καθώς το αέριο γίνεται πυκνότερο. Αυτό οφείλεται σε φαινόμενα αδράνειας, τα οποία αυξάνονται όσο αυξάνεται η συχνότητα ταλάντωσης και επηρεάζουν τη παροχή του βαρέος συστατικού περισσότερο σε σχέση με τη παροχή του ελαφρύτερου. Το φαινόμενο ενισχύεται και άλλο όταν η ροή γίνει πυκνότερη με αποτέλεσμα οι συγκρούσεις των μορίων να υπερισχύουν των φαινομένων διάχυσης, εφόσον όμως η συχνότητα ταλάντωσης είναι αρκετά μεγάλη. Έχει επιβεβαιωθεί ότι στις υψηλές συχνότητες, ο λόγος της παροχής του ελαφρύτερου συστατικού προς τη παροχή του βαρέος συστατικού τείνει στο λόγο της μοριακής μάζας του βαρύτερου προς το ελαφρύτερο, ανεξάρτητα από το βαθμό αραιοποίησης του αερίου. Επίσης, η υστέρηση φάσης της παροχής του βαρέος συστατικού είναι πάντοτε μεγαλύτερη από την αντίστοιχη του ελαφρύτερου, ενώ το φαινόμενο

της υψηλής ταχύτητας στα τοιχώματα γίνεται περισσότερο έντονο όσο αυξάνεται η μοριακή μάζα του κάθε συστατικού. Τα υπάρχοντα αποτελέσματα μπορούν να αξιοποιηθούν για το σχεδιασμό και την ανάπτυξη συσκευών διαχωρισμού αερίων που λειτουργούν σε μέτριες και υψηλές συχνότητες ταλάντωσης και σε όλο το εύρος της αραιοποίησης του αερίου και να εφαρμοστούν σε διάφορους τεχνολογικούς τομείς.

Στη συνέχεια, μελετάται η κλασσική ταλαντωτική ροή Couette και η δισδιάστατη ταλαντωτική αραιοποιημένη ροή σε διάταξεις comb που υπόκειται σε κάθετη ή σε παράλληλη αρμονική ταλάντωση του κινούμενου τοιχώματος. Η ροή Couette αναλύεται με το γραμμικοποιημένο κινητικό μοντέλο BGK και χρησιμοποιείται κυρίως για τη συγκριτική αξιολόγηση των μιγαδικών κινητικών κωδικών. Πολύ καλή σύγκριση παρατηρείται ανάμεσα στα υπάρχοντα αποτελέσματα και τα αποτελέσματα της βιβλιογραφίας. Επίσης, γίνεται αναφορά σε ένα υπολογιστικά αποδοτικό σχήμα τύπου marching όπου το πραγματικό και το φανταστικό μέρος της κινητικής εξίσωσης επιλύεται ξεχωριστά. Επιπλέον, γίνεται αναφορά σε δύο στρατηγικές παραλληλοποίησης με βάση τα πακέτα OpenMP και OpenACC. Το πλεονέκτημα των συγκεκριμένων πακέτων εντοπίζεται στην επιτάχυνση της διαδικασία επίλυσης του προβλήματος χωρίς να απαιτούνται σημαντικές τροποποιήσεις στον αρχικό κινητικό κώδικα. Στη συνέχεια, οι αναπτυγμένοι επαληθευμένοι παράλληλοι κώδικες επεκτείνονται και προσαρμόζονται και στις άλλες εξεταζόμενες ροές αερίων. Η χρονομεταβαλλόμενη ροή σε διάταξη comb επιλύεται με το γραμμικό κινητικό μοντέλο Shakhov σε οριακές συνθήκες πλήρους διάχυσης. Το τμήμα που ταλαντώνεται είναι το εσωτερικό και λόγω της ταλάντωσης εμφανίζονται πολύπλοκα μοτίβα ροής τα οποία εξαρτώνται από τη παράμετρο αραιοποίησης και ταλάντωσης καθώς και από τις διαστάσεις της διάταξης comb. Τα αποτελέσματα εστιάζουν στην μέση ορθή και διατμητική τάση στα κινούμενα τοιχώματα. Όταν αυξάνεται η παράμετρος αραιοποίησης, τα δύο πλάτη των τάσεων αρχικά μειώνονται μέχρι μια ελάχιστη τιμή, μετά αυξάνονται ελάχιστα και στη συνέχεια εμφανίζουν μια ταλαντωτική συμπεριφορά μέχρι οι τιμές τους να παραμείνουν σταθερές. Τα τοπικά ελάχιστα και μέγιστα στα πλάτη αντιστοιχούν σε συγκεκριμένες καταστάσεις αντι-συντονισμού και συντονισμού αντίστοιχα και αυτές οι καταστάσεις μπορούν να εφαρμοστούν για έλεγχο του συστήματος. Οι διαστάσεις της διάταξης comb επηρεάζουν τη ροή σημαντικά σε χαμηλές συχνότητες ταλαντώσεων. Αντίθετα, στη περιοχή υψηλής συχνότητας οι διαστάσεις της διάταξης comb δεν επηρεάζουν την κάθετη και τη διατμητική τάση οι οποίες παραμένουν σταθερές. Σε αυτές τις περιπτώσεις παρατηρείται εγκλωβισμός του αερίου και η ροή μπορεί να μοντελοποιηθεί ως μονοδιάστατη. Τα υπάρχοντα αποτελέσματα μπορούν να αξιοποιηθούν για την ανάπτυξη των αισθητήρων επιτάχυνσης νέας γενιάς και των ταλαντωτών.

Εν κατακλείδι, εξετάστηκαν διάφορες περιπτώσεις ταλαντωτικών ροών σε όλο το ε-
ύρος των παραμέτρων της αραιοποίησης του αερίου και της συχνότητας ταλάντωσης αφού
πρώτα χρησιμοποιηθήκαν συγκεκριμένες κινητικές μεθοδολογίες και τεχνικές προσομο-
ίωσης και μοντελοποίησης. Η μελέτη των ταλαντωτικών και παλμικών ροών μονοατομι-
κών αερίων και μειγμάτων αερίων σε αγωγούς με εξωτερικούς κινητήριους μηχανισμούς,
που έχουν είτε μικρό είτε μεγάλο πλάτος ταλάντωσης, καθώς επίσης και της απόκρισης
της ταλαντωτικής ροής σε διάταξη comb είναι καινοτόμα. Τα αντίστοιχα αποτελέσματα
παρουσιάζονται για πρώτη φορά στη βιβλιογραφία. Τα θεωρητικά ευρήματα και τα υπο-
λογιστικά αποτελέσματα που αναφέρθηκαν εδώ μπορεί να αξιοποιηθούν στον λεπτομερή
σχεδιασμό και τη βελτιστοποίηση διαφόρων τεχνολογικών συσκευών.

Λέξεις κλειδιά: Δυναμική αραιοποιημένων ροών, Ροές εκτός θερμοδυναμικής ι-
σορροπίας, Τεχνολογία κενού, Μικρορευστομηχανική, Ταλαντωτική ροή, Παλμική ροή,
Φαινόμενο Richardson, Μη γραμμική ταλαντωτική ροή, Ταλαντωτική ροή μείγματος αε-
ρίων, Διαχωρισμός αερίου, Διάταξη Comb-drive, Δυνάμεις απόσβεσης

Contents

xx

List of Tables

List of Figures

xxiv

xxvi

xxvii

Chapter 1

Introduction

1.1 General concepts

The field of rarefied gas dynamics is one of the most interesting and promising fields in engineering and physics. Rarefied gas dynamics has existed, in principle, since the nineteenth century but came in the foreground with space exploration [1]. It is considered as branch of fluid dynamics and its aim is to obtain macroscopic characteristics based on microscopic behavior of gaseous particles [2]. In general, the rarefied state of a gas is observed when the average value of the distance between two subsequent collisions of a molecule, i.e., the molecular mean free path, is not negligible in comparison with a characteristic length scale of the flow. When this assumption is valid, the gas is the rarefied state and must be modeled with approaches based on kinetic theory of gases. Otherwise, when the mean free path is too small compared to the characteristic length the flow may be considered as a continuous and the hydrodynamic equations, i.e., the Navier-Stokes-Fourier equations, may be successfully applied.

The restriction about the molecular mean free path, related to the definition of rarefied and continuum gas flows, must be always considered both in steady-state and unsteady gas flow. In nonstationary flows the additional restriction about the mean free time of gaseous particles must also be considered. More specifically, in time-dependent flows, the continuum medium approach is valid only if the mean free time is much smaller than a characteristic time scale of the flow [2]. If the macroscopic quantities are significantly changed in a very small time interval, the flow must be considered as rarefied and simulated with kinetic modeling even if the assumption about the molecular free path isn't valid [2].

Simulations of nonstationary rarefied gas flows have attracted considerable attention over the past years since they have theoretical interest and they are linked to several technological fields. A typical example is the oscillatory gas flow which can be classified as either boundary, or pressure/force driven. Depending on the oscillatory motion, the range of applications is varied. For oscillatory boundary driven flows, there are plenty of applications regarding microelectromechanical systems (MEMS) and particularly resonating filters, sensors [3] and actuators [4, 5, 3, 6]. The gyroscope and the accelerometer are two notable applications that include sensors and actuators. Besides, the MEMS-based accelerometer used in airbag ignition devices became the first high-volume product in the area of inertial MEMS [7]. The oscillatory pressure/force driven internal gas flows are commonly classified as either reciprocating or pulsating flows. In reciprocating flows, the amplitude of the oscillating velocity is larger than the mean-time velocity and the flow direction reverses periodically. Reciprocating flows may occur in reciprocating-piston machines [8], electronic cooling [9], pneumatic actuators and sensors [10], oscillating heat pipe technology [11], enhanced heat and mass transfer devices [12–14], gas separation and mixing technologies [15, 16] and vacuum pumping systems [17, 18]. In pulsating flows, the amplitude of the oscillating velocity is smaller than the mean-time velocity and the flow direction never reverses. Pulsating flows mainly occur in bioengineering in lungs and blood vessels of animals and humans [8, 19], as well as in engineering applications in pump discharging, pneumatic lines and control systems [12, 20] and pulse tubes [21, 22]. Of course, leading applications in rarefied gas dynamics also include devices in high altitude aerodynamics [23] and vacuum technology [22].

It is clear that the number of gas flow applications that operate in rarefied state is significant. Therefore, in the present dissertation, oscillatory gas flows due to harmonically oscillating pressure, force and molar fraction gradients as well as moving walls are investigated. Since the hydrodynamic equations have limitations, kinetic theory and modeling is used in order to properly simulate the gas flows without considering restrictions in the length or the time scale. The validity of the kinetic simulations is confirmed by comparisons between the various kinetic models and the hydrodynamic equations which are used in their range of applicability. A detailed description on the thesis contents and structure is provided in the next Section.

1.2 Dissertation structure and contents

The present thesis aims to the computational study of the pulsatile and oscillatory flows in the whole range of the rarefaction and oscillation parameter. The study involves pressure, force and boundary driven flows in various flow configurations. Depending on the problem, the geometry of the flow may be either simple such as flow between parallel plates or more complex such as flow in comb-type configurations. All oscillatory flows are assumed to be far from local equilibrium and the working medium is either a monoatomic gas or a mixture of gases. The detailed structure of the dissertation is presented:

In **Chapter 2**, a review on the theoretical framework is presented. First, the flow regimes based on the rarefaction of the gas and the oscillation frequency are analyzed. The review continues with the basic principles of kinetic theory along with the implemented numerical methods. Next, since oscillatory flows have been extensively studied in the hydrodynamic regime, a part of the published work is referenced, closely related to the present thesis is cited, followed by an extensive literature review on rarefied oscillatory gas flows.

In **Chapter 3**, the time-dependent isothermal fully-developed rarefied gas flow in a circular tube driven by harmonically oscillating pressure gradient is investigated, based on the linearized unsteady BGK kinetic model equation. The hydrodynamic and the slip solutions are also included. Computational results of the amplitude and the phase angle of the flow rates and the velocity distributions, as well as of the periodic time evolution of these macroscopic quantities, are provided.

In **Chapter 4**, the pulsatile pressure driven fully-developed flow of a rarefied gas through an orthogonal duct is studied, based on the time-dependent linear BGK equation, by decomposing the flow into its steady and oscillatory parts. The investigation is focused on the oscillatory part, which apart from the rarefaction and oscillation parameters it is also characterized by the duct aspect ratio and the accommodation coefficient specifying the gas-surface interaction. In addition to the flow rate and the velocity, the results include the mean acting forces, the mean wall shear stress, and the oscillatory time-dependent and average pumping powers. The kinetic formulation of the pulsatile pressure driven fully-developed flow of a rarefied gas between parallel plates is also considered for complimentary purposes.

In **Chapter 5**, the nonlinear oscillatory fully-developed rarefied gas flow between parallel plates due to an external harmonic force is investigated by stochastic and

deterministic methods, namely the Direct Simulation Monte Carlo and the Discrete Velocity methods respectively. The force amplitude may be arbitrarily large and therefore nonlinear effects are becoming more dominant. A comparison is made between nonlinear and linear results in order to access the nonlinear effects on the oscillatory macroscopic quantities. Another objective is to identify whether the increased force amplitude could generate oscillatory motion containing several harmonics. In addition, some work is performed with nonisothermal plates investigating the coupled flow and heat transfer phenomena in terms of the temperature ratio between the two plates.

In **Chapter 6**, the rarefied, oscillatory, pressure and molar fraction driven binary gas mixture flow between parallel plates is computationally investigated in terms of the mixture molar fraction and the molecular mass ratio of the species, in a wide range of the gas rarefaction and oscillation frequency. Modeling is based on the McCormack kinetic model. The output quantities are in dimensionless form and include the velocity distributions and flow rates of the species, as well as the flow rate, wall shear stress and pumping power of the mixture. The presented results are for He–Xe, He-Ar and Ne–Ar. In addition, the gas separation phenomenon, which occurs due to the higher speed of the light species particles compared to the heavy ones, is investigated.

In **Chapter 7**, the rarefied oscillatory Couette flow is studied in terms of the gas rarefaction and the oscillation frequency. This flow configuration has been investigated in the literature. However it is also included here since it is used for benchmarking purposes. Moreover, a parallelization technique based on OpenMP and OpenACC directives is applied in this flow configuration and it is easily extended in more complex geometries.

In **Chapter 8**, the oscillatory rarefied gas flow in a comb-type structure driven by the vertical/lateral harmonic motion of the moving surface is investigated, based on the linearized unsteady Shakhov kinetic model equation. Due to the element vibration, complex flow patterns are formed in the direction perpendicular and parallel to its surface depending mainly on the gas rarefaction and oscillation parameters. A detailed parametric study on the computation of the average normal and shear stresses of the moving walls is performed finding out the behavior of the forces in terms of the gas rarefaction, the oscillation frequency and the geometry.

In **Chapter 9**, an overview of Chapters 3-8 with the associated concluding remarks is provided. It also includes several thoughts about future work related to the aforementioned flow configurations.

1.3   Novelty and scientific contributions

The investigations of oscillatory and pulsatile flows of single gases and binary gas mixtures in capillaries due to externally imposed small or large amplitude driving mechanisms, as well as of the oscillatory boundary driven comb assembly, are novel and all corresponding results are reported for first time in the literature. In all flow setups the detailed flow behavior and characteristics are thoroughly investigated. The effects of the gas rarefaction, oscillation frequency, tangential accommodation coefficient and aspect ratio, as well as of the molar fraction and mixture composition on the velocity distributions and overall quantities (flow rates, wall shear and normal stress, pumping power) are provided in terms of their amplitude and phase angle. The most noticeable findings of the present Ph.D. thesis may be outlined as follows:

- The velocity overshooting near the walls (Richardson effect), well known in the hydrodynamic regime, is also observed in oscillatory pressure driven rarefied gas flows and depends both on the gas rarefaction and the oscillation frequency. As the gas rarefaction is increased higher oscillation frequencies are needed to trigger these phenomena.

- The time average pumping power is increased as the oscillation frequency is reduced and its maximum value is one half of the corresponding steady-state one.

- In nonlinear oscillatory flows, even with large force amplitudes, all macroscopic distributions, except the axial heat flow, have sinusoidal pattern with their fundamental frequency being the same with the driving frequency of the external force without the appearance of other harmonics.

- At small and moderate external forces, the agreement between nonlinear and linear flow rate amplitudes is very good and always remains less than 10%, while at large external forces the deviation in the flow rate amplitude reaches about 25%.

- At large external forces and highly rarefied flows with low oscillation frequencies the axial heat flow exhibits a complex non-sinusoidal pattern containing several harmonics.

- In oscillatory rarefied binary gas mixture flow as the oscillation frequency is increased, although the flow rate amplitudes of both species are decreased, the

5

relative difference between the flow rate amplitudes of the light and heavy species is increased and this behavior, due to inertia effects, becomes more pronounced as the gas rarefaction is decreased.

- At high frequencies the flow rate amplitude ratio of the light over the heavy species, independent of the gas rarefaction parameter, tends to the molecular mass ratio of the heavy over the light species.

- In comb-type assemblies, the wall normal and shear stresses affecting the system dissipation strongly depend on the gas rarefaction and the oscillation frequency parameters, as well as the comb geometry.

- Certain anti-resonance and resonance states have been identified.

- The comb dimensions affect the flow at low oscillation frequencies, while at high ones, due to gas trapping, the flow is not affected and may be modeled as one-dimensional.

- Based on the OpenMP and OpenACC directives, a parallelization strategy is proposed for solving deterministic kinetic equations with the so-called marching scheme

All computational results, along with the above outlined remarks, are described and justified in detail in the corresponding chapters of the present Ph.D. thesis.

Chapter 2

Literature review

2.1 Flow regimes based in oscillatory gas flows

In oscillatory gas flows the flow regimes are defined based on the Knudsen number (or the gas rarefaction parameter) and the oscillation parameter related to the flow space and time scales respectively.

The Knudsen number [24] is defined as

$$Kn = \frac{\lambda}{L} \tag{2.1}$$

where the molecular mean free path λ is defined as the average value of the distance between two subsequent collisions of a molecule and L is a characteristic length of the flow configuration or a length scale of a macroscopic gradient, given by $L = \varphi/(\partial\varphi/\partial x)$, where φ is a macroscopic flow quantity. The derivation of the molecular mean free path λ for hard-sphere molecules is found in [25] and may be written as

$$\lambda = \frac{1}{\sqrt{2}\pi d^2 n}, \tag{2.2}$$

where n is the number density and d is the molecular diameter. The Knudsen number can also be written in terms of the Mach and Reynolds numbers as

$$Kn = \sqrt{\frac{\gamma\pi}{2}}\frac{Ma}{Re}, \tag{2.3}$$

where γ is the ratio of the specific heats of the gas ($\gamma = 5/3$ for a monoatomic gas). Instead of the Knudsen number the gas rarefaction parameter may also be used. It is

based on an equivalent free path which is proportional to the molecular free path [2] and it is defined as

$$\delta = \frac{PL}{\mu v_0} \sim \frac{1}{Kn}, \tag{2.4}$$

where P is the gas pressure, μ is the gas viscosity at some reference temperature T and $v = \sqrt{2R_g T}$ is the most probable molecular speed ($R_g = k_B/m$, with k_B denoting the Boltzmann constant and m the molecular mass, is the gas constant). It is noted that the rarefaction parameter is proportional to the inverse Knudsen number. Based on the Knudsen number (or the rarefaction parameter), the flow regimes can be classified as follows: continuum ($Kn \leq 0.001$), slip ($10^{-3} < Kn \leq 10^{-1}$), transition ($10^{-1} < Kn \leq 10$), and the free molecular ($Kn > 10$).

The oscillation parameter is expressed in terms of the intermolecular collision frequency v and the oscillation frequency ω. The dimensionless oscillation frequency (or the oscillation speed parameter) has been introduced by Sharipov in [26] and ever since it has been widely used. Since the intermolecular collision frequency has the order of P/μ, the oscillation speed parameter [27, 26, 28] is defined as the ratio of the intermolecular collision frequency $\nu = P/\mu$, over the oscillation frequency ω:

$$\theta = \frac{P}{\mu\omega}. \tag{2.5}$$

Hence, small and large values of θ correspond to high and low oscillations respectively.

At this point it may be useful to point out that the Strouhal number (also known as the ballistic Stokes number), which is commonly applied in oscillatory flows, is related to the δ and θ parameters as follows: $St = (\omega L)/v_0 = \delta/\theta$. Also, it is readily found that the Stokes number β (or the Womersley number [29], or the kinetic Reynolds number β^2), which is a measure of viscous versus unsteady effects in oscillatory flow, may be written as $\beta = L\sqrt{\omega\rho/\mu} = \delta/\sqrt{2\theta}$ with ρ being the mass density. For the purposes of the present dissertation however, it is more convenient parameterizing the problem in terms of δ and θ, instead of replacing both of them with one of these classical fluid mechanics numbers, because it is easier to uncouple and separately investigate the effects due to gas rarefaction and oscillation frequency. Also, the limiting solutions are identified more clearly.

All investigated oscillatory flows are solved in the whole range of the two parameters (rarefaction and oscillation), which may vary from zero to infinity. Since an oscillatory flow is defined by two parameters, it is readily seen that the flow regimes depend now on both parameters. When the oscillation parameter is large (or the oscillation frequency

is small) and it is also larger than the rarefaction parameter ($\delta \ll \theta$), the steady-state regime is established. Here, the magnitude of the oscillatory flow quantities is almost the same as the corresponding steady-state ones. The flow is in the hydrodynamic and slip regimes when both $\delta \gg 1$ and $\theta \gg 1$, i.e., when both the equivalent mean free path is small compared to the characteristic length L and the collision frequency is much higher than the oscillation frequency ω [28]. In these regimes the solution is based on the unsteady Navier-Stokes equation with either no-slip or slip boundary conditions. Another limiting regime is the free molecular one ($\delta \ll 1$) which is seen for both steady-state and oscillatory flows. Finally, another regime of some interest is the high-frequency oscillation regime ($\theta \ll 1$) in which the oscillation frequency is much larger than the intermolecular collision frequency. In these high oscillation frequencies, the propagation of the gas is limited due to inertia forces.

A graphical view of all flow regimes is provided in Fig. 2.1, where they are defined quantitatively versus the rarefaction and oscillation parameters. In addition, the Knudsen number and the oscillation frequency are added as secondary axes. Time dependent kinetic modelling should always be used in the free molecular, transition and high frequency regimes and it can be easily verified with steady-state kinetic equations and continuum theory.

Finally, in Table 2.1, the rarefaction and the oscillation parameters are presented in terms of the pressure P and for the characteristic lengths $L = [10^{-6}, 10^{-3}, 10^{-1}]$ m and oscillation frequencies $\omega = [10^2, 10^4, 10^6]$ Hz. The chosen parameters are for Argon with temperature 293 K. Small dimensions and high frequencies are typical in MEMS, while the larger dimensions and lower frequencies at low pressures are common in vacuum technology.

2.2 Elementary principles of kinetic theory

It has been pointed out that solutions based on kinetic theory of gases are valid in all flow regimes [27, 28]. Here, some main aspects of kinetic theory of gases, which are implemented in the present thesis, are reviewed. Maxwell and Boltzmann were the first to realize that the exact dynamics of N particles could not be used in practical calculations since it would require a vast number of real variables [1] and therefore they had to recourse to statistics. Maxwell introduced a velocity distribution function $f(t, \boldsymbol{r}, \boldsymbol{\xi})$ [30, 31] which gives the probability of finding a molecule around the location $\boldsymbol{r}$, with velocity $\boldsymbol{\xi}$ at time t. This distribution function was named after him and it is

known as the Maxwell or Maxwellian distribution function. It is also known as the Maxwell-Boltzmann distribution function and it is given by

$$f^M\left(t, \boldsymbol{r}, \boldsymbol{\xi}\right) = n\left(t, \boldsymbol{r}\right) \left[\frac{m}{2\pi k_B T\left(t, \boldsymbol{r}\right)}\right]^{3/2} \exp\left[-\frac{m\left(\boldsymbol{\xi} - \boldsymbol{u}\left(t, \boldsymbol{r}\right)\right)^2}{2\pi k_B T\left(t, \boldsymbol{r}\right)}\right] \qquad (2.6)$$

where n, T and $\boldsymbol{u}$ denote the local density, temperature and velocity vector, m is the molecular mass and k_B is the Boltzmann constant.

Next, Boltzmann derived a transport equation for the distribution function which is written as [32]

$$\frac{\partial f}{\partial t} + \boldsymbol{\xi}\frac{\partial f}{\partial \boldsymbol{r}} + \boldsymbol{F}\frac{\partial f}{\partial \boldsymbol{\xi}} = Q\left(f, f'\right) \qquad (2.7)$$

where Q is the collision term and $\boldsymbol{F}$ is the acceleration which arises due to an external force field. It is known that the Boltzmann equation is a particle balance equation along a trajectory. The left hand side of Eq. (2.7) represents the streaming motion of the molecules along the trajectories associated with the force $\boldsymbol{F}$. The right hand side of Eq. (2.7) is expanded into

$$Q\left(f, f'\right) = \iint \left(f' f'_* - f f_*\right) g\sigma\left(\Omega\right) d\Omega d\boldsymbol{\xi}_* \qquad (2.8)$$

where $f f_*$ and $f' f'_*$ are the distribution functions of the molecules before and after collision, respectively, $g = |\boldsymbol{\xi} - \boldsymbol{\xi}_*|$ is the relative velocity, σ is the differential cross section and $d\Omega$ is the differential solid angle [25]. Inside the parenthesis, the first term is known as the gain part and it refers to particles that obtain a velocity around $\boldsymbol{\xi}$ while the second term is named as the lost part and the particles obtain a different velocity than $\boldsymbol{\xi}$. In general, the right hand side represents the effect of intermolecular collisions taking molecules in/out the streaming trajectory. It is noted that the derivation of the Boltzmann equation has two main assumptions with the first one being that only binary collisions are assumed, limiting its application to dilute gases. The second one is the hypothesis of molecular chaos ("Stosszahlansatz") which states that the distribution function f is uncorrelated with the distribution function f_* [32].

Another major contribution by Boltzmann is the H-Theorem which states that for a uniform gas with no external forces acting on the molecules the H-function is a non-increasing function of time [25]. The H-function is defined as

$$H = \int f \log f \, d\boldsymbol{\xi}. \qquad (2.9)$$

As $t \to \infty$, H will tend to a finite limit, corresponding to a state where $dH/dt = 0$ which leads to the Maxwellian distribution. Therefore, the Boltzmann equation describes a process which is irreversible in time. It is also noted that H-Theorem is equivalent to the second law of thermodynamics which states that entropy cannot decrease.

The solution of the Boltzmann leads to the distribution function which is then integrated to yield all the macroscopic quantities of interest. Therefore, the macroscopic quantities are expressed as moments of the distribution function:

- Number density

$$n\left(t,\boldsymbol{r}\right) = \int_{-\infty}^{\infty} f \, d\boldsymbol{\xi} \tag{2.10}$$

- Velocity vector

$$\boldsymbol{u}\left(t,\boldsymbol{r}\right) = \frac{1}{n\left(t,\boldsymbol{r}\right)} \int_{-\infty}^{\infty} f \, d\boldsymbol{\xi} \tag{2.11}$$

- Pressure

$$P\left(t,\boldsymbol{r}\right) = \frac{m}{3} \int_{-\infty}^{\infty} \left(\boldsymbol{\xi} - \boldsymbol{u}\right)^2 f \, d\boldsymbol{\xi} \tag{2.12}$$

- Stress tensor

$$P_{ij}\left(t,\boldsymbol{r}\right) = m \int_{-\infty}^{\infty} \left(\xi_i - u_i\right)\left(\xi_j - u_j\right) f \, d\boldsymbol{\xi} \tag{2.13}$$

- Temperature

$$T\left(t,\boldsymbol{r}\right) = \frac{m}{3k_B n\left(t,\boldsymbol{r}\right)} \int_{-\infty}^{\infty} \left(\boldsymbol{\xi} - \boldsymbol{u}\right)^2 f \, d\boldsymbol{\xi} \tag{2.14}$$

- Heat flux vector

$$\boldsymbol{q}\left(t,\boldsymbol{r}\right) = \frac{m}{2} \int_{-\infty}^{\infty} \left(\boldsymbol{\xi} - \boldsymbol{u}\right)^2 \left(\boldsymbol{\xi} - \boldsymbol{u}\right) f \, d\boldsymbol{\xi} \tag{2.15}$$

Eqs. (2.12) and (2.14) are combined to yield the ideal gas law

$$P\left(t,\boldsymbol{r}\right) = n\left(t,\boldsymbol{r}\right) k_B T\left(t,\boldsymbol{r}\right). \tag{2.16}$$

2.3 Kinetic models and boundary conditions

Even though the Boltzmann equation describes rigorously the transport phenomena related to gas flows, its solution is a very challenging task due to the five-fold collision integral. Therefore, in order to apply kinetic modelling in engineering problems the complex collision operator must be replaced with a simpler collision model. However,

each collision model must satisfy the collision invariants and the H-theorem as the Boltzmann collision integral does. It also needs to provide correct expressions for the transport coefficients.

The most widely known collision model is the Bhatnagar, Gross and Krook (BGK) model [33], which has been also proposed, independently, by Welander (1954) [34]. It is written as

$$Q = v \left(f^M - f \right) \tag{2.17}$$

where the collision frequency $v = P/\mu$ is assumed to be independent of the molecular velocity and f^M is the Maxwellian distribution. The BGK model produces a Maxwellian distribution after a single collision, while real molecules need a few collisions to attain this distribution. The advantages of the BGK model are the computational efficiency and its linearized form. The major shortcoming is that the correct expressions of both viscosity and thermal conductivity can not be proved simultaneously. As a result, it gives the Prandtl number $\mathrm{Pr} = 1$ instead of the correct one $\mathrm{Pr} = 2/3$ for monoatomic gases. However, it has been extensively used in rarefied gas flows and it has provided satisfying results in the whole range of the Knudsen number [35]. The BGK model along with the Shakhov model, mentioned in the next paragraph, are applied throughout the present dissertation.

The Shakhov model was introduced in [36] and its collision term is given by

$$Q = v \left(f^M \left[1 + \frac{2m}{15n \left(k_B T \right)^2} \boldsymbol{q} \cdot \left(\boldsymbol{\xi} - \boldsymbol{u} \right) \left[\frac{\left(\boldsymbol{\xi} - \boldsymbol{u} \right)^2}{2 k_B T} - \frac{5}{2} \right] \right] - f \right). \tag{2.18}$$

This model satisfies all collision invariants and provides correct expressions for the transport coefficients. However, the H-theorem can be proved only for its linearized form. In general, it is considered reliable and it provides accurate results. Another kinetic model, which satisfies all the prerequisites for the kinetic models but computationally is more intensive compared to the BGK and Shakhov models is the Ellipsoidal-Statistical (ES) model [37]. There are several kinetic models for monoatomic gases but the BGK, Shakhov and ES are the most common ones. In the present thesis both the BGK and Shakhov models are implemented. There are several other models that have been proposed for polyatomic gases [38, 39, 37, 40].

It is interesting to note that the distribution function can be linearized in terms of a small quantity. This quantity may be a boundary wall moving slowly or a small pressure gradient. The linearization is usually suitable for flow configurations that

are slightly perturbed from local equilibrium since it may significantly simplify their solution. In oscillatory flows, the amplitude of the small quantity is used in order to linearize the kinetic equations. The linear theory along with the linearized kinetic models is applied in the flow configurations of Chapters 3, 4, 6, 7 and 8. A complete analysis on linear theory is given in [2].

In the case of gaseous mixtures the involved phenomena are more complex than in single gases and many kinetic models for mixtures have been derived. They include the models by Sirovich [41], Morse [42], Hamel [43], McCormack [44], Andries [45] and Kosuge [46]. Each one has its own drawbacks or limitations and it seems that no general ideal model exists. Depending upon the specific flow setup each time the most suitable kinetic model may be chosen [47]. For the flow configurations considered in the present thesis, the widely used and successfully implemented linear kinetic model by McCormack is very well suited [48–50, 47, 51]. Its collision term is written as

$$
L_{\alpha\beta}\left(c_{a,i}\right) = -\gamma_{\alpha\beta}h_a + \gamma_{\alpha\beta}n_a + 2\left[\gamma_{\alpha\beta}u_{a,i} - v_{\alpha\beta}^{(1)}\left(u_{a,i} - \sqrt{\frac{m_a}{m_\beta}}u_{\beta,i}\right) - v_{\alpha\beta}^{(2)}\left(q_{a,i} - \left(\frac{m_a}{m_\beta}\right)^{3/2}q_{\beta,i}\right)\right]c_{a,i}
$$

$$
+\left[\gamma_{\alpha\beta}T_a - 2\frac{m_0}{m_\beta}\left(T_a - T_\beta\right)v_{\alpha\beta}^{(1)}\right]\left(c_a^2 - \frac{3}{2}\right) + 2\left[\left(\gamma_{\alpha\beta} - v_{\alpha\beta}^{(3)}\right)P_{a,ij} + v_{\alpha\beta}^{(4)}P_{\beta,ij}\right]c_{ai}c_{aj}+
$$

$$
\frac{8}{5}\left[\left(\gamma_{\alpha\beta} - v_{\alpha\beta}^{(5)}\right)q_{a,i} + v_{\alpha\beta}^{(6)}q_{\beta,i} - \frac{5}{8}v_{\alpha\beta}^{(2)}\left(u_a - \sqrt{\frac{m_\alpha}{m_\beta}}u_{\beta,i}\right)\right]c_{a,i}\left(c_a^2 - \frac{5}{2}\right)\bigg\} \qquad (2.19)
$$

where $i, j = x, y, z$, $i \neq j$, $a, \beta = 1, 2$, $\alpha \neq \beta$ and $c_{a,i} = u_i\left(m_a/2KT\right)^{1/2}$ is the dimensionless molecular velocity with m_a denoting the mass of the component. Also, the terms $v_{\alpha\beta}^{(k)}$ and $\gamma_{\alpha\beta}$ refer to type of collisions while m_0 denotes the reduced mass. It is noted that subscript a refers to each species of the gas mixture. The McCormack model has been chosen to simulate the oscillatory binary gas mixture flow in Chapter 6.

In order to solve a kinetic theory problem, the Boltzmann equation or the kinetic models must be complemented by the correct boundary conditions. Maxwell proposed two simple models for interaction of gas molecules with solid surfaces: the specular and the diffuse reflection models [52]. However, in order to present the models, the definition of the scattering kernel $W\left(\boldsymbol{\xi}' \to \boldsymbol{\xi}\right)$, which describes the probability that a molecule with velocity $\boldsymbol{\xi}'$ will be reflected from the boundary with velocity $\boldsymbol{\xi}$, must be specified. Then, the diffuse reflection model assumes that the molecules leaving the

surface scatter with a Maxwellian distribution, characterized by the velocity n_W and the temperature T_W of the surface. The model is written in terms of the scattering kernel as

$$W_D \left(\boldsymbol{\xi}' \to \boldsymbol{\xi} \right) = \frac{1}{2\pi} n \, \boldsymbol{\xi} \left(\frac{m}{k_B T_W} \right)^2 \exp \left[-\frac{m \left(\boldsymbol{\xi} - u_W \right)^2}{2 k_B T_W} \right] \tag{2.20}$$

where n is a unit vector normal to the surface and it is headed towards the flow direction. In the specular reflection model, only the normal to the wall part of the relative velocity reverses its direction, while the two tangential remain unchanged. The scattering kernel of the specular reflection is given by

$$W_S \left(\boldsymbol{\xi}' \to \boldsymbol{\xi} \right) = \delta \left[\boldsymbol{\xi}' - \boldsymbol{\xi} + 2 \left(\boldsymbol{\xi} \, n \right) n \right] \tag{2.21}$$

where δ is the Dirac function. The Maxwell diffuse – specular scattering model is completed when the two previous models are combined to yield

$$W \left(\boldsymbol{\xi}' \to \boldsymbol{\xi} \right) = a W_D \left(\boldsymbol{\xi}' \to \boldsymbol{\xi} \right) + \left(1 - a \right) W_S \tag{2.22}$$

where $0 \leq a \leq 1$ is the tangential momentum accommodation coefficient. The Maxwell scattering models have been widely implemented in several gas flow setups [53–55] and therefore they are also applied in the present thesis. There are more advanced scattering kernels such as the ones by Epstein [56] and by Cercignani-Lampis [57, 58], that may be applied in specific flow configurations, where a more detailed description of the gas-surface interaction is needed.

2.4   Numerical methods

It has been seen that the collision integral of the Boltzmann equation is simplified with the use of reliable kinetic models. The simplified kinetic models, along with recent advancements in computer science, have made the solution of kinetic theory problems feasible. There are several computational methods for obtaining proper solutions in the transitional regime. Some of them are considered as analytical, such as the moments method [59, 60], while other combine analytical and numerical methods such as the Integro-moment method [35, 61]. However, two numerical methods have been widely embraced by the scientific community: the Discrete Velocity Method (DVM) [62, 63] and the Direct Simulation Monte Carlo (DSMC) [64].

The DVM is a deterministic method and it converts the integrodifferential equation to a system of partial differential equations [1]. The method is based on the discretization of the molecular velocity space where the continuum spectrum is substituted by a discrete set of velocities. The discretization in the physical space is usually based on a 2nd order central difference schemes. Then, a partial (or an ordinary) differential equation is solved for each discrete velocity. Finally, the discretized equations are solved in an iterative manner. The complete formulation along with details on the iterative procedure is given in [2]. A well-known disadvantage of the method is the slow convergence in the hydrodynamic and slip regimes which increases computational time. It is also noted that the accuracy of the numerical results is increased as the number of the discrete velocities is increased.

The DSMC method, introduced by Bird [65], is a stochastic or probabilistic method. Each model molecule represents a large number of real gas molecules and their collisions are also representative. At first, the simulated molecules are moved without considering any collisions and subsequently the velocities are altered according to the collision model, which may be either a simple one as the hard sphere and the variable hard sphere (VHS) [64] model or a more complicated one as the variable soft sphere (VSS) model [66]. The main drawback of the method is the statistical scattering (or statistical noise) which is increased for flows with low Mach number. It has been proved that the DMSC method recovers the solution of the Boltzmann equation as the number of particles tends to infinity [67].

Oscillatory flows are considered as time dependent flows and in general require a time dependent kinetic formulation. In cases of harmonic motion however, the oscillation is composed of two parts: the first one represents the "transient" vibration which is soon damped; the second part characterizes the periodic harmonic motion with frequency equal to that of the driving force [68]. The second part is commonly called "periodic steady-state" and the periodic motion repeats itself exactly, every successive cycle. Both DVM and DSMC can capture the "full" oscillatory motion however, in most flow configurations the research interest lies on the second part. Thus, it is convenient to use the DVM method and subsequently the kinetic model equations to compute directly the "periodic steady-state" and omit the transient part. This can be done with various mathematical tools although the most well-known one is by introducing the complex factor $\exp\left(-i\,\omega\,t\right)$ into the kinetic equations. This procedure reduces computational time and it is analyzed in Chapters 3, 4, 6, 7 and 8 which deal with linear kinetic theory problems. On the contrary, in the nonlinear oscillatory flow

considered in Chapter 5 the time dependent formulation is applied. In this latter case the real and imaginary parts are not separable [68] and consequently the complex factor cannot be employed. It is noted that only the real part of the complex quantity has physical significance. Overall, the DVM method is the main numerical method applied throughout the present dissertation, while the DSMC method is also used only for nonlinear simulations.

2.5 Oscillatory flows via continuum modelling

Oscillatory flows have been widely investigated in the hydrodynamic regime, based on the Navier-Stokes equations. Oscillatory flow is originated by Stokes himself, considering one-dimensional shear flow of a viscous fluid near an oscillating plate parallel to the flow [69]. This problem is well known as the Stokes second problem. Another classic fluid mechanics problem is the oscillatory Poiseuille flow induced by an harmonically oscillating pressure gradient [70–72]. In spite its simplicity, interesting findings for the velocity field in terms of the oscillation speed have been reported. It has been seen that for small oscillation frequency the velocity distribution has the same phase as the pressure gradient, while for large oscillation frequencies the velocity lags the pressure gradient by 90^0. Furthermore, in the latter case the flow consists of the inviscid piston flow core layer and the frictional Stokes wall layer with the velocity overshooting. The overshoot is also known as the "Richardson annular effect" which was first observed by Richardson and Tyler [73] when they studied experimentally the reciprocating flow of air in a tube. They found that the velocity square exhibits its maximum within the Stokes layer and not, as expected, in the center of the core. This has been also proved theoretically by Sexl [74]. Several other researchers have solved the Navier-Stokes equations for velocity in oscillating pipe and channel flows [75–78]. An extended analysis for pulsating flow in a pipe has been done by Uschida [78]. Mathematical treatment of oscillatory flows in various geometries includes Fourier expansion [78], Laplace transform [77] and Green functions [79]. An early survey of the implemented analytical and semi-analytical methodologies may be found in [80]. Oscillating and pulsating pressure gradient flows, due to their theoretical and technological interest, remain an active area of research in the hydrodynamic regime using continuum based flow models [81, 9, 82–84].

The oscillatory pressure driven flows have also been applied in flow configurations with concentration gradients. It has been shown that the rate of mass transfer through

a long tube connecting two reservoirs of constant concentration with oscillatory flow is increased in comparison with pure molecular diffusion [85, 86]. This mass enhancement occurs even when the net flow rate over a cycle is zero. For fluids containing several species, the oscillatory motion will cause each species to transport at a different rate and therefore produce separation of the species [87–90]. This has been shown both theoretically [89] and experimentally [89] and the mechanism is better explained in [91]. Furthermore, it has been found that there are crossover oscillation frequencies [89, 91, 92], where the axial transport of each species is the same. Hence, determining the optimum parameters for the separation of species is not a trivial task and it is studied continuously [15, 93, 13]. In conclusion, this area of research, while it has been extensively studied with continuum based models, has received very little attention in the transition regime and therefore a similar analysis based on kinetic theory of gases is going to be presented in Chapter 6.

Owing to the analogy between mass and heat transfer, it has been seen by Kurzweg [94] that axial heat diffusion is enhanced by an oscillatory motion of the flow. More specifically, the heat transfer rate from a colder reservoir to the hotter one has been increased without an accompanying net convective mass transport. The optimum conditions to achieve maximum heat transfer have been later investigated by Kurzweg [95] and other researchers [96, 97]. Next, similar flow configurations, where an oscillatory flow is produced in a long heated pipe has attracted a lot of attention [98–104]. It has been a controversial point between researchers whether a superposed flow pulsation enhances heat transfer in the original steady flow. It has been reported that flow pulsation augments heat transfer in [99, 14], while on the contrary in [100, 102] that it deteriorates heat transfer. Also, in [101, 104] it is stated that heat transfer is not affected and finally in [105, 98, 103] it either augments or deteriorates heat transfer, depending on flow parameters. Clearly this issue it remains an open problem. It is noted that in Chapter 5 the heat transfer between parallel plates coupled to an oscillatory flow is investigated in the whole range of the Knudsen number.

Oscillatory boundary driven flows have always received considerable attention. The correct computation of damping forces along with the spring forces and the inertial forces is critical for the operation of several devices. Depending on the boundary motion, the flows are divided into two main categories: pressure-driven flow (squeeze-film effect), and shear-driven flow (slide damping, lateral damping) [106]. In the first one, the surface is oscillating vertically to its own plane while in the second one it is oscillating parallel to the flow direction. Since the bibliography in the current topics is

17

abundant, only selected references are cited. The squeeze-film problem has been the subject of investigation in several scientific disciplines. In tribology, the well-known Reynolds lubrication theory [107] has been successfully applied for many years. In fluid mechanics, the motion of the gas is modelled by hydrodynamic equations [108] while in acoustics, the gas is considered as compressible, inviscid medium with no mean flow and therefore it can be represented with the wave equation [109]. An excellent review for the different solutions on the problem of a plate vibrating in the direction normal to a wall has been given by Beltman [110]. Furthermore, the shear-driven flow is identified as the Couette flow for slowly moving plates and as Stokes flow for rapidly moving plates [7]. Here, the solution is mainly based on the Navier-Stokes equations [111–113] and it may include or exclude the inertia fluid terms depending on the oscillation frequency.

Both in the squeeze-film and shear-driven flows, significant work has been done by Veijola [114–116, 6, 117] in the slip regime, by including rarefied effects based on the implementation of slip boundary conditions in continuum models and increasing the range of applicability of the hydrodynamic equations. Of course, the aim of the present work is to compute damping forces in the whole range of the gas rarefaction and oscillation frequency and this is achieved by applying kinetic modeling, as presented in Chapters 7 and 8.

2.6 Oscillatory flows via kinetic modelling

Oscillatory flows in the transition regime may be due some gradient in the flow direction or due to moving boundaries. The former ones, so far, have not been investigated at all, while the latter ones have been considered at certain extend.

It is noted that steady-state pressure driven flows have been extensively investigated over the whole range of the Knudsen number [118–121]. In all these solutions the channel is assumed to be sufficiently long therefore the flow can be considered as fully developed. The results depend mainly on the Knudsen number and the cross section and they are obtained with linearized kinetic equations. However, as the length of the channel is reduced, the nonlinear kinetic equations or the DSMC method need to be solved [122–125] and the computational cost is increased except for channels with moderate lengths where the end effect theory may be applied [123, 126]. The corresponding oscillatory pressure driven flow configurations have not been addressed except for the ones introduced in the present thesis using the fully developed theory

[127, 128]. Since steady-state pressure/force driven flows are used as a validation tool for each oscillatory flow, more steady-state references are reported in the introduction of each Chapter.

Flow configurations due to oscillating boundaries have been investigated. The sound wave propagation in a rarefied gas due to mechanical vibration is one of the first problems to be solved with kinetic theory [129–131]. The solution is based on two different kinetic models [129, 130] and the Boltzmann equation [131] and the compared numerical and experimental results [132] are found to be in good agreement. The shear and thermal waves have also been analyzed with the BGK kinetic model [133]. The main outcome of all the aforementioned research is that the Navier-Stokes equations are applied only at low oscillation frequencies.

Recently, the development of MEMS has led to a reconsideration of all flow configurations related to sound/shear/thermal wave propagation in rarefied gases. Due to smaller dimensions and higher oscillation frequencies, kinetic modelling is used to access the range of applicability of the continuum-based models. The research work includes sound propagation in half space [28], between parallel plates [134–136, 27, 137, 138] and in rectangular cavities [139], as well as in nonplanar geometries [140–143]. The corresponding oscillatory shear driven flows between parallel plates [144–146, 28, 147] and in rectangular cavities [148] have also been considered. In addition to waves generated with mechanical vibrations, the thermoacoustic (or thermal) waves have been simulated either in simpler flow configurations (e.g. between parallel plates [149–151]) or in flows between coaxial cylinders [152]. Of course, all the research work is based mainly on kinetic type approaches. More specifically, the DSMC approach is applied in [140–142, 135, 145, 136, 150, 153, 146], the linearized Boltzmann equation in [144, 149, 134, 139, 148] and the linearized Bhatnagar–Gross–Krook (BGK) and Shakhov (S) models in [27, 152, 151, 28, 147, 143]. In the deterministic approaches, the velocity (or the temperature) amplitude of the oscillating plate is assumed to be adequately small so that the governing equations can be linearized. No restriction is applied to the oscillation frequency which may be arbitrary large. Also, in most cases 1st and 2nd order slip results, as well as free molecular analytical solutions are reported validating the kinetic solutions at the hydrodynamic and the free molecular limits respectively.

The considerable attention, that the time-dependent rarefied gas flows driven by harmonically oscillating boundaries have attracted, arises from their application in a variety of systems, such as resonating filters, sensors and actuators, where the

19

computation of the damping forces is crucial in order to control and optimize the resolution and sensitivity of the signal [106]. More specifically, the research is focused on the minimization of the damping forces by exploiting either the resonant behavior of the gas or the optimal combination of sound and thermal waves. It has been found that the damping force is reduced when the oscillation frequency is oscillating near the anti-resonance frequency of the gas [154, 155]. Also, combined effects of harmonically varying the boundary velocity and temperature have been considered to reduce the signal and achieve "acoustic cloaking" [153, 156].

The above cited works are based on the linearized Boltzmann equation or the linearized kinetic models, while the ones based on the DSMC method are restricted to small velocity (or temperature) amplitude of the oscillating plate. Nonlinear oscillatory flows due to large velocity or temperature amplitudes have been also investigated. For example, the nonlinear sound wave propagation has been computed with the DSMC method [157] and the BGK model [158–160]. Also, it has been shown that as the velocity amplitude of the oscillating wall is increased, the macroscopic quantities may contain several harmonics [161–163]. The corresponding nonlinear force driven flow has been recently examined with the DSMC method [164] and it is presented in Chapter 5 along with the deterministic formulation.

Closing this section, it is interesting to cite some works related to oscillatory binary gas mixture flows. The main flow configuration, that has been studied, is the sound wave propagation in binary gas mixtures [165, 166]. Also, the thermoacoustic wave in a binary gas mixtures has been recently investigated and the reciprocal relations between cross phenomena due to thermoacoustic and vibracoustic waves have been verified [167]. Another outcome of the oscillatory mixture flows is that that the resonances/anti-resonances found in single gases are not observed for gas mixtures near the continuum regime due to different excitation modes of each gas [168, 169]. The corresponding oscillatory binary gas mixture flow due to an harmonically oscillating pressure gradient has not been addressed so far and it is presented here in Chapter 6.

Table 2.1 Rarefaction and oscillation parameters in terms of pressure P for Argon, with $T = 293$ K, $L = [10^{-6}, 10^{-3}, 10^{-1}]$ m and $\omega = [10^2, 10^4, 10^6]$ Hz.

P [Pa]	$\delta\,(L = 10^{-6})$	$\delta\,(L = 10^{-3})$	$\delta\,(L = 10^{-1})$	$\theta\,(\omega = 10^2)$	$\theta\,(\omega = 10^4)$	$\theta\,(\omega = 10^6)$
0.001	1.35(-7)	1.35(-4)	1.35(-2)	7.5(-2)	7.5(-4)	7.5(-6)
0.01	1.35(-6)	1.35(-3)	1.35(-1)	7.5(-1)	7.5(-3)	7.5(-5)
0.1	1.35(-5)	1.35(-2)	1.35	7.5	7.5(-2)	7.5(-4)
1	1.35(-4)	1.35(-1)	1.35(+1)	7.5(+1)	7.5(-1)	7.5(-3)
10	1.35(-3)	1.35	1.35(+2)	7.5(+2)	7.5	7.5(-2)
100	1.35(-2)	1.35(+1)	1.35(+3)	7.5(+3)	7.5(+1)	7.5(-1)
1000	1.35(-1)	1.35(+2)	1.35(+4)	7.5(+4)	7.5(+2)	7.5
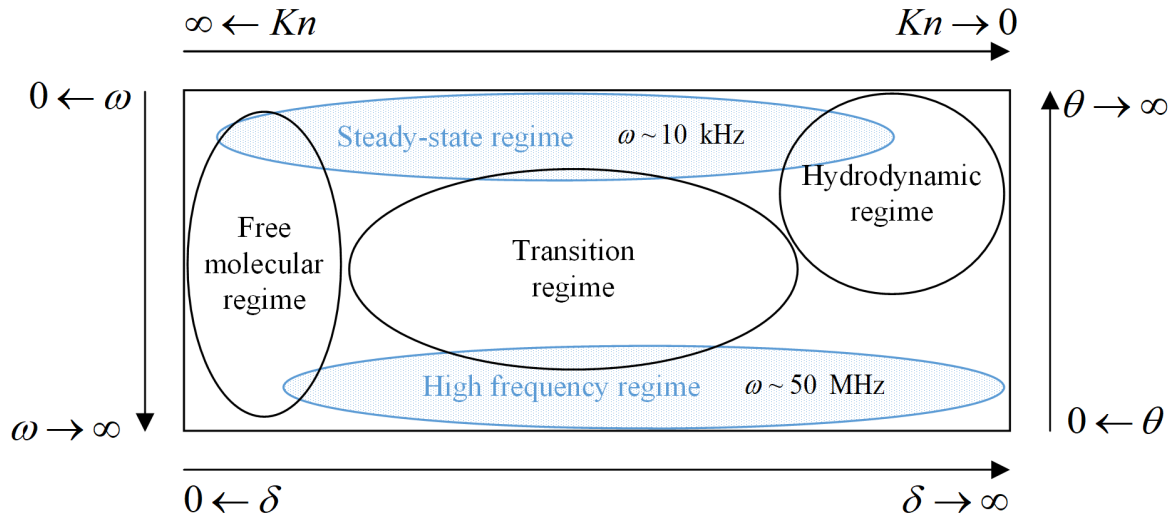
Figure 2.1 Flow regimes based on the gas rarefaction δ and oscillation θ parameters.

Chapter 3

Oscillatory pressure driven rarefied gas flow in long circular tubes

3.1 Introduction

The time-dependent fully-developed rarefied gas flow driven by harmonically oscillating pressure [127], which may be realized by a periodically moving piston or membrane, has received less attention than the corresponding rarefied oscillatory shear driven flows. Until recently, simulations have been presented only in the slip regime in an effort to model pneumatic actuators for pressure sensors [170, 10] and boundary layer flow controllers in order to improve vehicle stability [171, 172]. This Poiseuille type oscillatory flow may be also introduced in other applications related to fluidic resonators and oscillators including microcooling, measuring devices, microseparators and micropropulsion. A well-known effect in this flow is the "Richardson annular effect" which may causes problems in processes such as anomalous solid formation in low-pressure chemical vapor deposition [17]. Besides, this flow is used for lumped-parameter expressions for the impedance of an incompressible viscous fluid subjected to harmonic oscillations [173]. The exact expressions based on solutions of the unsteady Navier-Stokes equations are necessary to avoid large discrepancies in predicted behavior in microchannels.

Depending on the time and space characteristic scales, the oscillatory Poiseuille flow may be in all flow regimes. More specifically, when both the mean free path and the intermolecular collision frequency are less than the characteristic channel size and the oscillation frequency respectively, the oscillatory flow is in the hydrodynamic regime. In this regime, it may be analytically solved by applying the unsteady Stokes

23

equation subject to no-slip boundary conditions (oscillatory Poiseuille flow in channels and pipes) [70–72].

However, when either of the time or space restriction is relaxed the flow is in the transition or the free molecular regimes and the problem must be tackled via kinetic theory. In this context, the present Chapter is devoted to the kinetic solution of the rarefied gas flow in a circular tube due to harmonically oscillating pressure gradient [127] imposed in the longitudinal direction. The periodic flow is investigated by numerically solving the time-dependent linearized Bhatnagar-Gross-Krook (BGK) kinetic equation subject to diffuse boundary conditions. Detailed results of the amplitude and the phase of the bulk velocity and the flow rate are provided in terms of the reference gas rarefaction parameter and the oscillation parameter. The time evolution of the macroscopic quantities as well as the dimensional flow rate over an oscillation period is presented. The limiting solutions in the free molecular and hydrodynamic limits for very low and high oscillation frequencies are also discussed.

3.2   Flow configuration

Consider the isothermal flow of a monatomic rarefied gas through an infinite long circular tube of radius R. Let z' be the coordinate along the tube axis and $r' \in [0, R]$ the radial distance from the center. The flow is caused by an externally imposed oscillatory pressure gradient of the form

$$\frac{d\tilde{P}(z', t')}{dz'} = \frac{dP(z')}{dz'} \cos(\omega t') = \mathrm{R}\left[\frac{dP(z')}{dz'} \exp(-i\omega t')\right] \qquad (3.1)$$

where R denotes the real part of a complex expression, $i = \sqrt{-1}$, t' is the time independent variable, $dP(z')/dz'$ is the amplitude of the oscillating pressure gradient and ω is the oscillation (cyclic) frequency. The flow is assumed fully developed and therefore, the pressure distribution $\tilde{P}(z', t')$ is independent of r', i.e., spatially varies only in the flow direction. The oscillatory pressure gradient yields an unsteady gas flow in the $z'-$direction, which depends harmonically on time and it is characterized by its bulk velocity given by

$$\tilde{U}(t', r') = \mathrm{R}\left[U(r') \exp(-i\omega t')\right], \qquad (3.2)$$

24

where $U(r')$ is a complex function completely determining the oscillatory pressure driven flow. For $\omega = 0$ the well-known stationary cylindrical Poiseuille flow is deduced. It is clear from Eqs. (3.1) and (3.2), that in general, the pressure gradient and velocity are not in phase with each other.

The flow parameters defining the problem are the gas rarefaction parameter δ and the dimensionless oscillation frequency θ. The first one is the same as in steady-state configurations and it is given by

$$\delta = \frac{PR}{\mu \upsilon} \tag{3.3}$$

where μ is the gas viscosity at some reference temperature T and $\upsilon = \sqrt{2R_g T}$ is the most probable molecular speed ($R_g = k_B/m$, with k_B denoting the Boltzmann constant and m the molecular mass, is the gas constant). The rarefaction parameter is proportional to the inverse Knudsen number. The second one is the ratio of the intermolecular collision frequency $\nu = P/\mu$, over the oscillation frequency ω:

$$\theta = \frac{P}{\mu \omega} \tag{3.4}$$

Hence, small and large values of θ correspond to high and low pressure gradient oscillation respectively. The two parameters are independent of each other.

Next, it is convenient to introduce the dimensionless independent variables

$$x = x'/R, z = z'/R \quad \text{and} \quad t = t'\omega, \tag{3.5}$$

as well as the dimensionless amplitude of the local pressure gradient defined as

$$X_P = \frac{R}{P}\frac{dP}{dz'} \tag{3.6}$$

with the assumption of $X_P << 1$. This assumption is typical in fully developed flows (also in steady-state setups), in order to permit the linearization of the governing kinetic equation [2]. The dimensionless complex velocity distribution

$$u(r) = \frac{U(r')}{X_P \upsilon} = u_{Re}(r) + iu_{Im}(r) = u_A \exp(iu_P) \tag{3.7}$$

is also introduced. The subscripts Re and Im denote the real and imaginary parts, while the subscripts A and P denote the amplitude and the phase of the complex velocity. Then, the dimensionless time-dependent velocity distribution is accordingly

25

defined as

$$\tilde{u}(r,t) = \frac{\tilde{U}(r',t')}{X_P \upsilon} = \mathrm{R}\left[u(r)\exp(-it)\right] =$$

$$= \mathrm{R}\left[u_A(r)\exp\left[i\left(u_P(r) - t\right)\right]\right] = u_A(r)\cos\left[t - u_P(r)\right] \tag{3.8}$$

It is evident that both $u_A(r)$ and $u_P(r)$ are of main importance in determining the flow behavior and they will be computed in terms of the two main parameters, δ and θ, fully defining the flow.

In addition, the mass flow rate is also of major practical importance. It is defined as

$$\tilde{\dot{M}}(t') = \mathrm{R}\left[\dot{M}\exp(-i\omega t')\right] \tag{3.9}$$

where

$$\dot{M} = 2\pi\rho \int_0^R U(r')\, r' dr' \tag{3.10}$$

with ρ denoting the mass density. Introducing the dimensionless quantities defined in Eqs. (3.6)-(3.8) in Eq. (3.10) and implementing the equation of state $P = \rho\upsilon^2/2$ results to $\dot{M} = \pi R^2 P X_P G/\upsilon$, where

$$G = 4\int_0^1 u(r)\, r dr. \tag{3.11}$$

The dimensionless flow rate G may be written in complex notation as

$$G(\delta,\theta) = G_{Re}(\delta,\theta) + iG_{Im}(\delta,\theta) = G_A(\delta,\theta)\exp\left[iG_P(\delta,\theta)\right], \tag{3.12}$$

where its real G_{Re} and imaginary G_{Im} parts, as well as its amplitude G_A and phase G_P, may be computed by integrating the corresponding velocity distributions in Eq. (3.7). The time-dependent form of the dimensionless flow rate is given by

$$\tilde{G}(t,\delta,\theta) = \mathrm{R}\left[G\exp(-it)\right] = \mathrm{R}\left[G_A\exp\left[i\left(G_P - t\right)\right]\right] = G_A(\delta,\theta)\cos\left[t - G_P(\delta,\theta)\right] \tag{3.13}$$

It is expected that as $\omega \to 0$ (or $\theta \to \infty$), the imaginary parts of the macroscopic quantities are gradually diminishing and the solution tends towards the steady-state one.

3.3   Kinetic formulation and numerical scheme

For arbitrary values of the parameters δ and θ the flow may be simulated at the kinetic level by the time-dependent BGK kinetic model equation [33, 2], which for the present axisymmetric (r', z') set up may be written as [53, 2]

$$\frac{\partial \tilde{f}}{\partial t'} + \xi_r \frac{\partial \tilde{f}}{\partial r'} - \frac{\xi_\varphi}{r'} \frac{\partial \tilde{f}}{\partial \varphi} + \xi_z \frac{\partial \tilde{f}}{\partial z'} = \frac{P}{\mu} \left(f^M - \tilde{f} \right). \tag{3.14}$$

Here, $\tilde{f} = \tilde{f}(t', r', \xi)$ is the unknown distribution function, $\xi = (\xi_r, \xi_\varphi, \xi_z)$ is the molecular velocity vector, $\varphi \in (0, 2\pi)$ is the corresponding angle in the $r' - \varphi$ plane, P/μ is the collision frequency and

$$f^M = n \left(\frac{m}{2\pi k T} \right)^{3/2} \exp\left[-m \left[\xi - \tilde{U}(t', r') \right]^2 \Big/ (2kT) \right] \tag{3.15}$$

is the local Maxwellian distribution. Due to the assumption of isothermal fully developed flow the temperature T is constant and the number density n varies only in $z'-$direction. Also, the macroscopic velocity $\tilde{U}(t', r')$ is defined by Eq. (3.2) and may be obtained by the first moment of the distribution function according to

$$\tilde{U}(t', r') = \frac{1}{n} \int \xi_z \tilde{f}(t', r', \xi) \, d\xi. \tag{3.16}$$

Due to the condition of very small local pressure gradient ($X_P \ll 1$) the unknown distribution function is linearized as

$$\tilde{f}(t', r', \xi) = f_0 \left[1 + X_P \tilde{h}(t, r, c) + X_P z \exp(-it) \right], \tag{3.17}$$

where $c = \xi/\upsilon$, $f_0 = \frac{n}{\pi^{3/2} \upsilon^3} \exp\left[-c^2 \right]$ is the absolute Maxwellian and $\tilde{h}(t, r, c)$ is unknown perturbed distribution function. Substituting expression (3.17) into Eq. (3.14) and introducing the dimensionless variables as defined in Eqs. (3.5) and (3.6), yields the time-dependent linearized BGK kinetic model equation

$$\frac{\delta}{\theta} \frac{\partial \tilde{h}}{\partial t} + c_r \frac{\partial \tilde{h}}{\partial r} - \frac{c_\varphi}{r} \frac{\partial \tilde{h}}{\partial \varphi} + c_z e^{-it} = \delta \left(2 c_z \mathrm{R}(\tilde{u}) - \tilde{h} \right). \tag{3.18}$$

Here, δ and θ are defined by Eqs. (3.3) and (3.4) respectively, while $\tilde{u}(r, t)$ is the dimensionless time-dependent velocity distribution given in Eq. (3.8).

Next, it is convenient to introduce the complex distribution function $h(r,c)$ so that

$$\tilde{h}(t,r,c) = \mathrm{R}\left[h(r,c)\exp(-it)\right]. \tag{3.19}$$

Also, the molecular velocity vector $c = (c_r, c_\varphi, c_z)$ is transformed as $c = (\zeta, \varphi, c_z)$, where $c_r = \zeta\cos\varphi$ and $c_\varphi = \zeta\sin\varphi$. Then, Eq. (3.18) is rewritten in terms of h as

$$\zeta\cos\varphi\frac{\partial h}{\partial r} - \frac{\zeta\sin\varphi}{r}\frac{\partial h}{\partial\varphi} + h\left(\delta - \frac{\delta}{\theta}i\right) + c_z = 2\delta c_z u, \tag{3.20}$$

where the macroscopic velocity is given by

$$u(r) = \frac{1}{\pi}\int_{-\infty}^{\infty}\int_0^{2\pi}\int_0^{\infty} c_z h e^{-c^2}d\zeta d\varphi dc_z. \tag{3.21}$$

At this stage the $z-$component of the molecular velocity vector may be eliminated by applying the so-called projection procedure and introducing the reduced distribution function

$$Y(r,\zeta,\varphi) = \frac{1}{\pi}\int_{-\infty}^{\infty} h(r,\zeta,\varphi,c_z)\exp\left[-c_z{}^2\right]dc_z. \tag{3.22}$$

Equation (3.20) is multiplied by $c_z\exp(-c_z^2)/\sqrt{\pi}$ and the resulting equation is integrated over c_z to deduce

$$\zeta\cos\varphi\frac{\partial Y}{\partial r} - \frac{\zeta\sin\varphi}{r}\frac{\partial Y}{\partial\varphi} + \left(\delta - i\frac{\delta}{\theta}\right)Y = \delta u + \frac{1}{2}, \tag{3.23}$$

where $u(r)$ is defined by Eq. (3.7) and it is computed from the reduced distribution function according to

$$u(r) = \frac{1}{\pi}\int_0^{2\pi}\int_0^{\infty} Y e^{-\zeta^2}\zeta d\zeta d\varphi. \tag{3.24}$$

It is noted that $Y = Y_{Re} + iY_{Im}$ is complex and obviously, the same applies for u (see Eq. (3.7)). Equation (3.23) is the governing kinetic equation and it is valid in the whole range of δ and θ.

Turning now to the boundary conditions it is noted that purely diffuse scattering is assumed at the wall, i.e., $f^+ = f_w^M$, where the superscript (+) denotes particles departing from the wall and f_w^M is the Maxwellian distribution defined by the wall conditions. Based on the above and following the linearization and projection procedures it is readily deduced that the wall boundary $(r=1)$ is given by

$$Y(1,\zeta,\varphi) = 0, \pi/2 < \varphi < 3\pi/2. \tag{3.25}$$

28

At the symmetry axis $(r = 0)$, molecules are reflected specularly, i.e.,

$$Y(0, \zeta, \varphi) = Y(0, \zeta, \varphi - \pi), 0 < \varphi < \pi/2, 3\pi/2 < \varphi < 2\pi. \tag{3.26}$$

The flow setup is now properly defined by Eq. (3.23) with the associated condition (3.24) subject to boundary conditions (3.25) and (3.26). For each pair of input parameters δ and θ the complex velocity $u(r)$ and the corresponding complex flow rate G, given by Eq. (3.11), are computed.

The numerical solution is deterministic. The discretization in the molecular velocity space is performed using the discrete velocity method. The continuum spectrum $\zeta \in [0, \infty)$ is substituted by a discrete set ζ_m, $m = 1, 2 ... M$, which is taken to be the roots of the Legendre polynomial of order M, accordingly mapped from $[-1, 1]$ to $[0, \infty)$. Also, a set of discrete angles φ_n, $n = 1, 2 ... N$ equally spaced in $[0, 2\pi]$ is defined. The discretization in the physical space is based on a second order central difference scheme by dividing the distance $r \in [0, 1]$ into L segments. The discretized equations are solved in an iterative manner. The iteration map is concluded when the following criteria are fulfilled:

$$\left| u_{Re,i}^{(k+1)} - u_{Re,i}^{(k)} \right| < \varepsilon \quad \text{and} \quad \left| u_{Im,i}^{(k+1)} - u_{Im,i}^{(k)} \right| < \varepsilon, i = 1, 2 ... L + 1 \tag{3.27}$$

Here, the superscript k denotes the iteration index, $u_{Re,i}$ and $u_{Im,i}$ are the real and imaginary part of macroscopic velocity respectively at each node i and ε is the tolerance parameter. This numerical scheme has been extensively applied in steady-state and time-dependent flow configurations with considerable success [174, 175, 53]. In general, the number of iterations required for convergence is increased as either θ or δ are increased. The most computationally intensive cases are when both flow parameters are large and the flow is in the slip and hydrodynamic regimes. The numerical parameters have been gradually refined to ensure grid independent results up to at least three significant figures.

Furthermore, the revert to dimensional quantities is straightforward. The mass flow rate is written as

$$\tilde{\dot{M}}(t') = \text{R}\left[\frac{\pi R^3}{\upsilon} \frac{dP}{dz'} G \exp(-i\omega t') \right] = \text{R}\left[\dot{M}_A \cos(M_P - \omega t') \right] \tag{3.28}$$

29

where $\dot{M}_A = \frac{\pi R^3}{\upsilon} \frac{dP}{dz'} G_A$. Eq. (3.28) may also be restructured as

$$\frac{dP}{dz'} = \frac{\text{R}\left[\tilde{\dot{M}}(t')\right]}{\text{R}\left[\frac{\pi R^3 G}{\upsilon}\exp\left(-i\omega t'\right)\right]} = \frac{\text{R}\left[\upsilon\dot{M}_A\cos\left(M_P - \omega t'\right)\right]}{\text{R}\left[\pi R^3 G_A\cos\left(G_P - \omega t'\right)\right]} \overset{(M_P=G_P)}{=} \frac{\upsilon\dot{M}_A}{\pi R^3 G_A}. \qquad (3.29)$$

Eq. (3.29) is an ordinary differential equation with an unknown quantity $(\dot{M}_A)$. It can be simplified since the phase angle lag G_P is the same for both the dimensional and dimensionless flow rate. An iterative procedure is applied in order to fit $\dot{M}_A$ with the boundary conditions of Eq. (3.29). As the pressure is increased in a tube of length L, the dimensionless flow rate is evaluated either with the expression

$$G = \frac{1}{P_1 - P_2}\int_{P_1}^{P_2} G\left(\delta,\theta\right)dP = \frac{1}{\delta_1 - \delta_2}\int_{\delta_1}^{\delta_2} G\left(\delta,\theta\right)d\delta \qquad (3.30)$$

or with the similar one

$$G = \frac{1}{P_1 - P_2}\int_{P_1}^{P_2} G\left(\delta,\theta\right)dP = \frac{1}{\theta_1 - \theta_2}\int_{\theta_1}^{\theta_2} G\left(\delta,\theta\right)d\theta. \qquad (3.31)$$

Since both parameters are directly related to pressure, Eqs. (3.30) and (3.31) are always valid. As the pressure increases both parameters are increased. It is noted that the real and the imaginary parts are integrated separately and then the total amplitude G_A and the total phase G_P are computed.

Closing this section it is interesting to comment on the behavior of Eq. (3.23) at limiting values of θ or δ. As $\theta \to \infty$ ($\omega = 0$) and $\delta << \theta$ (finite values of δ), Eq. (3.23) is reduced to the one describing the steady-state cylindrical Poiseuille rarefied gas flow at the corresponding δ. In the specific case of $\delta = 0$ with $\theta > 0$, the kinetic equation for steady-state flow at the free molecular limit is recovered. At the other end, as $\theta \to 0$ ($\omega \to \infty$), Eq. (3.23) yields $Y \to 0$, i.e., the solution tends to vanish at very high frequencies due to fluid inertia. It is expected this behavior at the limiting conditions to be also present in the numerical solution.

3.4   Hydrodynamic and slip regimes

At the hydrodynamic and slip regimes the oscillatory fully developed flow is defined by the $z-$momentum equation [71, 72]

$$\rho \frac{\partial \tilde{U}^{(j)}}{\partial t'} = -\frac{d\tilde{P}}{dz'} + \mu \left(\frac{\partial^2 \tilde{U}^{(j)}}{\partial r'^2} + \frac{1}{r'} \frac{\partial \tilde{U}^{(j)}}{\partial r'} \right), \tag{3.32}$$

where the pressure gradient $d\tilde{P}\left(z', t'\right)/dz'$ is defined by Eq. (3.1) and the bulk velocity $\tilde{U}^{(j)}\left(t', r'\right)$, with $j = H, S$, denoting the hydrodynamic and slip solutions, is defined by Eq. (3.2).

Introducing the dimensionless quantities (3.5)-(3.8), along with the definitions (3.3) and (3.4), Eq. (3.32) is rewritten in dimensionless form in terms of the present notation as

$$\frac{\partial^2 u^{(j)}}{\partial r^2} + \frac{1}{r} \frac{\partial u^{(j)}}{\partial r} + 2i \frac{\delta^2}{\theta} u^{(j)} = -\delta. \tag{3.33}$$

Here $u^{(j)} = u^{(j)}\left(r\right)$ is the complex hydrodynamic or slip velocity and it may be written in the form of Eq. (3.7), as $u^{(j)}\left(r\right) = u_{Re}^{(j)}\left(r\right) + i u_{Im}^{(j)}\left(r\right) = u_A^{(j)}\left(r\right) \exp\left[i u_P^{(j)}\left(r\right)\right]$, $j = H, S$. Then, integrating the velocity distribution over the cross section, according to Eq. (3.11), the complex flow rate, $G^{(j)} = G_{Re}^{(j)} + i G_{Im}^{(j)} = G_A^{(j)} \exp\left(i G_P^{(j)}\right)$, $j = H, S$, is recovered. Equation (3.33), is valid in the hydrodynamic and slip regimes and in practice, it may be applied for large values of δ and θ.

In the hydrodynamic regime ($j = H$) the associated boundary conditions include the axi-symmetry condition at $r' = 0$ and the no-slip condition at $r' = R$, written as

$$\left. \frac{du^{(H)}\left(r\right)}{dr} \right|_{r=0} = 0, u\left(1\right) = 0 \tag{3.34}$$

Equation (3.33) subject to boundary conditions (3.34) is analytically solved to yield the velocity distribution and the flow rate in the hydrodynamic regime [71, 72]:

$$u^{(H)}(r) = i\frac{\theta}{2\delta}\left[1 - \frac{J_0\left(r\sqrt{2i}\delta/\sqrt{\theta}\right)}{J_0\left(\sqrt{2i}\delta/\sqrt{\theta}\right)}\right] \tag{3.35}$$

$$G^{(H)} = i\frac{\theta}{\delta}\left[1 - 2\frac{\sqrt{\theta}}{\sqrt{2i}\delta}\frac{J_1\left(\sqrt{2i}\delta/\sqrt{\theta}\right)}{J_0\left(\sqrt{2i}\delta/\sqrt{\theta}\right)}\right] \tag{3.36}$$

31

Here, J_0 and J_1 are the Bessel functions of the first kind of zero and first order respectively.

In the slip regime $(j = S)$ the axi-symmetry boundary condition at $r' = 0$ remains the same, while at the wall the slip boundary condition in introduced [2]:

$$\left. \frac{du^{(S)}(r)}{dr} \right|_{r=0} = 0, \, u^{(S)}(1) = -\frac{\sigma_P}{\delta} \left. \frac{du^{(S)}}{dr} \right|_{r=1} \tag{3.37}$$

The viscous slip coefficient $\sigma_P = 1.016$ is known and it is computed by solving the corresponding half-space viscous slip flow setup (or Kramers problem) based on the linearized BGK model equation [2]. Equation (3.33) subject to boundary conditions (3.37) is analytically solved to yield the velocity distribution and flow rate in the slip regime:

$$u^{(S)}(r) = i\frac{\theta}{2\delta} \left[1 - \frac{J_0\left(\sqrt{2i}\frac{\delta}{\sqrt{\theta}}r\right)}{J_0\left(\sqrt{2i}\frac{\delta}{\sqrt{\theta}}\right) - \sqrt{2i}\frac{\sigma_P}{\sqrt{\theta}}J_1\left(\sqrt{2i}\frac{\delta}{\sqrt{\theta}}\right)} \right] \tag{3.38}$$

$$G^{(S)} = i\frac{\theta}{\delta} \left[1 - 2\frac{\sqrt{\theta}}{\sqrt{2i}\delta} \frac{J_1\left(\sqrt{2i}\frac{\delta}{\sqrt{\theta}}\right)}{J_0\left(\sqrt{2i}\frac{\delta}{\sqrt{\theta}}\right) - \sqrt{2i}\frac{\sigma_P}{\sqrt{\theta}}J_1\left(\sqrt{2i}\frac{\delta}{\sqrt{\theta}}\right)} \right] \tag{3.39}$$

These analytical solutions are implemented to check the accuracy of the numerical scheme at large values of δ and θ.

In both the hydrodynamic and slip regimes, two limiting solutions may be considered based on the quantity $\delta/\sqrt{\theta}$, which is proportional to the ballistic Stokes number and measures viscous versus unsteady effects in oscillatory flows. The analysis is applied only in the flow rate expressions. First, assuming $1 \ll \delta \ll \sqrt{\theta}$, i.e., that the oscillation frequency is very slow ($\omega \to 0$ or $\theta \to \infty$), Eqs. (3.36) and (3.39) are manipulated by expanding the Bessel functions for small arguments $\delta/\sqrt{\theta} \ll 1$. By keeping only the main terms the well-known flow rates of the stationary cylindrical Poiseuille flow subject to constant pressure gradient are recovered in the hydrodynamic and slip regimes [2]:

$$G^{(H)} = \frac{\delta}{4}, \, G^{(S)} = \frac{\delta}{4} + \sigma_P. \tag{3.40}$$

Secondly, assuming $\delta \gg \sqrt{\theta} \gg 1$, the Bessel functions in Eqs. (3.36) and (3.39) are now expanded for large arguments $\delta/\sqrt{\theta} >> 1$ and, following some manipulation, the following expressions are obtained:

$$G^{(H)} = \frac{\theta^{3/2}}{\delta^2} + i\frac{\theta}{\delta}\left(1 - \frac{\sqrt{\theta}}{\delta}\right) \tag{3.41}$$

32

$$G^{(S)} = \frac{\theta^{3/2}}{\delta^2} + i\frac{\theta}{\delta}\left[1 - \frac{\sqrt{\theta}}{\delta}\left(1 + \frac{2\sigma_P}{\sqrt{\theta}}\right)^{-1}\right] \tag{3.42}$$

The closed-form expressions (3.40)-(3.42) are also applied to examine the accuracy of the kinetic solutions at these limits provided that the corresponding restrictions in terms of δ and θ are fulfilled.

3.5   Results and discussion

The fully developed rarefied gas flow in a cylindrical tube due to an imposed oscillatory pressure gradient has been simulated in a wide range of the gas rarefaction and oscillation parameters. The computed dimensionless complex velocity distributions and flow rates are based on the kinetic formulation, while some complimentary analytical results in the slip regime are also reported. The results include the amplitude and the phase angle, as well as the periodic time evolution of the macroscopic quantities.

In Table 3.1, the flow rate amplitude $G_A(\delta, \theta)$ is presented in terms of the gas rarefaction $\delta \in [10^{-4}, 10^2]$ and the oscillation parameter $\theta = [0.1, 1, 10, 50, 10^2]$. In addition, the flow rate amplitude in the slip regime $G_A^{(S)}(\delta, \theta)$, based on the analytical expression (3.39), is provided in the 7th and 8th column of Table 3.1 for $\theta = 50$ and $\theta = 10^2$ respectively and for $\delta \geq 1$. In the last column of Table 3.1, the well-known flow rates of the steady-state cylindrical Poiseuille flow with constant pressure gradient $(\theta \to \infty)$, denoted by $G_{SS}(\delta)$, for $\delta \leq 10$ are also included [2].

By comparing $G_A(\delta, \theta)$ with the corresponding $G_A^{(S)}(\delta, \theta)$ it is readily seen that the agreement is, in general, good and more important that it is improved as both δ and θ are increased. On the contrary, even for these two relatively large values of θ, the discrepancies are gradually increased as δ is decreased. This comparison demonstrates the efficiency of the kinetic results to properly recover the analytical slip solution, as well as the range of validity of the slip solution depending on the required accuracy. Next, the values $G_A(\delta, \theta)$ for the large oscillation parameter $\theta = 10^2$ (or very small oscillation frequency ω) are compared to the corresponding steady-state flow rates $G_{SS}(\delta)$. It is seen that the agreement is very good in small and intermediate values of δ (free molecular and part of transition regimes) and then, as δ is further increased the discrepancies also increase. It is evident that in order to recover the steady-state solution it requires: a) the oscillation parameter to be large (which it is, since $\theta = 10^2$) and b) $\delta << \theta$ (which is not, when $\delta > 10$). This is in agreement with the reported behavior of the kinetic equation (3.23) as $\theta \to \infty$ approaching the

33

stationary solution (last paragraph in Section 3.3), as well as with the analytical results in the hydrodynamic and slip regimes, where it has been shown that the steady-state solution is recovered as $\theta \to \infty$, with $\delta \ll \sqrt{\theta}$ (Section 3.4). In general, steady-state conditions may be reached faster as the flow becomes more rarefied (or as δ is decreased) provided of course that the oscillation parameter is adequately large (ω adequately small).

The discussion on Table 3.1 is continued by analyzing the behavior of the flow rate amplitude $G_A(\delta, \theta)$ in the whole range of δ and θ. For any given δ, $G_A(\delta, \theta)$ is monotonically increased as θ is increased, with $G_A(\delta, \theta)$ being always less than the corresponding stationary solution $G_{SS}(\delta)$. The dependency of $G_A(\delta, \theta)$ on δ is more complex. For $\theta \leq 1$, as δ is increased, $G_A(\delta, \theta)$ is monotonically decreased, while for $\theta \geq 10$ it is initially decreased until $\delta = 0.5$, where a local minimum is observed, then it is increased up to some δ, which depends on θ, and finally as δ is further increased it is again decreased. It is noted that for all θ, as $\delta \to 0$, the well-known analytical steady-state free molecular flow rate equal to $8/(3\sqrt{\pi}) = 1.504$ [2], is properly recovered. Also, for small values of θ and adequately dense atmosphere (large values of δ), $G_A(\delta, \theta)$ tends to diminish. This behavior, which appears in high oscillation frequencies (small θ) is due to inertia forces (the fluid has great difficulty to reach a peak flow) and will be further analyzed, later on, by examining the velocity distributions.

In Table 3.2, the dimensionless flow rate phase $G_P(\delta, \theta)$ is presented in terms of the same parameters as in Table 3.1. The phase angles vary between zero and $\pi/2 = 1.571$, which correspond to no phase and maximum phase difference respectively between the flow rate and the pressure gradient. The dimensionless flow rate phase in the slip regime $G_P^{(S)}(\delta, \theta)$, based on the analytical expression (3.39), is also provided in the last two columns of Table 3.2 for $\theta = 50$ and $\theta = 10^2$ with $\delta \geq 1$. The comparison between the corresponding $G_P(\delta, \theta)$ and $G_A^{(S)}(\delta, \theta)$ support all remarks previously made for the flow rate amplitudes and also, establishes more confidence to the kinetic solution, which is in very good agreement with the slip analytical solution, provided that the oscillatory flow is in the slip regime.

Furthermore, it is seen from Table 3.2 that, as expected, for any given δ, the phase difference $G_P(\delta, \theta)$ is increased as θ is decreased, i.e., as the oscillation frequency is increased. Taking into consideration the corresponding values of $G_A(\delta, \theta)$ in Table 3.1, it is concluded that as the oscillation frequency is increased the flow rate amplitude is decreased, while the phase shift is increased. At very high frequencies and adequately large δ, this may result to almost zero amplitude with $\pi/2$ phase difference. Also, for

any given θ, $G_P(\delta, \theta)$ is monotonically increased with δ, i.e., the phase difference is almost zero in the free molecular regime and then, it is increased as the oscillatory flow becomes less rarefied, reaching the maximum phase angle lag in the hydrodynamic limit.

A view, in graphical form, of the flow rate amplitude $G_A(\delta, \theta)$ and phase $G_P(\delta, \theta)$ is provided in Figure 3.1, where these quantities are plotted versus δ/θ for $\theta = [0.1, 1, 10, 50, 10^2]$. The behavior of $G_A(\delta, \theta)$ in terms of the ratio δ/θ is qualitatively similar to the one observed in Table 3.1 in terms of δ. For $\theta = [0.1, 1]$, $G_A(\delta, \theta)$ is monotonically reduced, while for $\theta = [10, 50, 10^2]$ is initially decreased, then it is increased up to some $\delta/\theta \in [0.1, 1]$ and finally it is decreased. This behavior is justified by the fact that when the oscillation frequency is adequately high ($\theta = [0.1, 1]$), $G_A(\delta, \theta)$ is significantly affected and it is monotonically reduced, while when the oscillation frequency is not high enough ($\theta = [10, 50, 10^2]$), $G_A(\delta, \theta)$ has some resemblance with the steady-state flow rate profile including the Knudsen minimum, as long as δ/θ is sufficiently small to ensure $\delta << \theta$ (as reported above steady-state conditions are reached as $\theta \to \infty$, with $\delta << \theta$). Then, as δ/θ is further increased the inequality condition does not hold and $G_A(\delta, \theta)$ is decreased. With regard to the phase difference, $G_P(\delta, \theta)$ is monotonically increased with δ/θ. At very small values of δ/θ (free molecular regime) it is almost zero, then at moderate values of δ/θ (transition regime) it is rapidly increased and finally at large values of δ/θ (slip and hydrodynamic regimes) it is asymptotically increased reaching the limiting value of $\pi/2$. An interesting and useful outcome of Figure 3.1 may be the determination of the optimal gas rarefaction level for a given oscillation frequency to induce the maximum flow rate amplitude $G_A(\delta, \theta)$.

In Figure 3.2, the time evolution of the dimensionless flow rate, defined in Eq. (3.13) as $\tilde{G}(t, \delta, \theta) = G_A \cos(t - G_P)$, is plotted over one period of oscillation $t \in [0, 2\pi]$ for typical values of δ and θ. The time evolution of the dimensionless pressure gradient is equal to $\cos t$ and it is also plotted to facilitate the phase shift observation between pressure gradient and dimensionless flow rate. It is seen that $\tilde{G}(t, \delta, \theta)$ depends heavily both on the gas rarefaction parameter and the oscillation frequency. When $\delta = 0.1$, the $\tilde{G}(t, \delta, \theta)$ profiles for $\theta = [1, 10, 10^2]$ (low and moderate oscillation frequencies) are very close to each and in phase with the pressure gradient, while for $\theta = 0.1$ (high oscillation frequency) $\tilde{G}(t, \delta, \theta)$ has a significantly smaller amplitude and a lagging phase angle. As δ is increased the effect of θ becomes more dominant. At $\delta = 1$, the $\tilde{G}(t, \delta, \theta)$ profiles only for $\theta = [10, 10^2]$ are close to each other and in phase, while for $\theta = [0.1, 1]$ the amplitude is reduced and the phase angle lag is increased. Actually now,

for $\theta = 0.1$ the amplitude is very small and the phase angle lag is almost $\pi/2$. This behavior is further enhanced at $\delta = 10$, where the effect of the oscillation frequency is very significant for $\theta = [0.1, 1, 10]$ and remains not important only for $\theta = 10^2$. As expected these results are in very good agreement with the remarks made in Table 3.1 and Table 3.2. It is also concluded that the peak of the flow rate amplitude always falls short of reaching the corresponding flow rate of the steady-state Poiseuille flow with constant pressure gradient. This is clearly contributed to the inertia of the fluid, which must be accelerated in each cycle and therefore this effect is intensified as the flow becomes more viscous and the oscillation frequency is increased.

Similar to Figure 3.2, in Figure 3.3 the mass flow rate $\tilde{\tilde{M}}(t)$ of Helium is presented over time t' for a tube of length $L = 0.1$ m. The radius of the tube is $R = 0.016$ m and the pressure at the beginning of the tube is $P_1 = 1$ Pa while at the end is $P_2 = 5$ Pa. The properties of Helium at $T_0 = 25\ ^0$C are $v = 1103$ m/s and $\mu = 1.939 \times 10^5$ Pa s. The mass flow rate is plotted for three oscillation frequencies $\omega = [250, 570, 2000]$ Hz. The purpose here is to observe the differences between the dimensional and dimensionless results. It is clear that the behavior of the mass flow rate is similar to the dimensionless flow rate and it is decreased as the oscillation frequency is increased. However, results based on different oscillation frequencies cannot be easily compared since the dimensionless oscillation period isn't the same as it has been in Figure 3.2. Here, the oscillation period is decreased as the oscillation frequency is increased. Therefore, it is more convenient to use dimensionless results instead of dimensional ones in oscillatory flows.

Next, the behavior of the velocity distributions in terms of δ and θ is investigated. In Figure 3.4, the amplitude $u_A(r)$ and the phase angle $u_P(r)$ of the velocity distribution are plotted for $\delta = [0.1, 1, 10]$ and $\theta = [10^{-2}, 10^{-1}, 1, 10]$ covering a wide range of the flow parameters. As the oscillation parameter is decreased, i.e., the oscillation frequency is increased, the amplitude is reduced and the phase angle lag is increased. This behavior is expected and it is in accordance to the flow rate results studied above. Here, it is more interesting to focus on the radial variation of the velocity amplitude and phase angle with regard to δ and θ. Starting with $u_A(r)$ it is seen that for some δ and θ (e.g., $\delta = 0.1$ and $\theta \geq 0.1$) the velocity amplitudes have the expected shape with their maximum at $r = 0$, while the corresponding phase angles are small and almost constant in the radial direction. However, as δ is increased and θ is reduced, $u_A(r)$ remains constant from the center of the tube until close to the wall, where it rapidly changes. In these cases (e.g., $\delta = 1$ and $\theta \leq 0.1$ or $\delta = 10$ and $\theta \leq 1$) near the

36

wall there is a region where the velocity amplitude is higher than in the center of the flow. The corresponding values of $u_P(r)$ are large, resulting to phase angle lags up to 90^0 with regard to the pressure gradient and also, they are constant from the center of the tube until this region close to the wall, where they change significantly in an oscillatory manner. The thickness of this region is decreased as δ is increased and θ is reduced. Therefore, in high or even moderate frequencies (it depends on δ), the flow consists of two layers: the inviscid piston flow in the core, dominated by inertia forces and the frictional Stokes wall layer dominated by viscous forces. This flow description, including the velocity overshoot, which is known as "annular effect" or "Richardson effect", is well known in classical hydrodynamics [70–72]. It is interesting however, to see that these effects are also present in oscillatory rarefied flows. Of course as the gas rarefaction is increased, higher oscillation frequencies are needed to trigger these flow patterns.

In Figure 3.5, the time evolution of the dimensionless velocity distribution, defined in Eq. (3.8) as $\tilde{u}(r,t) = u_A \cos(t - u_P)$, is plotted versus the radial distance r at certain times $t \in [0, 2\pi]$ covering one period of oscillation for $\delta = 1$ with $\theta = [10^{-2}, 10^{-1}, 1, 10]$. The observed radial variation of the velocity distribution at these timeframes is the typical one expected, as the oscillation parameter is increased, i.e., as the oscillation frequency is decreased. The two layers flow pattern with the core oscillating in a plug-flow mode and the velocity maximum (or minimum) inside the thin Stokes layer plus the small amplitude and large phase angle lag, are all clear at $\theta = 10^{-2}$ and then, as θ is increased these effects are reduced and finally, they are diminishing at $\theta = 10$, where the velocity profile has an amplitude close to the corresponding steady-state one and the phase angle lag with the pressure gradient is small. Furthermore, it is interesting to note that at high frequencies ($\theta = 10^{-2}, 0.1$) and at times $t = 0$ and $t = \pi$ the velocity distribution along the radial direction changes sign and may be either positive or negative. This velocity reversal does not show up at low frequencies (large θ). In addition, the position of the maximum or the minimum of the velocity distribution is moving with time in the radial direction inside the Stokes layer. This is clearly shown in the case of $\theta = 0.1$ where the overshoot is carried away from the wall [176]. Although this motion is due to viscous diffusion it does have some resemblance with transverse decaying waves from the boundary towards the centerline of the pipe.

Closing this section a remark with regard to the Strouhal number, defined as $St = \delta/\theta$, is made. In Figure 3.6, $\tilde{u}(r,t)$, is plotted versus the radial distance r at certain times $t \in [0, 2\pi]$ covering one period of oscillation for $\delta = \theta = 0.1$ and

$\delta = \theta = 10$. In both setups, $St = 1$. It readily seen that the radial variation of $\tilde{u}(r,t)$ in the two setups at the same time steps, although the Strouhal number is the same, is completely different. This is a clear indication that the St number is not adequate, only by itself, to characterize the flow. Furthermore, according to previous observations, for $\delta = 0.1$ the flow is highly rarefied and even with $\theta = 0.1$, it behaves like a low oscillation flow, while for $\delta = 10$, the flow is dense enough and even with $\theta = 10$, it start to behave like a moderate to high frequency flow. In this latter case the Stokes layer is thick and affects the whole velocity profile. The corresponding time dependent flow rates obtained by integrating the velocity profiles presented in Figs. 3.4 and 3.5 may be found, in most cases, in Fig. 3.2.

3.6   Concluding remarks

The time-dependent isothermal fully-developed rarefied gas flow in a cylindrical tube driven by harmonically oscillating pressure gradient is investigated based on the linearized unsteady BGK kinetic model equation. The two parameters characterizing the flow are the gas rarefaction and the oscillation parameters. Computational results for the amplitude and the phase angle of the flow rates and the velocity distributions have been provided in a wide range of these two parameters in tabulated and graphical form. In addition, the time evolution of the macroscopic quantities over a cycle is also reported. The limiting flow rates in the slip and free molecular regimes for very low and high speed oscillations are properly recovered by the kinetic solution and very good agreement with analytical solutions in these regimes has been obtained.

The flow rate amplitude is decreased as the oscillation frequency is increased. However, in terms of the gas rarefaction the dependency is not monotonic and it is found that for a given oscillation parameter, there is an optimum gas rarefaction level to obtain the maximum flow rate amplitude. The phase shift of the flow rate is monotonically increased as the oscillation frequency is increased and the gas rarefaction is decreased. At low oscillation frequencies the flow rate and velocity distribution are in phase with the pressure gradient, while as the frequency is increased the amplitude of the macroscopic quantities is decreased and the phase angle lag is increased. At high frequencies the flow consists of the core oscillating in a plug-flow mode and the Stokes layer with a velocity overshoot. These effects, which are well-known in classical hydrodynamics, are also present in oscillatory rarefied flows. Of course, as the gas rarefaction is increased it is more difficult for energy to be transferred from the initial

oscillation to the bulk flow and therefore higher oscillation frequencies are needed to observe these phenomena.

Table 3.1 Flow rate amplitude $G_A(\delta,\theta)$ in terms of gas rarefaction parameter δ and oscillation parameter θ.

δ	$G_A(\delta,\theta)$					$G_A^{(S)}(\delta,\theta)$		G $_{SS}(\delta)$
	$\theta=0.1$	$\theta=1$	$\theta=10$	$\theta=50$	$\theta=100$	$\theta=50$	$\theta=100$	$\theta\to\infty$
0.0001	1.502	1.504	1.504	1.504	1.504			1.504
0.001	1.488	1.499	1.499	1.499	1.499			1.499
0.01	1.381	1.472	1.476	1.476	1.476			1.476
0.05	1.073	1.413	1.430	1.430	1.430			1.430
0.1	8.151(-1)	1.369	1.404	1.404	1.404			1.404
0.5	2.014(-1)	1.142	1.383	1.386	1.387			1.387
1	1.002(-1)	8.512(-1)	1.444	1.458	1.458	1.266	1.266	1.458
2	4.999(-2)	4.837(-1)	1.575	1.654	1.657	1.513	1.515	1.658
4	2.500(-2)	2.457(-1)	1.570	2.078	2.103	1.985	2.008	2.111
6	1.667(-2)	1.646(-1)	1.300	2.444	2.550	2.380	2.480	2.588
8	1.250(-2)	1.238(-1)	1.046	2.670	2.956	2.627	2.903	3.074
10	1.000(-2)	9.919(-2)	8.649(-1)	2.723	3.282	2.695	3.242	3.564
15	6.667(-3)	6.630(-2)	6.034(-1)	2.383	3.594	2.372	3.576	
20	5.000(-3)	4.979(-2)	4.635(-1)	1.953	3.342	1.946	3.333	
30	3.334(-3)	3.323(-2)	3.167(-1)	1.407	2.575	1.404	2.570	
40	2.500(-3)	2.494(-2)	2.405(-1)	1.100	2.052	1.098	2.050	
50	2.000(-3)	1.996(-2)	1.939(-1)	9.022(-1)	1.706	9.009(-1)	1.704	
100	1.000(-3)	1.009(-2)	1.058(-1)	4.747(-1)	9.228(-1)	4.743(-1)	9.223(-1)	

Table 3.2 Flow rate phase $G_P(\delta, \theta)$ (rad) in terms of gas rarefaction parameter δ and oscillation parameter θ.

δ	$G_P(\delta, \theta)$					$G_P^{(S)}(\delta, \theta)$	
	$\theta = 0.1$	$\theta = 1$	$\theta = 10$	$\theta = 50$	$\theta = 100$	$\theta = 50$	$\theta = 100$
0.0001	4.646(-3)	5.632(-4)	5.767(-5)	1.156(-5)	5.780(-6)		
0.001	3.254(-2)	4.088(-3)	4.200(-4)	8.415(-5)	4.208(-5)		
0.01	1.905(-1)	2.709(-2)	2.793(-3)	5.588(-4)	2.794(-4)		
0.05	5.774(-1)	9.447(-2)	9.857(-3)	1.972(-3)	9.862(-4)		
0.1	8.730(-1)	1.613(-1)	1.699(-2)	3.399(-3)	1.700(-3)		
0.5	1.461	5.837(-1)	6.797(-2)	1.362(-2)	6.810(-3)		
1	1.512	9.535(-1)	1.395(-1)	2.807(-2)	1.404(-2)	2.564(-2)	1.282(-2)
2	1.542	1.278	3.173(-1)	6.557(-2)	3.282(-2)	6.276(-2)	3.141(-2)
4	1.557	1.434	7.217(-1)	1.762(-1)	8.883(-2)	1.727(-1)	8.702(-2)
6	1.561	1.480	1.015	3.287(-1)	1.692(-1)	3.250(-1)	1.672(-1)
8	1.564	1.503	1.175	5.053(-1)	2.715(-1)	5.022(-1)	2.694(-1)
10	1.565	1.517	1.263	6.809(-1)	3.901(-1)	6.790(-1)	3.882(-1)
15	1.567	1.535	1.371	1.008	7.012(-1)	1.009	7.004(-1)
20	1.568	1.544	1.423	1.177	9.451(-1)	1.179	9.456(-1)
30	1.569	1.553	1.473	1.321	1.194	1.322	1.195
40	1.569	1.557	1.498	1.387	1.299	1.388	1.300
50	1.570	1.560	1.513	1.426	1.357	1.426	1.358
100	1.570	1.565	1.542	1.500	1.468	1.500	1.468
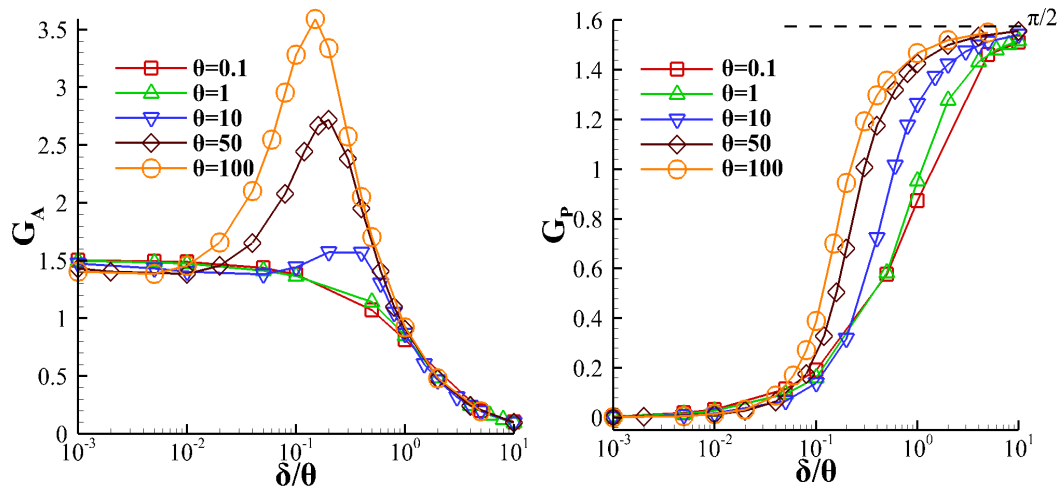
Figure 3.1 Flow rate amplitude $G_A(\delta, \theta)$ and phase $G_P(\delta, \theta)$ (rad) in terms of the ratio of the gas rarefaction parameter δ over the oscillation parameter θ, with $\theta = [0.1, 1, 10, 50, 10^2]$.
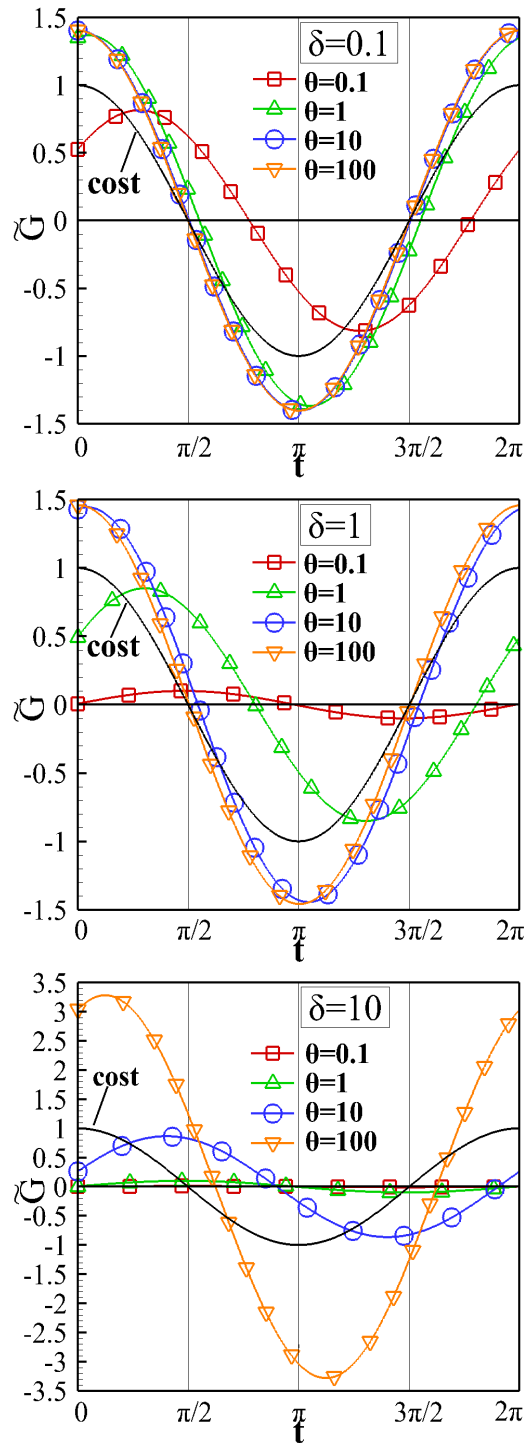
Figure 3.2 Time evolution of flow rate $\tilde{G}(t, \delta, \theta)$ over one period of oscillation for $\delta = [0.1, 1, 10]$ and $\theta = [0.1, 1, 10, 10^2]$; the time evolution of the dimensionless pressure gradient equal to $\cos t$ is also included.

43
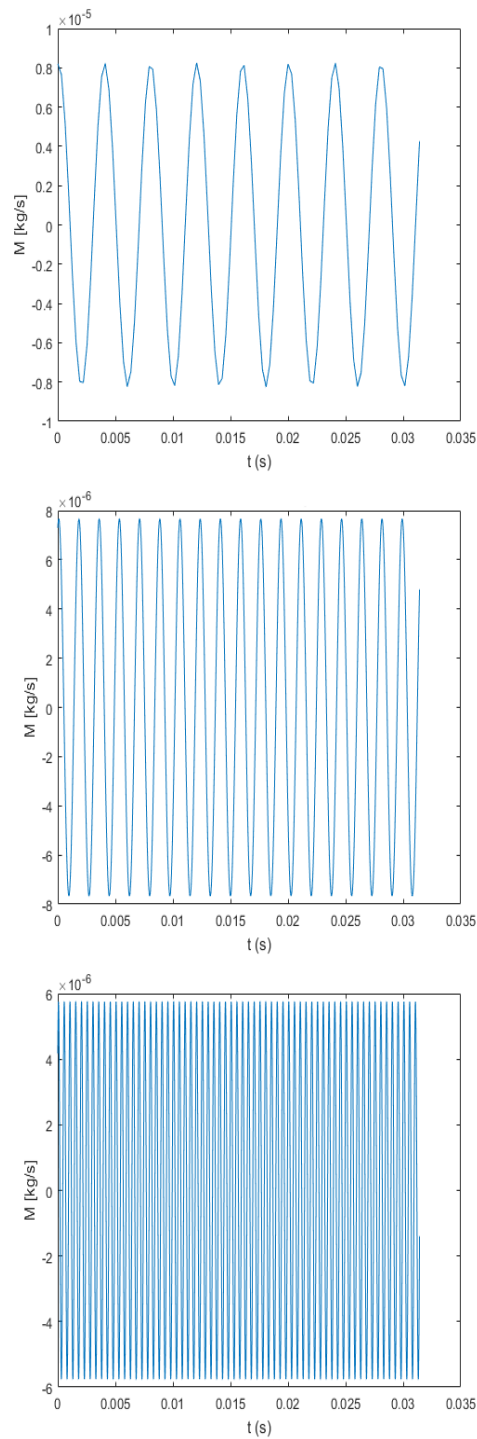
Figure 3.3 Time evolution of mass flow rate $\tilde{M}(t')$ kg/s over time t' s for $\omega = 250$ Hz (top), $\omega = 570$ Hz (middle) and $\omega = 2000$ Hz (bottom).

44
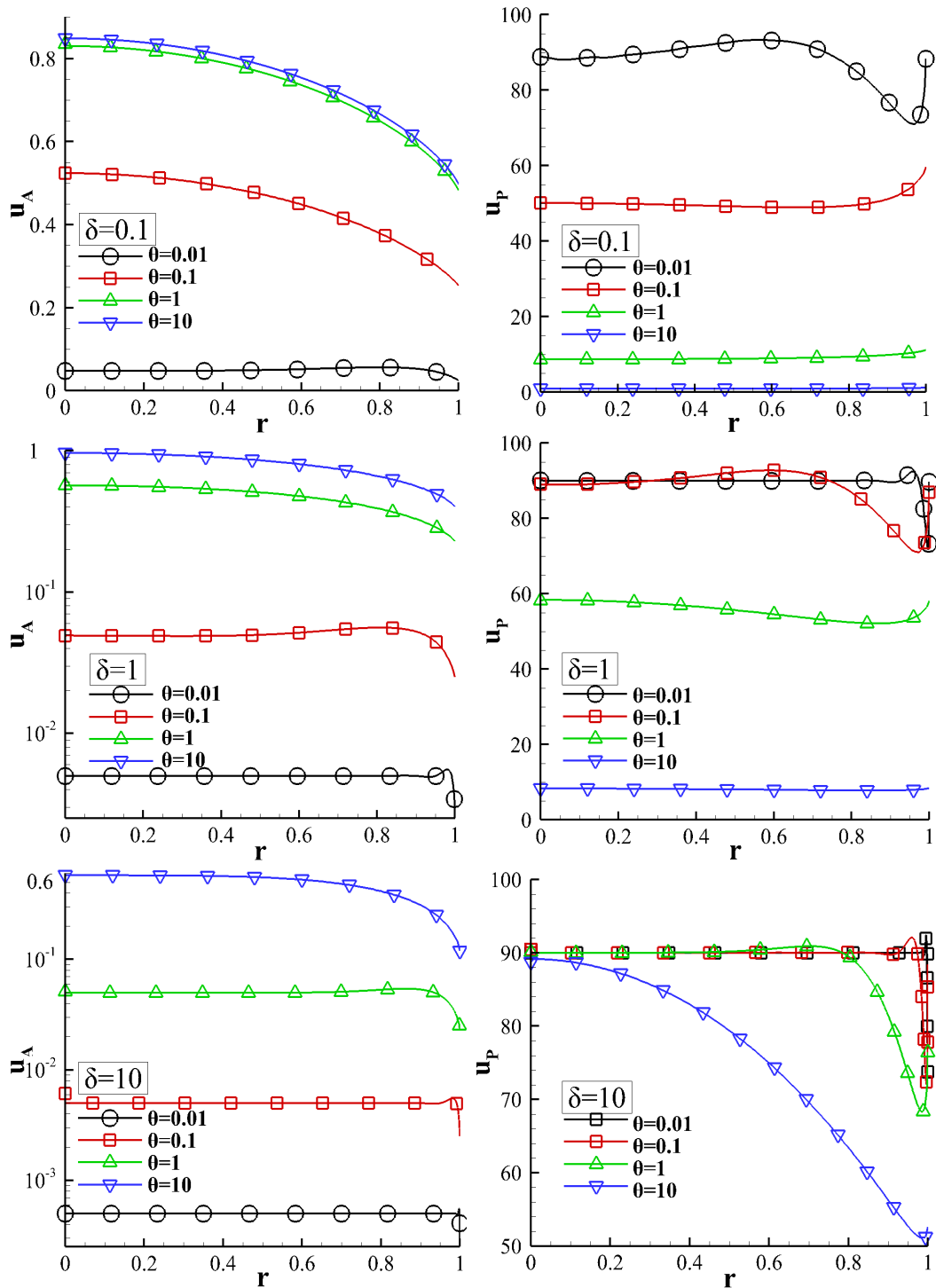
Figure 3.4 Velocity distribution amplitude $u_A(r)$ and phase angle $u_P(r)$ versus radial distance r for $\delta = [0.1, 1, 10]$ and $\theta = [10^{-2}, 10^{-1}, 1, 10]$.
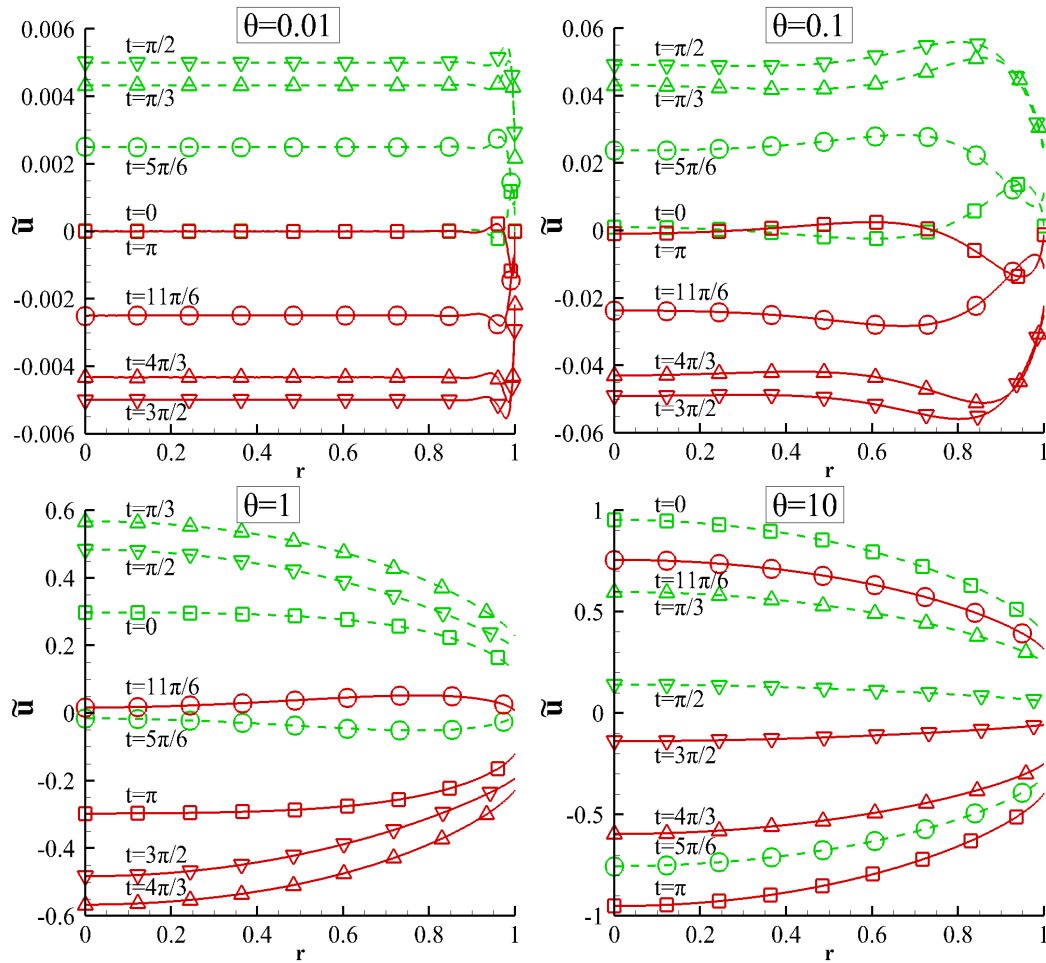
Figure 3.5 Time evolution of velocity distribution $\tilde{u}(r,t)$ versus radial distance r at certain times $t \in [0, 2\pi]$ over one period of oscillation for $\delta = 1$ with $\theta = [10^{-2}, 10^{-1}, 1, 10]$ (dashed lines refer to $t \in [0, \pi)$ and solid lines to $t \in (\pi, 2\pi]$).

46
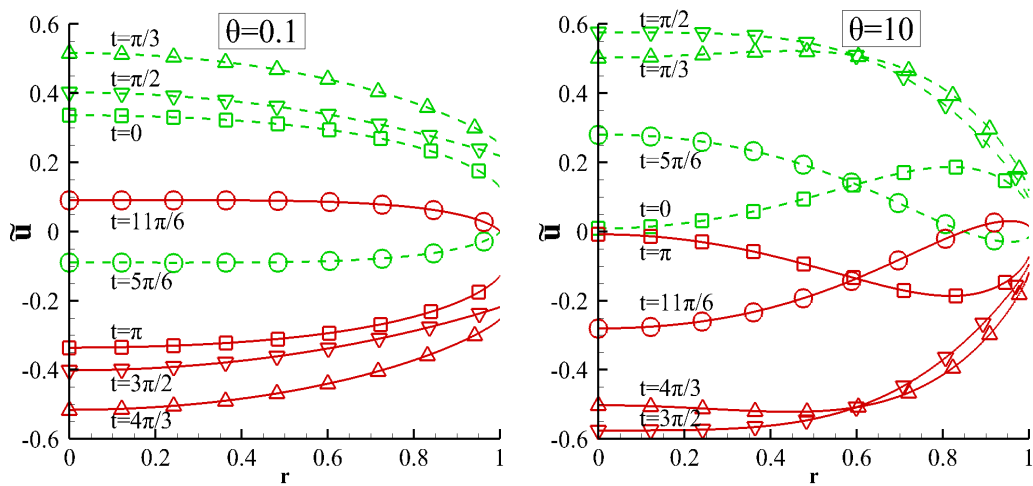
Figure 3.6 Time evolution of velocity distribution $\tilde{u}(r,t)$ versus radial distance r at certain times $t \in [0, 2\pi]$ over one period of oscillation for $\delta = \theta = 0.1$ (left) and $\delta = \theta = 10$ (right); the Strouhal number in both cases is equal to 1 (dashed lines refer to $t \in [0, \pi)$ and solid lines to $t \in (\pi, 2\pi]$).

Chapter 4

Pulsatile pressure driven rarefied gas flow in rectangular ducts

4.1 Introduction

Pulsatile pressure driven flows have been extensively investigated in the hydrodynamic regime. However, in the transition and the free molecular regimes it hasn't been studied. In this Chapter, the rarefied gas flow due to pulsating pressure gradient in channels of rectangular cross section is investigated [128]. It is noted that superimposing the reciprocating flow and the corresponding steady-state flow yields the pulsatile pressure driven flow which it simulated based on the linearized BGK equation, with the assumption of small pressure gradients. Since the analysis in the previous Chapter is focused only on the velocity distributions and the flow rates as well as the comparison between the flow regimes, computational results for more macroscopic quantities are provided here. Except for the velocities and the flow rates, the following quantities are presented: the mean wall shear stress, the acting viscous, pressure and inertia forces and the pumping power. Therefore, in this Chapter a more detailed analysis about the pulsatile flow and correspondingly the oscillatory flow is presented. It is noted that following the theoretical understanding of the involved flow parameters on the macroscopic quantities in all flow regimes, rarefied pulsatile flows may be introduced in several microfluidics and vacuum technology applications [177, 92, 22]. More specifically, a typical application is the pulse tube cryocooler where the correct phase response between gas movement and pressure oscillation is vital to the heat transfer. The relevant heat transfer is based on a thermoacoustic oscillation of a small gas portion (reservoir) that "undulates" back and forth [178].

<div align="center">49</div>

The Chapter is organized as follows: In Section 4.2, all macroscopic quantities of the rarefied pulsatile gas flow are described in detail, decomposing the flow into the oscillatory and steady parts. Also, the dimensionless parameters characterizing the flow are specified. In Section 4.3, the kinetic formulation of pulsatile flow through a duct and between parallel plates with the associated boundary conditions and the implemented numerical scheme are provided. The numerical results are presented in Section 4.4 and they include the amplitude, phase angle and time evolution of the most important macroscopic quantities in terms of the parameters specifying the flow. The velocities and flow rates are given in Section 4.4.1 and Section 4.4.2 respectively, the mean wall shear stresses and the acting forces in Section 4.4.3 and the pumping powers in Section 4.4.4. The concluding remarks are outlined in Section 4.5. Finally, in Appendix A.1, closed form expressions in the hydrodynamic and slip regimes are provided respectively.

4.2   Flow configuration and definition of macroscopic quantities

Consider the time-dependent isothermal flow of a monatomic rarefied gas through a long duct with a constant rectangular cross section restricted as $-H/2 \leq y' \leq H/2$ and $-W/2 \leq x' \leq W/2$. Without loss of generality, the height is assumed to be smaller or equal to the width of the channel ($H \leq W$). The area and the perimeter of the channel cross section are defined by $A' = H \times W$ and $\Gamma' = 2(H + W)$ respectively. The flow is caused by a pulsatile pressure gradient that consists of a constant part that does not vary in time and that produces a steady flow forward, plus an oscillatory part, with the oscillation frequency ω, that moves the fluid only back and forth and that produces zero net flow over each cycle. Furthermore, the duct is considered as adequately long, in order to ignore end effects and assume pulsatile fully-developed flow. This flow set-up has been extensively investigated in the hydrodynamic regime [72], while the corresponding work in the transition and free molecular regimes is limited [127].

Next, the main flow quantities of the pulsatile flow are introduced first in dimensional and then, in dimensionless form. The local pulsatile pressure gradient depends on the flow direction z' and time t'. It may be written as

$$\frac{d\hat{P}_{PUL}(t', z')}{dz'} = \frac{dP_S(z')}{dz'} + \frac{d\hat{P}(z', t')}{dz'} = \frac{dP_S(z')}{dz'} + \frac{dP(z')}{dz'}\cos(\omega t') =$$

$$= \frac{dP_S(z')}{dz'} + \frac{dP(z')}{dz'} \mathrm{R}\left[\exp\left(-i\omega t'\right)\right] \tag{4.1}$$

where $d\hat{P}_{PUL}/dz'$, dP_S/dz' and $d\hat{P}/dz'$ refer to the pulsatile, steady and oscillatory pressure gradients, $dP(z')/dz'$ is the amplitude of the oscillating pressure gradient, while R denotes the real part of a complex expression, with $i = \sqrt{-1}$. It is evident that the time average over one period of the pressure gradient of the oscillatory flow is zero, while of the pulsatile flow is different than zero and equal to the steady pressure gradient. Due to the linearity of Eq. (4.1), the steady and oscillatory parts of the pulsatile fully-developed flow can be solved independently of each other. This is a useful breakdown, because the steady part of the flow has already been solved in [58, 179] and therefore, only the oscillatory part remains for investigation.

The pulsatile pressure gradient generates a gas flow in the $z'-$direction, which is characterized by its pulsatile velocity and shear stress distributions given by

$$\hat{U}_{PUL}(t', x', y') = U_S(x', y') + \hat{U}(t', x', y') = U_S(x', y') + \mathrm{R}\left[U(x', y')\exp\left(-i\omega t'\right)\right] \tag{4.2}$$

and

$$\hat{\Pi}_{PUL,jz'}(t', x', y') = \Pi_{S,jz'}(x', y') + \hat{\Pi}_{jz'}(t', x', y') =$$
$$= \Pi_{S,jz'}(x', y') + \mathrm{R}\left[\Pi_{jz'}(x', y')\exp\left(-i\omega t'\right)\right], j = x', y' \tag{4.3}$$

respectively. In all cases the pulsatile quantities consist of the steady and oscillatory parts. The superscript $\wedge$ always denotes time-dependent quantities. The complex functions $U(x', y')$, $\Pi_{x'z'}(x', y')$ and $\Pi_{y'z'}(x', y')$ completely determine the oscillatory pressure driven flow. From Eqs. (4.1)-(4.3), it is seen that in general, the pressure gradient, the velocity and the shear stress are not in phase with each other. Integrating the velocity over the cross section and the wall shear stress along the perimeter of the cross section the mean velocity and mean wall shear stress are defined:

$$\bar{\hat{U}}_{PUL}(t') = \frac{1}{A'}\iint_{A'}\hat{U}_{PUL}(t', x', y')\,dA' = \bar{U}_S + \bar{\hat{U}}(t') = \bar{U}_S + \mathrm{R}\left[\bar{U}\exp\left(-i\omega t'\right)\right] \tag{4.4}$$

$$\bar{\hat{\Pi}}_{PUL,W}(t') = \int_{\Gamma'}\hat{\Pi}_{PUL,jz}(t', x', y')\,d\Gamma' = \bar{\Pi}_{S,W} + \bar{\hat{\Pi}}_W(t') = \bar{\Pi}_{S,W} + \mathrm{R}\left[\bar{\Pi}_W\exp\left(-i\omega t'\right)\right] \tag{4.5}$$

The quantities with the subscript "S" always denote the steady part, while $\bar{U}$ and $\bar{\Pi}_W$ are complex and related to the oscillatory part.

Furthermore, the pulsatile mass flow rate is defined as

$$\hat{\dot{M}}_{PUL}\left(t'\right) = \iint_{A'} \rho\left(t', z'\right) \hat{U}_{PUL}\left(t', x', y'\right) dA' = \dot{M}_S + \dot{M}\left(t'\right) = \dot{M}_S + \mathrm{R}\left[\dot{M}\exp\left(-i\omega t'\right)\right]$$
$$(4.6)$$

where $\dot{M}_S$ and $\dot{M}\left(t'\right)$ denote the steady and oscillatory mass flow rates, while the mass density $\rho = \rho\left(t', z'\right)$ varies in time and in the axial direction (it is constant at each cross section) and it is defined by the equation of state once the operating pressure and temperature are specified. The net oscillatory mass flow rate over one oscillation cycle is zero.

Next, based on the mean velocity and wall shear stress, the inertia (or acceleration) $\hat{F}'_I\left(t'\right)$ and viscous $\hat{F}'_V\left(t'\right)$ forces acting on a fluid volume $A'dz'$ passing through the channel are given by

$$\hat{F}'_{PUL,I}\left(t'\right) = \rho dz' A' \frac{\partial \bar{\hat{U}}_{PUL}\left(t'\right)}{\partial t'} = \rho dz' A' \frac{\partial \bar{\hat{U}}\left(t'\right)}{\partial t'} = \hat{F}'_I\left(t'\right) \qquad (4.7)$$

and

$$\hat{F}'_{PUL,V}\left(t'\right) = F'_{S,V} + \hat{F}'_V\left(t'\right) = dz' \Gamma' \left(\bar{\Pi}_{S,W} + \bar{\hat{\Pi}}_W\left(t'\right)\right). \qquad (4.8)$$

As expected the inertia force is related only to the oscillatory part, while the viscous force has both steady and oscillatory parts. At any point in time, the driving pressure force

$$\hat{F}'_{PUL,P}\left(t'\right) = F'_{S,P} + \hat{F}'_P\left(t'\right) = A'dP_S + A'd\hat{P}\left(t'\right) \qquad (4.9)$$

must equal the net sum of the viscous and inertia forces that may add or subtract from each other at different times within the oscillatory cycle. Then, the following steady and oscillatory force balances are formed:

$$\text{Steady:} \quad A'dP_S = dz'\Gamma'\bar{\Pi}_{S,W} \qquad (4.10)$$

$$\text{Oscillatory:} \quad A'd\hat{P}\left(t'\right) = \rho dz' A' \frac{\partial \bar{\hat{U}}\left(t'\right)}{\partial t'} + dz'\Gamma'\bar{\hat{\Pi}}_W\left(t'\right). \qquad (4.11)$$

It is noted that due to the fully-developed flow there is no net momentum flux.

Finally, the pumping power needed to drive the pulsatile flow is defined as

$$\hat{E}'_{PUL}\left(t'\right) = E'_S + \hat{E}'\left(t'\right) \qquad (4.12)$$

52

where the steady the oscillatory pumping powers are given by the product of the corresponding acting pressure forces times the mean velocities written as

$$E'_S = A'dP_S\bar{U}_S \tag{4.13}$$

and

$$\hat{E}'(t') = A'd\hat{P}(t')\bar{U}(t') = A'dP\cos(\omega t')\,\text{R}\left[\bar{U}\exp(-i\omega t')\right] \tag{4.14}$$

respectively. Since the oscillatory part $\hat{E}'(t')$ does not produce any net flow forward and since the steady part E'_S is the same as that in steady flow, any power expenditure on the oscillatory part of the flow reduces the efficiency of the flow. It is noted that the integral of the oscillatory pumping power over one cycle in nonzero, hence oscillatory flow requires energy to maintain even the net flow is zero. This energy expenditure is required to balance the energy dissipation at the channel wall, while the net energy expenditure for accelerating and decelerating the flow is zero [72].

The parameters which define the problem in dimensional form include the gas properties, the operating pressure and temperature, the channel geometry and the oscillation frequency. They are significantly reduced by introducing the corresponding quantities in dimensionless form, allowing in parallel, a more detailed flow investigation. To achieve that the two dimensionless flow parameters defining the present pulsatile flow are specified [127]. The first one is the gas rarefaction parameter δ and it is given by

$$\delta = \frac{PH}{\mu\upsilon} \tag{4.15}$$

where μ is the gas viscosity at some reference temperature T and $\upsilon = \sqrt{2RT}$ is the most probable molecular speed ($R = k_B/m$, with k_B denoting the Boltzmann constant and m the molecular mass, is the gas constant). The second one is the frequency parameter θ and it is given by

$$\theta = \frac{P}{\mu\omega} \tag{4.16}$$

where (P/μ) is the intermolecular collision frequency and ω the oscillation frequency. As $\theta \to \infty$, the oscillatory part of the flow diminishes.

Also, the dimensionless independent space and time variables

$$x = x'/H, y = y'/H, z = z'/H \quad \text{and} \quad t = t'\omega, \tag{4.17}$$

with $-1/2 \leq y \leq 1/2$ and $-H/(2W) \leq x \leq H/(2W)$ are introduced. The dimensionless area and perimeter of the channel cross section are defined by $A = A'/H^2$ and $\Gamma = \Gamma'/H$ respectively, while $\Gamma/A = 2(1 + H/W)$. The dimensionless amplitude of the local oscillatory pressure gradient is

$$X = \frac{H}{P(z')}\frac{dP(z')}{dz'} = \frac{1}{P(z)}\frac{dP(z)}{dz}, \tag{4.18}$$

with $X << 1$. This assumption is typical in fully-developed flows (also in steady-state setups), in order to permit the linearization of the governing kinetic equation and it is valid for any pressure difference provided that the channel is adequately long [179, 2]. For comparison purposes between the oscillatory and steady flow, the amplitude of the oscillatory pressure gradient is taken equal to the steady one ($dP/dz' = dP_S/dz'$). In this way, $X = X_S$, and the peak values of the macroscopic quantities (velocity, flow rate, shear stress, and pumping power) of the oscillatory flow can be compared with the corresponding ones of the steady flow.

All velocities (pulsatile, oscillatory and steady) are non-dimensionalized by the most probable speed v. More specifically, Eq. (4.2) is divided by (vX) to yield

$$\hat{u}_{PUL}(t,x,y) = u_S(x,y) + \hat{u}(t,x,y) \tag{4.19}$$

where $u_S(x,y)$ is the steady flow velocity and $\hat{u}(t,x,y)$ is the oscillatory flow velocity, which may be written as

$$\hat{u}(t,x,y) = \mathrm{R}\left[u(x,y)\exp(-it)\right] = \mathrm{R}\left[u_A(x,y)\exp(i(u_P(x,y) - t))\right] =$$

$$= u_A(x,y)\cos\left[t - u_P(x,y)\right] \tag{4.20}$$

In Eq. (4.20) the subscripts A and P denote the amplitude and the phase angle of the complex oscillatory velocity $u(x,y)$. The mean velocities are also non-dimensionalized by the most probable speed v and the resulting mean steady and oscillatory velocities are denoted by $\bar{u}_S$ and $\bar{\hat{u}}(t)$ respectively.

Next, the dimensionless flow rate is defined by introducing (4.17), (4.19) and (4.20) along with the equation of state $P = \rho v^2/2$ into Eq. (4.6) to obtain $\tilde{\dot{M}}_{PUL}(t') = H^2 P X \hat{G}_{PUL}(t)/v$, where

$$\hat{G}_{PUL}(t) = G_S + \hat{G}(t). \tag{4.21}$$

In Eq. (4.21), G_S is the well-known steady flow rate given by [179]

$$G_S = 2\frac{H}{W} \int_{-1/2}^{1/2} \int_{-W/(2H)}^{W/(2H)} u_S(x, y)\, dxdy \tag{4.22}$$

and $\hat{G}(t)$ is the oscillatory flow rate given by

$$\hat{G}(t) = 2\frac{H}{W} \int_{-1/2}^{1/2} \int_{-W/(2H)}^{W/(2H)} \hat{u}(t, x, y)\, dxdy. \tag{4.23}$$

The oscillatory flow rate $\hat{G}(t)$ may be also written as

$$\hat{G}(t) = \mathrm{R}\left[G \exp(-it)\right] = \mathrm{R}\left[G_A \exp(i(G_P - t))\right] = G_A \cos(G_P - t) \tag{4.24}$$

where the flow rate G, as well its amplitude G_A and phase angle G_P, may be computed by integrating accordingly the corresponding velocity quantities. Based on the above definitions it is readily seen that the dimensionless flow rates may be connected to the dimensionless mean velocities by the following expressions: $G_S = 2\bar{u}_S$ and $\hat{G}(t) = 2\bar{\hat{u}}(t)$.

All stresses (pulsatile $\hat{\tau}_{PUL}$, oscillatory $\hat{\tau}$ and steady τ_S) are non-dimensionalized by $(2PX)$. The mean pulsatile wall shear stress $\bar{\hat{\tau}}_{PUL,W}(t)$ which consists of the steady mean wall shear stress $\bar{\tau}_{S,W}$ plus the oscillatory one $\bar{\hat{\tau}}_W(t)$ written as

$$\bar{\hat{\tau}}_W(t) = \mathrm{R}\left[\bar{\tau}_W \exp(-it)\right] = \mathrm{R}\left[\bar{\tau}_{W,A} \exp(i(\bar{\tau}_{W,P} - t))\right] = \bar{\tau}_{W,A} \cos(t - \bar{\tau}_{W,P}). \tag{4.25}$$

In Eq. (4.25) the subscripts A and P denote the amplitude and the phase angle of the corresponding oscillatory complex shear stresses.

All forces in Eqs. (4.7)-(4.9) are divided by (PX_PH^2) to yield the corresponding dimensionless ones:

$$\hat{F}_{PUL,I}(t) = \hat{F}_I(t) = dzA\frac{\delta}{\theta}\frac{d\hat{G}}{dt} = dzA\frac{\delta}{\theta}G_A \sin(G_P - t) \tag{4.26}$$

$$\hat{F}_{PUL,V}(t) = F_{S,V} + \hat{F}_V(t) = 2dz\Gamma\left[\bar{\tau}_{S,W} + \bar{\hat{\tau}}_W(t)\right] = 2dz\Gamma\left[\bar{\tau}_{S,W} + \bar{\tau}_{W,A} \cos(\bar{\tau}_{W,P} - t)\right] \tag{4.27}$$

$$\hat{F}_{PUL,P}(t) = F_{S,P} + \hat{F}_P(t) = Adz(1 + \cos t) \tag{4.28}$$

The balance equations of the steady $F_{S,V} = F_{S,P}$ and oscillatory $\hat{F}_I(t) + \hat{F}_V(t) = \hat{F}_P(t)$ forces in dimensionless form are:

$$\text{Steady:} \quad \bar{\tau}_{S,W} = A/(2\Gamma) = \left[4\left(1 + \frac{H}{W}\right)\right]^{-1} \tag{4.29}$$

$$\text{Oscillatory:} \quad \frac{\delta}{\theta}G_A\sin(G_P - t) + 4\left(1 + \frac{H}{W}\right)\bar{\tau}_{W,A}\cos(\bar{\tau}_{W,P} - t) = \cos t. \tag{4.30}$$

Equation (4.29) has been also reported in previous works related to steady fully-developed flows through channels of various cross sections [180, 181]. Equation (4.30) is the corresponding one for oscillatory flow. The first and second terms at the left hand side refer to the inertia and viscous forces respectively, while the right hand side refers to the pressure forces. In Section 4.4.3, these forces are plotted for various values of δ and θ.

Finally, the dimensionless pumping power is derived by dividing Eqs. (4.12)-(4.14) by $(\upsilon X)(XP)H^2$ to find $\hat{E}_{PUL}(t) = E_S + \hat{E}(t)$, where the steady pumping power is $E_S = AdzG_S/2$ and the oscillatory one is written as

$$\hat{E}(t) = \frac{1}{2}Adz\cos t\,G(t) = \frac{1}{2}Adz\cos t\,\text{R}\left[G\exp(-it)\right] =$$

$$= \frac{1}{2}Adz\cos t\,\text{R}\left[G_A\exp(i(G_P - t))\right] = \frac{1}{2}AdzG_A\cos t\cos(G_P - t). \tag{4.31}$$

By integrating Eq. (4.31) over one oscillation cycle, the average pumping power over the cycle is formed as

$$\bar{E} = \frac{1}{2\pi}\int_0^{2\pi}\hat{E}(t)\,dt = \frac{1}{4}AdzG_A\cos(G_P). \tag{4.32}$$

In the low frequency regime, where $G_P \to 0$ and $G_A \simeq G_S$, it is seen that the average oscillatory pumping power is half of the corresponding steady one ($\bar{E} \simeq E_S/2$).

The prescribed pulsatile flow is solved here in the whole range of δ and θ, which may vary from zero to infinity and for various aspect ratios $H/W \in [0, 1]$. The solution is based on the kinetic modeling described in the next section. The oscillatory flow rate G, mean wall shear stress $\bar{\tau}_W$ and pumping powers $\hat{E}(t)$ and $\bar{E}$ are probably the most important quantities from a technological point of view, while the oscillatory velocity $u(x, y)$ is more important from a theoretical point of view providing an insight view of the flow characteristics. All these quantities along with their time evolution are provided in the results section.

56

4.3 Kinetic formulation and numerical scheme

4.3.1 Pulsatile flow in a rectangular duct

For arbitrary values of the parameters δ and θ the flow must be simulated based on kinetic theory, where the main unknown is the distribution function $f = f(t', \boldsymbol{r}', \xi)$, which is a function of time t', position vector $\boldsymbol{r}' = (x', y', z')$ and molecular velocity vector $\boldsymbol{\xi} = (\xi_x, \xi_y, \xi_z)$. The unknown distribution obeys the time-dependent nonlinear two-dimensional BGK equation [182]

$$\frac{\partial f}{\partial t'} + \xi_x \frac{\partial f}{\partial x'} + \xi_y \frac{\partial f}{\partial y'} + \xi_z \frac{\partial f}{\partial z'} = \frac{P}{\mu} \left(f^M - f \right) \qquad (4.33)$$

where (P/μ) is the collision frequency and

$$f^M (t', \boldsymbol{r}', \xi) = n \left(\frac{m}{2\pi kT} \right)^{3/2} \exp \left[-\boldsymbol{m} \left(\xi - \hat{\boldsymbol{U}}_{PUL} \right)^2 \Big/ (2kT) \right] \qquad (4.34)$$

is the local Maxwellian distribution. Due to the assumption of isothermal fully-developed flow the temperature T is constant and the number density $n = n(z')$ varies only in the $z'-$direction. Also, the macroscopic velocity has only the $z'-$component and it is the same with the pulsatile velocity defined in Eq. (4.2), i.e., $\hat{\boldsymbol{U}}_{PUL} = \left(0, 0, \hat{U}_{PUL} \right)$. The pulsatile velocity and shear stress (defined in Eq. (4.3)) at some position z' in the flow direction may be obtained by the first and second moments of f according to

$$\hat{U}_{PUL} (t', x', y') = \frac{1}{n} \int \xi_z \tilde{f}(t', \boldsymbol{r}', \boldsymbol{\xi}) \, d\xi \qquad (4.35)$$

and

$$\hat{\Pi}_{PUL, jz'} (t', x', y') = m \int \xi_j \left(\xi_z - \hat{U}_{PUL} \right) f(t', \boldsymbol{r}', \xi) \, d\xi, j = x', y' \qquad (4.36)$$

respectively.

The condition of small local pressure gradient $(X \ll 1)$ allows the linearization of Eq. (4.33) by representing the unknown distribution function as

$$f(t', \boldsymbol{r}', \boldsymbol{\xi}) = f_0 \left[1 + X\hat{h}_{PUL}(t, x, y, \boldsymbol{c}) + Xz \left(1 + \exp(-it) \right) \right], \qquad (4.37)$$

where $\boldsymbol{c} = \boldsymbol{\xi}/\upsilon$, $f_0 = \frac{n}{\pi^{3/2} \upsilon^3} \exp \left[-\boldsymbol{c}^2 \right]$ is the absolute Maxwellian and $\hat{h}_{PUL}(t, x, y, \boldsymbol{c})$ is the unknown perturbed distribution function referring to the pulsatile fully-developed

flow, which may be decomposed as

$$\hat{h}_{PUL}(t, x, y, \boldsymbol{c}) = h_S(x, y, \boldsymbol{c}) + \hat{h}(t, x, y, \boldsymbol{c}) \tag{4.38}$$

with $\hat{h}_S(x, y, \boldsymbol{c})$ and $\hat{h}(t, x, y, \boldsymbol{c})$ referring to the steady and oscillatory parts respectively. Substituting expressions (4.37) and (4.38) into Eq. (4.33) and introducing the dimensionless variables, yields the following two linearized BGK kinetic model equations:

$$c_x \frac{\partial h_S}{\partial x} + c_y \frac{\partial h_S}{\partial y} + c_z = \delta \left[2 c_z u_S(x, y) - h_S(x, y, \boldsymbol{c}) \right] \tag{4.39}$$

$$\frac{\delta}{\theta} \frac{\partial \hat{h}}{\partial t} + c_x \frac{\partial \hat{h}}{\partial x} + c_y \frac{\partial \hat{h}}{\partial y} + c_z e^{-it} = \delta \left[2 c_z \mathrm{R} \hat{u}(t, x, y) - \hat{h}(t, x, y, \boldsymbol{c}) \right] \tag{4.40}$$

The first one describes the steady fully-developed flow through an orthogonal duct and it is solved in [179, 2]. The second one describes the oscillatory fully-developed flow and it is the one to be solved in the present work.

Since Eq. (4.40) is linear, it is convenient to introduce the complex distribution function $h(x, y, \boldsymbol{c})$ so that

$$\hat{h}(t, x, y, \boldsymbol{c}) = \mathrm{R}\left[h(x, y, \boldsymbol{c}) \exp(-it) \right]. \tag{4.41}$$

Also, the molecular velocity vector $\boldsymbol{c} = (c_x, c_y, c_z)$ is transformed as $\boldsymbol{c} = (\zeta, \varphi, c_z)$, where $c_r = \zeta \cos \varphi$ and $c_\varphi = \zeta \sin \varphi$. Then, Eq. (4.40) is rewritten in terms of h as

$$\zeta \cos \varphi \frac{\partial h}{\partial x} + \zeta \sin \varphi \frac{\partial h}{\partial y} + h \left(\delta - \frac{\delta}{\theta} i \right) + c_z = 2 \delta c_z u(x, y). \tag{4.42}$$

The non-dimensionalization, linearization and the molecular velocity vector transformation are also applied to the velocity and the shear stress given by Eqs. (4.35) and (4.36) to obtain:

$$u(x, y) = \frac{1}{\pi} \int_{-\infty}^{\infty} \int_0^{2\pi} \int_0^{\infty} c_z h e^{-c^2} d\zeta d\varphi dc_z \tag{4.43}$$

$$\tau_{xz}(x, y) = \frac{1}{\pi} \int_{-\infty}^{\infty} \int_0^{2\pi} \int_0^{\infty} (\zeta \cos \varphi) c_z h e^{-c^2} d\zeta d\varphi dc_z \tag{4.44}$$

$$\tau_{yz}(x, y) = \frac{1}{\pi} \int_{-\infty}^{\infty} \int_0^{2\pi} \int_0^{\infty} (\zeta \sin \varphi) c_z h e^{-c^2} d\zeta d\varphi dc_z. \tag{4.45}$$

At this stage the component c_z of the molecular velocity vector may be eliminated by applying the so-called projection procedure and introducing the reduced perturbed

distribution function

$$Y(x, y, \zeta, \varphi) = \frac{1}{\pi} \int_{-\infty}^{\infty} h(x, y, \zeta, \varphi, c_z) \exp\left[-c_z{}^2\right] dc_z. \tag{4.46}$$

Equation (4.46) is multiplied by $c_z \exp\left(-c_z^2\right)/\sqrt{\pi}$ and the resulting equation is integrated over c_z to deduce

$$\zeta \cos\varphi \frac{\partial Y}{\partial x} + \zeta \sin\varphi \frac{\partial Y}{\partial y} + \left(\delta - i\frac{\delta}{\theta}\right) Y = \delta u - \frac{1}{2}. \tag{4.47}$$

Operating similarly on the moments of h, given by Eqs. (4.43)-(4.45), yields:

$$u(x, y) = \frac{1}{\pi} \int_0^{2\pi} \int_0^{\infty} Y e^{-\zeta^2} \zeta d\zeta d\varphi \tag{4.48}$$

$$\tau_{xz}(x, y) = \frac{1}{\pi} \int_0^{2\pi} \int_0^{\infty} (\zeta \cos\varphi) Y e^{-\zeta^2} \zeta d\zeta d\varphi \tag{4.49}$$

$$\tau_{yz}(x, y) = \frac{1}{\pi} \int_0^{2\pi} \int_0^{\infty} (\zeta \sin\varphi) Y e^{-\zeta^2} \zeta d\zeta d\varphi \tag{4.50}$$

It is noted that $Y = Y_{Re} + iY_{Im}$ is complex and the same applies for the velocity $u(x, y)$ and the shear stresses $\tau_{jz}(x, y)$, $j = x, y$.

Turning now to the boundary conditions it is noted that Maxwell diffuse-specular boundary conditions are used. The gas–surface interaction is modeled as [182]

$$f^+ = \alpha f_W^M + (1 - \alpha) f^-, \boldsymbol{c} \cdot \boldsymbol{n} > 0, \tag{4.51}$$

where the superscripts $(+)$ and $(-)$ denote distributions leaving from and arriving to the boundaries respectively, f_W^M is the Maxwellian defined by the wall conditions, $0 \leq \alpha \leq 1$ is the tangential momentum accommodation coefficient corresponding to the percentage of diffuse reflection of the gas at the wall and $\boldsymbol{n}$ is the unit vector normal to the boundaries and pointing towards the flow. Following the linearization and projection procedures as defined above it is readily deduced that at the wall boundaries

$$Y^+ = (1 - \alpha) Y^-, \boldsymbol{c} \cdot \boldsymbol{n} > 0. \tag{4.52}$$

These boundary conditions are applied at $y = \pm 1/2$ and $x = \pm H/(2W)$.

Closing this section it is interesting to comment on the behavior of Eq. (4.47) at limiting values of θ and δ. When both $\delta >> 1$ and $\theta >> 1$, the flow is in the

hydrodynamic or slip regimes [127]. In these regimes analytical solutions, based on the unsteady Stokes equation with either no-slip or slip boundary conditions, have been obtained and presented in Appendix A.1. As $\theta \to \infty$ ($\omega \to 0$) and $\delta << \theta$ (finite values of δ), Eq. (4.47) is reduced to the one describing the steady fully-developed flow through a rectangular duct at the corresponding δ. In the specific case of $\delta = 0$, with $\theta > 0$, the kinetic equation for steady-state flow at the free molecular limit is recovered. At the other end, as $\theta \to 0$ ($\omega \to \infty$), Eq. (4.47) yields $Y \to 0$, i.e., the solution tends to vanish at very high frequencies due to fluid inertia. It is expected the behavior of Eq. (4.47) at the limiting conditions to be reflected in the numerical results.

4.3.2   Limiting case of oscillatory flow between parallel plates

It is seen that as the aspect ratio H/W is reduced, the two-dimensional flow gradually tends to the corresponding one-dimensional flow between parallel plates. In this Section, the formulation of the kinetic equation with the associated conditions for the limiting case of $H/W = 0$ is provided.

The flow setup is reduced to pulsatile flow between two parallel plates and it is modeled by the one-dimensional time-dependent BGK model in the domain $-1/2 \leq y \leq 1/2$. Following a mathematical manipulation similar to the one presented in Section 4.3.1, the steady and oscillatory parts of the pulsatile flow are modeled. The steady part results to the well-known kinetic formulation of steady Poiseuille flow between parallel plates [2]. The oscillatory part results to the following equations:

$$c_y \frac{\partial h}{\partial y} + h\left(\delta - \frac{\delta}{\theta}i\right) + c_z = 2\delta c_z u(y), \tag{4.53}$$

$$u(y) = \frac{1}{\pi^{3/2}} \int_{-\infty}^{\infty} \int_{-\infty}^{\infty} \int_{-\infty}^{\infty} c_z h e^{-c^2} dc_x dc_y dc_z, \tag{4.54}$$

$$\tau_{xz}(y) = \frac{1}{\pi^{3/2}} \int_{-\infty}^{\infty} \int_{-\infty}^{\infty} \int_{-\infty}^{\infty} c_y c_z h e^{-c^2} dc_x dc_y dc_z. \tag{4.55}$$

Next, the c_x and c_z components of the molecular velocity vector are eliminated by introducing the reduced distribution function

$$Y(y, c_y) = \frac{1}{\pi} \int_{-\infty}^{\infty} \int_{-\infty}^{\infty} h(x, c_x, c_y, c_z) \exp\left[-c_z{}^2 - c_x{}^2\right] dc_x dc_z. \tag{4.56}$$

60

Equation (4.53) is multiplied by $c_x c_z \exp\left(-c_x^2 - c_z^2\right)/\pi$ and the resulting equation is integrated over c_x and c_z to deduce

$$c_y \frac{\partial Y}{\partial y} + \left(\delta - i\frac{\delta}{\theta}\right) Y\left(y, c_y\right) = \delta u\left(y\right) - \frac{1}{2} \tag{4.57}$$

with Y being a complex function, while the velocity and shear stress distributions are

$$u\left(y\right) = \frac{1}{\sqrt{\pi}} \int_{-\infty}^{\infty} Y e^{-c_y^2} dc_y \quad \text{and} \quad \tau\left(y\right) = \frac{1}{\sqrt{\pi}} \int_{-\infty}^{\infty} c_y Y e^{-c_y^2} dc_y. \tag{4.58}$$

The Maxwell diffuse-specular boundary conditions become

$$Y^+\left(\mp 1/2, c_y\right) = \left(1 - \alpha\right) Y^-\left(\mp 1/2, c_y\right), c_x \gtrless 0. \tag{4.59}$$

The one-dimensional oscillatory flow problem ($H/W = 0$), defined by Eqs. (4.57)-(4.59), is solved in order to have a complete view of the effect of the channel aspect ratio $H/W \in [0, 1]$ on the oscillatory flow characteristics.

4.3.3 Numerical scheme

The kinetic formulation of the oscillatory fully-developed flow in a rectangular duct is properly defined by Eq. (4.47) with the associated moments (4.48)-(4.50) subject to boundary conditions (4.52). The numerical solution is deterministic. The discretization in the molecular velocity space is performed using the discrete velocity method. The continuum spectrum $\zeta \in [0, \infty)$ is substituted by a discrete set $\zeta_m, m = 1, 2...M$, which is taken to be the roots of the Legendre polynomial of order M, accordingly mapped from $[-1, 1]$ to $[0, \infty)$. Also, a set of discrete angles φ_n, $n = 1, 2...N$ equally spaced in $[0, 2\pi]$ is defined. The discretization in the physical space is based on a second order central difference scheme. The discretized equations are solved in an iterative manner and the iteration map is concluded when the criteria

$$\left|u_{Re,i,j}^{(k+1)} - u_{Re,i,j}^{(k)}\right| < \varepsilon \quad \text{and} \quad \left|u_{Im,i,j}^{(k+1)} - u_{Im,i,j}^{(k)}\right| < \varepsilon \tag{4.60}$$

is fulfilled. Here, ε is the tolerance parameter, the superscript k denotes the iteration index, $i, j = 1, 2...L + 1$ are the nodes in the physical space, while $u_{Re,ij}$ and $u_{Im,ij}$ are the real and imaginary part of macroscopic velocity respectively at each node (i, j). This numerical scheme has been extensively applied in steady-state and time-dependent

flow configurations with considerable success [174, 175, 180, 181, 127]. The numerical parameters have been gradually refined to ensure grid independent results up to at least three significant figures. The numerical solution of the oscillatory flow between parallel plates is similar to the one described above. It is also easier to solve since only the y- component of the molecular velocity vector is needed.

Once the kinetic problem is solved the oscillatory complex velocity $u(x,y) = u_A(x,y)\exp[iu_P(x,y)]$ and shear stress $\tau_{jz}(x,y) = \tau_{jz,A}(x,y)\exp[i\tau_{jz,P}(x,y)]$, $j = x,y$ are computed in terms of δ, θ, H/W and α. The overall oscillatory quantities of the flow rate, the mean wall shear stress and the pumping power are deduced in a straightforward manner, based on the expressions provided in Section 4.2. The pulsatile flow quantities are also readily deduced by adding the corresponding steady ones.

4.4   Results and discussion

Numerical results of the time evolution, as well as of the amplitude and phase angle of the main macroscopic quantities in terms of the gas rarefaction parameter δ, the oscillation parameter θ, the duct aspect ratio H/W and the accommodation coefficient α are provided, in four subsections. Section 4.4.1 describes the velocity distributions in pulsatile and oscillatory flows. Sections 4.4.2 and 4.4.3 describe the overall quantities of flow rate and mean acting forces (including the mean wall shear stress) respectively. Since the corresponding steady parts are well-known results are provided only for the oscillatory parts. Finally, Section 4.4.4 describes the oscillatory time-dependent and average pumping powers including a comparison with the corresponding steady pumping powers.

4.4.1   Velocity distributions

In Figure 4.1, the time evolution over one cycle of the oscillatory $\hat{u}(t,0,y)$ and pulsatile $\hat{u}_{PUL}(t,0,y) = u_S(0,y) + \hat{u}(t,0,y)$ velocity distributions, given in Eqs. (4.19)-(4.20), are plotted with respect to $y \in [-1/2, 1/2]$ at $x = 0$ in the case of a square duct ($H/W = 1$). The plots are for $\delta = [0.1, 1, 10]$ covering a wide range of the gas rarefaction and $\theta = 0.1, 10$ referring to high and low frequency oscillation respectively. The evolution is shown with a time step of $\pi/2$, at $t = 0, \pi/2, \pi$ and $3\pi/2$. As expected, the oscillatory velocity over one cycle, takes both positive and negative values (the fluid is moved forth and back) and the time average velocity over one cycle is zero (no net

flow). The effect of θ on the amplitude of the oscillatory velocity is significant. As it is seen, it is greatly reduced as θ is decreased and this behavior becomes even stronger as δ is increased (less gas rarefaction). The time evolution of the pulsatile velocity is obtained by superimposing on the oscillatory velocity the corresponding steady one, which depends only on δ. Since the steady flow is independent of θ the behavior of the pulsatile velocity with respect to θ is qualitatively the same with the oscillatory one. Consequently, at large θ (e.g., $\theta = 10$), where the amplitude of the oscillatory velocity is large, the difference between the amplitude of the pulsatile velocity and the corresponding steady one is also large. On the contrary, as the oscillatory flow tends to diminish, which is happening as θ is decreased and δ is increased, the pulsatile velocity gradually tends to the steady one at the corresponding δ. This is particularly evident at $\theta = 0.1$ and $\delta = 10$, where $\hat{u}_{PUL}(t, 0, y) \simeq u_S(0, y)$. As it is outlined in Section 4.2, the present results are based on the assumption that the amplitude of the oscillatory pressure gradient is the same with the steady pressure gradient ($dP_S/dz' = d\hat{P}/dz'$). Having this in mind it is interesting to note that the pulsatile velocity takes only positive values, i.e., there is no flow reversal at any time. This observation may be technologically significant in applications where a pulsatile flow is desired, e.g. in order to enhance mixing or heat transfer under rarefied conditions, without however having particles moving opposite to the pumping direction or hot gas transported backwards into colder regions. In any case, if $dP_S/dz' < d\hat{P}/dz'$, although the net flow is nonzero, flow reversal may be present.

In Figure 4.2, the contours of the oscillatory velocity amplitude $u_A(x, y)$ are presented in a two dimensional layout for square ($H/W = 1$) and orthogonal ($H/W = 0.1$) ducts, with $\delta = [0.1.1, 10]$ and $\theta = 0.1$. As it is seen at this relatively high oscillation frequency the effect of δ moving from the free molecular ($\delta = 0.1$) through the transition ($\delta = 1$) up to the slip ($\delta = 10$) regime is remarkable. At $\delta = 0.1$ there is a very close qualitative resemblance with the corresponding steady one, with the velocity amplitude taking its maximum values at the center of the cross section of the duct and then, it is monotonically reduced towards the walls of the cross section. At $\delta = 10$, the situation is reversed, with the maximum amplitudes appearing in a very thin layer adjacent to the walls, while outside this layer the velocity amplitude is smaller and almost constant. At the intermediate value of $\delta = 1$ the maximum amplitudes occur in a wider region between the center and the walls of the duct. This description is valid for both aspect ratios. Furthermore, the velocity overshooting (known as the

"Richardson effect"), is well-known in the hydrodynamic regime [72] and it has been also recently observed in oscillatory rarefied gas flow through a tube [127].

The oscillatory velocity amplitude u_A and phase angle u_P along the symmetry axis $x = 0$ are plotted in Figs. 4.3 and 4.4 for oscillatory flow through a square duct ($H/W = 1$) and an orthogonal duct ($H/W = 0.1$) respectively for various values of δ and θ. In the former case $x \in [-1/2, 1/2]$ and in the latter one $x \in [-H/(2W), H/(2W)]$. The objective here is to comment on the dependency of u_A and u_P on δ and θ, as well as to observe the effect of the aspect ratio H/W. Always, as θ is decreased, i.e., the oscillation frequency is increased, the amplitude u_A is reduced and the phase angle lag u_P is increased. It is also seen that in general at small δ and large θ (e.g., $\delta = 0.1$ and $\theta \geq 0.1$) the velocity amplitudes have the expected shape with their maximum appearing at the center of the duct, while the corresponding phase angles are small. However, as δ is increased and θ is reduced the velocity amplitude is flattening in the core of the flow and the maximum amplitude is appearing in a region far from the center of the orthogonal duct. At large δ and small θ (e.g., $\delta = 10$ and $\theta \leq 1$) u_A remains constant from the center of the duct until close to the wall and then, in a thin layer adjacent to the wall it is rapidly increased and decreased. The corresponding phase angle lags u_P are large, even up to $\pi/2$ with regard to the pressure gradient and they remain constant from the center of the duct until the wall layer, where they change significantly in an oscillatory manner. The thickness of the region where the velocity overshooting occurs is decreased as δ is increased and θ is reduced. Therefore, in high or even moderate frequencies (it depends also on δ), the flow consists of two layers: the inviscid piston flow in the core, dominated by inertia forces and the frictional Stokes wall layer dominated by viscous forces. Comparing the corresponding results in Figs. 4.3 and 4.4, it is clearly seen that the velocity overshooting (or Richardson effect) appears first in the orthogonal duct and then in the square duct. For example at $\delta = \theta = 0.1$, $\delta = \theta = 1$ and $\delta = \theta = 10$, the velocity amplitudes for $H/W = 1$ (Figure 4.3) take their maximum values at the duct center, while for $H/W = 0.1$ (Figure 4.4) their maximum values occur far from the duct center. It is concluded that as the aspect ratio H/W is reduced the velocity overshooting appears at smaller δ and/or larger θ.

4.4.2 Flow rates

The behavior of the oscillatory flow rates $\hat{G} = G_A \cos(t - G_P)$ in terms of δ, θ, the aspect ratio H/W and the accommodation coefficient α is investigated.

64

In Figure 4.5, the flow rate amplitude G_A and phase angle G_P are provided in terms of δ with $\theta = [1, 10, 10^2]$ and $H/W = [1, 0.5, 0.1, 0]$. The case of $H/W = 0$ corresponds to oscillatory flow between parallel plates. Purely diffuse reflection is assumed at the wall ($\alpha = 1$). It is clearly seen that θ has a strong effect on the amplitude G_A, while its effect on G_P is very weak. More specifically, for $\theta = 1$, G_A is monotonically decreased as δ is increased, while for $\theta = [10, 10^2]$ it is initially decreased, then it is increased up to some local maximum appearing at $\delta \in [5, 15]$ and finally it is decreased. This behavior is justified by the fact that at adequately high oscillation frequencies (e.g., $\theta = 1$), G_A is significantly affected and it is monotonically reduced with increasing δ. On the contrary at low oscillation frequencies (e.g., $\theta = [10, 10^2]$), the variation of G_A with δ has some resemblance with the steady flow rate including the presence of a Knudsen minimum, as long as δ is sufficiently small to ensure $\delta << \theta$. Then, as δ is further increased the inequality does not hold and G_A is decreased. With regard to the phase angle, G_P is always monotonically increased with δ and it is almost independent of the oscillation frequency θ. At very small values of δ it is almost zero, then at moderate values of δ it is rapidly increased and finally, at large values of δ it is asymptotically increased reaching the limiting value of $\pi/2$. The described behavior of G_A and G_P with regard to δ and θ is qualitatively the same in all aspect ratios H/W. It is clear however, that the aspect ratio has quantitatively a significant effect on G_A and a weak effect on G_P, which becomes even weaker as θ is increased and the flow becomes stationary. In general, G_A is always increased as H/W is decreased and this is more evident for $\delta < 1$. Concerning the value of the local maximum of G_A at large θ within some $\delta \in [5, 15]$ again it is increased as the aspect ratio H/W is decreased obtaining the maximum value in the case of flow between parallel plates ($H/W = 0$).

In Figure 4.6, the flow rate amplitude G_A and phase angle G_P are provided in terms of δ with $\theta = [0.1, 1, 10]$, $H/W = [1, 0.1]$ and the accommodation coefficient $\alpha = [1, 0.85, 0.7]$. As expected, $G_A(\delta, \theta)$ is monotonically increased as α is decreased, i.e., the reflection becomes more specular. The phase angle G_P however, does not strongly depend on the type of gas-surface interaction. As α is decreased the phase angle lag is only slightly increased for the same δ and θ, which becomes more evident as θ is decreased and at moderate values of δ.

In Figure 4.7, the oscillatory flow rate $\hat{G} = G_A \cos(t - G_P)$, is plotted versus time $t \in [0, 2\pi]$ for typical values of δ and θ with $H/W = [1, 0.1]$. The time evolution of the dimensionless pressure gradient is equal to $\cos t$. It is seen that $\hat{G}$ strongly depends on both the gas rarefaction parameter and the oscillation frequency. When

65

$\delta = 0.1$, the $\hat{G}$ profiles for $\theta = [1, 10, 10^2]$ (low and moderate oscillation frequencies) are very close to each and in phase with the pressure gradient, while for $\theta = 0.1$ (high oscillation frequency) $\hat{G}$ has a smaller amplitude and a larger lagging phase angle. As δ is increased the effect of θ becomes gradually more dominant. At $\delta = 1$, the $\hat{G}$ profiles only for $\theta = [10, 10^2]$ are close to each other and in phase, while for $\theta = [0.1, 1]$ the amplitude is reduced and the phase angle lag is increased. This behavior is further enhanced at $\delta = 10$, where the effect of the oscillation frequency is very significant for $\theta = [0.1, 1, 10]$ and remains not important only for $\theta = 10^2$. It is seen that at $\delta = 1$ and $\theta = 0.1$, as well as at $\delta = 10$ and $\theta = 0.1, 1$ the amplitudes are very small and the phase angle lags are almost $\pi/2$. These observations are valid for both aspect ratios. Quantitatively, as H/W is decreased moving from the square duct to the parallel plates setup the amplitude is increased and the phase angle lag is slightly increased, which is in agreement with the observations in Figure 4.6. It is also noted that the peak of the flow rate amplitude always falls short of reaching the corresponding steady flow rate, which is clearly contributed to the inertia of the fluid, which must be accelerated and decelerated in each cycle.

Tabulated results of the flow rate amplitude G_A and phase angle G_P for the specific case of an orthogonal duct with $H/W = 0.1$ are presented in Tables 4.1 and 4.2 respectively in terms of the gas rarefaction $\delta \in [10^{-4}, 10^2]$ and the oscillation parameter $\theta = [0.1, 1, 10, 50, 10^2]$. In addition, the flow rate amplitude $G_A^{(S)}$ and phase angle $G_P^{(S)}$ in the slip regime, based on the analytical expression (A.9), are provided for $\delta \geq 1$ with $\theta = 50$ and $\theta = 10^2$. In the last column of Table 4.1, the well-known steady flow rates ($\theta \to \infty$), denoted by $G_S(\delta)$, for $\delta \leq 15$ are also included [179]. By comparing G_A and G_P with the corresponding $G_A^{(S)}$ and $G_P^{(S)}$ it is readily seen that there is very good agreement up to at least two significant figures for $\delta > 10$ (both δ and θ must be large) and then, as δ is decreased the discrepancies are gradually increased. Also, the values $G_A(\delta, \theta)$ for the large oscillation parameter $\theta = 10^2$ are in very good agreement with the corresponding steady flow rates $G_S(\delta)$ in small and intermediate values of δ and then, as δ is further increased the discrepancies also increase. This is expected since steady conditions are recovered provided that the oscillation parameter is large (which it is, since $\theta = 10^2$) and also $\delta << \theta$ (which is the case only when $\delta < 10$). These comparisons demonstrate the accuracy of the kinetic results.

Furthermore, it is seen in Table 4.1 that for any given δ, G_A is monotonically increased with θ, being always less than the corresponding stationary solution $G_S(\delta)$. Also, as δ is increased, for $\theta \leq 1$, G_A is monotonically decreased, while for $\theta \geq 10$ it is

initially decreased until $\delta = 1$, where a local minimum is observed, then it is increased up to some δ, which depends on θ, and finally as δ is further increased it is again decreased. As $\delta \to 0$ and for all θ, the solution tends to the semi-analytical steady free molecular flow rate, which is equal to 1.991 (see Table II in [179]). For small values of θ and adequately large values of δ, G_A tends to diminish, since due to the high oscillation frequency and the deduced inertial forces the gas has great difficulty to reach a peak flow.

In Table 4.2, for any given δ the phase angle G_P is increased as θ is decreased, i.e., as the oscillation frequency is increased. At very high frequencies and adequately large δ, this may result to almost zero amplitude with $\pi/2$ phase angle. Also, for any given θ, G_P is monotonically increased with δ, being almost zero in the free molecular regime and then, it is increasing as the oscillatory flow becomes less rarefied, reaching the maximum phase angle lag in the hydrodynamic limit. Overall, as the oscillation frequency is increased the flow rate amplitude is decreased, while the phase angle is increased, which in accordance with the observations made in Section 4.4.1 for the velocity distributions.

4.4.3 Mean wall shear stresses and acting forces

Next, the behavior of the oscillatory mean wall shear stress $\bar{\hat{\tau}}_W = \bar{\tau}_{W,A} \cos\left(t - \bar{\tau}_{W,P}\right)$ in terms of δ, θ and H/W is investigated. It is noted that the steady mean wall shear stress $\bar{\tau}_{S,W} = 0.25 \left(1 + H/W\right)^{-1}$ is independent of δ and depends only on the aspect ratio H/W (Section 4.2, Eq. (4.29)).

In Figure 4.8, the oscillatory mean wall shear stress amplitude $\bar{\tau}_{W,A}$ and phase angle $\bar{\tau}_{W,P}\left(\delta, \theta\right)$ are plotted in terms of δ with $\theta = [1, 10, 10^2]$ and $H/W = [1, 0.5, 0.1, 0]$. For very small values of δ the mean wall shear stress amplitude $\bar{\tau}_{W,A}$ takes the same value as the corresponding steady one $\bar{\tau}_{S,W}$ at the same H/W. Then, as δ is increased it is slightly reduced and then, from some δ in the late transition or slip regimes it is rapidly decreased. The value of δ where this rapid decrease of $\bar{\tau}_{W,A}$ is starting depends on θ and it is increasing as θ is decreasing. At $\theta = [1, 10, 10^2]$ the corresponding values of δ are about $\delta = [0.1, 2, 10]$. Thus, the variation of $\bar{\tau}_{W,A}$ does not include the local maxima observed in the variation of G_A (Figure 4.5). This overall behavior of $\bar{\tau}_{W,A}$ is valid for all values of the aspect ratio H/W. Also, it is seen that $\bar{\tau}_{W,A}$ depends strongly on the aspect ratio, particularly in the free molecular and slip regimes and it is always increased as H/W is decreased. The dependency of the oscillatory mean wall shear stress phase angle $\bar{\tau}_{W,P}$ on δ, θ and H/W is very close to the corresponding one of

67

the flow rate phase angle G_P in Figure 4.5. More specifically, it is increased with δ having a rapid increase in the transition regime, it is also increased as θ is decreased and finally, it demonstrates a weak dependency on H/W.

It is noted that comparing the corresponding phase angle lags $\bar{\tau}_{W,P}$ and G_P, it has been found (although it is not clear in Figs. 4.5 and 4.8) that $\bar{\tau}_{W,P}$ is almost always slightly smaller than G_P leading to the fact that the mean wall shear stress has a smaller phase angle lag than the flow rate. This observation is always true in the slip and hydrodynamic regimes [78, 72]. It has been found however, that in some narrow band of the transition regime close to $\delta \simeq 1$ and high oscillation frequency $\theta \leq 1$, $\bar{\tau}_{W,P}$ may be slightly larger than G_P.

In Figure 4.9, the oscillatory shear stress $\bar{\tilde{\tau}}_W (t, \delta, \theta) = \bar{\tau}_{W,A} \cos(t - \bar{\tau}_P)$ is plotted versus time $t \in [0, 2\pi]$ for typical values of δ and θ with $H/W = [1, 0.1]$. The time evolution of the dimensionless pressure gradient is equal to $\cos t$. As expected, $\bar{\tilde{\tau}}_W$ depends on both the gas rarefaction parameter and the oscillation frequency and behaves similarly to the flow rate $\hat{G}$ (Figure 4.7). As θ is decreased the amplitude is decreased and the lagging phase angle is increased and this behavior becomes more intense as δ is increased. Furthermore, as H/W is decreased, the amplitude is increased, while the phase angle is slightly increased.

Next in Figure 4.10, the oscillatory inertia $\hat{F}_I$, viscous $\hat{F}_V$ and pressure $\hat{F}_P$ forces, as defined in Eq. (4.30) are plotted over one oscillation period $t \in [0, 2\pi]$ for $\delta = [0.1, 1, 10]$, $\theta = [0.1, 1, 10]$ and $H/W = 1$. The forces are readily computed based on the amplitudes and phase angles of the flow rate and mean wall shear stress. In all cases the force balance equation (4.30) is satisfied. The inertia forces refer to the core flow and the viscous forces refer to the Stokes layer. It is interesting to observe the behavior of $\hat{F}_I$ and $\hat{F}_V$ in terms of δ and θ. The phase difference between these two forces is always $\pi/2$. In the cases of $(\delta = \theta = 0.1)$, $(\delta = \theta = 1)$ and $(\delta = \theta = 10)$ the viscous and inertia forces lag and lead the corresponding pressure force respectively by a phase angle of $\pi/4$. The amplitudes of the two forces are about the same. Then, in the cases of $(\delta = 10, \theta = 1, 0.1)$ and $(\delta = 1, \theta = 0.1)$, the inertia forces almost coincide with the corresponding pressure forces, while the viscous forces lag the other two forces by almost $\pi/2$ and their amplitudes are close to zero. The flow consists of two regions: the core region oscillating in a plug mode and, adjacent to the wall, the oscillating thin viscous or Stokes layer with the velocity overshooting. Finally, in the cases of $(\delta = 1, \theta = 10)$ and $(\delta = 0.1, \theta = 1, 10)$ this behavior is reversed, i.e., the viscous coincide with pressure forces, while the inertia forces lead by almost $\pi/2$ and their amplitudes are close to

zero. The flow consists of one oscillating region with no velocity overshooting. This description clarifies the behavior of the inertia and viscous forces in terms of θ and more important in terms of δ, e.g., at $\delta = 10$ and $\theta \leq 1$ the flow is dominated mainly by inertia forces, while at $\delta = 0.1$, the flow will be dominated by inertia forces only if $\theta < 0.1$.

It is noted finally, that based on the computed quantities, Eq. (4.30) is satisfied very accurately, which of course provides additional confidence about the validity of the numerical results.

4.4.4 Pumping power

In Figure 4.11, the oscillatory pumping power, defined as $\hat{E}/(Adz) = = G_A \cos{(G_P - t)} \cos{t}/2$ (see Eq. (4.31)), is plotted in terms of $t \in [0, 2\pi]$ for $\delta = [0.1, 1, 10]$ and $\theta = [0.1, 1, 10, 10^2]$ with $H/W = 0.1$. The pumping power has two peaks within each oscillatory cycle because it consists of the product of the oscillatory pressure times the oscillatory flow. Its integral over one cycle is not zero in order to drive the oscillatory flow, although the oscillatory net flow is zero. The dependency of the oscillatory pumping power on δ and θ is similar to the one observed for the flow rate, i.e. in general, as θ is decreased (the oscillation frequency is increased) its amplitude is decreased and its phase angle lag is increased. This behavior becomes more dominant as δ is increased.

As pointed above, even when the flow is reversed, which is occurring at the second half of the oscillation cycle at time $t \in [\pi/2, \pi]$ where the flow rate is negative, the pumping power remains positive. It is seen however, in Fig. 4.11 that at certain times $t \in [0, 2\pi]$, the oscillatory pumping power may become negative. This is more evident at large δ and small θ and it is occurring because in dense gases and at relatively high frequencies the flow rate is completely out of phase with the pressure gradient (it becomes proportional to a sinusoidal function). Thus, when the pressure gradient becomes negative and the flow is reversed, the sign of the flow rate remains positive for a certain time interval and during this interval the overall pumping power becomes negative. This time interval is increased as θ is decreased. Of course in rarefied gases and/or low frequencies $\hat{E}$ is always positive because the flow rate is in phase with the pressure gradient.

Finally, in Figure 4.12, the average oscillatory pumping power $\bar{E}/Adz = G_A \cos{(G_P)}/4$ (see Eq.(4.32)) over one period of oscillation in terms of δ are plotted, with $\theta = [0.1, 1, 10, 10^2]$ and for ducts with $H/W = 1$ and 0.1. The steady pumping power

$E_S = AdzG_S/2$, which depends only on δ, is also plotted for comparison purposes. It is seen that as the oscillatory flow approaches steady conditions, which is the case of $\theta = 10^2$ and $\delta \leq 10$, as expected, $\bar{E}$ is about half of E_S. This behaviour is even extended to smaller values of θ provided that δ is adequately small ($\delta << \theta$). Also, as $\delta \to 0$ and for all θ the steady free molecular flow is recovered, $\bar{E}$ is exactly one half of the steady free molecular pumping power. Furthermore, in cases where $\delta \geq \theta$ the average oscillatory pumping power is smaller than these limiting values and it is significantly decreased with θ. This is expected since at very high frequencies the flow rate amplitude tends to diminish. Also, the local maximum values of $\bar{E}$ at large θ are appearing due to the corresponding behaviour of G_A, shown in Figure 4.5. With regards to the aspect ratio, $\bar{E}$ is increased as H/W is increased.

4.5   Concluding remarks

The pulsatile isothermal fully-developed flow in an orthogonal duct is investigated by decomposing the flow into the steady and oscillatory parts. The steady part is well-known and therefore, the investigation is focused mainly on the oscillatory part, which is numerically solved, based on the time-dependent linear BGK equation, in a wide range of the gas rarefaction parameter $\delta \in [0, 10^2]$ and the oscillation parameter $\theta \in [10^{-2}, 10^2]$, as well as for various values of the duct aspect ratio $H/W \in [1, 0]$ and the tangential momentum accommodation coefficient $\alpha \in [0, 1]$. It is noted that δ and θ are inversely proportional to the Knudsen number and the oscillation frequency respectively. The results are in dimensionless form and include all macroscopic quantities of theoretical and technological interest and more specifically, the amplitude and phase angle, as well as the time evolution of the velocity distribution, the flow rate, the mean wall shear stress, the acting inertial and viscous forces, the pumping power and the time average pumping power. The results have been successfully validated at limiting values of δ and θ by comparison with corresponding analytical results in the slip regime (both $\delta >> 1$ and $\theta >> 1$), in the free molecular regime ($\delta \to 0$) and with numerical results for steady fully-developed flow ($\theta \to \infty$ and $\delta << \theta$).

Always as θ is decreased (i.e., the oscillation frequency is increased) the amplitude of all macroscopic quantities is decreased and their phase angle lag with respect to the pressure gradient is increased. Actually, at very small θ the amplitude tends to diminish and the phase angle lag approaches the limiting value of $\pi/2$. It is important

70

to note however, that as δ is decreased (i.e., the gas becomes more rarefied) higher frequencies are needed to trigger the behavior described above.

For comparison purposes the amplitude of the oscillatory pressure gradient is taken to be equal with the steady pressure gradient. Having this in mind it is useful to note that the pulsatile velocity distribution, which is obtained by adding the oscillatory and steady velocities, is always positive and therefore, there is no flow reversal. Furthermore, the amplitudes of the flow rate and the mean wall shear stress are increased with θ being always smaller than the corresponding steady ones. In terms of gas rarefaction the dependency of the flow rate amplitude is not monotonic indicating that at moderate and large θ there is a critical δ to obtain the maximum flow rate. The mean wall shear stress amplitude remains almost constant in the free molecular and transition regimes and then it is rapidly reduced. Comparing the corresponding phase angle lags of the flow rate and the mean wall shear stress it has been found that in most cases the former one is slightly larger, while this situation is reversed in a narrow band of the transition regime and high oscillation frequencies. Concerning the duct aspect ratio, it has been found that as the aspect ratio H/W is decreased the flow rate and mean wall shear stress amplitudes are increased, while their phase angle lags are slightly affected. Similarly, the gas-surface interaction at the wall, specified by the accommodation coefficient α, has a significant effect at the amplitudes and almost no effect at the phase angles of the macroscopic quantities.

The inertia and viscous forces, having always a phase difference of $\pi/2$, are computed in a wide range of δ and θ. Their amplitudes are about the same when $\delta = \theta$. As δ is increased and θ is decreased the inertia forces dominate causing a core oscillating plug-flow with a thin Stokes layer. In the opposite situation (i.e., as δ is decreased and θ is increased) the viscous forces become more important causing a typical viscous oscillatory flow without velocity overshooting.

Finally, the oscillatory pumping power has two peaks within each oscillatory cycle and its integral over one cycle is not zero. The nonzero time average pumping power is needed to maintain the oscillatory flow, although the oscillatory net flow is zero and it is increased as the oscillation frequency is reduced. Actually, as stationary conditions are reached, the time average pumping power is obtaining its maximum values, which have been found to be one half of the corresponding steady ones. Adding the time average oscillatory pumping power with the steady one, yields the total average power to maintain the pulsatile flow.

Table 4.1 Flow rate amplitude $G_A(\delta,\theta)$ in terms of gas rarefaction parameter δ and oscillation parameter θ for $H/W = 0.1$.

δ	$G_A(\delta,\theta)$					$G_A^{(S)}(\delta,\theta)$		$G_{SS}(\delta)$
	$\theta=0.1$	$\theta=1$	$\theta=10$	$\theta=50$	$\theta=100$	$\theta=50$	$\theta=100$	$\theta\to\infty$
0.0001	1.984	1.988	1.988	1.988	1.988			1.988
0.001	1.939	1.973	1.974	1.974	1.974			1.974
0.01	1.648	1.892	1.903	1.903	1.903			1.903
0.05	1.057	1.712	1.758	1.759	1.759			1.759
0.1	7.543(-1)	1.583	1.666	1.667	1.667			1.667
0.5	2.033(-1)	1.116	1.451	1.456	1.456			1.456
1	9.992(-2)	8.084(-1)	1.411	1.426	1.427	1.104	1.104	1.427
2	4.999(-2)	4.793(-1)	1.431	1.492	1.494	1.263	1.265	1.494
4	2.499(-2)	2.462(-1)	1.414	1.719	1.732	1.567	1.578	1.737
6	1.666(-2)	1.646(-1)	1.245	1.952	1.999	1.841	1.881	2.016
8	1.250(-2)	1.237(-1)	1.042	2.142	2.262	2.059	2.168	2.307
10	9.999(-3)	9.914(-2)	8.720(-1)	2.259	2.503	2.198	2.428	2.605
15	6.666(-3)	6.627(-2)	6.043(-1)	2.216	2.918	2.191	2.874	3.364
20	5.000(-3)	4.977(-2)	4.622(-1)	1.931	2.989	1.920	2.966	
30	3.333(-3)	3.323(-2)	3.157(-1)	1.409	2.548	1.405	2.541	
40	2.500(-3)	2.494(-2)	2.398(-1)	1.093	2.054	1.091	2.050	
50	2.000(-3)	1.996(-2)	1.934(-1)	8.959(-1)	1.698	8.941(-1)	1.696	
100	1.000(-3)	9.990(-3)	9.832(-2)	4.725(-1)	9.167(-1)	4.721(-1)	9.159(-1)	

72

Table 4.2 Flow rate phase angle $G_P(\delta, \theta)$ (rad) in terms of gas rarefaction parameter δ and oscillation parameter θ for $H/W = 0.1$.

δ	$G_P(\delta, \theta)$					$G_P^{(S)}(\delta, \theta)$	
	$\theta = 0.1$	$\theta = 1$	$\theta = 10$	$\theta = 50$	$\theta = 100$	$\theta = 50$	$\theta = 100$
0.0001	9.593(-3)	1.179(-3)	1.201(-4)	2.403(-5)	1.201(-5)		
0.001	6.085(-2)	8.113(-3)	8.321(-4)	1.665(-4)	8.324(-5)		
0.01	3.015(-1)	4.828(-2)	5.024(-3)	1.005(-3)	5.026(-4)		
0.05	6.989(-1)	1.487(-1)	1.582(-2)	3.166(-3)	1.583(-3)		
0.1	9.217(-1)	2.343(-1)	2.541(-2)	5.087(-3)	2.544(-3)		
0.5	1.442	6.409(-1)	8.037(-2)	1.612(-2)	8.062(-3)		
1	1.510	9.416(-1)	1.451(-1)	2.924(-2)	1.462(-2)	2.242(-2)	1.121(-2)
2	1.540	1.241	2.901(-1)	5.970(-2)	2.988(-2)	5.191(-2)	2.597(-2)
4	1.555	1.421	6.145(-1)	1.410(-1)	7.085(-2)	1.320(-1)	6.629(-2)
6	1.560	1.473	8.931(-1)	2.481(-1)	1.261(-1)	2.385(-1)	1.210(-1)
8	1.563	1.497	1.082	3.753(-1)	1.949(-1)	3.658(-1)	1.896(-1)
10	1.565	1.512	1.202	5.130(-1)	2.758(-1)	5.044(-1)	2.704(-1)
15	1.567	1.532	1.345	8.340(-1)	5.113(-1)	8.293(-1)	5.067(-1)
20	1.568	1.542	1.405	1.057	7.463(-1)	1.056	7.433(-1)
30	1.569	1.551	1.462	1.274	1.076	1.275	1.075
40	1.569	1.556	1.490	1.360	1.239	1.361	1.240
50	1.570	1.559	1.507	1.405	1.322	1.406	1.322
100	1.570	1.565	1.539	1.492	1.455	1.492	1.455

73
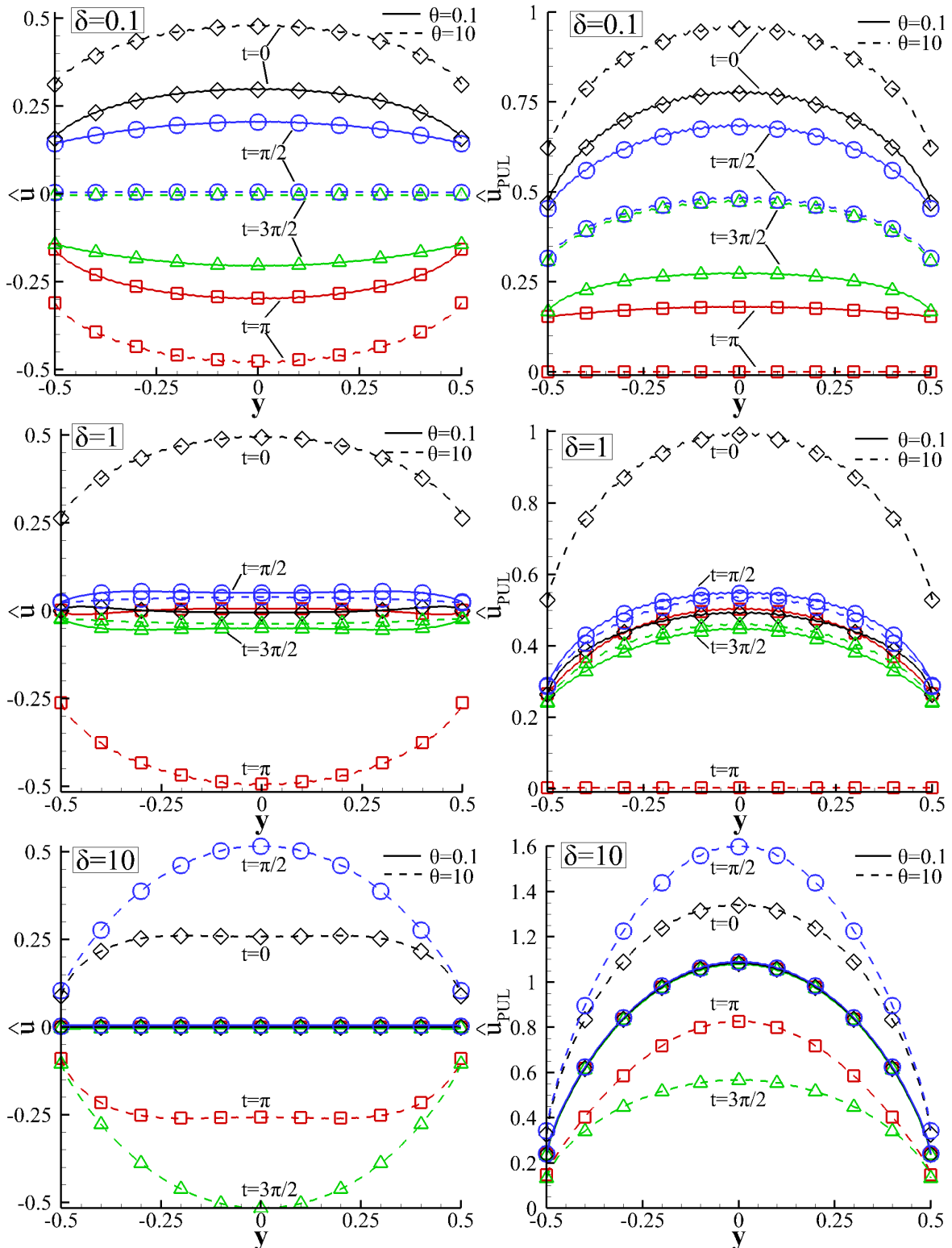
Figure 4.1 Time evolution of oscillatory $\hat{u}(0, y, t)$ (left) and pulsatile $\hat{u}_{PUL}(0, y, t)$ (right) velocity distributions in terms of distance $y \in [-1/2, 1/2]$ at certain times $t \in [0, 2\pi]$ for $H/W = 1$, $\delta = [0.1, 1, 10]$ and $\theta = [0.1, 10]$.

74
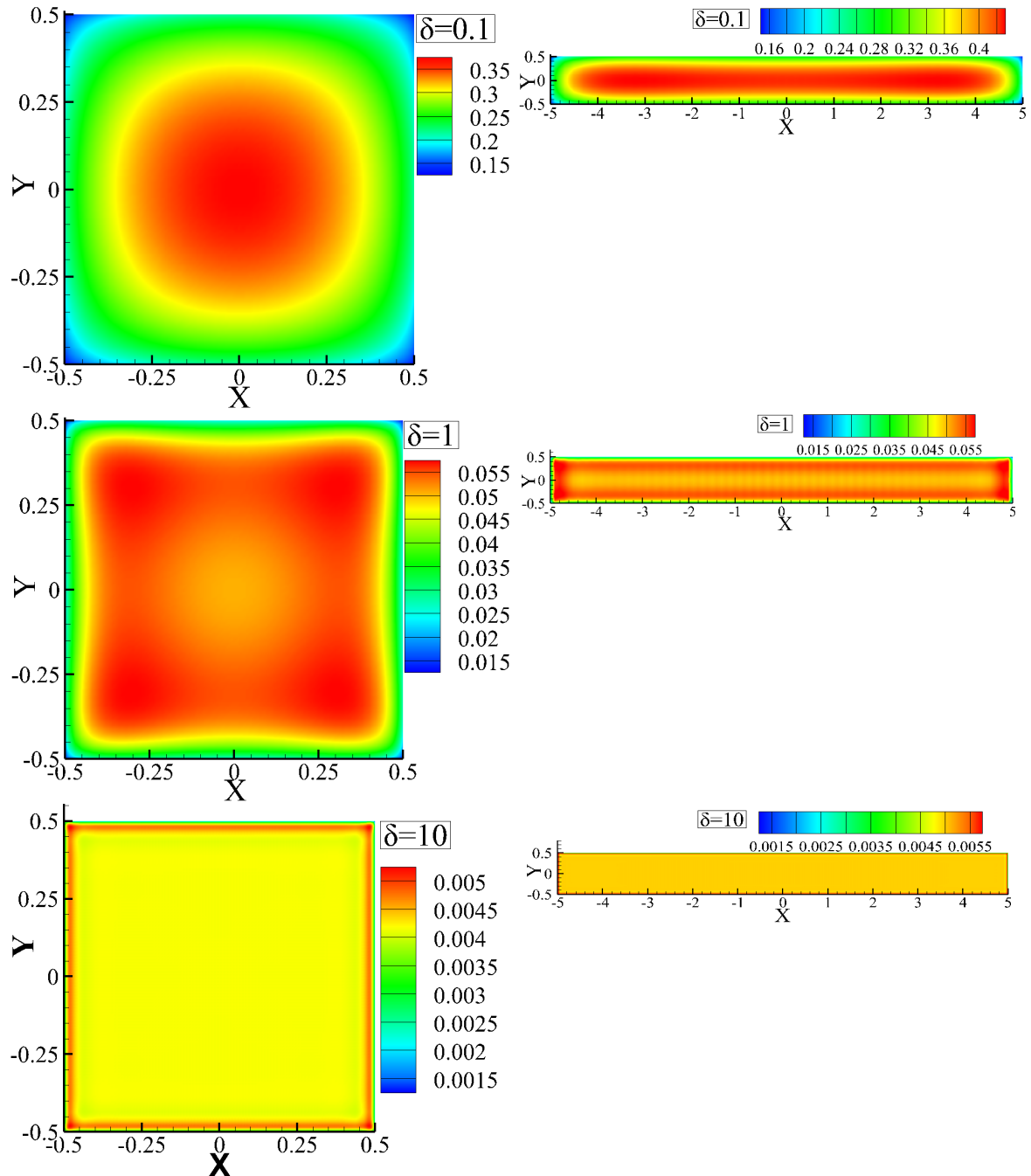
Figure 4.2 Contours of oscillatory velocity amplitude $u_A(x, y)$ for $H/W = 1$ (left) and $H/W = 0.1$ (right), $\delta = [0.1, 1, 10]$ and $\theta = 0.1$.

75
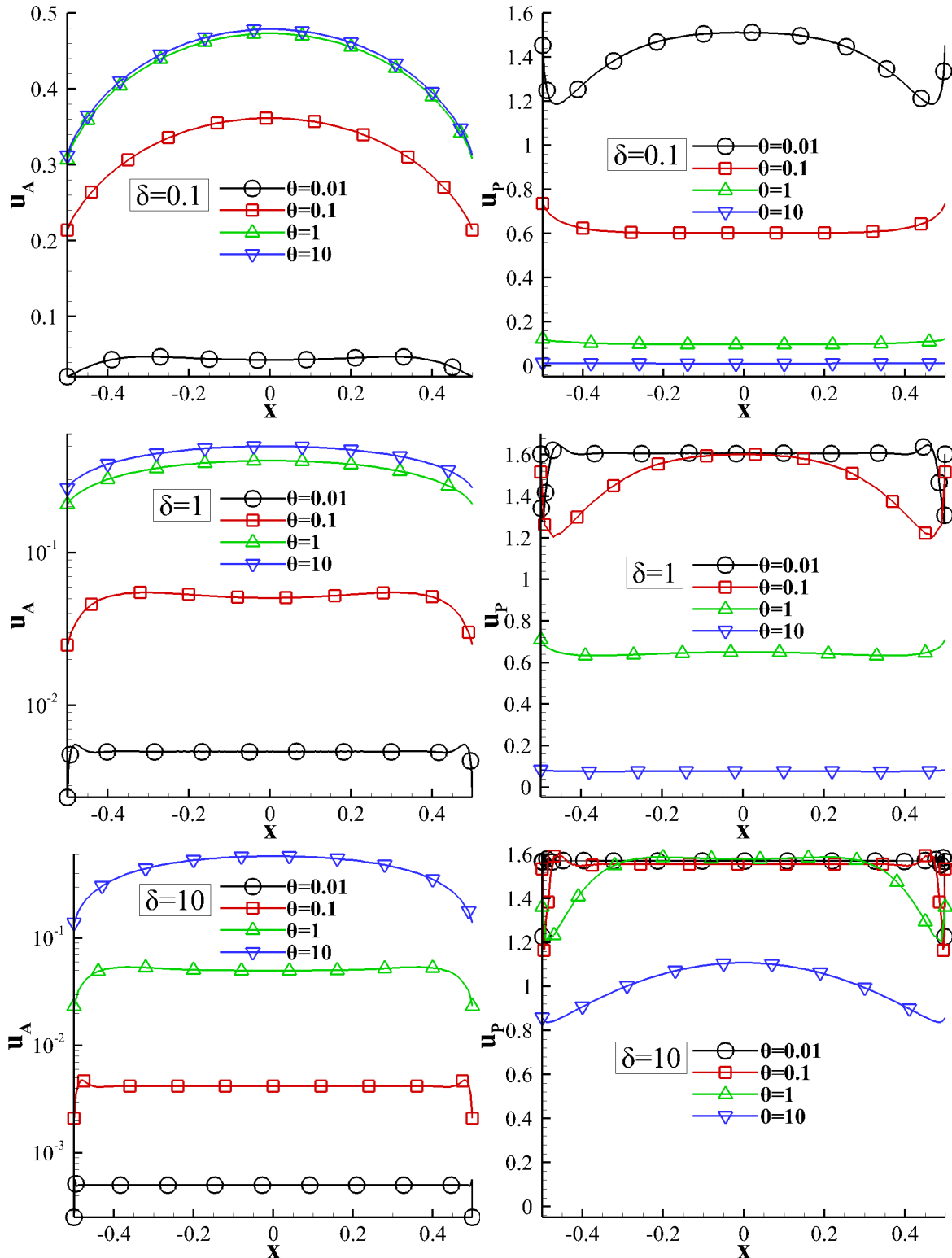
Figure 4.3 Oscillatory velocity amplitude $u_A(x, 0)$ and phase angle $u_P(x, 0)$ in terms of distance $x \in [-1/2, 1/2]$ for $H/W = 1$, $\delta = [0.1, 1, 10]$ and $\theta = [10^{-2}, 0.1, 1, 10]$.

76
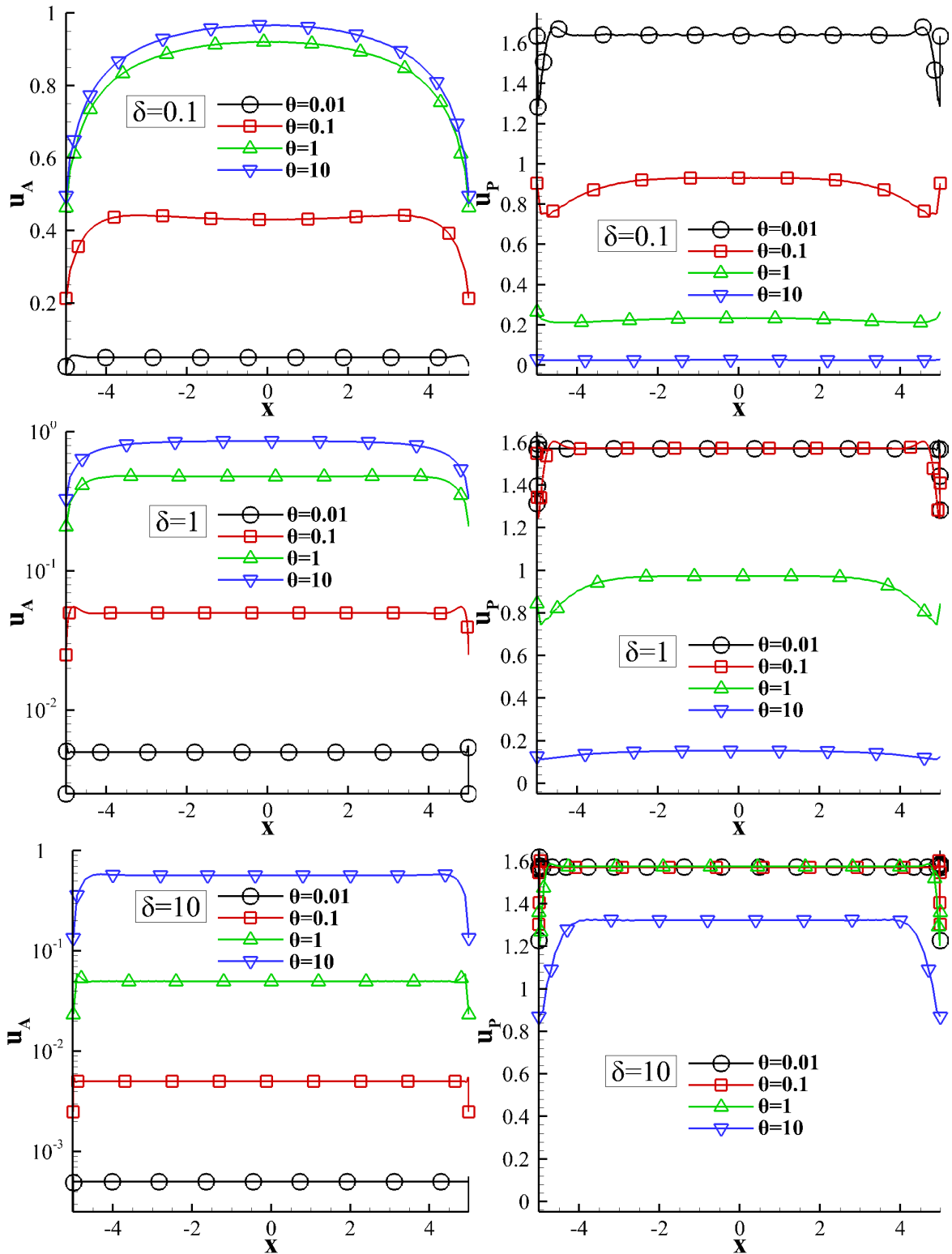
Figure 4.4 Oscillatory velocity amplitude $u_A(x, 0)$ and phase angle $u_P(x, 0)$ in terms of distance $x \in [-H/(2W), H/(2W)]$ for $H/W = 0.1$, $\delta = [0.1, 1, 10]$ and $\theta = [10^{-2}, 0.1, 1, 10]$.

77
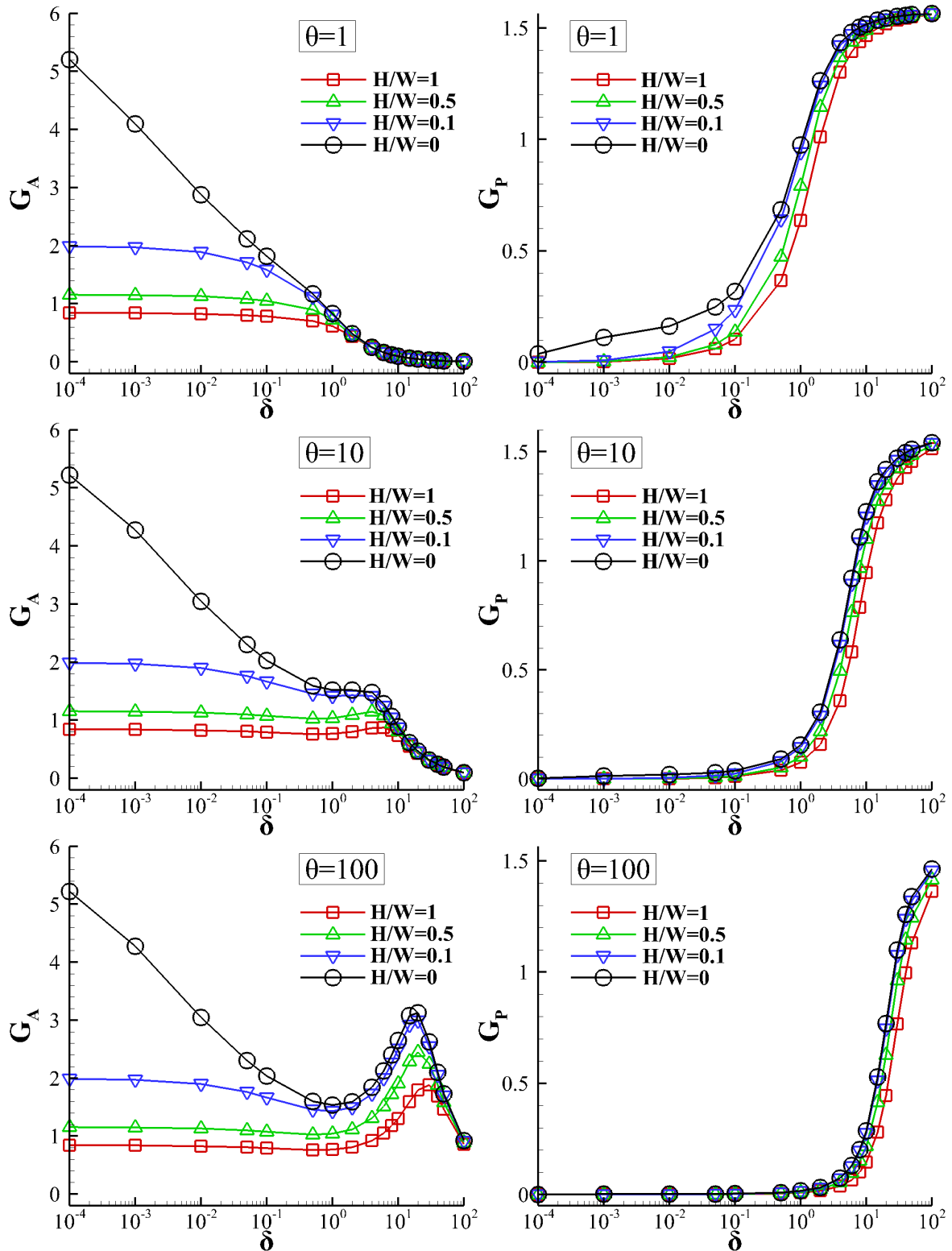
Figure 4.5 Oscillatory flow rate amplitude G_A and phase angle G_P in terms of gas rarefaction parameter δ for $\theta = [1, 10, 10^2]$ and $H/W = [1, 0.5, 0.1, 0]$.
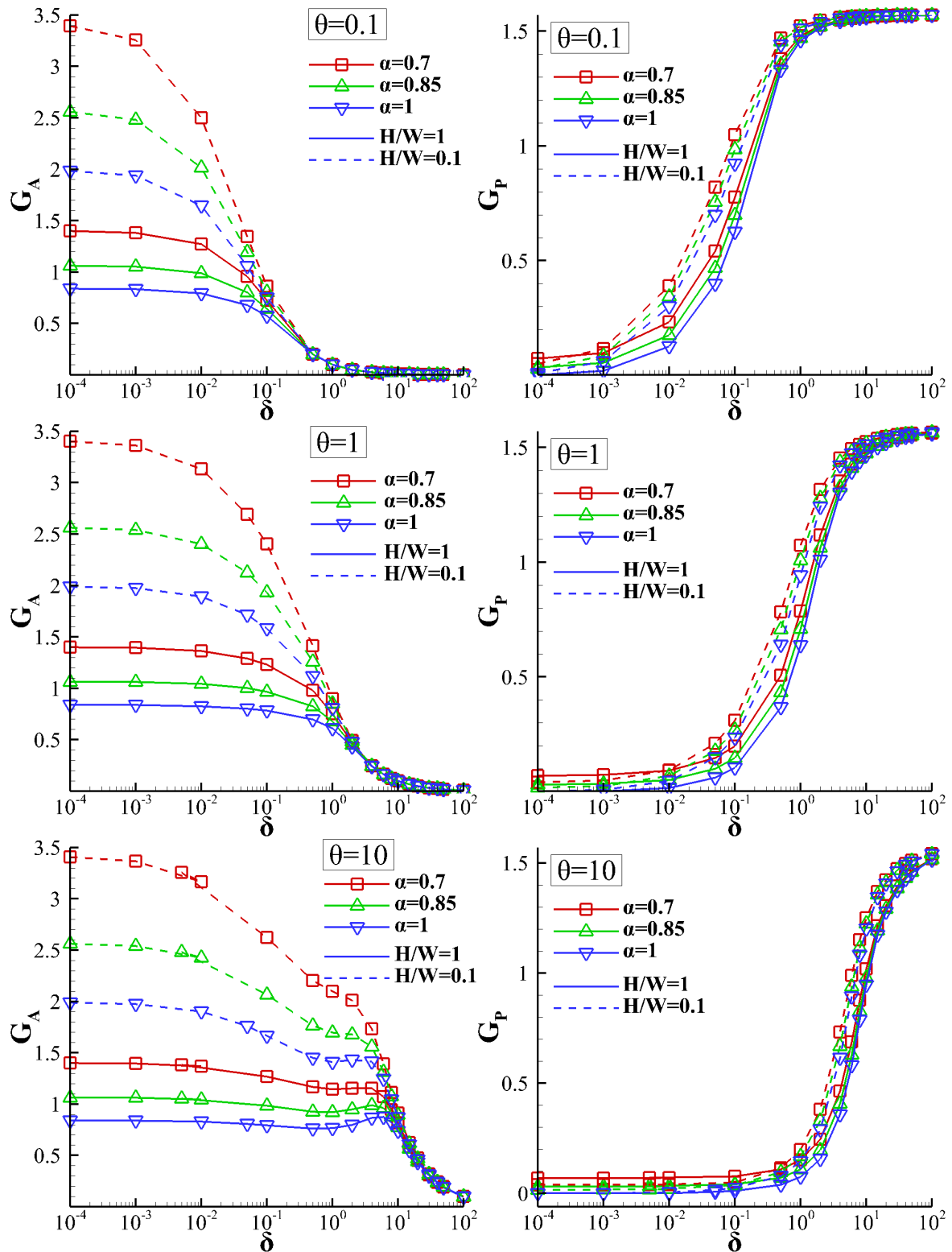
Figure 4.6 Oscillatory flow rate amplitude G_A and phase angle G_P in terms of the gas rarefaction parameter δ for $H/W = 1$ (solid lines) and $H/W = 0.1$ (dashed lines), $\theta = [10^{-1}, 1, 10]$ and accommodation coefficient $\alpha = [1, 0.85, 0.7]$.

79
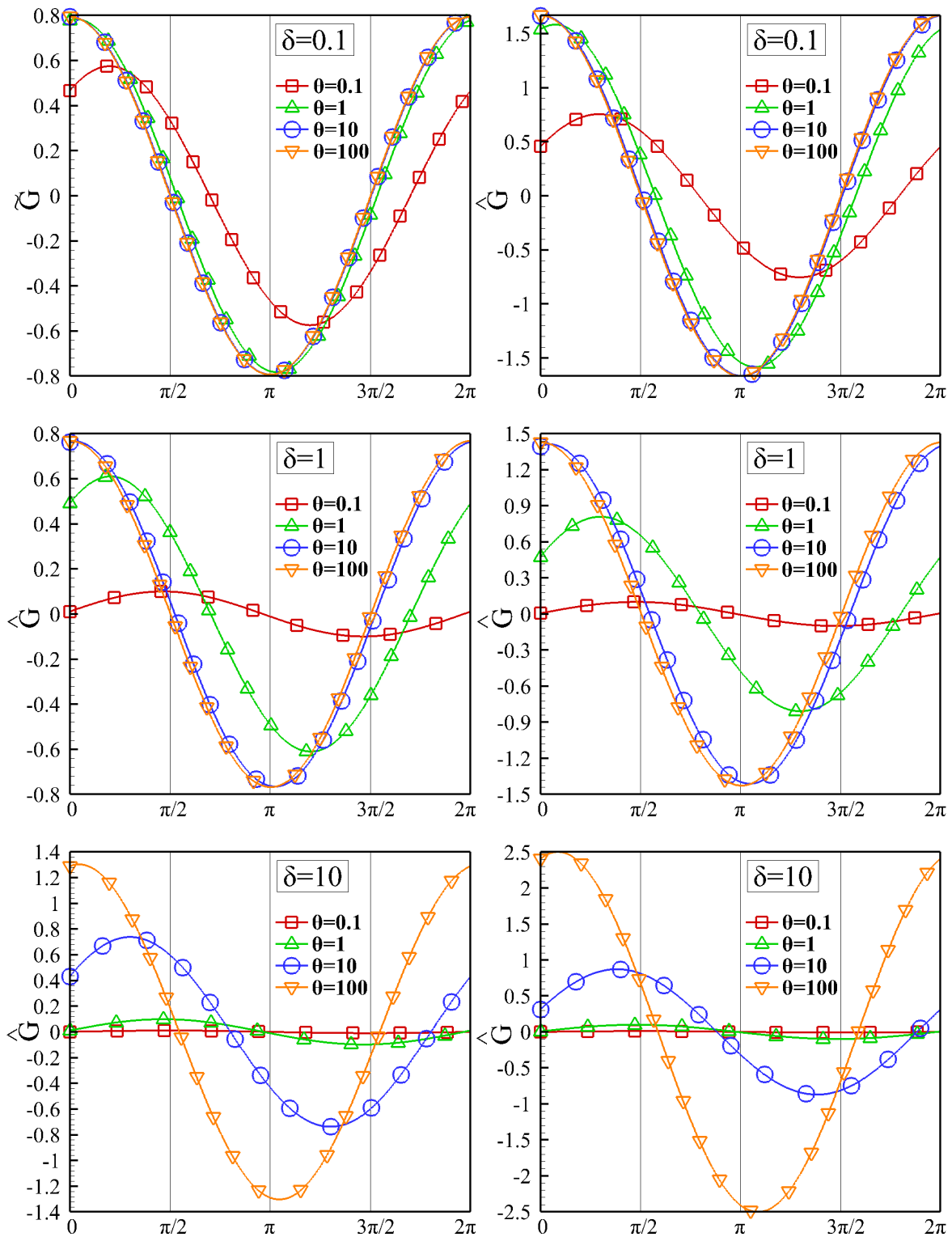
Figure 4.7 Oscillatory flow rate $\hat{G}$ over one oscillation period for an orthogonal duct with $H/W = 1$ (left) and $H/W = 0.1$ (right) for $\delta = [0.1, 1, 10]$ and $\theta = [0.1, 1, 10, 10^2]$.

80
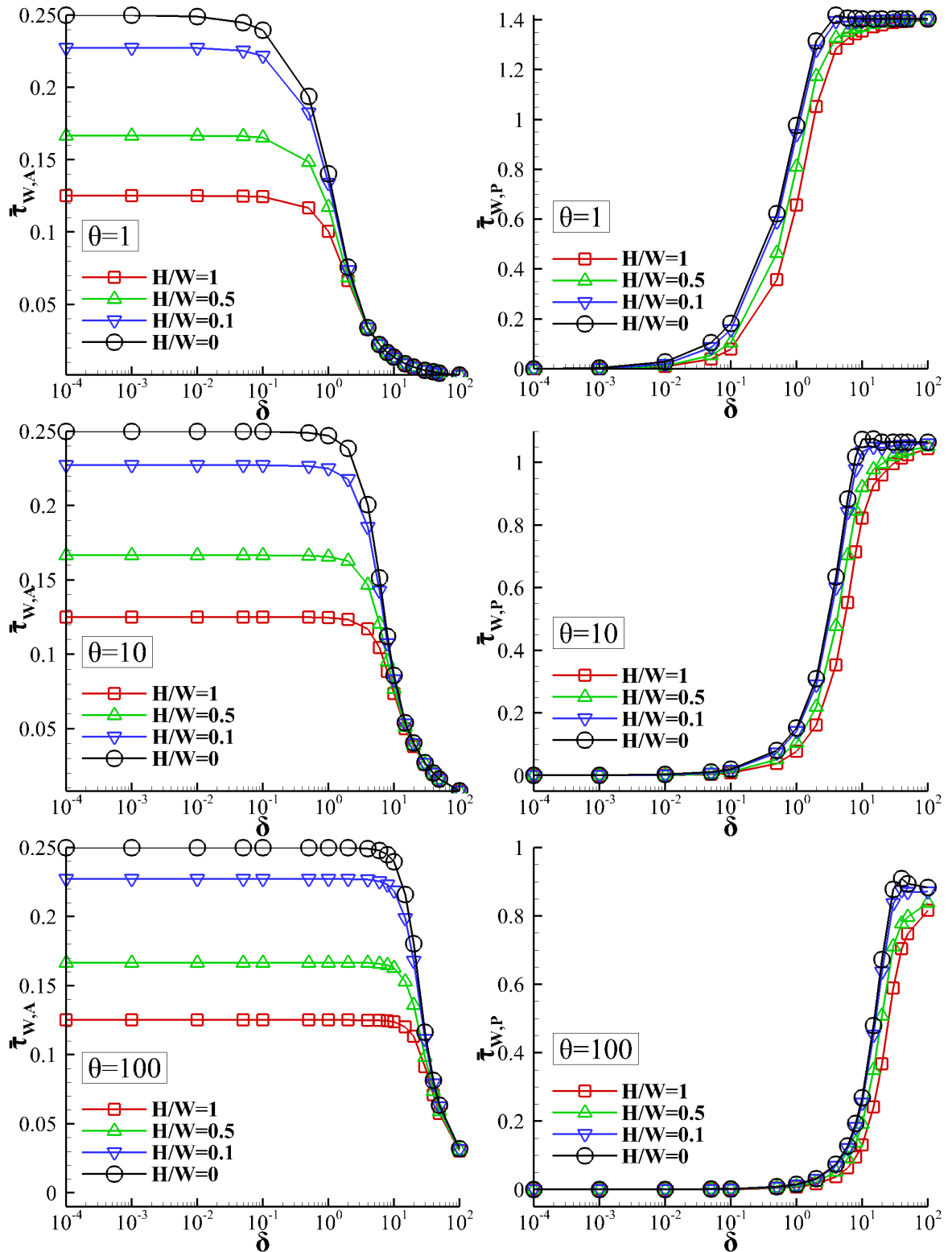
Figure 4.8 Oscillatory mean wall shear stress amplitude $\bar{\tau}_{W,A}(\delta, \theta)$ and phase angle $\bar{\tau}_{W,P}(\delta, \theta)$ in terms of the gas rarefaction parameter δ for $\theta = [1, 10, 10^2]$ and $H/W = [1, 0.5, 0.1, 0]$.

81
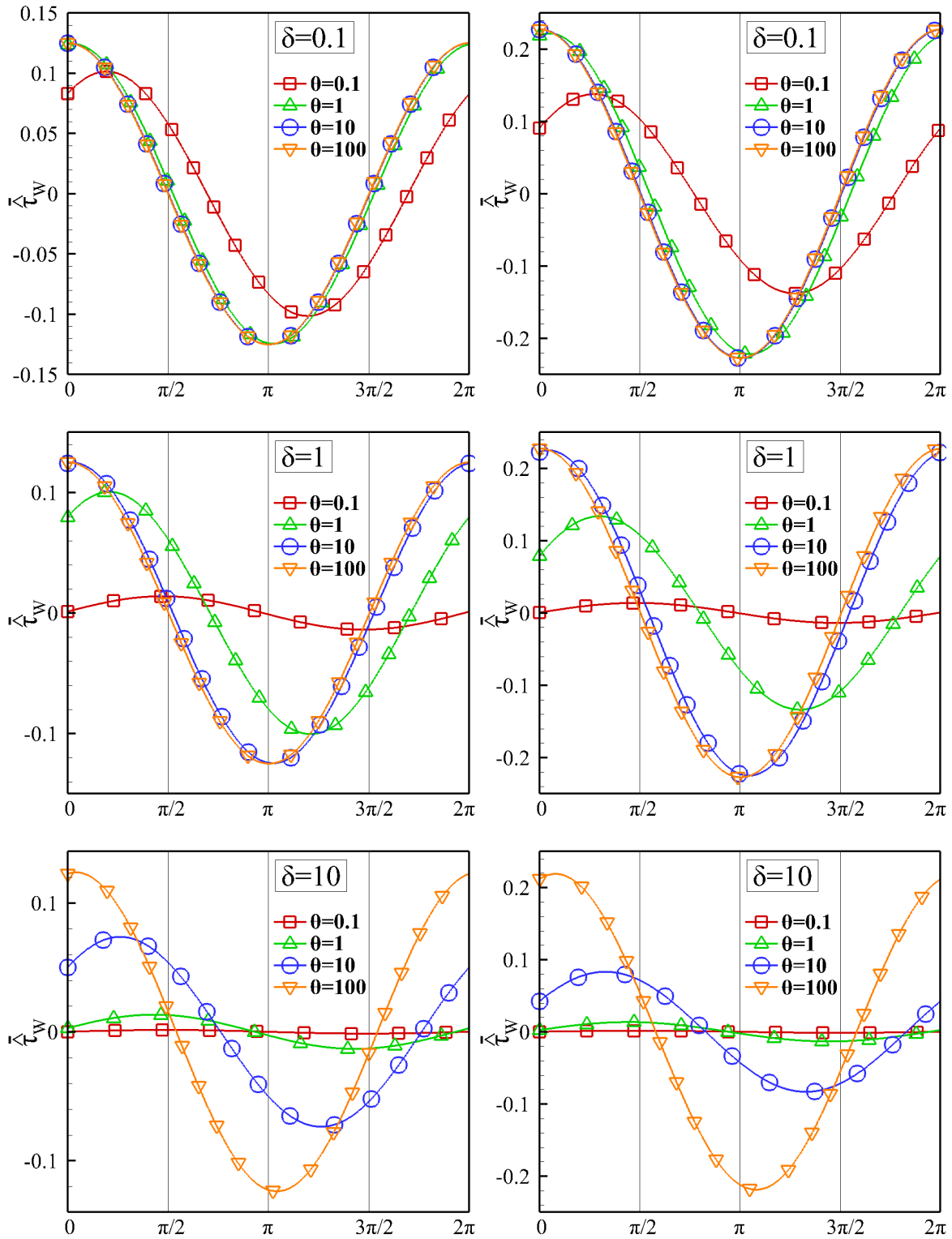
Figure 4.9 Oscillatory mean wall shear stress $\bar{\hat{\tau}}_W$ over one oscillation period for $H/W = 1$ (left) and $H/W = 0.1$ (right), $\delta = [0.1, 1, 10]$ and $\theta = [0.1, 1, 10, 10^2]$.
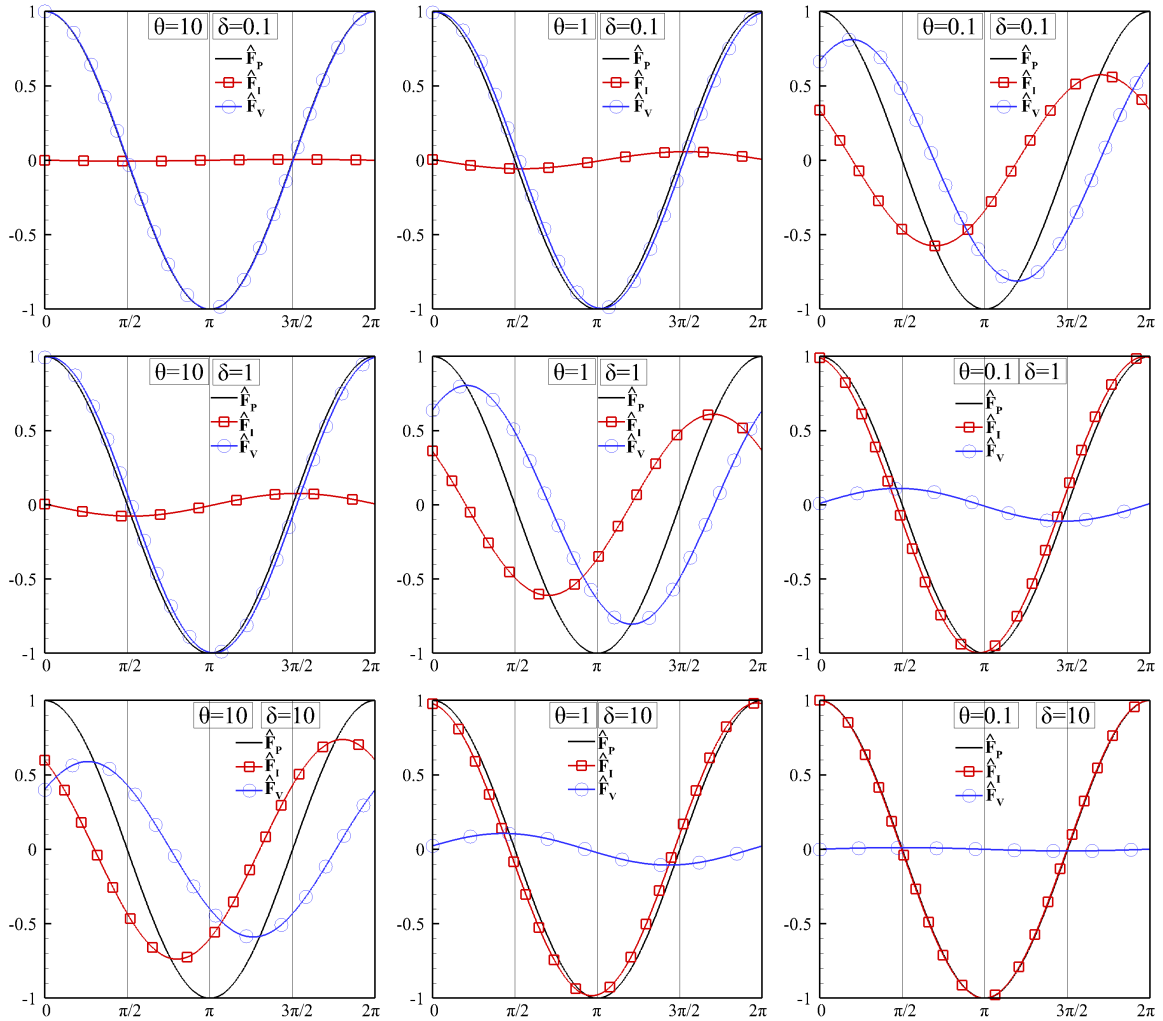
Figure 4.10 Oscillatory inertia $\hat{F}_I$, viscous $\hat{F}_V$ and pressure $\hat{F}_P$ forces over one oscillation period for $\delta = [0.1, 1, 10]$, $\theta = [0.1, 1, 10]$ and $H/W = 1$ (all forces are divided by Adz).

83
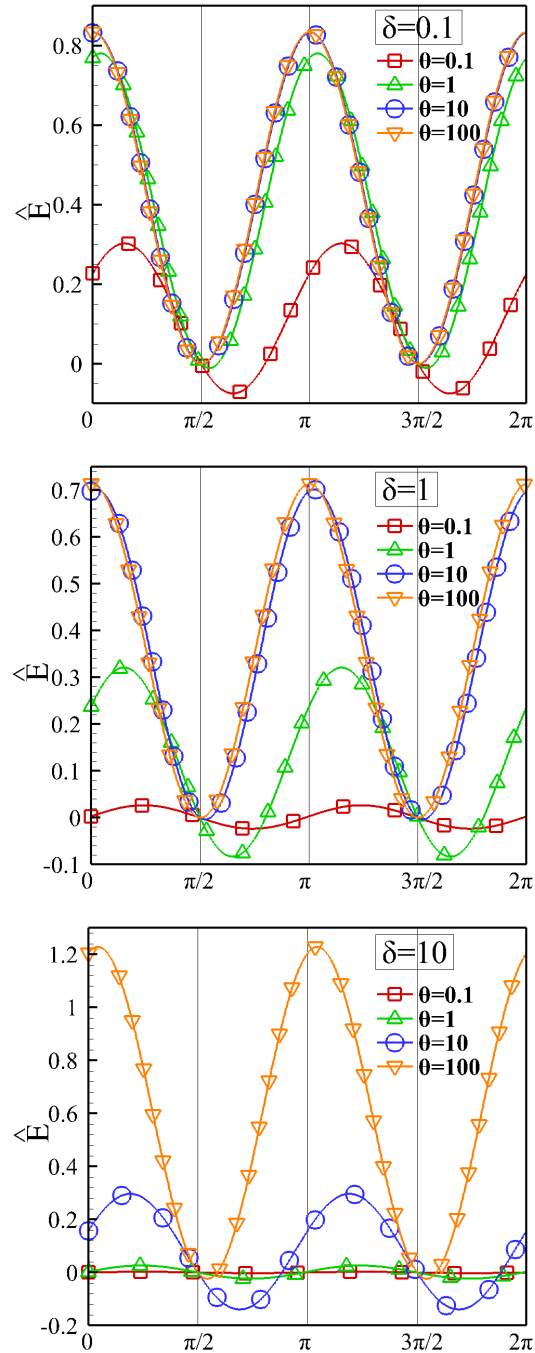
Figure 4.11 Oscillatory pumping power $\hat{E}$ over one oscillation period for $\delta = [0.1, 1, 10]$, $\theta = [0.1, 1, 10, 10^2]$ and $H/W = 0.1$ (pumping power is divided by Adz).

84
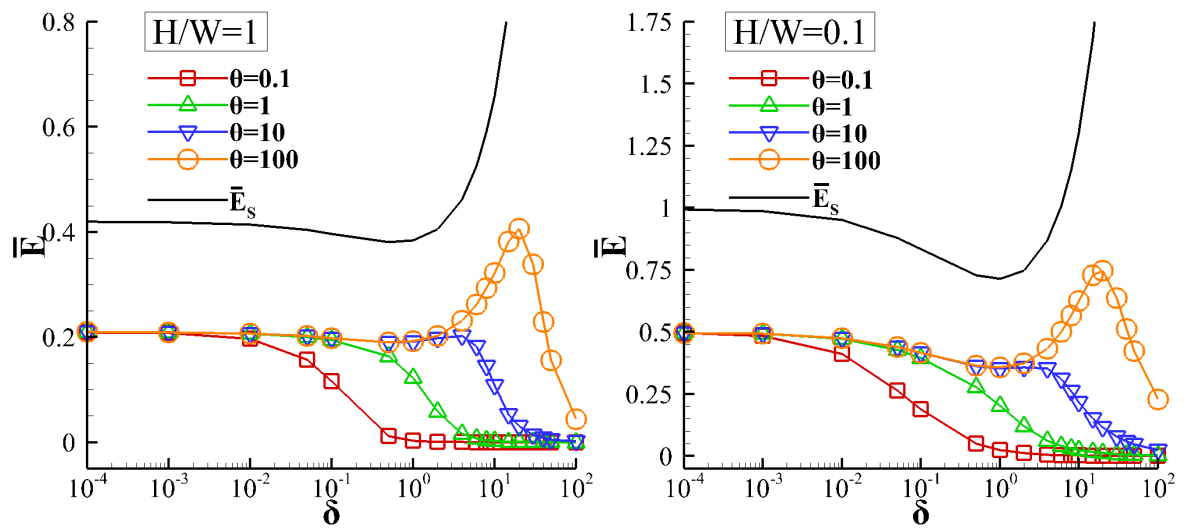
Figure 4.12 Average pumping power $\bar{E}$ over one period of oscillation along with the steady-state pumping power $\bar{E}_S$ in terms of the rarefaction parameter δ for $H/W = 1$ (left) and $H/W = 0.1$ (right) with $\theta = [0.1, 1, 10, 10^2]$ (pumping powers are divided by Adz).

Chapter 5

Nonlinear oscillatory fully-developed rarefied gas flow between parallel plates

5.1 Introduction

The coupled flow and heat transfer phenomena in simple flow configurations is of major importance in many applications. However, the linearized kinetic equations cannot capture the heat transfer effects since the flow and heat transfer phenomena are decoupled due to linear theory. Therefore, in this Chapter the assumption of the small oscillatory pressure gradient is removed and the nonlinear time-dependent rarefied gas flow due to an external oscillatory force with arbitrary magnitude is studied.

It is noted that steady-state force driven Poiseuille type flows have been investigated [183–188] based on kinetic theory and modelling, clarifying certain phenomena and paradox appearing near the continuum regime that cannot be described by the typical hydrodynamic approach. Such phenomena include the non-constant pressure profile across the channel, the bimodal shape of the temperature profile with a slight shallow at the channel center and the presence of axial heat flow. The analysis has been based on asymptotic methods [183, 185, 188], kinetic model equations [183, 186] and the DSMC method [184, 185, 187] and is extended in a wide range of the Knudsen number [183, 184, 186–188].

Considering all above and taking into consideration that in Chapters 3-4 (or in [127, 128]), the results are formally limited to small amplitudes of the oscillating pressure

87

gradient, in the present Chapter, the nonlinear time-dependent fully-developed rarefied gas flow between parallel plates, driven by an oscillating external force, is considered. Modelling is based on the DSMC method [64], the BGK [33] and the Shakhov [36] models focusing on the effect of the external force on the coupled flow and heat transfer phenomena in a wide range of the gas rarefaction and oscillation frequency. The time behavior of the macroscopic quantities, including the flow rate, the friction factor, the heat flow vector and the pumping power in terms of the flow conditions is analyzed. The accuracy of the results is benchmarked in various ways including the comparison with the corresponding oscillatory linearized results as the amplitude of the external oscillating force is reduced and steady-state results as the oscillation frequency tends to zero.

In addition, the heat transfer part is very interesting in rarefied flow conditions due to a promising application that is related to cooling of micro-electronic equipment. There the flow is in the late transition and early slip regimes and the pulsatile mechanism is applied to enhance advection. Therefore, a related flow configuration may be the nonlinear oscillatory flow coupled to an applied heat transfer between parallel plates. The plates are nonisothermal and a heat flow is beginning from the hotter plate to the colder one. In parallel, the nonlinear oscillatory flow is maintained and the oscillation frequency, the force magnitude and the temperature difference between the plates may be arbitrary large. Thus, it is interesting to investigate whether a flow oscillation enhances heat transfer. In this part of the Chapter, the normal and axial heat flows are mostly discussed since they are the direct aim of this study. Some other macroscopic quantities such as the mass flow rate, the velocity and the temperature are also considered. It is reminded that this flow configuration has been extensively studied in the hydrodynamic regime and several references have been mentioned in Section 2.5.

The remaining of the Chapter is structured as follows: In Section 5.2, the flow configuration is presented, all involved quantities are described in detail and the dimensionless parameters defining the flow are prescribed. In Section 5.3, the details of the DSMC modeling, including the implemented numerical parameters, are presented. The deterministic formulation is included in Section 5.4. The numerical results and the discussion are presented in Section 5.5, which is divided for clarity purposes into five subsections. The first four subsections are devoted to the nonlinear oscillatory force driven flow with isothermal plates while the last one is devoted to the nonlinear

oscillatory force driven flow with nonisothermal plates. The concluding remarks are outlined in Section 5.5.

5.2 Flow configuration

Consider the oscillatory nonlinear fully-developed flow of a monoatomic rarefied gas, confined between two parallel infinite plates located at $y' = \pm H/2$, due to an external harmonic force acting on the gas per unit mass in the $x-$direction parallel to the plates. The plates are kept at constant temperatures T_1 and T_2. The external force is defined as

$$\tilde{F}'\left(\omega,\ t'\right) = F' \cos\left(\omega\ t'\right), \tag{5.1}$$

where ω is the oscillation frequency, t' is the time and F' is the force amplitude. The convenient complex factor $\exp\left(-i\omega t'\right)$ [127, 128] cannot be employed since the force amplitude F' may be arbitrarily large and in nonlinear oscillatory flows the real and imaginary parts are not separable. The induced flow is in the $x-$direction and the gas moves back and forth producing zero net flow over one cycle.

The flow is assumed to be fully-developed and the oscillatory macroscopic distributions of practical interest, characterizing the flow, include the $x-$component $U_{x'}\left(y',t'\right)$ of the velocity vector, the number density $N\left(y',t'\right)$, the temperature $T\left(y',t'\right)$, the shear stress $\Pi_{x'y'}\left(y',t'\right)$ and the axial and normal heat flow components $Q_{x'}\left(y',t'\right)$ and $Q_{y'}\left(y',t'\right)$ respectively, with $-H/2 \le y' \le H/2$ and $0 \le t' \le 2\pi/\omega$. The local pressure between the plates is given by the equation of state $P = N k_B T$, where k_B is the Boltzmann constant.

Furthermore, the overall quantities of main importance for technological purposes are, the mass flow rate

$$M'\left(t'\right) = m \int_{-H/2}^{H/2} N\left(y',t'\right) U_{x'}\left(y',t'\right) dy', \tag{5.2}$$

where m is the molecular mass, the space-average number density, velocity and axial heat flow

$$\bar{N}\left(t'\right) = \frac{1}{H} \int_{-H/2}^{H/2} N dy', \bar{U}_{x'}\left(t'\right) = \frac{1}{H} \int_{-H/2}^{H/2} U_{x'} dy' and \bar{Q}_{x'}\left(t'\right) = \frac{1}{H} \int_{-H/2}^{H/2} Q_{x'} dy' \tag{5.3}$$

respectively (the space-average of the normal heat flow is zero) and the pumping power defined as the product of the acting force times the mean velocity, written for the fluid

89

element $(H \times dx')$ as

$$E'(t) = (Hdx') \left(m\bar{N}F' \cos(\omega t') \right) \bar{U}_x(t').$$ (5.4)

It is also noted that the corresponding steady-state nonlinear Poiseuille-type flow has been considered in [183–185, 189, 188].

The parameters defining the above dimensional flow setup include the external force amplitude, the oscillation frequency and the distance between the plates, as well as the operating pressure and temperature and the gas properties. They can be all grouped into four dimensionless parameters, fully characterizing the flow:

1. The first one is the gas rarefaction parameter δ given by

$$\delta = \frac{P_0 H}{\mu_0 \upsilon_0},$$ (5.5)

   where P_0 is a reference pressure, μ_0 is the gas viscosity at reference wall temperature T_2 and $\upsilon_0 = \sqrt{2 R_g T_2}$ is the most probable molecular speed ($R_g = k_B/m$ is the gas constant).

2. The second one is the frequency parameter θ given by

$$\theta = \frac{P_0}{\mu_0 \omega},$$ (5.6)

   where (P_0/μ_0) is the reference intermolecular collision frequency and ω, as specified above, is the oscillation frequency. As $\theta \to \infty$ ($\omega \to 0$), the steady-state flow configuration is reached [183–185, 189, 188].

3. The third one is the force amplitude parameter

$$F = \frac{F'H}{\upsilon_0^2}$$ (5.7)

   and it is the inverse of the square of the Froude number (Fr). The effect of the external force on the flow is increased with F and nonlinear effects are becoming dominant. On the contrary, as F is decreased the corresponding linear oscillatory flow, which is linearly proportional to the force magnitude, is gradually recovered.

90

4. The final one is the temperature ratio defined as

$$\beta = \frac{T_1}{T_2} \tag{5.8}$$

When the ratio is $\beta = 1$, the temperature at the plates is kept constant and equal leading to the nonlinear oscillatory rarefied gas flow. If the ratio is $\beta > 1$, then the coupled nonlinear oscillatory flow with heat transfer between parallel plates is obtained.

At this point it is convenient to introduce the following dimensionless variables:

$$x = \frac{x'}{H}, dx = \frac{dx'}{H}, y = \frac{y'}{H}, dy = \frac{dy'}{H}, t = \frac{t'}{(H/v_0)} \tag{5.9}$$

$$n = \frac{N}{N_0}, u_x = \frac{U_{x'}}{v_0}, \tau = \frac{T}{T_2}, p_{xy} = \frac{\Pi_{x'y'}}{2P_0}, p = \frac{P}{2P_0}, q_x = \frac{Q_{x'}}{v_0 P_0}, q_y = \frac{Q_{y'}}{v_0 P_0} \tag{5.10}$$

The equation of state becomes $p = n\tau/2$. Then, introducing the dimensionless parameters (5.5)-(5.7) and variables (5.9) and (5.10) into Eqs. (5.1)-(5.4) the corresponding quantities are readily deduced. The dimensionless external force acting on the gas per unit mass becomes

$$\tilde{F}(\delta, \theta, \ t) = F \cos\left(\frac{\delta}{\theta} t\right). \tag{5.11}$$

The dimensionless flow rate, space-average number density, velocity, axial and normal heat flow and the pumping power are given by

$$M(t) = \frac{M'}{2P_0(H/v_0)} = \int_{-1/2}^{1/2} n(t,y)u(t,y)\,dy, \quad \bar{n}(t) = \int_{-1/2}^{1/2} n(y,t)\,dy, \tag{5.12}$$

$$\bar{u}_x(t) = \int_{-1/2}^{1/2} u_x(y,t)\,dy, \quad \bar{q}_x(t) = \int_{-1/2}^{1/2} q_x(y,t)\,dy, \quad \bar{q}_y(t) = \int_{-1/2}^{1/2} q_y(y,t)\,dy \tag{5.13}$$

and

$$E(t) = \frac{E'(t')}{HP_0 v_0} = 2dx\bar{n}(t)\bar{u}(t)F\cos\left(\frac{\delta}{\theta}t\right) \tag{5.14}$$

respectively. Although the cycle-average net flow is zero, the corresponding average pumping power is not, in order to maintain the oscillatory flow. The cycle-average pumping power over one oscillation is computed as

$$\bar{E} = \frac{1}{2\pi}\int_0^{2\pi} E(t)\,dt = \frac{Fdx}{\pi}\int_0^{2\pi} \bar{u}(t)\cos\left(\frac{\delta}{\theta}t\right)dt. \tag{5.15}$$

Similarly, the cycle-average wall shear stress at the channel wall may be defined as

$$\bar{p}_W = \frac{1}{2\pi} \int_0^{2\pi} \sqrt{p_W^2} dt, \tag{5.16}$$

where $p_W = p_{xy}(1/2, t)$ denotes the dimensionless wall shear stress.

The balance of all forces per unit length acting on a fluid volume Hdx' may be written as $\tilde{F}'_D(t') = \tilde{F}'_I(t') + \tilde{F}'_V(t')$, where $\tilde{F}'_D(t')$, $\tilde{F}'_I(t')$ and $\tilde{F}'_V(t')$ are the external, inertia (or acceleration) and viscous forces respectively, given by

$$\tilde{F}'_D(t') = m\bar{N}F'(\omega, t') Hdx', \tag{5.17}$$

$$\tilde{F}'_I(t') = m\bar{N}\frac{\partial \bar{U}(t')}{\partial t'} Hdx' \tag{5.18}$$

and

$$\tilde{F}'_V(t') = 2\Pi'_W(t') dx', \tag{5.19}$$

with $\Pi'_W(t') = \Pi'_{x'y'}(H/2, t')$ denoting the dimensional wall shear stress. Then, introducing the dimensionless variables the force balance equation reads as

$$\frac{\partial \bar{u}(t)}{\partial t} + \frac{2p_W(t)}{\bar{n}(t)} = F\cos(\delta t/\theta). \tag{5.20}$$

Equation (5.20) is applied to ensure the accuracy of the computational results for all values of δ, θ and F.

The solution of the problem described above is obtained in a stochastic manner by numerically solving the DSMC method and in a deterministic manner by the nonlinear BGK and Shakhov model equations presented in Sections 5.3 and 5.4, respectively.

5.3 Stochastic DSMC formulation

The typical DSMC approach, with the No Time Counter (NTC) scheme proposed by Bird [64], is implemented. The time evolution of the particle system within a small time interval $\Delta t'$ is split into two consecutive steps: free motion of all particles and binary collisions of particles. The molecular velocity vector $\boldsymbol{\xi} = (\xi_x, \xi_y, \xi_z)$ and the time step $\Delta t'$ are non-dimensionalized as $\boldsymbol{\zeta} = (\zeta_x, \zeta_y, \zeta_z) = \boldsymbol{\xi}/\upsilon_0$ and $\Delta t = \Delta t'/(H/\upsilon_0)$ respectively. Purely diffuse boundary conditions are considered at the walls ($y = \pm 1/2$),

while periodic boundary conditions are applied in the $x-$ and $z-$directions. Hard sphere (HS) molecules are assumed.

The external force is introduced by accordingly altering the particle velocities at each time step, during the free motion of the DSMC algorithm. The particle velocities in the $x-$direction are altered according to

$$\hat{\zeta}_x = \zeta_x + F \cos\left(\frac{\delta}{\theta}t\right)\Delta t \tag{5.21}$$

where ζ_x and $\hat{\zeta}_x$ denote the $x-$component of the molecular velocity of some particle before and after the external acceleration is applied and Δt is the dimensionless time step size.

The maximum number of collisions in each cell is given by

$$N_{col} = \frac{N\left(N-1\right)F_N\sigma_T g'_{r,\max}\Delta t'}{2V'_C} \tag{5.22}$$

where N is the number of model particles in the cell, $V_C^{'}$ is the volume of the cell, F_N is the number of real particles per model particle, σ_T is the total collision cross section and $g'_{r,\max}$ is the maximum relative velocity. The number of collisions is also written in terms of dimensionless quantities as

$$N_{col} = \frac{N\left(N-1\right)g_{r,\max}\delta\Delta t}{\sqrt{2\pi}V_C N_P} \tag{5.23}$$

where N_P is the total number of model particles, $V_C = V'_C/H^3$ is the dimensionless cell volume and $g_{r,\max} = g'_{r,\max}/\upsilon_0$ is the dimensionless relative velocity.

The distance between the parallel plates is divided into $N_C = 200$ uniform cells with 2 collision subcells in each cell and the average number of particles per cell is 100 resulting in a total of $N_P = 2\times 10^4$ particles. The time step is chosen such that it is about $1/3$ of the cell transversal time $H/\left(N_C\upsilon_0\right)$ and also less than 10^{-3} times the period of oscillation. The macroscopic quantities are sampled for specific time steps and ensemble averaged over a large number of process trajectories. The number of trajectories ranges from 10^3 to 5×10^5, depending on the case. This gives a sample size ranging from 10^5 to over 10^7 for each cell, which is sufficiently large to reduce the statistical scatter of the macroscopic quantities. It is noted that, as δ/θ is decreased the oscillation period is increased and therefore the required computational load for a single trajectory is also increased. On the other hand, as δ/θ is increased the required

computational effort is decreased. Thus, the largest number of trajectories (5×10^5) is seen for $\theta = 0.1$ and $\delta = 50$. At the other limit for $\theta = 10^2$ and $\delta = 0.1$, although the number of trajectories is much smaller (about 10^3), the statistical scatter is also small.

The macroscopic quantities are volume based calculated and are given by the following expressions:

$$n = \frac{N\left(t_k\right)}{\left(N_P/N_C\right)} \tag{5.24}$$

$$u_a = \frac{1}{N\left(t_k\right)} \sum_{i=1}^{N(t_k)} \zeta_{\alpha,i}\left(t_k\right), \quad \alpha = x, y, z \tag{5.25}$$

$$\tau = \frac{2}{3N\left(t_k\right)} \sum_{i=1}^{N(t_k)} \left(\zeta_{x,i}^2\left(t_k\right) + \zeta_{y,i}^2\left(t_k\right) + \zeta_{z,i}^2\left(t_k\right)\right) - \frac{2}{3}\left(u_x^2 + u_y^2 + u_z^2\right) \tag{5.26}$$

$$p_{\alpha\beta} = \frac{n}{N\left(t_k\right)} \sum_{i=1}^{N(t_k)} \left(\zeta_{\alpha,i}\left(t_k\right) \zeta_{\beta,i}\left(t_k\right)\right) - nu_\alpha u_\beta, \quad \alpha, \beta = x, y, z \tag{5.27}$$

$$p = \eta\tau/2 \tag{5.28}$$

$$q_a = \frac{n}{N\left(t_k\right)} \sum_{i=1}^{N(t_k)} \left[\zeta_{\alpha,i}\left(t_k\right) \left(\zeta_{x,i}^2\left(t_k\right) + \zeta_{y,i}^2\left(t_k\right) + \zeta_{z,i}^2\left(t_k\right)\right)\right]$$

$$- \frac{3}{2}n\tau u_a - 2\left(u_x p_{\alpha x} + u_y p_{\alpha y} + u_z p_{az}\right) - n\left(u_x^2 + u_y^2 + u_z^2\right)u_a, \quad \alpha = x, y, z \tag{5.29}$$

In Eqs. (5.24)-(5.29), t_k denotes the different time step in which the sampling is performed and $N\left(t_k\right)$ is the number of particles in the cell at time t_k. It is noted that the averaging is performed across all ensemble average trajectories.

5.4   Deterministic formulation

In deterministic kinetic modeling the main unknown is the distribution function $f\left(t', y', \boldsymbol{\xi}\right)$, which for this flow configuration is a function of time t', space variable y' and molecular velocity vector $\boldsymbol{\xi} = \left(\xi_x, \xi_y, \xi_z\right)$. The flow is simulated by two different kinetic models, the BGK model [33] and the Shakhov model [190]. The unknown distribution obeys the time-dependent nonlinear one-dimensional BGK equation

$$\frac{\partial f}{\partial t'} + \xi_y \frac{\partial f}{\partial y'} + \tilde{F}' \frac{\partial f}{\partial \xi_x} = \frac{P}{\mu}\left(f^M - f\right) \tag{5.30}$$

where $\mu = \mu(T)$ is the viscosity at temperature T. The local Maxwellian distribution, denoted as f^M, is defined as

$$f^M = \frac{N}{(2\pi R_g T_0)^{3/2}} \exp\left(-\frac{m}{2k_B T_0}\left((\xi_x - U_x)^2 + \xi_y^2 + \xi_z^2\right)\right). \tag{5.31}$$

Similar to the BGK model, the distribution f obeys the time-dependent nonlinear one-dimensional Shakhov equation

$$\frac{\partial f}{\partial t'} + \xi_y \frac{\partial f}{\partial y'} + \tilde{F}' \frac{\partial f}{\partial \xi_x} = \frac{P}{\mu}\left(f^S - f\right) \tag{5.32}$$

where

$$f^S = f^M\left[1 + \frac{2m}{15N(k_B T)^2}\left(Q_x(\xi_x - U_x) + Q_y\xi_y\right)\left(\frac{m}{2k_B T}\left[(\xi_x - U_x)^2 + \xi_y^2 + \xi_z^2\right] - \frac{5}{2}\right)\right]. \tag{5.33}$$

The dimensionless distribution function $g = f u_0^3/N_0$ and molecular velocity, along with the rarefaction parameter defined by Eq. (5.5), the dimensionless quantities defined by Eqs. (5.9)-(5.10) and the expression for the viscosity given by the inverse power law (IPL) molecular interaction, are introduced into Eqs. (5.30), (5.31), (5.32) and (5.33) to yield the corresponding equations in dimensionless form:

$$\frac{\partial g}{\partial t} + \zeta_y \frac{\partial g}{\partial y} + F \cos\left(\frac{\delta}{\theta}t\right)\frac{\partial g}{\partial \zeta_x} = \delta\rho\tau^{1-\omega_P}\left(g^M - g\right), \tag{5.34}$$

$$g^M = \frac{\rho}{(\pi\tau)^{3/2}}\exp\left(-\frac{(\zeta_x - u_x)^2 + \zeta_y^2 + \zeta_z^2}{\tau}\right), \tag{5.35}$$

$$\frac{\partial g}{\partial t} + \zeta_y \frac{\partial g}{\partial y} + F \cos\left(\frac{\delta}{\theta}t\right)\frac{\partial g}{\partial \zeta_x} = \delta\rho\tau^{1-\omega_P}\left(g^S - g\right), \tag{5.36}$$

$$g^S = g^M\left[1 + \frac{2}{15\rho\tau^2}\left(q_x(\zeta_x - u_x) + q_y\zeta_y\right)\left(\frac{(\zeta_x - u_x)^2 + \zeta_y^2 + \zeta_z^2}{\tau} - \frac{5}{2}\right)\right]. \tag{5.37}$$

Instead of non dimensionalizing time t with H/v_0, the non dimensional time t may be defined as $t = t'\omega$. Therefore, an alternate form of the Eq. (5.34) is given by

$$\frac{\delta}{\theta}\frac{\partial g}{\partial t} + \zeta_y \frac{\partial g}{\partial y} + F \cos(t)\frac{\partial g}{\partial \zeta_x} = \delta\rho\tau^{1-\omega_P}\left(g^M - g\right). \tag{5.38}$$

95

The S model kinetic equation is similar to (5.38). The advantage of the non dimensionalization of time with frequency is that the oscillation period is the same for different oscillation parameters. Hence, the comparison between results with different values of θ is straightforward.

Furthermore, the ζ_x and the ζ_z components of the molecular velocity can be eliminated by introducing the following reduced distribution functions

$$Y(t, y, \zeta_y) = \int_{-\infty}^{+\infty} \int_{-\infty}^{+\infty} g(t, y, \zeta_x, \zeta_y, \zeta_z) \, d\zeta_x d\zeta_y d\zeta_z, \tag{5.39}$$

$$\Phi(t, y, \zeta_y) = \int_{-\infty}^{+\infty} \int_{-\infty}^{+\infty} \zeta_x g(t, y, \zeta_x, \zeta_y, \zeta_z) \, d\zeta_x d\zeta_y d\zeta_z, \tag{5.40}$$

$$\Lambda(t, y, \zeta_y) = \int_{-\infty}^{+\infty} \int_{-\infty}^{+\infty} \zeta_z^2 g(t, y, \zeta_x, \zeta_y, \zeta_z) \, d\zeta_x d\zeta_y d\zeta_z, \tag{5.41}$$

$$\Psi(t, y, \zeta_y) = \int_{-\infty}^{+\infty} \int_{-\infty}^{+\infty} \zeta_x^2 g(t, y, \zeta_x, \zeta_y, \zeta_z) \, d\zeta_x d\zeta_y d\zeta_z, \tag{5.42}$$

$$\Omega(t, y, c_y) = \int_{-\infty}^{+\infty} \int_{-\infty}^{+\infty} \zeta_x \left[\zeta_x^2 + \zeta_z^2\right] g(t, y, \zeta_x, \zeta_y, \zeta_z) \, d\zeta_x d\zeta_y d\zeta_z. \tag{5.43}$$

By operating accordingly on Eqs. (5.34) and (5.35) the following coupled integrodifferential equations are obtained for the BGK model

$$\frac{\partial Y}{\partial t} + \zeta_y \frac{\partial Y}{\partial y} = \delta\rho\tau^{1-\omega_P}\left(Y^M - Y\right) \tag{5.44}$$

$$\frac{\partial \Phi}{\partial t} + \zeta_y \frac{\partial \Phi}{\partial y} - F\cos\left(\frac{\delta}{\theta}t\right)Y = \delta\rho\tau^{1-\omega_P}\left(\Phi^M - \Phi\right) \tag{5.45}$$

$$\frac{\partial \Lambda}{\partial t} + \zeta_y \frac{\partial \Lambda}{\partial y} = \delta_0\rho\tau^{1-\omega_P}\left(\Lambda^M - \Lambda\right) \tag{5.46}$$

$$\frac{\partial \Psi}{\partial t} + \zeta_y \frac{\partial \Psi}{\partial y} - 2F\cos\left(\frac{\delta}{\theta}t\right)\Phi = \delta\rho\tau^{1-\omega_P}\left(\Psi^M - \Psi\right) \tag{5.47}$$

$$\frac{\partial \Omega}{\partial t} + \zeta_y \frac{\partial \Omega}{\partial y} - F\cos\left(\frac{\delta}{\theta}t\right)(3\Psi + \Lambda) = \delta\rho\tau^{1-\omega_P}\left(\Omega^M - \Omega\right) \tag{5.48}$$

where

$$Y^M = \frac{\rho}{\sqrt{\pi\tau}}\exp\left(-\frac{c_y^2}{\tau}\right), \tag{5.49}$$

$$\Phi^M = Y^M u_x, \tag{5.50}$$

$$\Lambda^M = Y^M\frac{\tau}{2} \tag{5.51}$$

96

$$\Psi^M = Y^M \frac{\left[2u_x^2 + \tau\right]}{2}, \tag{5.52}$$

$$\Omega^M = \Phi^M \left[u_x^2 + 2\tau\right]. \tag{5.53}$$

It is noted that the corresponding differential force terms have been transformed into non-differential source terms by utilizing integration by parts [186]. The projection procedure is the same for the S model and the governing equations are identical to the ones of the BGK model except for the equilibrium distribution functions which are given by

$$Y^S = Y^M \left(1 + \frac{2\zeta_y q_y \left(2\zeta_y^2 - 3\tau\right)}{15\rho\tau^3}\right), \tag{5.54}$$

$$\Phi^S = \Phi^M \left(1 + \frac{4\zeta_y^3 q_y u_x + 2\zeta_y \tau \left(\zeta_y q_y - 3u_x q_y\right) - \tau^2 q_x}{15\rho u_x \tau^3}\right), \tag{5.55}$$

$$\Lambda^S = \Lambda^M \left(1 + \frac{4\zeta_y^3 q_y - 2\zeta_y q_y \tau}{15\rho\tau^3}\right), \tag{5.56}$$

$$\Psi^S = \Psi^M \left(1 + \frac{8\zeta_y^2 q_x u_x \tau - 4q_x u_x \tau^2 + 4\zeta_y^3 q_y \left(u_x^2 + \tau\right) - 2\zeta_y \tau q_y \left(3u_x^2 + \tau\right)}{15\rho\tau^3 \left(u_x^2 + \tau\right)}\right), \tag{5.57}$$

$$\Omega^S = \Omega^M (1 + \frac{q_x \tau^2 \left(-3u_x^2 + 2\tau\right) + 4\zeta_y^3 q_y u_x \left(u_x^2 + 2\tau\right)}{15\rho\tau^3 u_x \left(u_x^2 + 2\tau\right)} - \frac{\left(2\zeta_y^2 q_x \tau - 2u_x \zeta_y \tau q_y\right) \left(3u_x^2 + 2\tau\right)}{15\rho\tau^3 u_x \left(u_x^2 + 2\tau\right)}). \tag{5.58}$$

The macroscopic quantities in Eqs. (5.49)-(5.58) are readily deduced by applying the same non-dimensionalization and projection procedures. They are written in terms of the associated distribution functions:

$$\text{Number density:} \quad n\left(t, y\right) = \int_{-\infty}^{\infty} Y d\zeta_y \tag{5.59}$$

$$\text{Velocity:} \quad u_x\left(t, y\right) = \frac{1}{\rho} \int_{-\infty}^{\infty} \Phi d\zeta_y \tag{5.60}$$

$$\text{Temperature:} \quad \tau\left(t, y\right) = \frac{2}{3\rho} \int_{-\infty}^{\infty} \left[\left(\zeta_y^2 + u_x^2\right) Y - 2u_x \Phi + \Lambda + \Psi\right] d\zeta_y \tag{5.61}$$

$$\text{Heat flow:} \quad q_x\left(t, y\right) = \int_{-\infty}^{\infty} \left(\Omega - 2u_x \Psi + 3u_x^2 \Phi - u_x^2 Y + \zeta_y^2 \Phi - u_x \zeta_y^2 Y - u_x \left(\Lambda + \Psi\right)\right) d\zeta_y \tag{5.62}$$

$$q_y\left(t, y\right) = \int_{-\infty}^{\infty} \left(c_y^3 Y + c_y \left(\Lambda + \Psi\right) - 2u_x c_y \Phi\right) dc_y \tag{5.63}$$

$$\text{Shear stress:} \quad p_{xy}\left(t, y\right) = \int_{-\infty}^{\infty} \zeta_y \Phi d\zeta_y \tag{5.64}$$

97

At the boundaries, the reduced distribution functions representing outgoing particles are denoted by $\left[Y^+, \Phi^+, \Lambda^+, \Psi^+, \Omega^+ \right]$. They are equal to the Maxwellian distributions which are defined by the wall conditions. Based on the above and following the projection procedure, the boundary conditions are formed

$$Y\left(\mp\frac{1}{2}, \zeta_y\right) = \frac{n_\mp}{\sqrt{\pi}\beta_\mp} \exp\left(\frac{-\zeta_y^2}{\beta_\mp}\right), \tag{5.65}$$

$$\Phi\left(\mp\frac{1}{2}, \zeta_y\right) = 0, \tag{5.66}$$

$$\Lambda\left(\mp\frac{1}{2}, c\right) = \frac{n_\mp}{2}\sqrt{\frac{\beta_\mp}{\pi}} \exp\left(\frac{-\zeta_y^2}{\beta_\mp}\right), \tag{5.67}$$

$$\Psi\left(\mp\frac{1}{2}, \zeta_y\right) = \frac{n_\mp}{2}\sqrt{\frac{\beta_\mp}{\pi}} \exp\left(\frac{-\zeta_y^2}{\beta_\mp}\right), \tag{5.68}$$

$$\Omega\left(\mp\frac{1}{2}, c\right) = 0, \tag{5.69}$$

where the parameter $\beta_\mp$ receives the values

$$\beta_\mp = \left\{ \begin{array}{ll} \beta, & \zeta_y > 0 \\ 1, & \zeta_y < 0 \end{array} \right\} \tag{5.70}$$

and $n_\mp$ are parameters which they are given in terms of the ingoing distributions satisfying the impermeability wall conditions in Eqs. (5.71)-(5.72)

$$n_- = -2\sqrt{\frac{\pi}{\beta}} \int_{-\infty}^{0} \zeta_y Y\left(-\frac{1}{2}, \zeta_y\right) d\zeta_y, \zeta_y > 0 \tag{5.71}$$

$$n_+ = 2\sqrt{\pi} \int_{0}^{+\infty} \zeta_y Y\left(\frac{1}{2}, \zeta_y\right) d\zeta_y, \zeta_y < 0 \tag{5.72}$$

It is noted that as $\beta = 1$ the boundary conditions correspond to the nonlinear flow with isothermal plates.

The kinetic formulation of the nonlinear oscillatory fully-developed flow setup is defined by Eqs. (5.44)-(5.53) (or Eqs. (5.54)-(5.58) for the S model) with the associated moments (5.59)–(5.64) subject to boundary conditions (5.65)-(5.69). The numerical solution is obtained by discretizing the molecular velocity, physical and temporal spaces. The discretization in the molecular velocity space is performed using the discrete velocity method and in the physical space it is based on a second order

central difference scheme. The velocity continuum spectrum $\zeta \in [0, \infty)$ is substituted by a discrete set $\zeta_m, m = 1, 2...M$, which is taken to be the roots of the Legendre polynomial of order M, accordingly mapped from $[-1, 1]$ to $[0, \infty)$. Concerning the temporal discretization, a semi-implicit scheme is used as in [175] and at each time step the governing equations are solved to find the unknown distribution functions. Then, the macroscopic quantities are estimated from Eqs. (5.59)-(5.64) based on a Gauss–Legendre quadrature. The numerical parameters, i.e., the time and space steps as well as the number of the discrete molecular velocities, have been gradually refined to ensure grid independent results up to at least two significant figures. The results presented in the Section 5.5 have been obtained with 1001 nodes in the physical space, $M = 80$ and time step $\Delta t = 10^{-4}$.

5.5   Results and discussion

Numerical results of the main macroscopic quantities are provided in terms of the force amplitude $F = [0.05, 0.1, 0.5]$, corresponding to small, moderate and large force amplitudes and in a wide range of the gas rarefaction and oscillation parameters $\delta = [0.1, 1, 10, 20, 50]$ and $\theta = [0.1, 1, 10, 20, 10^2]$ respectively as well as the temperature ratio $\beta = [1.22, 3, 19]$ for the oscillatory flow with the nonisothermal walls. Most of the results are computed with the DSMC method and results obtained with the deterministic models are reported when they are used. The presented results have reached the "periodic steady-state", implying that as time is further increased, the solution remains the same between cycles. The time t of an oscillation period is always multiplied with δ/θ in order to compare the results for different values of δ and θ on the same basis. All results are in dimensionless form.

Five subsections are provided describing the effect of F, δ and θ and β on all macroscopic quantities of theoretical and technological interest. The results in Sections 5.5.1-5.5.4 are based on the oscillatory flow with isothermal walls. In Section 5.5.1 the flow rate behavior, including a comparison with corresponding oscillatory linear and steady-state nonlinear results, is presented. Section 5.5.2 deals with the behavior of the space-dependent and the space-average macroscopic quantities (axial velocity, temperature, pressure and wall shear stress) between the plates. The behavior of the axial and normal heat flow distributions between the plates, as well as of the space-average axial heat flow are discussed in Section 5.5.3. Section 5.5.4 describes the oscillatory and cycle-average pumping powers. Finally, in Section 5.5.5 the space-

average normal and axial heat flow as well as the mass flow rate and the distributions of axial velocity and temperature based on the oscillatory flow with nonisothermal walls are presented.

5.5.1 Flow rates

In Figure 5.1 the flow rate $M(t)$, given by Eq. (5.12), is plotted over one cycle for $\delta = [0.1, 1, 10]$, $\theta = [0.1, 1, 10, 20, 10^2]$ and $F = [0.05, 0, 5]$. It is observed that for all values of δ, θ and more important for both values of F, corresponding to weak and strong driving external forces, the flow rate always has sinusoidal pattern with its fundamental frequency being the same with the driving frequency of the external harmonic force without the appearance of other harmonics. There is a phase angle lag between the flow rate and the external force, which has been also observed in [127, 128] and it is clearly contributed to the variation of δ and θ. It is noted that the external force varies as a cosine function. Roughly speaking the flow rate and the external force are almost in phase when δ is much smaller than θ and out of phase when δ is about the same or larger than θ. This behavior however, remains identical for both values of F and therefore the external force has no effect on the phase angle lag. Furthermore, it is seen that the amplitude of the flow rate is significantly reduced when the oscillation parameter is decreased (i.e., when the oscillation frequency ω is increased) due to inertia effects and this becomes more evident as the gas rarefaction parameter is increased and the flow becomes more viscous. Again, this description remains the same for both values of F and therefore, it may be stated that the external force magnitude does not have an effect on the qualitative behavior of the flow rate in terms of δ and θ. Of course, as F is increased the flow rate amplitude is also increased. The ratio of the strong over the weak implemented force amplitudes is equal to ten. It may be observed however, that the corresponding ratio of the flow rate amplitudes in some cases (e.g. when $\delta < \theta$) is not necessarily the same. This is due to the presence of nonlinear effects and it is more clearly demonstrated in the following discussion concerning Table 5.1, where tabulated results of the flow rate amplitudes are presented.

In Table 5.1, the flow rate amplitude M_A is tabulated for $\delta = [0.1, 1, 10, 20, 50]$, $\theta = [0.1, 1, 10, 20, 10^2]$ and $F = [0.05, 0.1, 0.5]$. More specifically, in order to directly compare with the corresponding linear results and since the linear solution is directly proportional to F, the present DSMC flow rate amplitudes are divided by the external force F and are provided as M_A/F in the 3rd, 4th and 5th column of Table 5.1. The linear flow rate amplitudes $G_A(\delta, \theta)$ obtained in [128] (see Fig. 5 in [128]) by solving

the linearized BGK model equation are also provided in the 6th column of Table 5.1. In the last three columns of Table 5.1 the relative difference on a percentage basis between linear and DSMC flow rate amplitudes, defined as $|M_A/F - G_A|/G_A$, are tabulated. It is seen that for $F = 0.05$ and $F = 0.1$ the deviation between the corresponding DSMC and linear solutions is less than 3% for $\delta \geq 1$ and for all values of θ, while for $\delta = 0.1$ and $\theta = 10, 20, 10^2$ the deviation is increased up to about 10%. It is evident that nonlinear effects are becoming more pronounced in highly rarefied atmospheres (small δ) and low frequencies (large θ). For $F = 0.5$ all deviations between DSMC and linear results are further increased due to nonlinear effects. Again however, the largest deviations reaching up to about 25% are occurring at $\delta = 0.1$ and $\theta = 10, 20, 10^2$ ($\delta << \theta$). Furthermore, for $F = 0.5$ it is seen that the deviations remain small in the transition regime ($\delta = 1$) and then, as δ is further increased the deviations are also increased at low frequencies reaching up to about 10%, 13% and 16% at $\delta = 10$, 20 and 50 respectively when $\theta = 10^2$. It must be noted that the qualitative behavior of the nonlinear flow rate amplitude in terms of δ and θ remains the same as of the linear results. More specifically with regard to δ for $\theta = [0.1, 1]$ the amplitude is decreased monotonically as δ is increased, while for $\theta = [10, 20, 10^2]$ it is initially decreased, then it is increased up to some local maximum and finally, it is again decreased. With regard to θ it is monotonically increased with θ (or as the oscillation frequency ω is decreased).

Overall it may be stated that the presence of strong external harmonic forces does not significantly affect the mass flow rate of the oscillatory flow, i.e., there is no distortion of the amplitude-frequency response curve. In a very wide range of gas rarefaction and oscillation frequencies, at small and moderate external forces the agreement between DSMC and linear flow rates is very good and always remains less than 10%, while at large external forces the deviation in the flow rate amplitude reaches about 25% indicating that nonlinear effects are becoming more significant. In addition, the accuracy of the DSMC solution in the linear limit is benchmarked.

In Figure 5.2, a comparison between the DSMC flow rate $M(t)$ with the corresponding flow rates obtained with the BGK and the Shakhov kinetic models, presented in Section 5.4, is performed for $F = [0.05, 0.5]$. It is readily seen that the agreement between the kinetic models and the DSMC method is always very good except for $\delta = 0.1$, $\theta = 10$ or in highly rarefied atmospheres and low frequencies. The small discrepancies are gradually decreased as the rarefaction parameter is increased and/or as the oscillation parameter is decreased. This behavior is seen for both values of the

101

force amplitude F. The comparison demonstrates the accuracy of both the stochastic and the deterministic results for various rarefaction and oscillation parameters covering a wide range of the flow regimes.

In Table 5.2, a comparison between the present DSMC normalized flow rate amplitude M_A/F with the corresponding normalized slip flow rate amplitude $M_A^{(S)}/F$, presented in Appendix A.2, as well as with the steady-state flow rate $M^{(st)}/F$ based on a steady-state DSMC code is performed for $F = 0.5$. The slip solution is valid for large values of both δ and θ, while the steady-state solution holds for $\theta \to \infty$ ($\omega = 0$) and for all δ. Therefore, the comparison with the slip solution is performed for $\theta = [10, 20, 10^2]$ and $\delta = [5, 10, 20, 50]$ and with the steady solution for the same θ and in a much wider range of δ. It is seen that for all three values of θ the agreement between the corresponding DSMC M_A/F and slip $M_A^{(S)}/F$ flow rate amplitudes is very good, up to at least 2-3 significant figures, for $\delta = [50, 20]$ and it drops to 1-2 significant figures, for $\delta = 10$, while there are significant discrepancies for $\delta = 5$, which are further increased for smaller δ and θ. Furthermore, there is very good agreement between the DSMC flow rate amplitudes M_A/F for $\theta = 10^2$ and the corresponding steady-state flow rates $M^{(st)}/F$ in the whole range of the gas rarefaction parameter δ. It is also seen that the deviations increase with δ, which is also expected, since steady conditions are recovered provided that the oscillation parameter is large (which it is, since $\theta = 10^2$) and also $\delta << \theta$ (which is the case only when $\delta < 10$). Also, as expected the deviations are increased as θ is decreased. The results in Table 5.2 indicate the range of applicability of the slip solution, as well as the validity of the DSMC solution in the range of parameters where the slip solution is valid and in the limit of very small oscillation frequencies.

Since all the aforementioned results are based on HS molecules, it is interesting to note the differences between the intermolecular collision models. Thus, in Table 5.3, the flow rate amplitude M_A/F divided by the external force F is tabulated for $\delta = [0.1, 1, 10]$, $\theta = [0.1, 1, 10, 10^2]$ and $F = [0.05, 0.5]$. The results are based on the nonlinear BGK model and three intermolecular collision models (HS, IPL, Maxwell) are presented. It is well known that the effect of the collision model is not significant in nonlinear pressure driven flows [191] and this is also seen here for highly rarefied atmospheres and low frequencies or when $\delta < \theta$ is valid. These small discrepancies are only present for $F = 0.5$, while for $F = 0.05$ the mass flow rate amplitude is the same for values of δ and θ. It is also clear that as θ is decreased the differences between the intermolecular collision models are reduced and they are diminished for $\delta \geq \theta$.

102

Therefore, in high and very high oscillation frequencies the intermolecular potential doesn't affect the mass flow rate even for large force amplitudes.

5.5.2 Velocity, temperature, pressure and wall shear stress distributions

The time evolution of the axial velocity $u_x(y, t)$, the normalized pressure distribution $p(y, t)/p(0, t)$ and the temperature $\tau(y, t)$ are considered, in terms of the distance $y \in [-1/2, 1/2]$ between the parallel plates at certain time steps $t = [0, \pi/2, \pi, 3\pi/2]$ over one cycle $t \in [0, 2\pi]$ for $F = 0.5$. The objective is to investigate, in parallel, the oscillatory behavior of the macroscopic distributions between the plates in dense and rarefied atmospheres. The presented results are for selected pairs of (δ, θ), which are considered from the physical point of view as the most representative and interesting.

The velocity distributions $u_x(y, t)$, shown in Figure 5.3 for $\delta = 0.1$, with $\theta = [0.1, 1, 10]$ and $\delta = 10$, with $\theta = [10, 20, 10^2]$ are qualitatively very similar to the corresponding ones obtained solving the linear oscillatory flow in [128], while quantitatively there are deviations, which are analogous to the deviations discussed in the flow rates in Section 3.5. Over one cycle the velocity distributions, as expected, take both positive and negative values and the cycle-average velocity is zero. As θ is decreased (higher frequency) the velocity amplitude is reduced and this behavior becomes stronger as δ is increased (less rarefied). Actually, in the cases of $\theta < \delta$ the velocity amplitude is almost diminished, even for $F = 0.5$. Also, as θ is decreased the phase angle lag between the velocity and the external force is increased and therefore, they are almost in phase when $\delta < \theta$ and out of phase for $\delta \geq \theta$ (the phase angle lag is about $\pi/2$). In all cases presented in Figure 5.3, except for $(\delta, \theta) = (10, 10)$, the velocity profiles have the typical shape with their amplitudes appearing a maximum at the channel center and reducing monotonically toward the walls. For $(\delta, \theta) = (10, 10)$ however, at $t = [0, \pi]$ the velocity profiles have two maximum amplitudes appearing between the channel center and the walls. This phenomenon, called "Richardson effect" or "velocity overshooting", is well known in oscillatory internal flows in the continuum regime [72] and has been recently analyzed in the transition regime [127, 128]. In general, as δ is increased and θ is decreased the velocity amplitude remains constant from the center of the channel until close to the walls and the velocity overshooting occurs in a thin viscous layer adjacent to the wall. This description is not discussed here, in detail, since it has been shown before and only a typical case is shown in Figure 5.4. Thus, the

Richardson effect is also present in nonlinear oscillatory flow and of course the bimodal velocity profile encountered at high frequencies and adequately dense atmospheres is not physically related by any means with the bimodal temperature profiles encountered in steady-state nonlinear force driven Poiseuille type flows [183–185, 189, 188].

In Figure 5.5, the temperature distributions $\tau(y,t)$ are plotted in terms of y at $t = [0, \pi/2, \pi, 3\pi/2]$ for the same flow parameters F, δ and θ with the ones in Figure 5.3 for the velocity distributions plus the intermediate case of $\delta = 1$, with $\theta = [1, 10, 10^2]$. The temperature has been non-dimensionalized with the wall temperature (Eq. (5.10)) and over one cycle it takes positive values above one (no cooling is observed). Similarly to the velocity, as θ is decreased the temperature amplitude is reduced and the phase angle lag with respect to the external force is increased. It is seen that the plotted temperature profiles coincide at $t = [0, \pi]$, as well as at $t = [\pi/2, 3\pi/2]$, which is justified since the temperature and velocity distributions are in phase with the former ones taking only positive values. Comparing the temperature profiles between $\delta = 0.1$, $\delta = 1$ and $\delta = 10$ it seen that they are qualitatively different. For $\delta = 0.1$ the temperature always has its minimum value at the channel center and then, is monotonically increased toward the walls. At the other end, for $\delta = 10$ the temperature profile possesses the bimodal shape observed in steady-state flow setups. At certain times, the temperature has a shallow at the channel center, then moving toward the walls it is symmetrically increased, with respect to y, up to some maximum and finally, it is decreased again. At other times however, the temperature has its maximum at $y = 0$ and it is monotonically decreased toward the walls. In the intermediate value of $\delta = 1$ the temperature profiles combine the characteristics of the temperature profiles from both cases of $\delta = 0.1$ and $\delta = 10$. Overall, as θ is decreased, although the temperature amplitude attenuates, on a relative basis the temperature well at $y = 0$ is about the same, while the maximum values are pushed closer to the walls. This bimodal behavior is due to the non-equilibrium effects predicted in [183–185, 188]. However, the oscillatory DSMC results may be affected, at some extend, by the oscillatory velocity overshooting. At this stage the contribution of the Richardson effect in the bimodal temperature numerics remains subtle and indistinguishable due to statistical noise fluctuations, which do not allow a detailed investigation for flow setups for $\theta < \delta$, where the velocity overshooting becomes more dominant. Conclusively, it may be stated that the temperature profiles may be at $\delta = 10$ (dense atmospheres) either convex or convex/concave and at $\delta = 0.1$ (rarefied atmospheres) only concave. This transition, as seen in Figure 5.5 ($\delta = 1$), occurs gradually as the gas rarefaction is decreased.

A complete view of the temperature oscillation over one cycle, is shown in Figure 5.6 where the time evolution of the temperature at the channel center, denoted by $\tau(0,t)$, over one cycle is plotted for $\delta = [0.1, 1, 10]$, $\theta = [0.1, 1, 10, 20, 10^2]$ and $F = 0.5$. It is seen that the temperature has two maxima (and two minima) per cycle. As it has been noted before, clearly the amplitude of the oscillation is reduced with θ and for $\delta = 1$ and $\theta = 0.1$, as well as for $\delta = 10$ and $\theta = [0.1, 1]$ it almost diminishes. This is expected since the velocity amplitude at these values of δ and θ is also diminished, the heat dissipation is significantly reduced and the gas temperature remains almost isothermal. Also, for $\delta < \theta$ the temperature profiles are in phase with the external force, while for $\delta \geq \theta$ they are out of phase, with the maximum phase angle lag occurring at the highest frequency ($\theta = 0.1$). Although the presented results are only for $F = 0.5$ it is noted that as F is decreased, the temperature variation is gradually reduced and linear isothermal oscillatory flow is recovered.

In Figure 5.7, the time evolution of the normalized pressure distribution $p(y,t)/p(0,t)$ is plotted in terms of y at $t = [0, \pi/2, \pi, 3\pi/2]$ for the same flow parameters F, δ and θ with the ones in Figure 5.3 for the velocity distributions. The pressure $p(0,t)$ refers to the pressure at the center of the channel ($y = 0$) and the ratio $p(y,t)/p(0,t)$, over one cycle is positive with values larger than or equal to one. It is clearly seen that the pressure distribution between the plates is not constant, which has been also observed in the corresponding steady-state. The deviation of the normalized pressure from one, appears in all examined values of δ, θ and its behavior has a very close qualitative resemblance with the corresponding deviation of temperature.

In Figure 5.8, the instantaneous wall shear stress $p_W = p_{xy}(1/2)$ is plotted over one cycle for $\delta = [0.1, 1, 10]$, $\theta = [0.1, 1, 10, 20, 10^2]$ and $F = [0.05, 0.5]$. For all values of δ, θ and for both values of F the wall shear stress behaves as a sinusoidal function having the same frequency with the one of the external force. Also, the wall shear stress is in phase with the flow rate plotted in Fig. 5.1 and therefore, as it was observed for the flow rate, the shear stress phase angle lag remains the same for both force amplitudes. Furthermore, the amplitude of the wall shear stress oscillation is monotonically decreased with θ and this becomes more evident as δ is increased. As F is increased the amplitude of the wall shear stress is increased in a similar manner with the flow rate amplitude. Overall, it is clear that the wall shear stress qualitatively closely resembles the behavior of the flow rate in terms of all flow parameters.

An overall quantity of practical interest in oscillatory flows is the cycle-average wall shear stress $\bar{p}_W$ [8], given by Eq. (5.16). In Figure 5.9, the normalized cycle-average wall

105

shear stress $\bar{p}_W/2F$ is provided in terms of δ for $\theta = [0.1, 1, 10, 20, 10^2]$ and $F = 0.5$. As δ is increased, in general, the cycle-average wall shear stress is decreased. For $\theta = [0.1, 1]$, $\bar{p}_W$ is reduced rapidly in the transition regime and then very slowly in the slip regime, while for $\theta = [10, 20, 10^2]$ this behavior is reversed, i.e., it is reduced very slowly in the transition regime and then rapidly in the slip regime. In all cases $\bar{p}_W$ is increased with θ. The present description is representative for all force amplitudes.

Closing this section it is noted that the accuracy of the computed macroscopic variables has been successfully tested based on the balance equation (5.20). More specifically, for all values of F, δ and θ considered here, the corresponding space-average velocity, density and wall shear stress satisfy Eq. (5.20) over a time cycle with great accuracy.

5.5.3   Axial and normal heat flow distributions

The behavior of the axial $q_x(y,t)$ and normal $q_y(y,t)$ components of the heat flow vector, parallel and vertical to the plates respectively, as well as of the space-average axial flow $\bar{q}_x(t)$ are discussed in terms of the flow parameters δ, θ and F. The space-average normal flow is zero.

The space-average axial flow $\bar{q}_x(t)$, given by Eq. (5.13), is plotted over one cycle in Figure 5.10 for $\delta = [0.1, 1, 10]$ and $\theta = [0.1, 1, 10, 20, 10^2]$ with $F = [0.05, 0, 5]$. It is readily seen that there are significant qualitative differences between the corresponding cycle-average heat flow for $F = 0.05$ and $F = 0.5$. For the small external force amplitude $F = 0.05$, $\bar{q}_x(t)$ for all values of δ and θ has a sinusoidal behavior over time. It is also observed that with respect to the corresponding flow rates, presented in Figure 5.1, it has a phase angle lag of about $\pi/2$ and therefore, as expected from the corresponding steady-state results [183–185, 188], the space-average axial flow is in most cases opposite to the flow rate. For the large external force amplitude $F = 0.5$, $\bar{q}_x(t)$ shows over one cycle various patterns. Observing carefully the results, it is seen that for $\delta = 0.1$ with $\theta = 0.1$, $\delta = 1$ with $\theta = [0.1, 1]$ and for $\delta = 10$ and $\theta = [0.1, 1, 10]$, i.e. in all cases where $\delta \geq \theta$, $\bar{q}_x(t)$ exhibits a sinusoidal pattern having with respect to the corresponding flow rates about the same phase angle lag of $\pi/2$. On the contrary, in all cases where $\delta < \theta$, $\bar{q}_x(t)$ exhibits a rather complex non-sinusoidal pattern indicating that the introduced nonlinearities are responsible for the generation of oscillatory motion containing several harmonics. In addition, the phase angle lag between the corresponding cycle-average axial flow and flow rate is not $\pi/2$ and depending on the specific parameters it varies from zero to $\pi/2$. These results are in agreement

with the discussion in Table 5.1, where the DSMC results for $F = [0.05, 0.1, 0.5]$ have been compared with corresponding linear results to find out that nonlinear effects are becoming more significant in highly rarefied flow (small δ) and low oscillation frequencies (large θ). Thus, at $F = 0.5$ the space-average axial flow for $\delta \geq \theta$ should be in most cases opposite to the flow rate, while for $\delta < \theta$, depending on the phase angle lag, it may flow either in the same or the opposite direction. Furthermore, it is noted that when the external force amplitude is increased from $F = 0.05$ to $F = 0.5$, i.e., ten times, the amplitude of $\bar{q}_x(t)$ is increased for all δ and θ about five times. Also, for both values of F, the amplitude of $\bar{q}_x(t)$, as with all other macroscopic quantities, is reduced with θ and almost diminishes at very high frequencies as the gas becomes less rarefied and this is the reason that in Fig. 5.10, the plots for $\delta = 10$ and $\theta = [0.1, 1]$ are omitted as indistinguishable.

The behavior of the nonlinear $\bar{q}_x(t)$ patterns for $\delta = [1, 10]$ and $\theta = [10, 20, 10^2]$ is further investigated with the assistance of Fourier transform analysis to find out that the space-average axial heat flow may be well-fitted by a sinusoidal function as

$$\bar{q}_x(t) = \bar{q}_{x,A}^{(1)} \cos\left(t - \bar{q}_{x,P}^{(1)}\right) + \bar{q}_{x,A}^{(3)} \cos\left(t - \bar{q}_{x,P}^{(3)}\right), \qquad (5.73)$$

where $\bar{q}_{x,A}^{(1)}$, $\bar{q}_{x,P}^{(1)}$ and $\bar{q}_{x,A}^{(3)}$, $\bar{q}_{x,P}^{(3)}$ are the amplitude and the phase of the 1st and 3rd harmonics. The amplitude of the 2nd, as well as of higher than the 3rd order harmonics is at least one order of magnitude smaller than the 1st and 3rd order harmonics and are not included in Eq. (5.73). Tabulated results of the amplitudes and phases of Eq. (5.73) are presented in Table 5.4. It is seen that space-average axial heat flow for $\delta = \theta$ evolves with a single oscillation frequency, which is the same with the one of the external harmonic force, while for $\delta < \theta$ a third harmonic emerges with an amplitude, which may be of the same or even larger order of the first one. This distortion of the sinusoidal pattern is clearly contributed to nonlinear interaction and has been already pointed out in [161, 163].

In Figure 5.11, the axial $q_x(y, t)$ and normal $q_y(y, t)$ heat flow distributions are plotted in terms of y at certain times $t = [0, \pi/2, \pi, 3\pi/2]$ over a cycle for $F = 0.5$ and the following selected pairs of $(\delta, \theta) = [(0.1, 1), (1, 10), (10, 10^2)]$. The specific values of the gas rarefaction and oscillations parameters fulfill the condition $\delta < \theta$ and are the ones where nonlinear effects are mostly pronounced (see discussions for Table 5.1 and Figure 5.10). The corresponding steady-state heat flow is also included for comparison purposes. Starting with the axial heat flow distributions $q_x(y, t)$ it is seen that the

profiles for specific times may take both positive and negative values (e.g. $\delta = 1$, $\theta = 10$, $t = 0$ or $t = \pi$). This is expected and also happens at the corresponding steady-state profiles. It is found however, that this specific behavior is present only when $F = 0.5$ and $\delta < \theta$, while in all other cases examined here, the $q_x(y,t)$ profiles along y will be either only larger or only smaller than zero. Therefore, the complex behavior of the space-average heat flow $\bar{q}_x(t)$ observed at $F = 0.5$ and $\delta < \theta$ may be due to the fact that $q_x(y,t)$ at fixed times $t \in [0, 2\pi]$ may be both positive and negative.

Continuing with the normal heat flow distributions $q_y(y,t)$, it is seen that the profiles over one cycle are oscillating about a mean value curve. In most cases they are taking negative and positive values at the lower ($-0.5 \leq y < 0$) and upper ($0 < y \leq 0.5$) half of the channel, which is justified by the fact that heat flows from the gas towards the channel walls. For some values of δ and θ however, e.g. for $\theta = 1$ and $\delta = 0.1$, at certain times over a cycle, the normal heat flow distributions in the lower and upper half may not follow this behavior and take far from the boundaries positive and negative values respectively. Of course, the profiles are always antisymmetric about $y = 0$, where $q_y(0,t) = 0$, resulting to $\bar{q}_y(t) = 0$.

5.5.4 Pumping power

The pumping power $E(t)$ and the cycle-average pumping power $\bar{E}$ are discussed in terms of the flow parameters δ, θ and F. Even though the net flow is zero, the cycle average pumping power is not, in order to maintain the oscillatory flow and it is important to compute it mainly for technological purposes.

In Figure 5.12, the pumping power $E(t)$, given by Eq. (5.14), is plotted over one cycle for $\delta = [0.1, 1, 10]$, $\theta = [0.1, 1, 10, 20, 10^2]$ and $F = [0.05, 0, 5]$. The pumping power is proportional to the product of the external force $F'(t)$ times the space-average axial velocity $\bar{u}_x(t)$. The behavior of $\bar{u}_x(t)$ is similar to the flow rate $M(t)$ since in most cases the mean number density is close to one ($\bar{n}(t) \sim 1$). Thus, since $E(t)$ is proportional to $\cos^2(t)$ it has two maxima (and two minima) within each cycle, as seen in Figure 5.12. By increasing the external force amplitude by one order of magnitude the pumping power amplitude is increased approximately by two orders. However the qualitative behavior of $E(t)$ remains the same for both values of F, as it should, since it is related with macroscopic quantities which are not affected qualitatively by the amplitude of the external force. As the oscillation frequency is increased its amplitude is decreased and its phase angle lag is increased. The negative values of $E(t)$, shown in

Figure 5.11 at some times $t \in [0, 2\pi]$, are due to the large phase angle lag between the mean velocity and the external force and this issue has already been analyzed in [128].

The cycle-average pumping power $\bar{E}/dx$, given by Eq. (5.15), is provided in Figure 5.13 in terms of δ for $\theta = [0.1, 1, 10, 20, 10^2]$ with $F = [0.05, 0.5]$. The steady-state pumping power $E^{(st)}/dx$ is also plotted for comparison purposes. Roughly speaking, $\bar{E}$ is increased proportionally to the square of F. Qualitatively there is very good agreement between linear and nonlinear pumping powers. The average pumping power remains about constant for $\delta < \theta$ and it is decreased for $\delta \geq \theta$, except for $\theta = 10^2$ where a local maximum is observed at some $\delta \sim 25$, which is due to the corresponding behavior of the flow rate amplitude M_A shown in Table 5.1. Comparing the oscillatory and steady-state results it is seen that the former one is about one-half of the latter one when $\delta < \theta$. However, the detailed nonlinear results indicate that the nonlinear normalized average pumping power solution $\bar{E}/F$ is smaller than the corresponding linear one, following the same trend of the flow rates.

5.5.5 Flow with nonisothermal walls

At first, the reported results include the mass flow rate and the distributions of the axial bulk velocity and the temperature. They are presented mainly in terms of the temperature ratio and the differences between the flows with isothermal and nonisothermal walls are pointed out. Next, the space-average as well as the distributions of the axial and normal heat flow are studied in terms of the temperature ratio, the force magnitude, the rarefaction and oscillation parameters.

In Figure 5.14, the flow rate $M(t)$ is plotted over one cycle for $\delta = [0.1, 1, 10]$, $\theta = 1$ $F = 0.5$ and $\beta = [1.22, 3, 19]$. The flow rate with the isothermal plates ($\beta = 1$) is also included for comparison purposes. The results are based on the Shakhov model even though similar remarks can be derived with the DSMC method and the BGK model. The behavior of $M(t)$ has been thoroughly analyzed in Section 5.5.1 and therefore here the comments are given in terms of the temperature ratio. It is observed that the temperature ratio does not have an effect on the qualitative behavior of the flow rate in terms of δ and θ. However, as β is increased the flow rate is reduced for small rarefaction parameters. The interesting part here is that for larger values of δ the effect of the temperature ratio is reduced leading to the conclusion that the flow rate is affected by β only for high gas rarefaction and for $\delta \gg \theta$.

In Figure 5.15, the axial velocity distributions $u_x(y, t)$ are presented for $\delta = 10$, $\theta = 1$ and $F = 0.5$ with $\beta = [1.22, 3, 19]$. They are plotted in terms of y at certain

times $t = [0, \pi/2, \pi, 3\pi/2]$. It has been seen that as $\delta > \theta$ the velocity amplitude remains constant from the center of the channel until close to the walls and the velocity overshooting occurs in a thin viscous layer adjacent to the wall. This annular effect isn't affected for small temperature ratios. However, as β is increased this behavior is distorted near the hotter plate and the overshoot is vanished at the $t = [\pi/2, 3\pi/2]$. The magnitude of the velocity isn't altered since the rarefaction parameter is larger than the oscillation parameter leading to high frequency oscillations where the effect of the temperature ratio on the flow properties is weak.

Moreover, the temperature distributions $\tau(y, t)$ are presented in terms of y at certain times $t = [0, \pi/2, \pi, 3\pi/2]$ and for $\theta = 1$, $F = 0.5$, $\beta = [1.22, 3, 19]$ with $\delta = 0.1$ (left) and $\delta = 10$ (right). At first, it is seen that as the temperature ratio is increased the temperature is also increased for both rarefaction parameters. In terms of δ however the magnitude of the temperature depends also on the temperature ratio. For small values of β, the temperature is decreased as the rarefaction parameter is increased. This behavior has already been seen in Section 5.5.2 where as $\delta > \theta$ and for $\beta = 1$ the high frequency oscillations reduce the magnitude of the temperature. It is interesting to note that for $\delta = 0.1$ the temperature profile may be concave at certain times while for $\delta = 10$ the profile is almost linear. As β is increased, the temperature profile becomes linear for both values of the rarefaction parameter. In addition, the temperature coincides at $t = [0, \pi/2, \pi, 3\pi/2]$ which states that the temperature isn't affected by the high frequency oscillation in all temperature ratios. On the other hand, for $\delta = 0.1$ the plotted temperature profiles coincide at $t = [0, \pi]$, as well as at $t = [\pi/2, 3\pi/2]$ which shows that the temperature retains its oscillatory motion even though the temperature ratio is increased. Therefore, in low oscillation frequencies, the temperature has a sinusoidal behavior due to the force however as the frequency is increased it is advanced without any periodicity.

Next, in Figs. 5.17-5.19 the space average heat flow $\bar{q}_y(t)$ is presented over time t for $\beta = [1.22, 3, 19]$, $\delta = [0.1, 1, 10]$ and $\theta = [0.1, 1, 10]$ with $F = 0.05$ (left) and $F = 0.5$ (right). The space average heat flow coupled to a steady state force is also included. The presented results have been computed with the BGK kinetic model. At first, it is seen that as β is increased the temperature ratio is increased and therefore $\bar{q}_y$ is also increased. Also, it is increased more gradually for larger temperature ratios than for smaller ones. While the heat flow coupled to a steady state force is constant for all involving parameters, the heat flow coupled to an oscillatory force is affected by the oscillation and begins oscillating even though the temperature ratio is constant. It

110

is interesting to note that $\bar{q}_y$ may be oscillating however its maximum never exceeds the heat flow coupled to steady state force. In all cases, the oscillation parameter doesn't increase the magnitude of the heat flow which is always equal or lesser than the steady-state case. Thus, the main outcome from Figs. 5.17-5.19 is that as the oscillation frequency of the force is increased the normal heat flow isn't enhanced for any rarefaction and oscillation parameter.

However, it is also clear that the time evolution of $\bar{q}_y$ is altered according to the oscillation and rarefaction parameters. More specifically, in Fig. 5.17, the heat flow is oscillating for all values of θ. The amplitude and the phase lag of the heat flow $\bar{q}_y$ is decreased and increased respectively as the oscillation parameter is decreased. Hence, the oscillation of the force creates a forced oscillation in the heat flow $\bar{q}_y$. This behavior is also seen as the rarefaction parameter is increased in Figure 5.18 except for $\theta = 0.1$ where the heat flow is increased without periodicity. It seems that as $\delta > \theta$, the high frequency oscillations stall the evolution of the normal heat flow and consequently it needs more time to reach its maximum value. The largest time is always seen for the largest temperature ratios. Despite the high oscillation frequency, the normal heat flow advances in time without oscillating. Besides, there remarks are also confirmed in Fig. 5.19 where the normal heat flow shows small periodicity only for $\theta = 10$. In Fig. 5.19, the normal heat flow $\bar{q}_y$ hasn't converged into its final value for $\theta = 0.1$ and even though it is not seen here, it will reach a maximum value (close to the value of the heat flow coupled to steady state force) at $t = 300$.

Finally, the dependency on the force amplitude is analyzed. The behavior of the $\bar{q}_y$ is qualitatively the same for both values of the force amplitude F. However, as δ is increased the effect of the oscillating force is decreased for small force magnitudes ($F = 0.05$). This behavior is confirmed with the small deviations of $\bar{q}_y$ and the lack of periodicity for $\delta = 1$ and small values of θ. It seems that as F is increased the forced oscillation of $\bar{q}_y$ becomes more significant only for small rarefaction parameters (e.g. $\delta = [0.1, 1]$). It is noted that the commented behavior is also encountered in the Shakhov and DSMC results.

In Table 5.5, the space average heat flow $\bar{q}_y$ is presented at the final time instant $t = 10 \cdot 2\pi$ and for $\beta = [1.22, 3, 19]$, $\delta = [0.1, 1, 10]$ and $\theta = 1$ with $F = [0.05, 0.5]$. The results are based on the DSMC method as well as the kinetic models, BGK and Shakhov. Since the behavior of the $\bar{q}_y(t)$ has already been described, here a comparison between the DSMC heat flow with the corresponding heat flows obtained with the BGK and the Shakhov kinetic models is performed. At first, the BGK model is compared

with the DSMC method. It is seen that the agreement between the two of them is good for small rarefaction parameters (e.g., $\delta = [0.1, 1]$) and for all temperature ratios. However, as δ is increased the BGK model fails to capture the DSMC solution and the deviations are also increased. Even though the relative errors are not shown here, the largest deviation between the DSMC method and the BGK model is 30% for $\delta = 10$ and $\beta = 3$. Of course, the BGK model isn't suitable for nonisothermal flows and therefore the Shakhov model is investigated next. The deviations between the Shakhov model and the DSMC method remain small for all values of the rarefaction parameter as well as the temperature ratios. It is interesting to note that the largest deviation is seen for $\delta = 0.1$ and $\beta = 1.22$ however for larger temperature ratios the relative error between the Shakhov model and the DSMC method is reduced. It is also noted that the force amplitude has a very weak effect on all the comparisons. Overall, the Shakhov model is considered as a more reliable model for nonisothermal flows than the BGK model since it recovers the correct Prandtl number. The following results are based on the Shakhov model.

The space-average axial heat flow $\bar{q}_x(t)$ is plotted over one cycle in Figure 5.20, for $\delta = [0.1, 1, 10]$, $\theta = 1$ and $\beta = [1, 1.22, 3, 19]$ with $F = 0.5$. It is readily seen that the heat flow exhibits the same behavior for all the small temperature ratios. For $\delta = 0.1$, as β is increased the behavior of the axial heat flow $\bar{q}_x(t)$ changes completely. Not only it is opposite to the other cases but it also is out of phase with them. In addition, the magnitude of $\bar{q}_x(t)$ is decreased even though the normal heat flow is increased. However, as δ is increased, the aforementioned behavior is reversed. The magnitude of $\bar{q}_x(t)$ is increased and all the heat flows seem to be in phase with each other. Thus, the behavior of $\bar{q}_x(t)$ depends heavily on δ and θ and depending on the temperature ratio it may change completely. It has already been seen in Section 5.5.3 that when $\delta \geq \theta$ the sinusoidal behavior is always established and this is also valid here for all values of the temperature ratio.

In Figure 5.21, the normal $q_y(y, t)$ heat flow distribution is plotted in terms of y at certain times $t = [0, \pi/2, \pi, 3\pi/2]$ over a cycle for $F = 0.5$, $\theta = 1$ and $\beta = [1.22, 3, 19]$ with $\delta = 0.1$ (left) and $\delta = 10$ (right). It is seen that the profiles over one cycle are oscillating about a mean value curve for small values of δ and β. As the temperature ratio β is increased the profiles at the time steps $t = [0, \pi]$ are getting larger than the corresponding ones at $t = [\pi/2, 3\pi/2]$. Also, the certain profiles cease to be symmetric about a mean value. Next, as δ is increased the behavior of $q_y(y, t)$ is completely altered. The propagation of heat flow is the same at all time steps. As the temperature

112

ratio is increased the profile of the heat flow becomes nonlinear and its magnitude is increased. The commented behavior is in accordance with the remarks related to Figs. 5.17-5.19.

Continuing with the axial heat flow distributions $q_x(y,t)$, they are presented in Figure 5.22. They are plotted in terms of y at certain times $t = [0, \pi/2, \pi, 3\pi/2]$ over a cycle for $F = 0.5$, $\theta = 1$ and $\beta = [1.22, 3, 19]$ with $\delta = 10$. Here, the rarefaction parameter is larger than the oscillation one leading to high oscillation frequencies. It is clear that the axial heat flow is larger near the walls than in the center of the flow field. This behavior has already been seen in Section 5.5.2 where the velocity shows overshootings near the walls. It seems that the axial heat flow has similar overshootings which are present at all time steps. Also, the profiles are symmetrical for the small temperature ratio. As β is increased the heat flow is increased and it becomes larger near the upper half of the channel. The heat flow overshootings are still seen in certain time steps even though the symmetry of the profiles is lost due to the larger temperature ratios.

5.6 Concluding remarks

The oscillatory nonlinear fully-developed flow of a monoatomic gas between parallel plates due to an external harmonic force acting on the gas per unit mass is numerically investigated in a wide range of the gas rarefaction parameter δ (inversely proportional to the Knudsen number) and of the oscillation parameter θ (inversely proportional to the oscillation frequency) for force amplitudes $F = [0.05, 0.1, 0.5]$ (inversely proportional to the square of the Froude number) corresponding to small, moderate and large amplitudes. An extra parameter is the temperature ratio β between the two plates and it is used for investigating the coupled flow and heat transfer phenomena. Modelling and simulations are based on the DSMC method, the BGK and the Shakhov kinetic models. The results are in dimensionless form and include the macroscopic distributions of axial velocity, temperature, pressure, wall shear stress and heat flow vector, as well as space- and/or cycle-averaged macroscopic variables to deduce overall quantities such as the flow rate, the average wall shear stress, the average axial heat flow and pumping power. The first part of the concluding remarks is related to the oscillatory flow with isothermal plates and the second one with nonisothermal plates.

The DSMC results have been systematically compared with corresponding linear BGK results. Of course, the comparison has been limited to the axial velocity and

the flow rate since linear theory cannot capture coupled momentum and heat transfer effects. At small and moderate external forces, the agreement between DSMC and linear flow rates is very good and always remains less than 10%, while at large external forces the deviation in the flow rate amplitude reaches about 25%. Nonlinear effects are becoming more significant in highly rarefied flow and low oscillation frequencies, i.e., when $\delta < \theta$. For all values of F, δ and θ however, the flow rate has a sinusoidal pattern with its fundamental frequency being the same with the driving frequency of the external harmonic force without the appearance of other harmonics. Thus, the behavior of the present DSMC flow rates have a close qualitative resemblance with the corresponding linear ones in terms of δ and θ. It may also be stated that the applicability range of linear theory is well beyond its mathematical restriction of infinitesimal small force amplitudes.

Concerning the temperature and pressure profiles across the channel it has been seen that they strongly depend on δ and θ. The bimodal shape of the temperature profile and the not constant pressure profile, appearing in steady-state setups have been also observed here. The temperature profiles at certain times over a cycle are at small δ only concave having a minimum at the channel center and monotonically increasing toward the walls, while as δ is increased the profiles become either convex/concave or only convex. The deviation of the pressure from the reference one appears in all values of examined values of δ, θ and has a very close qualitative resemblance with the corresponding temperature deviation. Both quantities as well as the wall shear stress behave as sinusoidal functions having the same frequency with the one of the external force and they are about in phase with the flow rate. In all cases as the oscillation frequency is increased (θ is decreased) the amplitude of the oscillation is decreased and the phase angle lag with the external force is increased.

The axial heat flow is the macroscopic quantity which is most affected by the external force F. For $F = 0.05$ and all values of δ, θ, as well as for $F = 0.5$ and $\delta \geq \theta$ it has a sinusoidal pattern, while for $F = 0.5$ and $\delta < \theta$ it exhibits a rather complex non-sinusoidal pattern indicating that the introduced nonlinearities are responsible for the generation of oscillatory motion containing several harmonics. This has been confirmed by a Fourier transform analysis showing that a third harmonic emerges with the same or even larger amplitude from the first one. Therefore, the space-average axial heat flow, depending on the phase angle lag with the flow rate, may be in the opposite or the same direction with the flow rate. The normal heat flow is affected by the external force in a manner similar to the other macroscopic distributions (except

the axial heat flow) and exhibits a sinusoidal behavior. The normal heat flow profiles oscillate about a nonzero mean curve taking negative and positive values at the lower and upper half of the channel and this remains valid for all flow parameters.

The cycle-averaged oscillatory pumping power is not zero, although there is no net flow, in order to maintain the oscillatory flow. Approximately, it is increased proportionally to the square of F. The detailed results indicate that the nonlinear average pumping power is smaller than the corresponding linear one, following the same trend of the flow rates. In general, there is very good qualitative agreement between the corresponding linear and nonlinear pumping powers.

Next, remarks based on the oscillatory nonlinear flow with nonisothermal plates are given. It has been seen that in the hydrodynamic regime the heat transfer enhancement due to oscillatory motion has been a controversial issue. Here, it seen that the axial oscillatory motion doesn't enhance the normal heat flow which arises due to the different plate temperatures. In fact, it is either equal or lesser than the corresponding normal heat flow of the steady-state force driven flow with nonisothermal plates. It is also seen that in low force frequencies (or when $\delta \ll \theta$) the normal heat flow is affected by the oscillation and it shows a sinusoidal behavior even though its driving force isn't an harmonic excitation. In high frequencies (or when $\delta \gg \theta$), this periodic behaviour is diminished and the normal heat flow advances very slowly in time since the high frequency flow stalls its evolution. It is also noted that the magnitude of the force has a weak effect on the normal heat flow. Furthermore, the axial heat flow depends heavily on the rarefaction and oscillation parameters as well as the temperature ratio. For small rarefaction parameters δ, it is decreased as β is increased while for larger values of δ, it is increased.

It also interesting to note that the effect of the temperature ratio on the mass flow rate is significant only for small rarefaction and larger oscillation parameters. It has been seen that the velocity overshooting is affected by the large temperature ratios and the profile of the velocity changes near the hotter plate. Also, the temperature depends heavily on the rarefaction parameter and the temperature ratio. As the ratio is increased it is always increased and its behavior is altered in terms of δ, for small values it coincides at certain times while for large ones it coincides at all times.

Overall, it seems that in low oscillation frequencies the normal heat flow and the temperature present periodic behavior due to the driving oscillatory force while in high frequencies they propagate in time without periodicity.

Table 5.1 Normalized flow rate amplitude M_A/F for $F = [0.05, 0.1, 0.5]$ and various values of δ and θ along with the relative difference with the linear results [128].

δ	θ	M_A/F			LinearG_A	Relative difference		
		$F = 0.05$	$F = 0.1$	$F = 0.5$		$F = 0.05$	$F = 0.1$	$F = 0.5$
0.1	0.1	7.69(-1)	7.69(-1)	7.69(-1)	7.68(-1)	0.16	0.16	0.16
	1	1.78	1.77	1.57	1.82	2.07	2.76	13.9
	10	1.91	1.85	1.53	2.03	5.91	8.87	24.6
	20	1.91	1.85	1.53	2.03	5.96	8.95	24.7
	100	1.89	1.83	1.52	2.03	7.06	9.83	25.4
1	0.1	1.00(-1)	9.99(-2)	9.99(-2)	1.00(-1)	0.09	0.05	0.02
	1	8.30(-1)	8.30(-1)	8.29(-1)	8.29(-1)	0.09	0.10	0.10
	10	1.49	1.48	1.36	1.52	2.13	2.50	10.5
	20	1.50	1.49	1.36	1.53	2.21	2.65	11.3
	100	1.50	1.49	1.36	1.54	2.31	2.85	11.7
10	0.1	1.00(-2)	1.00(-2)	1.00(-2)	1.00(-2)	0.02	0.03	0.03
	1	9.92(-2)	9.92(-2)	9.92(-2)	9.93(-2)	0.46	0.42	0.38
	10	8.89(-1)	8.90(-1)	8.88(-1)	8.89(-1)	1.76	1.98	7.41
	20	1.54	1.54	1.53	1.55	1.95	2.31	9.87
	100	2.62	2.60	2.22	2.65	1.82	2.50	10.9
20	0.1	4.98(-3)	5.01(-3)	5.00(-3)	5.00(-3)	0.04	0.09	0.02
	1	4.99(-2)	4.98(-2)	4.98(-2)	4.98(-2)	0.01	0.01	0.01
	10	4.66(-1)	4.66(-1)	4.65(-1)	4.66(-1)	0.63	0.63	1.90
	20	8.90(-1)	8.90(-1)	8.89(-1)	8.91(-1)	1.29	1.50	6.70
	100	3.11	3.10	2.85	3.13	1.92	2.45	13.1
50	0.1	2.01(-3)	2.00(-3)	2.00(-3)	2.00(-3)	0.05	0.03	0.01
	1	1.99(-2)	2.00(-2)	2.00(-2)	2.00(-2)	0.03	0.03	0.03
	10	1.94(-1)	1.94(-1)	1.94(-1)	1.94(-1)	0.05	0.08	0.13
	20	3.79(-1)	3.79(-1)	3.79(-1)	3.79(-1)	0.18	0.23	1.17
	100	1.72	1.72	1.71	1.73	1.41	2.05	16.4

116

Table 5.2 Normalized nonlinear and slip flow rate amplitudes M_A and $M_A^{(S)}$ for $F = 0.5$ and various values of δ and θ along with the corresponding steady solution $M^{(st)}$.

δ	M_A			$M_A^{(S)}$			$M^{(st)}$
	$\theta = 10$	$\theta = 20$	$\theta = 100$	$\theta = 10$	$\theta = 20$	$\theta = 100$	$\theta \to \infty$
0.1	1.53	1.53	1.52				1.53
1	1.36	1.36	1.36				1.36
2	1.41	1.42	1.42				1.42
5	1.37	1.66	1.72	0.662	0.828	0.915	1.72
10	0.888	1.53	2.22	0.874	1.516	2.561	2.23
20	0.466	0.889	2.85	0.461	0.883	3.093	3.06
50	0.194	0.379	1.71	0.193	0.378	1.721	

Table 5.3 Normalized flow rate amplitude M_A/F for different intermolecular potentials (HS, IPL, Maxwell), $F = [0.05, 0.5]$ and various values of δ and θ obtained with the BGK model.

δ	θ	Hard sphere ($\omega_P = 1/2$)		IPL ($\omega_P = 0.7$)		Maxwell ($\omega_P = 1$)	
		$F = 0.05$	$F = 0.5$	$F = 0.05$	$F = 0.5$	$F = 0.05$	$F = 0.5$
0.1	0.1	7.68(-1)	7.68(-1)	7.68(-1)	7.68(-1)	7.68(-1)	7.67(-1)
	1	1.82	1.69	1.82	1.71	1.82	1.73
	10	2.02	1.70	2.02	1.73	2.02	1.79
	100	2.02	1.70	2.02	1.73	2.03	1.79
1	0.1	1.00(-1)	1.00(-1)	1.00(-1)	1.00(-1)	1.00(-1)	1.00(-1)
	1	8.28(-1)	8.27(-1)	8.28(-1)	8.26(-1)	8.28(-1)	8.26(-1)
	10	1.52	1.40	1.52	1.40	1.52	1.40
	100	1.54	1.40	1.54	1.40	1.54	1.40
10	0.1	1.00(-2)	1.00(-2)	1.00(-2)	1.00(-2)	1.00(-2)	1.00(-2)
	1	9.96(-2)	9.96(-2)	9.96(-2)	9.96(-2)	9.96(-2)	9.96(-2)
	10	8.81(-1)	8.78(-1)	8.81(-1)	8.78(-1)	8.81(-1)	8.79(-1)
	100	2.62	2.19	2.62	2.13	2.62	2.05

Table 5.4 Amplitudes and phases of the space-average axial heat flow $\bar{q}_x(t)$ corresponding to Eq. (5.73) for specific values of δ and θ, with $F = 0.5$.

δ	θ	$\bar{q}_{x,A}^{(1)}$	$\bar{q}_{x,A}^{(3)}$	$\bar{q}_{x,P}^{(1)}$	$\bar{q}_{x,P}^{(3)}$
1	1	7.39(-2)	2.63(-3)	1.67	-0.140
	10	5.16(-2)	3.82(-2)	-3.09	-0.875
	20	4.84(-2)	3.83(-2)	-3.10	-0.419
	100	4.72(-2)	3.82(-2)	-3.13	-0.0683
10	10	1.31(-2)	3.79(-4)	1.88	-0.643
	20	1.73(-2)	3.01(-3)	2.39	1.28
	100	8.44(-3)	1.42(-2)	-1.03	-1.08

Table 5.5 Space average heat flow $\bar{q}_y(t = 10 \cdot 2\pi)$ for $\theta = 1$, $F = [0.05, 0.5]$ and $\delta = [0.1, 1, 10]$ obtained with the DSMC method as well as the BGK and Shakhov models.

$\bar{q}_y(t = 62.8)$		DSMC		BGK		Shakhov	
β	δ	$F = 0.05$	$F = 0.5$	$F = 0.05$	$F = 0.5$	$F = 0.05$	$F = 0.5$
1.22	0.1	1.091(-1)	1.186(-1)	1.233(-1)	1.327(-1)	1.248(-1)	1.343(-1)
	1	8.239(-2)	8.294(-2)	8.446(-2)	8.499(-2)	9.186(-2)	9.220(-2)
	10	2.780(-2)	2.777(-2)	2.306(-2)	2.307(-2)	2.944(-2)	2.944(-2)
3	0.1	1.328	1.388	1.348	1.397	1.367	1.416
	1	1.019	1.025	9.430(-1)	9.474(-1)	1.028	1.032
	10	3.607(-1)	3.603(-1)	2.722(-1)	2.722(-1)	3.482(-1)	3.483(-1)
19	0.1	1.586(+1)	1.607(+1)	1.621(+1)	1.634(+1)	1.662(+1)	1.674(+1)
	1	1.330(+1)	1.333(+1)	1.307(+1)	1.309(+1)	1.450(+1)	1.451(+1)
	10	6.296	6.297	4.969	4.970	6.367	6.367

118
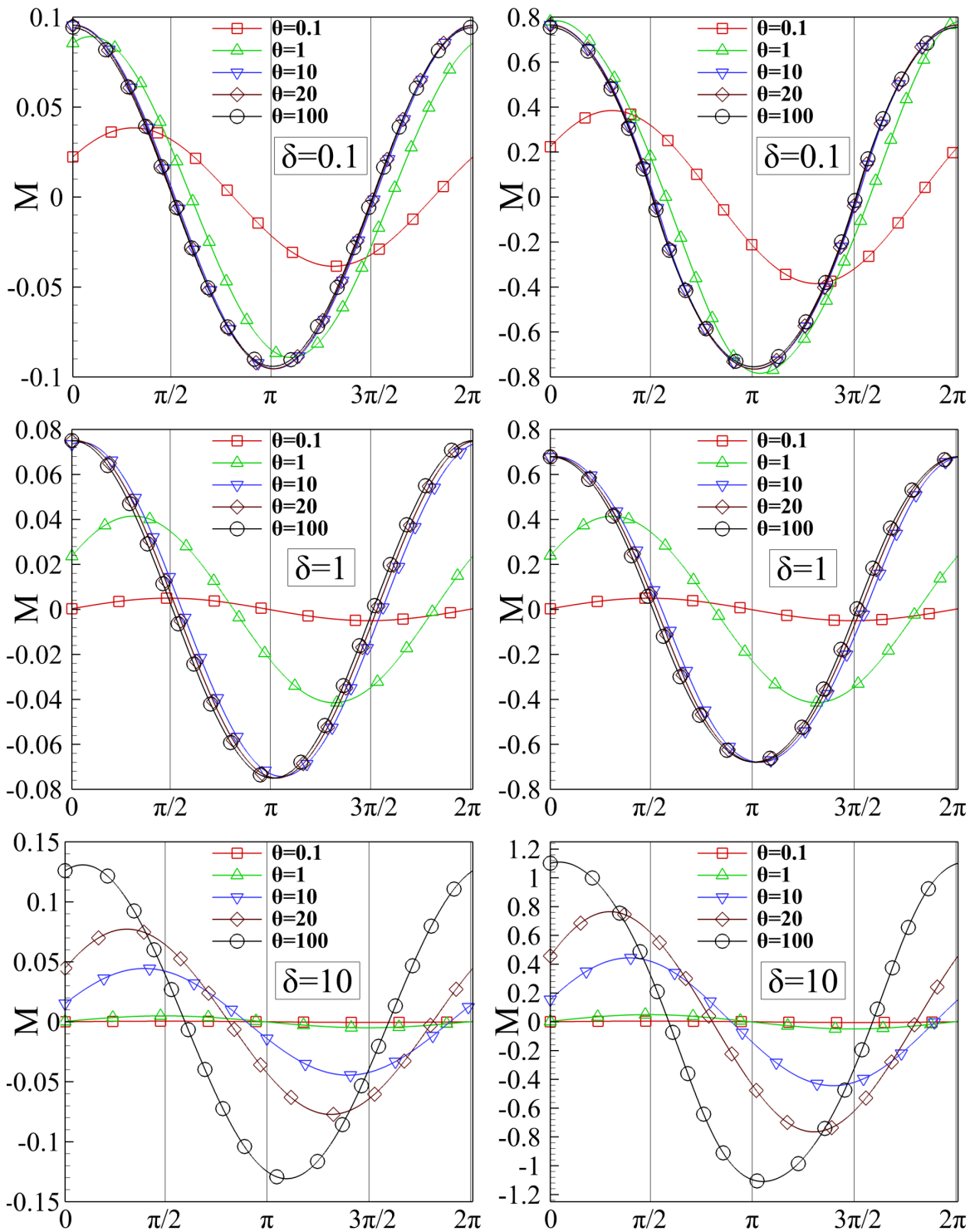
Figure 5.1 Flow rate $M(t)$ over one oscillation cycle $t \in [0, 2\pi]$ for various values of δ and θ with $F = 0.05$ (left) and $F = 0.5$ (right).

119
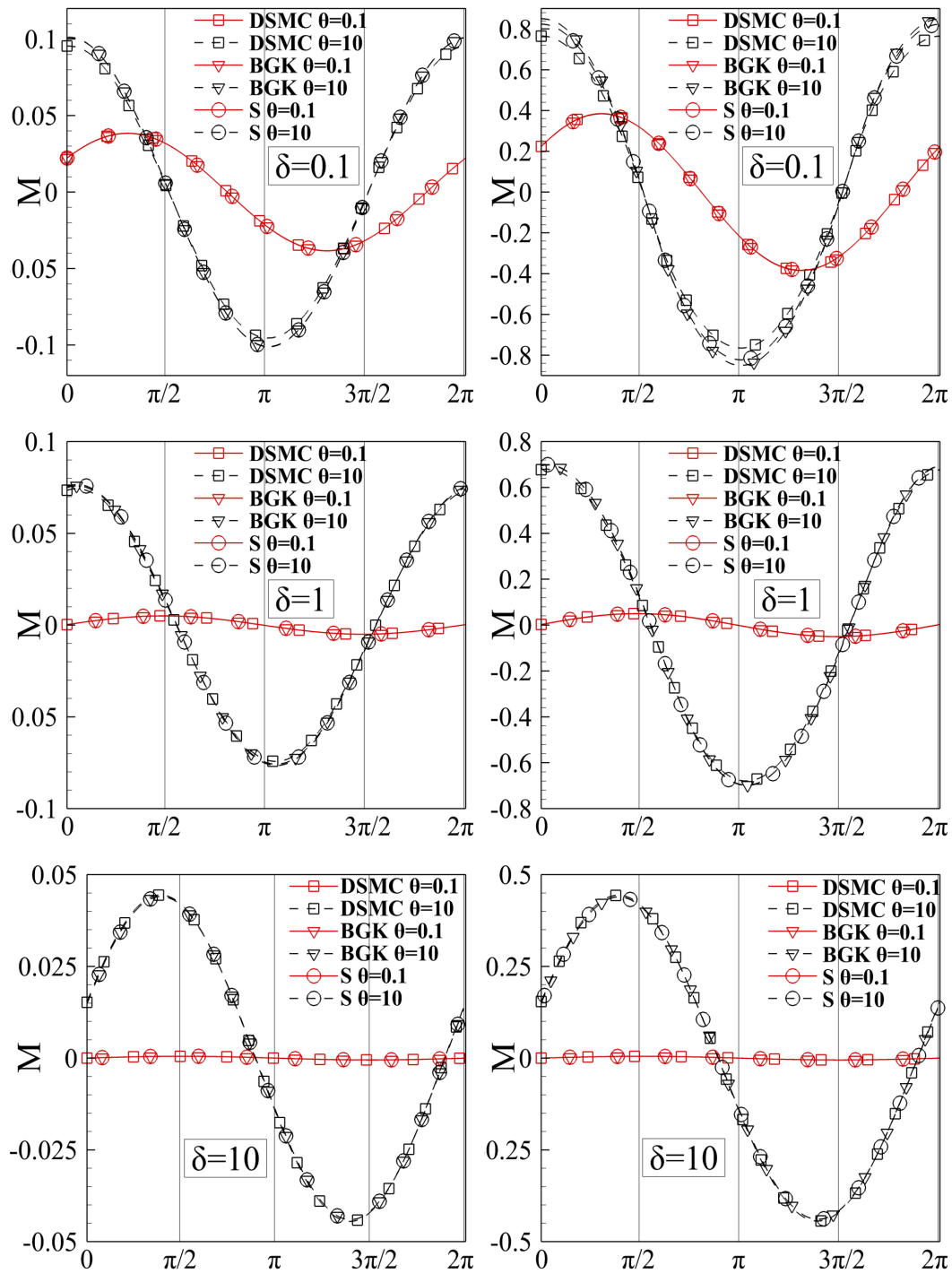
Figure 5.2 Flow rate $M(t)$ obtained with the DSMC method, the BGK and the Shakhov kinetic models over one oscillation cycle $t \in [0, 2\pi]$ for various values of δ and θ with $F = 0.05$ (left) and $F = 0.5$ (right).

120
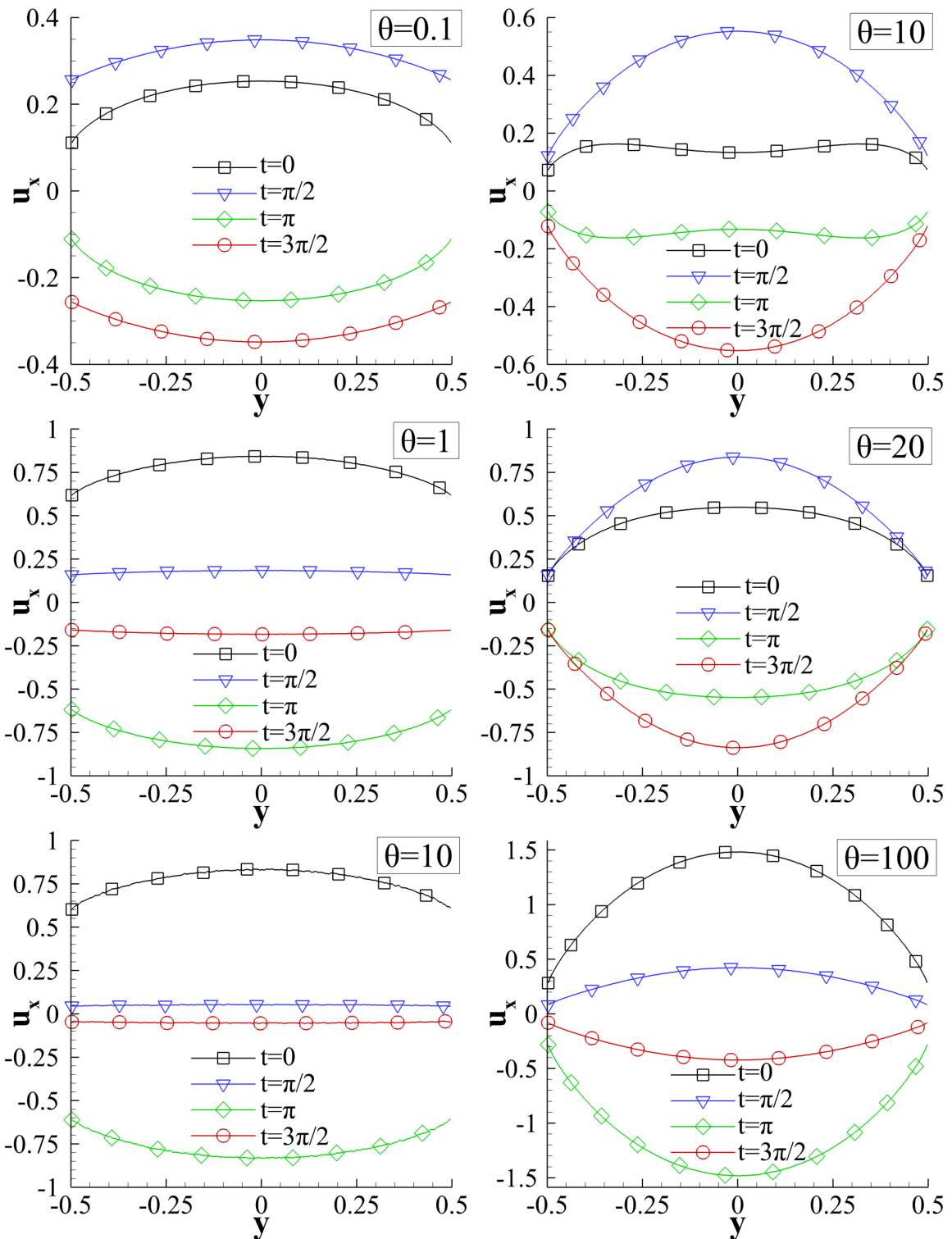
Figure 5.3 Time evolution of velocity $u_x(y,t)$ at certain time steps $t \in [0, 2\pi]$ for various values of θ, $F = 0.5$ and $\delta = 0.1$ (left) and $\delta = 10$ (right).

121
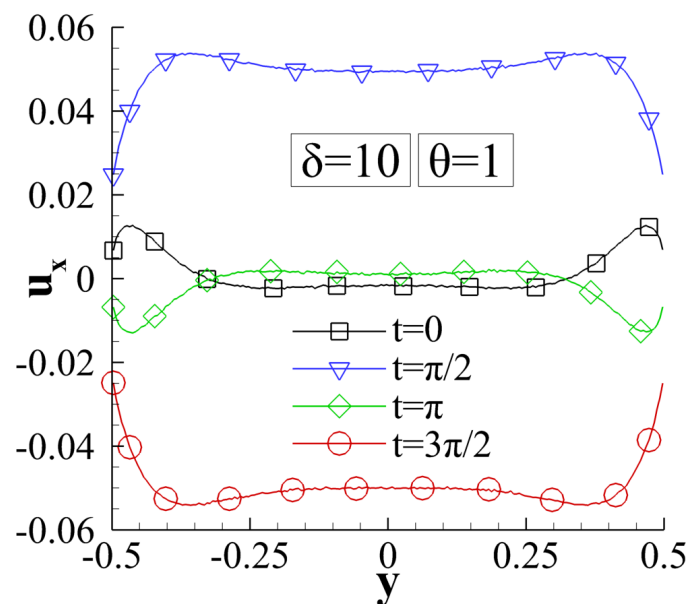
Figure 5.4 Time evolution of velocity $u_x(y,t)$ at certain time steps $t \in [0, 2\pi]$ for $\delta = 10$, $\theta = 1$ and $F = 0.5$.
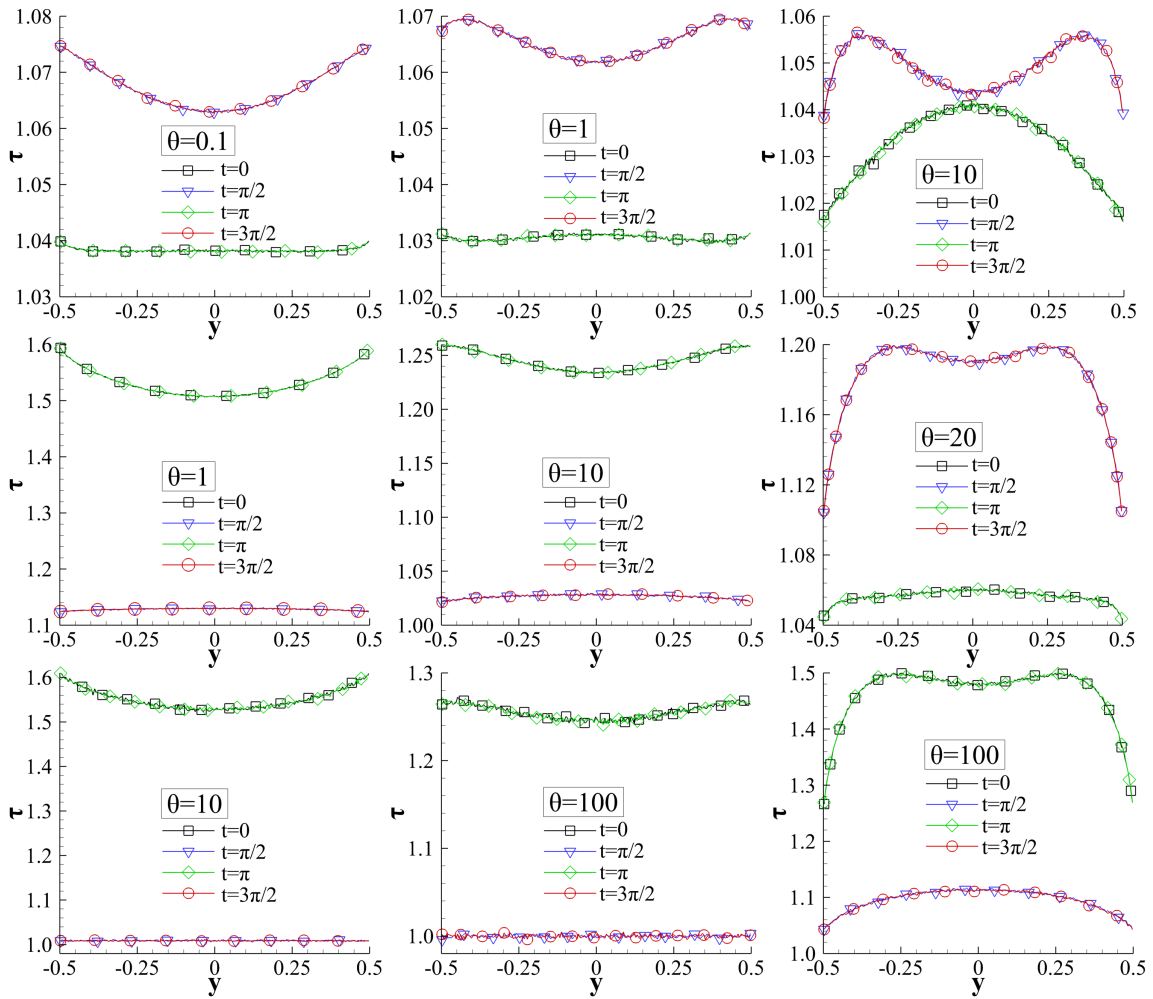
Figure 5.5 Time evolution of temperature $\tau(y, t)$ at certain time steps $t \in [0, 2\pi]$ for various values of θ, $F = 0.5$ and $\delta = 0.1$ (left), $\delta = 1$ (middle) and $\delta = 10$ (right).

123
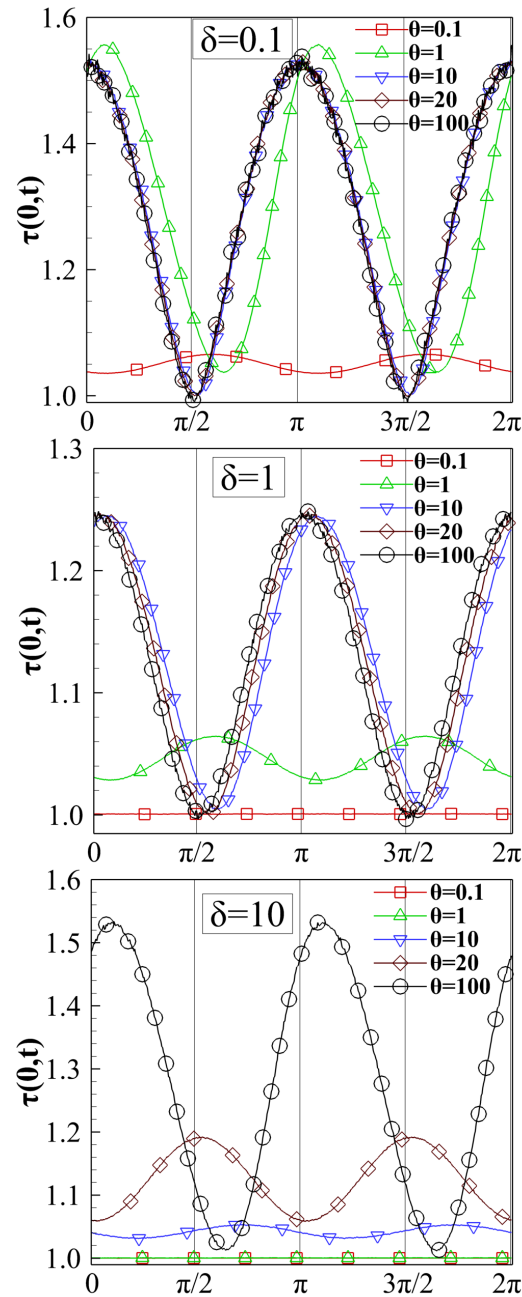
Figure 5.6 Temperature $\tau(0,t)$ over one oscillation cycle $t \in [0, 2\pi]$ for $\delta = [0.1, 1, 10]$, $\theta = [0.1, 1, 10, 20, 10^2]$ and $F = 0.5$.
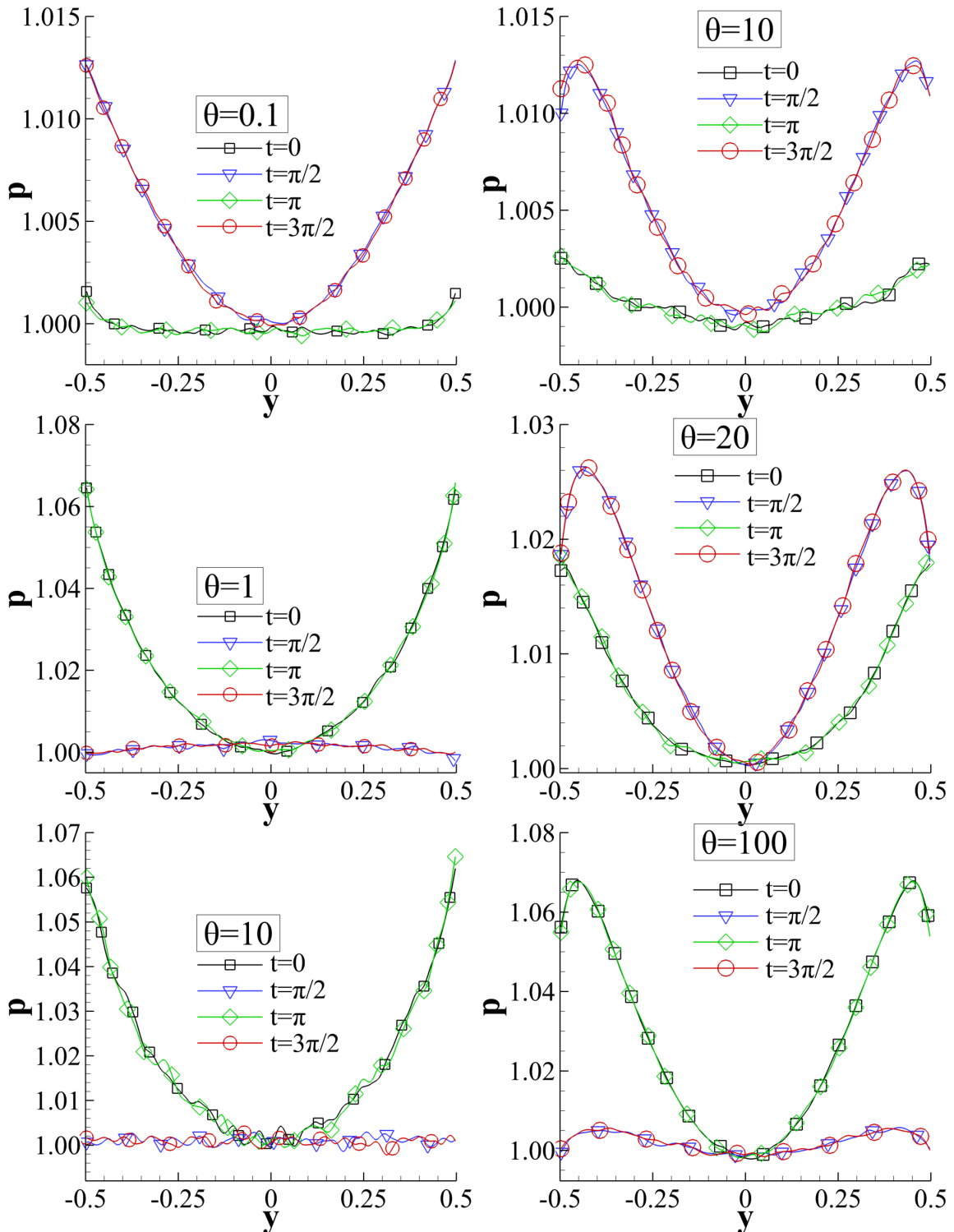
Figure 5.7 Time evolution of normalized pressure $p(y,t)/p(0,t)$ at certain time steps $t \in [0, 2\pi]$ for various values of θ, $F = 0.5$ and $\delta = 0.1$ (left) and $\delta = 10$ (right).
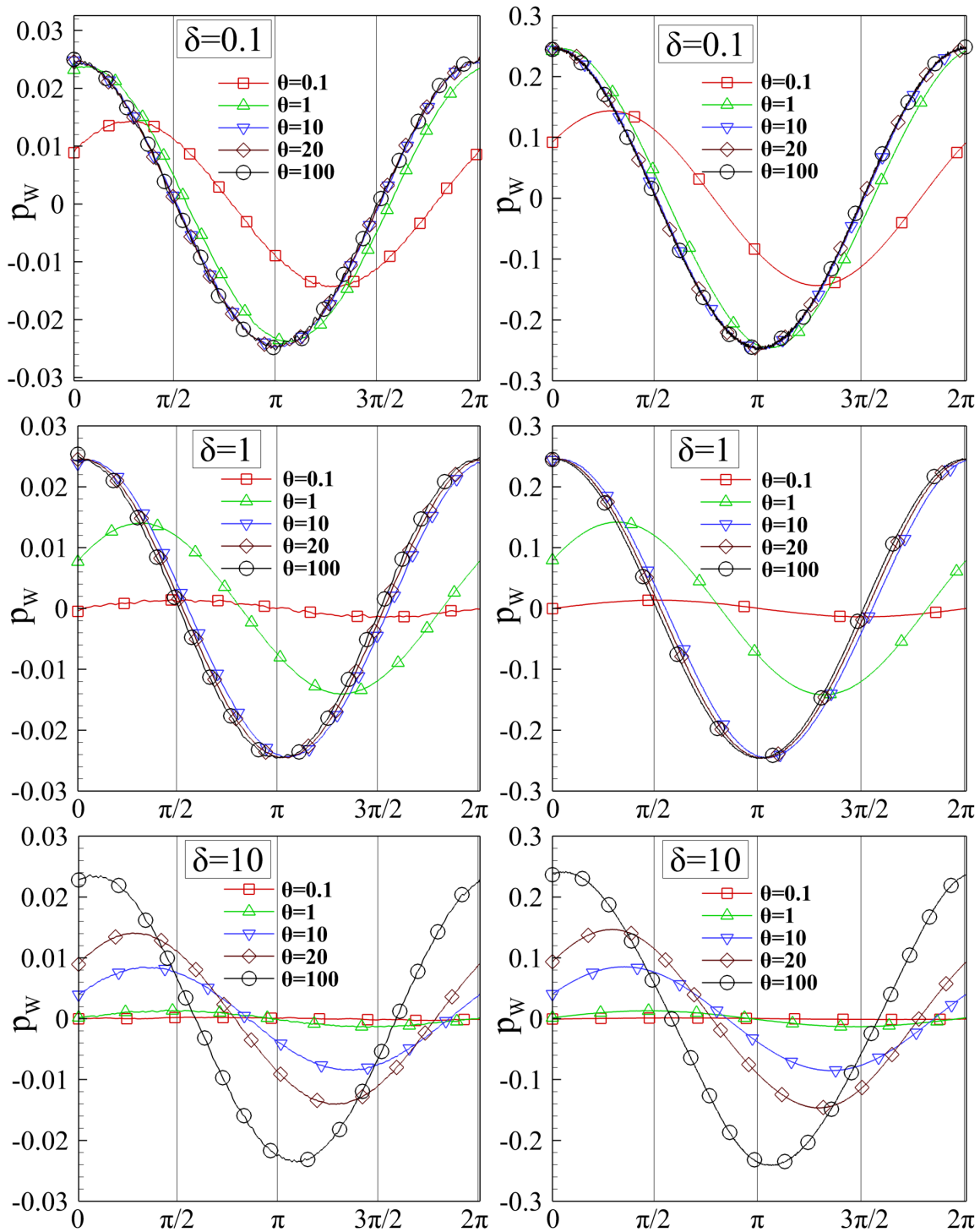
Figure 5.8 Wall shear stress $p_W(t)$ over one oscillation cycle $t \in [0, 2\pi]$ for various values of δ and θ with $F = 0.05$ (left) and $F = 0.5$ (right).

126
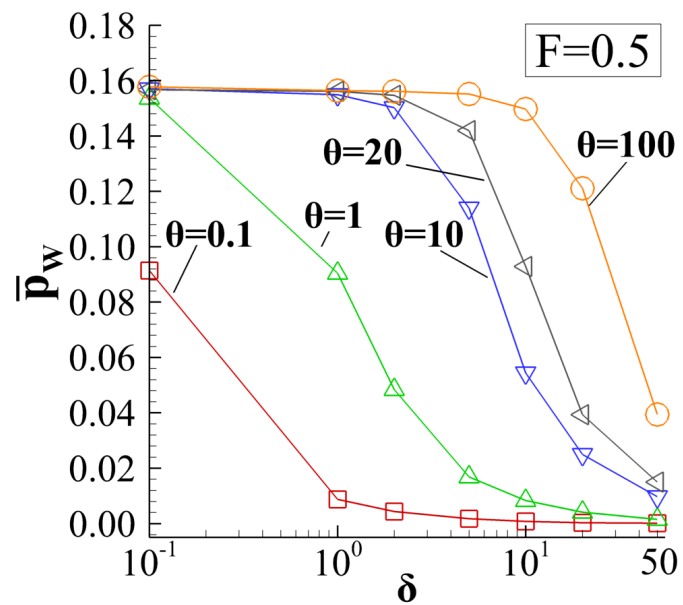
Figure 5.9 Normalized cycle-average wall shear stress $\bar{p}_W / (2F)$ in terms of δ for various values θ and $F = 0.5$.
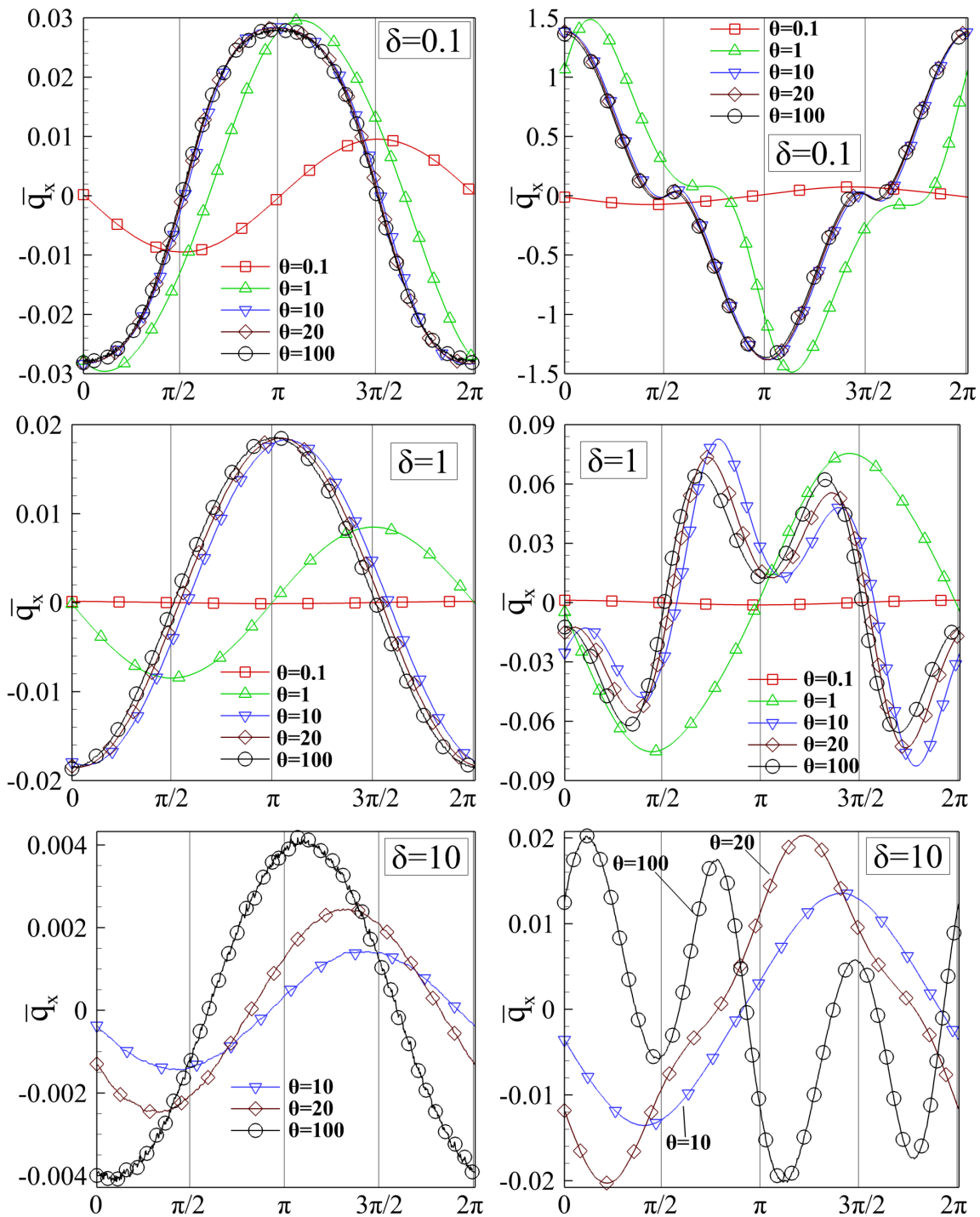
Figure 5.10 Space-average axial heat flow $\bar{q}_x(t)$ over one oscillation cycle $t \in [0, 2\pi]$ for various values of δ and θ with $F = 0.05$ (left) and $F = 0.5$ (right).

128
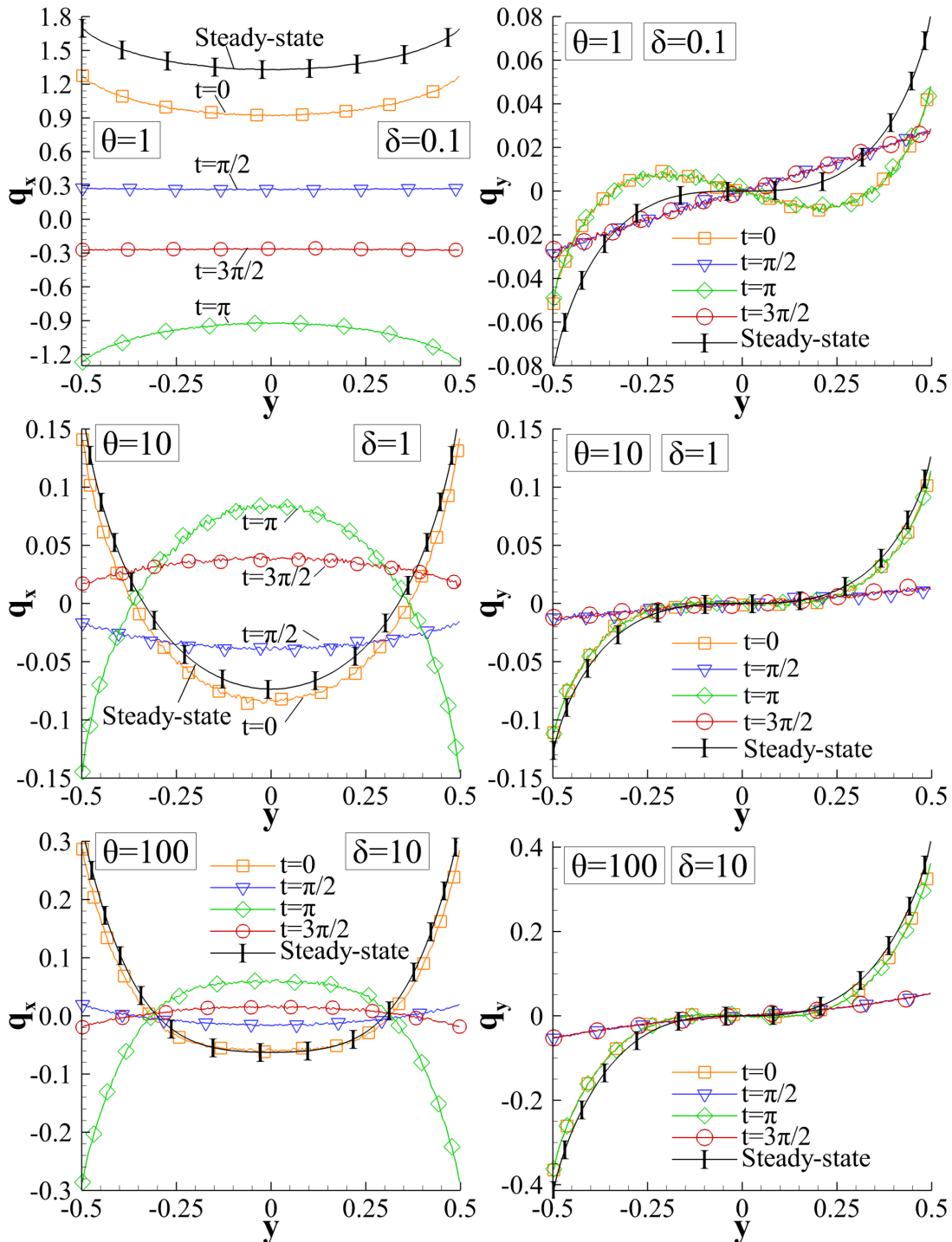
Figure 5.11 Time evolution of axial $q_x(y,t)$ (left) and normal $q_y(y,t)$ (right) heat flow at certain time steps $t \in [0, 2\pi]$ for $F = 0.5$ and various values of θ and δ; the corresponding steady-state axial and normal heat flows are also included.
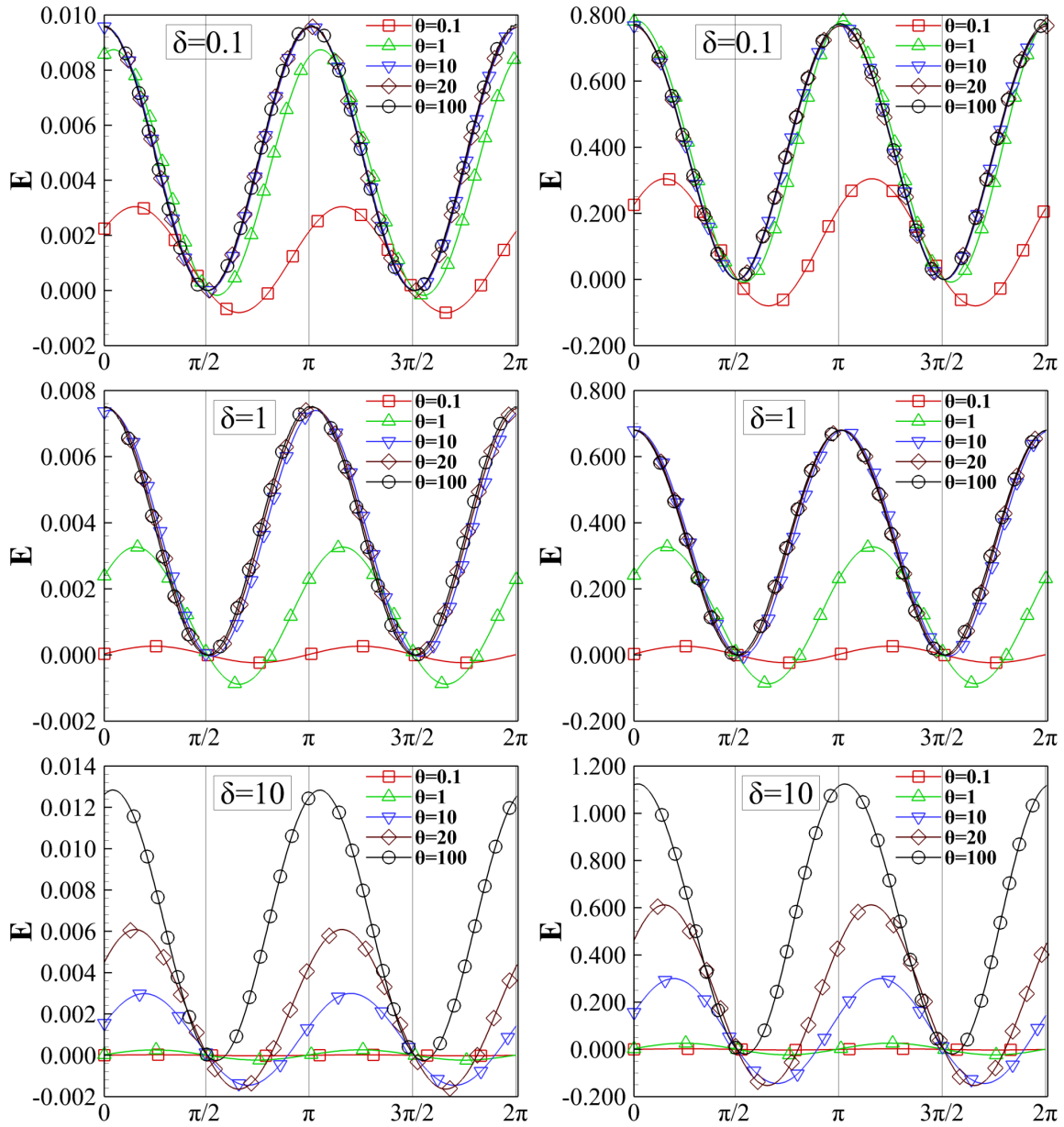
Figure 5.12 Pumping power $E(t)$ over one oscillation cycle $t \in [0, 2\pi]$ for various values of δ and θ with $F = 0.05$ (left) and $F = 0.5$ (right).
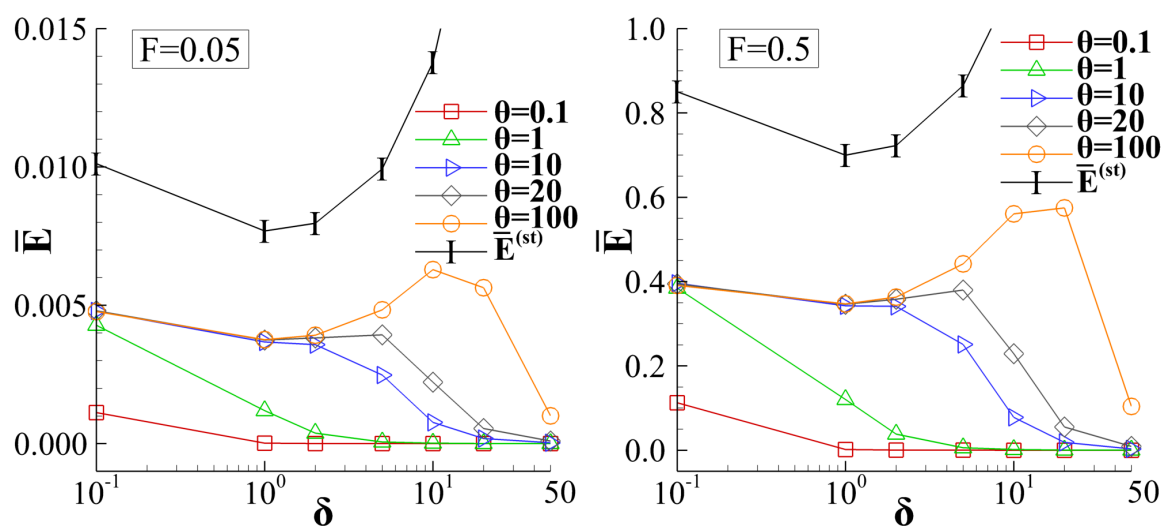
Figure 5.13 Cycle-average pumping power $\bar{E}$ in terms of δ for $F = [0.05, 0.5]$ and $\theta = [0.1, 1, 10, 20, 10^2]$.

131
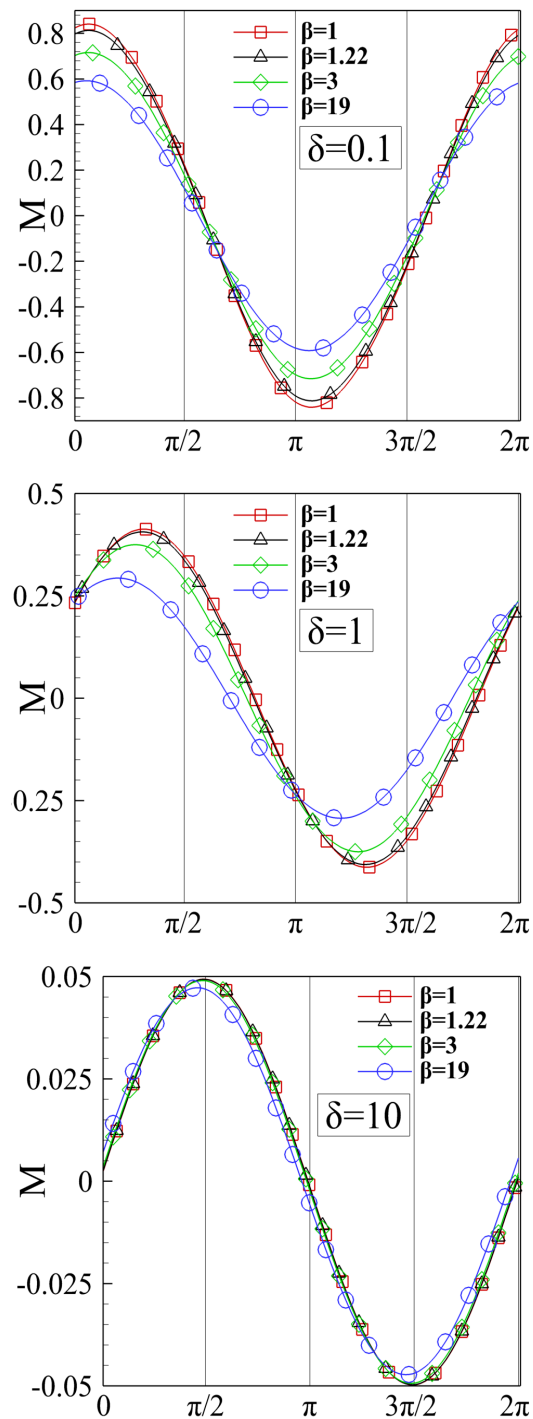
Figure 5.14 Flow rate $M(t)$ (S-model) over one oscillation cycle $t \in [0, 2\pi]$ for $F = 0.5$, $\theta = 1$ and $\beta = [1.22, 3, 19]$ with $\delta = [0.1, 1, 10]$.
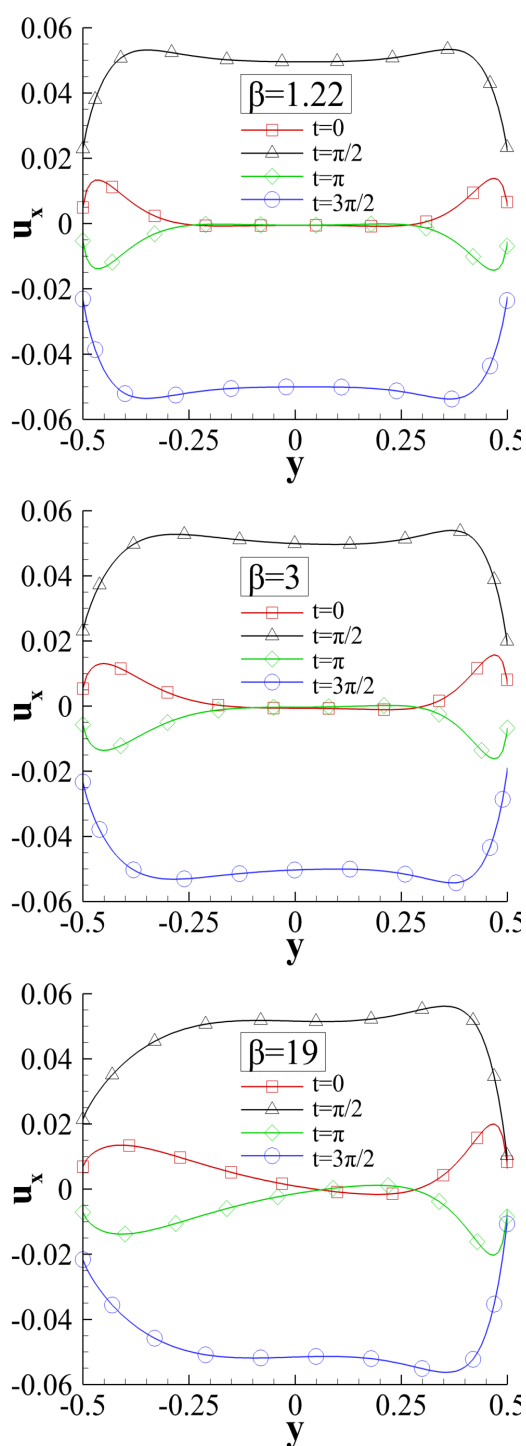
Figure 5.15 Time evolution of velocity $u_x\left(y,t\right)$ (S-model) at certain time steps $t \in [0, 2\pi]$ for $F = 0.5$, $\theta = 1$ and $\beta = [1.22, 3, 19]$ with $\delta = 10$.

133
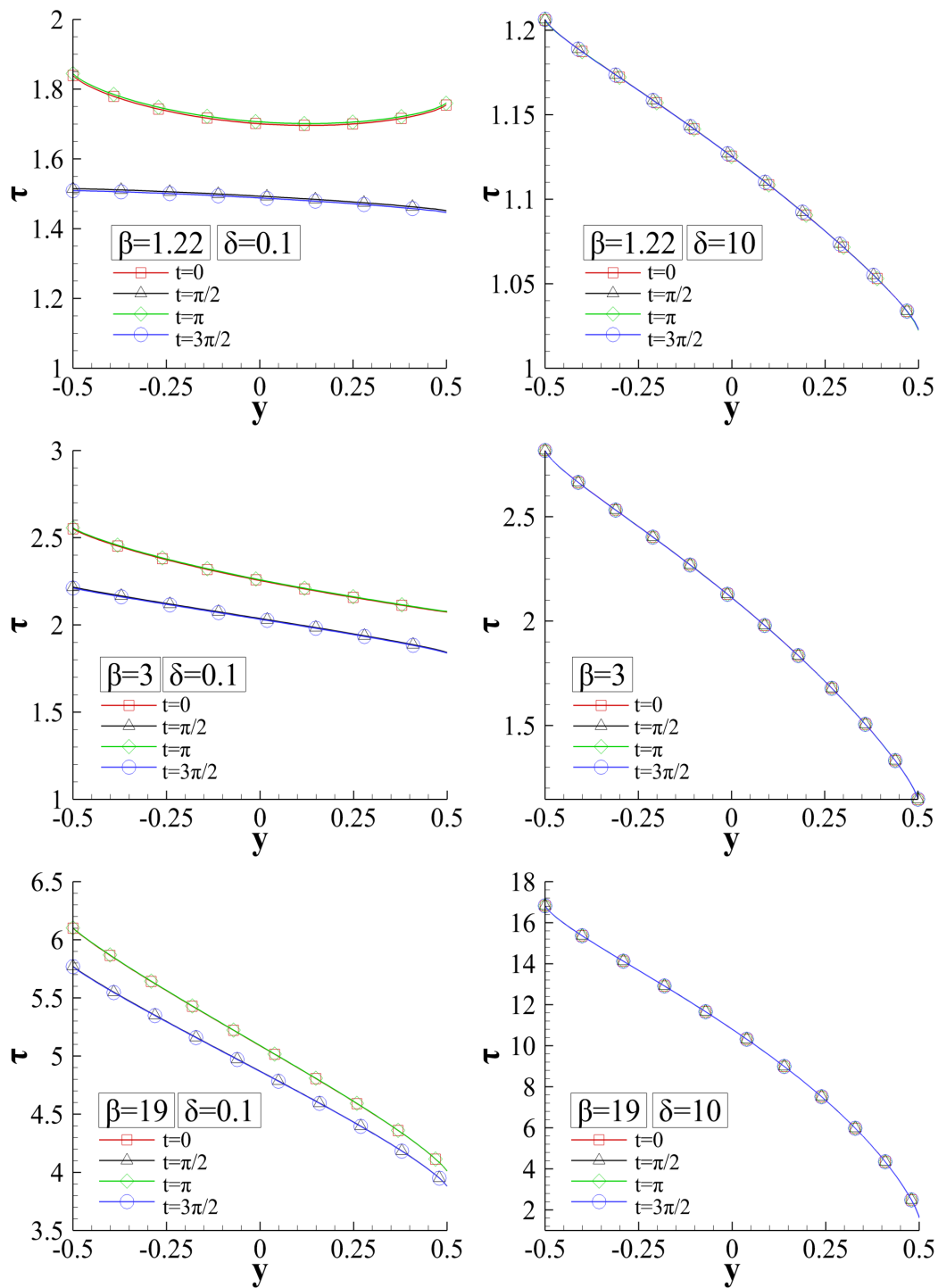
Figure 5.16 Time evolution of temperature $\tau\left(y, t\right)$ (S-model) at certain time steps $t \in [0, 2\pi]$ for $F = 0.5$, $\theta = 1$ and $\beta = [1.22, 3, 19]$ with $\delta = 0.1$ (left) and $\delta = 10$ (right).

134
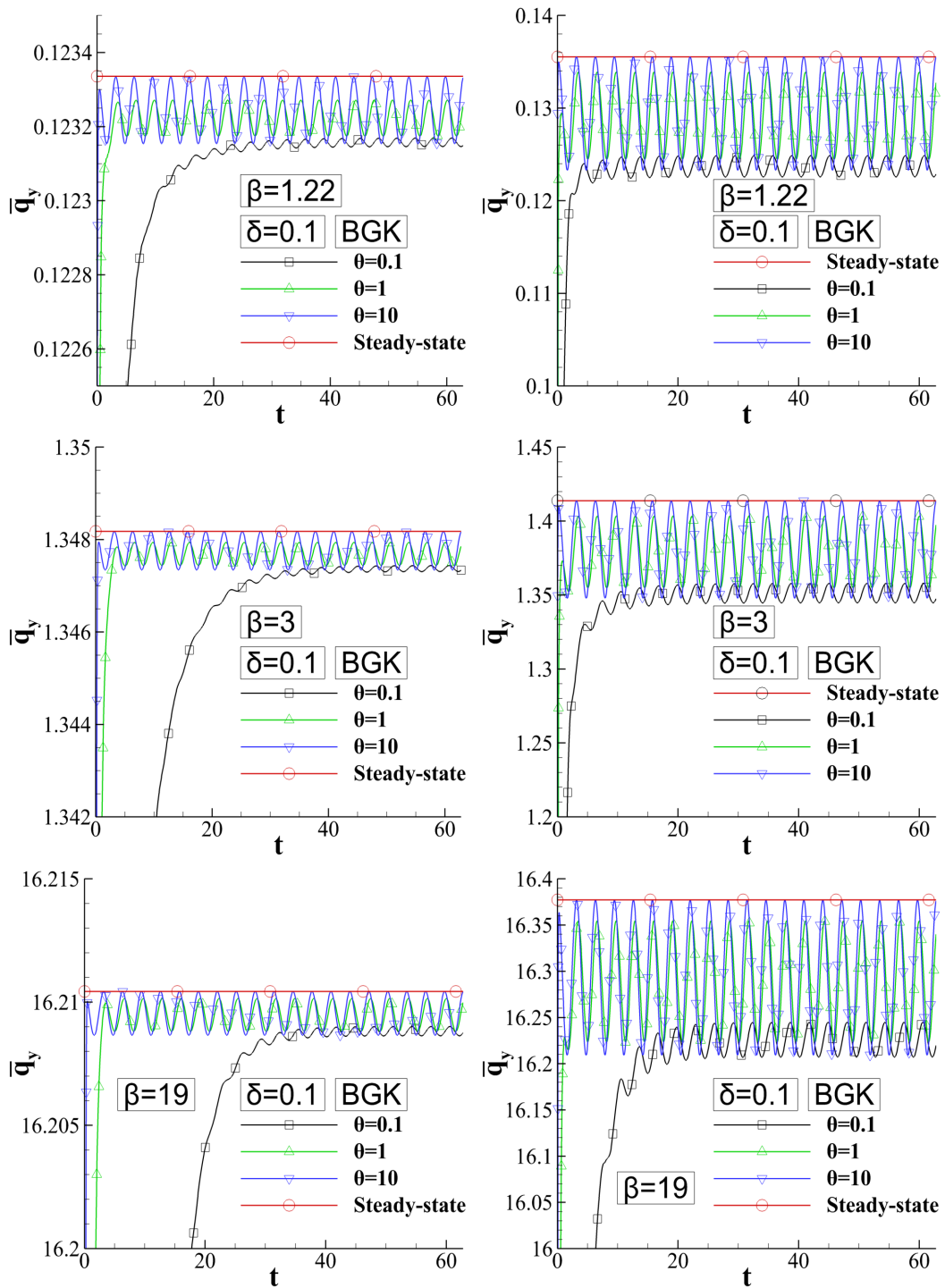
Figure 5.17 Space average heat flow $\bar{q}_y(t)$ over time t for $\beta = [1.22, 3, 19]$, $\delta = 0.1$ and $\theta = [0.1, 1, 10]$ with $F = 0.05$ (left) and $F = 0.5$ (right).

135
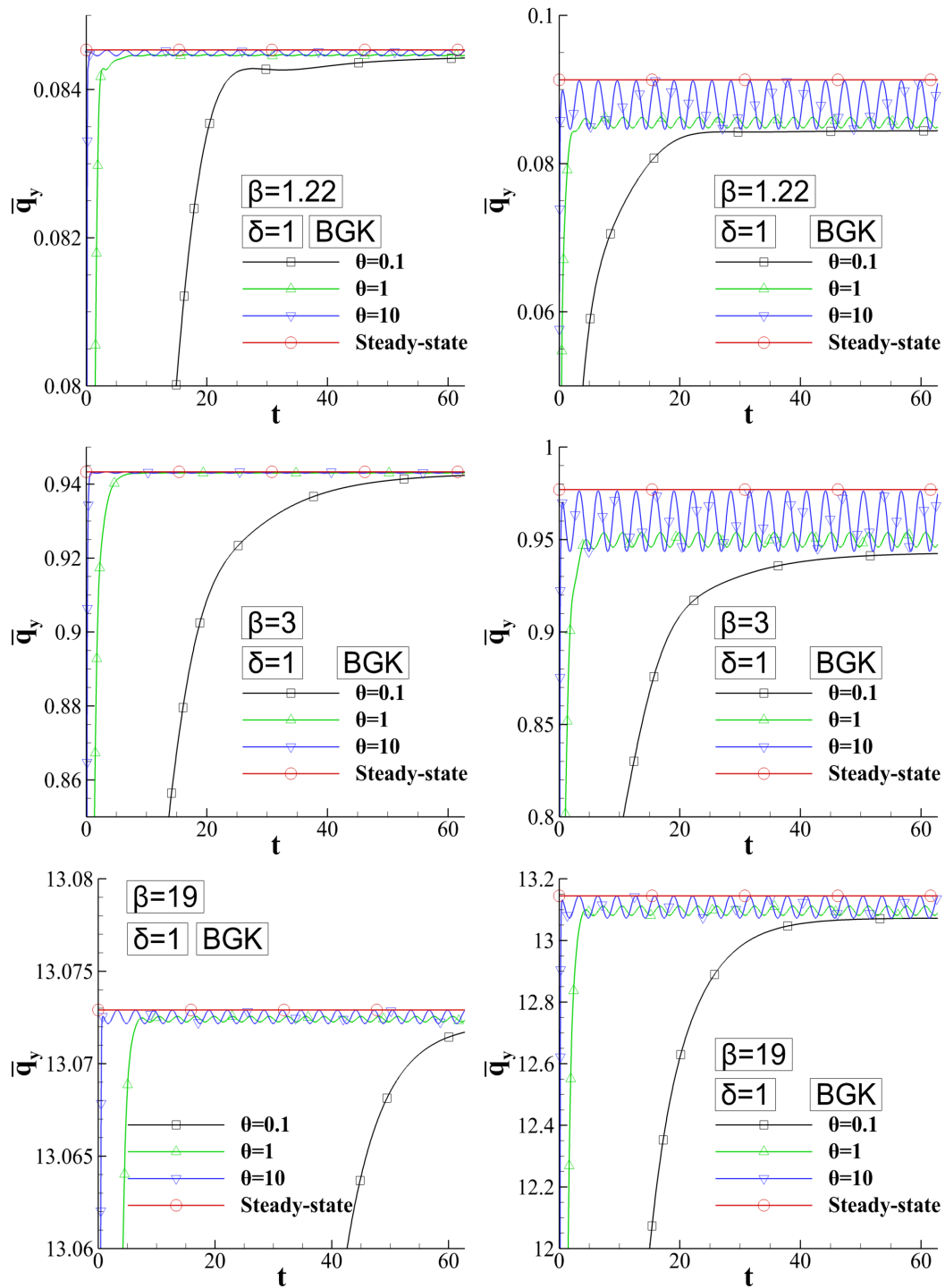
Figure 5.18 Space average heat flow $\bar{q}_y(t)$ over time t for $\beta = [1.22, 3, 19]$, $\delta = 1$ and $\theta = [0.1, 1, 10]$ with $F = 0.05$ (left) and $F = 0.5$ (right).

136
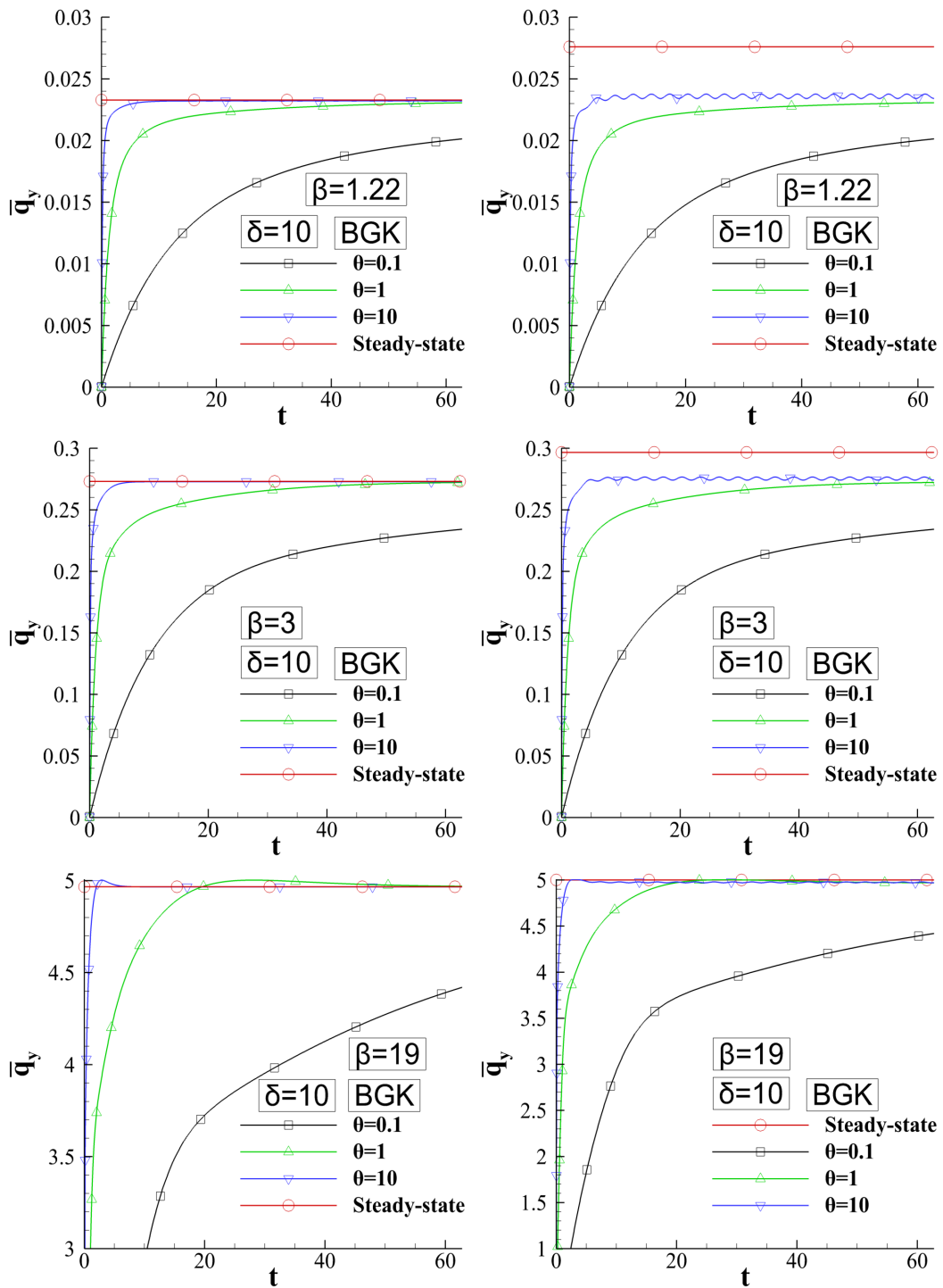
Figure 5.19 Space average heat flow $\bar{q}_y(t)$ over time t for $\beta = [1.22, 3, 19]$, $\delta = 10$ and $\theta = [0.1, 1, 10]$ with $F = 0.05$ (left) and $F = 0.5$ (right).
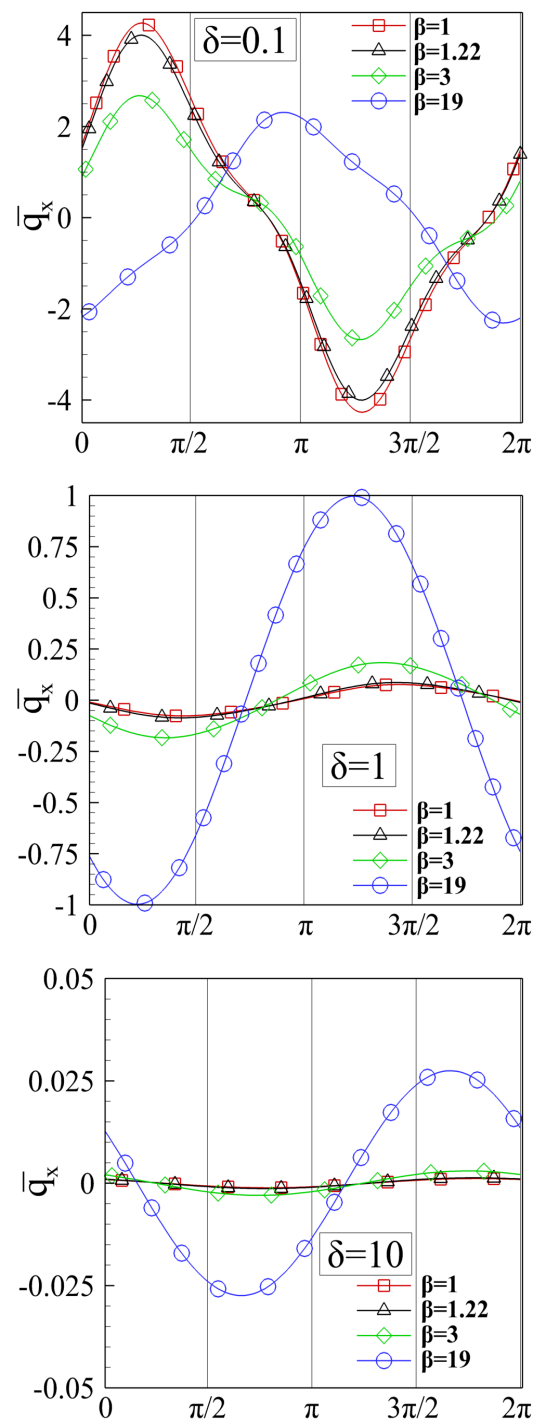
Figure 5.20 Space average heat flow $\bar{q}_x(t)$ (S-model) over time t for $\beta = [1.22, 3, 19]$, $\theta = 1$ and $\delta = [0.1, 1, 10]$ and $F = 0.5$.

138
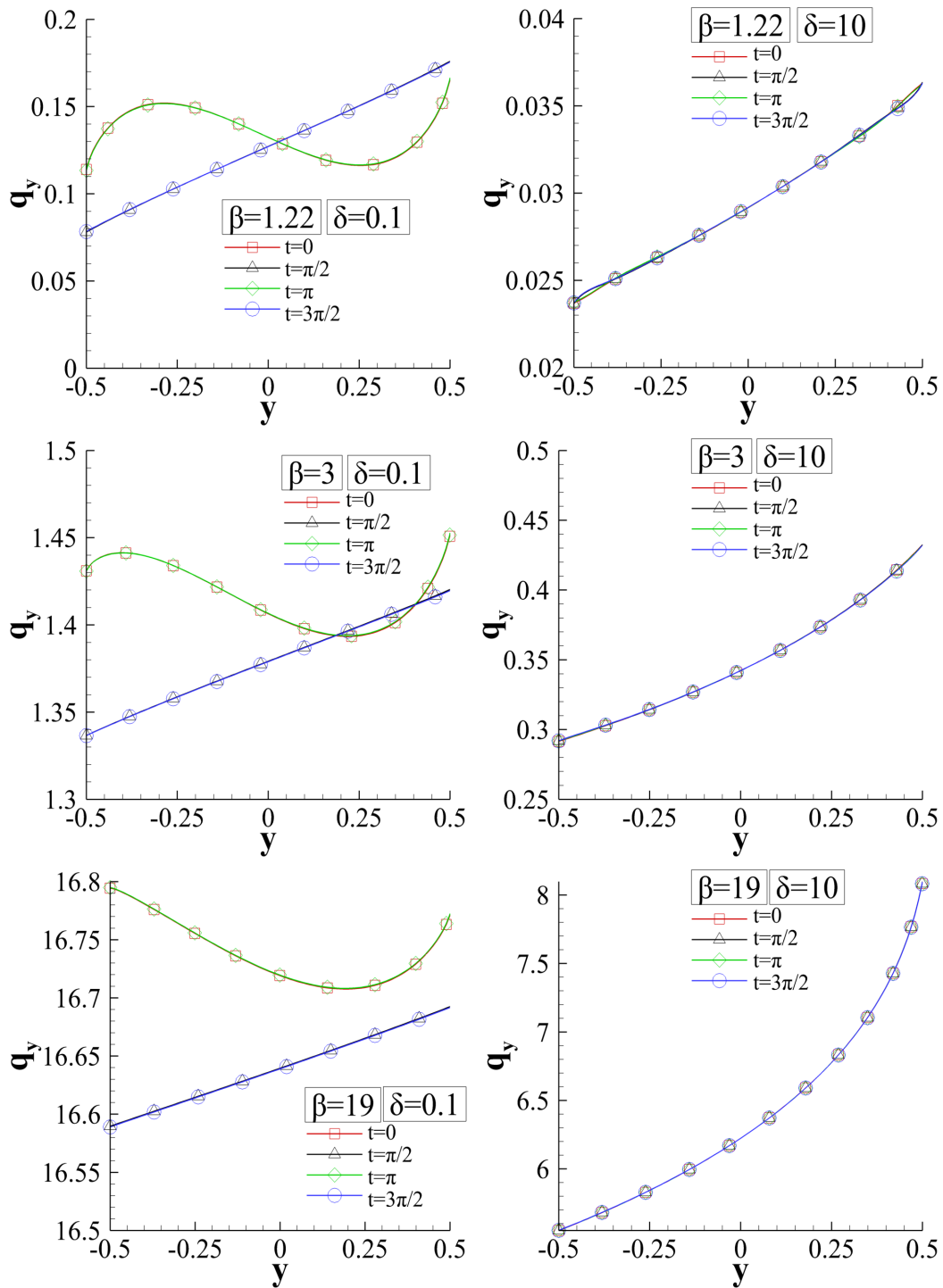
Figure 5.21 Time evolution of normal heat flow $q_y(y, t)$ (S-model) at certain time steps $t \in [0, 2\pi]$ for $F = 0.5$, $\theta = 1$ and $\beta = [1.22, 3, 19]$ with $\delta = 0.1$ (left) and $\delta = 10$ (right).

139
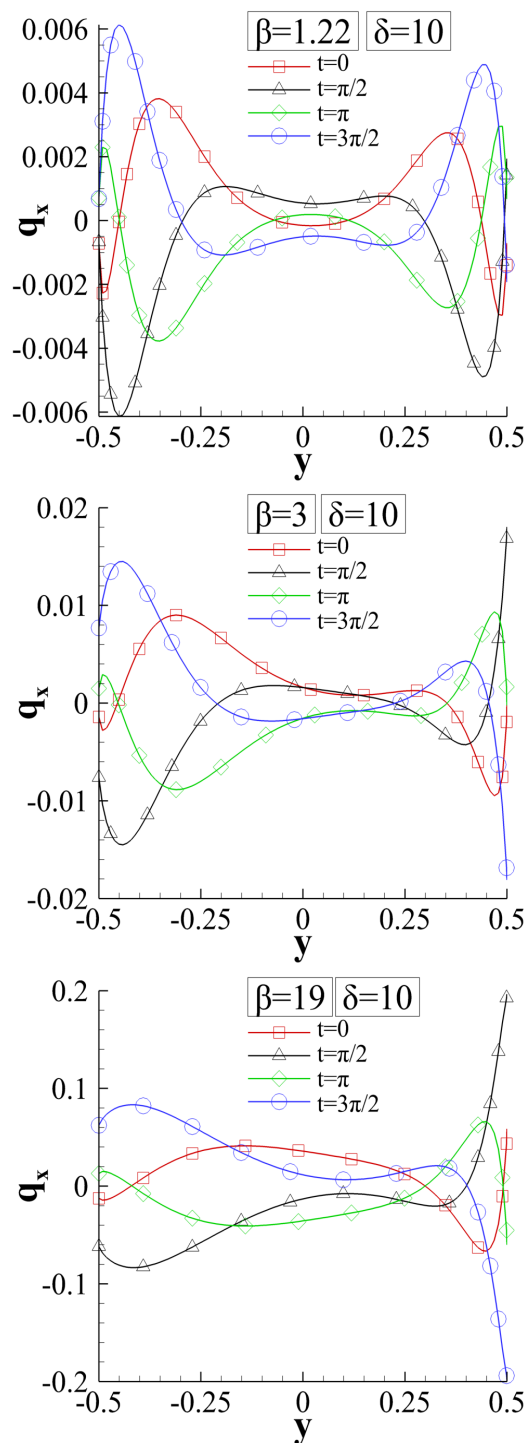
Figure 5.22 Time evolution of axial heat flow $q_x(y,t)$ (S-model) at certain time steps $t \in [0, 2\pi]$ for $F = 0.5$, $\theta = 1$ and $\beta = [1.22, 3, 19]$ with $\delta = 10$.

140

Chapter 6

Oscillatory pressure and molar fraction driven rarefied binary gas mixture flow between parallel plates

6.1 Introduction

In several flow configurations it is possible that a gas mixture is found instead of a single gas. Even though modelling of monoatomic gases is always needed, it is also beneficial to investigate gas mixtures. A suitable kinetic model for this type of flows is the well-known McCormack collision model. It is noted that the McCormack model is used only in the linearized framework where the speed of the flow is small compared to the characteristic molecular velocity. Moreover, rarefied oscillatory gas mixture flows encountered in enclosures, driven by moving boundaries oscillating parallel or vertical to the main flow have already been reported in Section 2.6. On the other hand, the oscillatory pressure-and molar fraction driven binary gas mixture flows haven't been investigated.

In this context, the Chapter is devoted to the kinetic solution of the rarefied oscillatory binary gas mixture flow between parallel plates due to harmonically either oscillating pressure gradient or molar fraction gradient, imposed parallel to the plates. Modeling is based on the time-dependent linearized McCormack kinetic model equation subject to diffuse boundary conditions via the discrete velocity method. The

141

investigation is focused on the effect of the molecular mass ratio of the components of the mixture and of its molar fraction on the oscillatory behavior of the velocity distribution, the kinetic coefficients, the wall shear stress and the pumping power of the species (only for the pressure-driven flow) and of the mixture, in a wide range of the gas rarefaction and the oscillation frequency. Specific attention is also given to the effect of the oscillation frequency on gas separation, which, as it is well-known, is contributed to the different molecular velocities of the light and heavy species of the mixture [192–194]. Due to its technological interest, gas separation has attracted considerable attention in previous investigations concerning steady-state binary gas mixture flow through long and short capillaries [195, 48, 49, 196–198], time-dependent binary gas mixture expansion through short tubes into vacuum [199, 200] and in microchannels with oscillating barriers [201] and moving walls [202] in the free molecular regime.

The Chapter is structured as follows: In Section 6.2, the flow configuration is described and all input and output quantities, including the dimensionless parameters characterizing the flow, are prescribed. In Section 6.3, the kinetic formulation and the implemented numerical scheme are presented. The numerical results are presented and discussed in Section 6.4, which is divided for clarity purposes into four subsections. The concluding remarks are outlined in Section 6.5.

6.2   Flow configuration

Consider the rarefied oscillatory fully-developed isothermal binary gas mixture flow between two infinite long parallel plates. The flow is in the $x'-$direction parallel to the plates, which are fixed at $y' = \pm H/2$. At some arbitrary fixed position along the plates, the flow is caused by either an externally imposed harmonically oscillating pressure gradient of the form

$$\frac{d\tilde{P}}{dx'} = \text{R}\left[\frac{dP}{dx'}\exp\left(-i\omega t'\right)\right], \tag{6.1}$$

or an harmonically oscillating molar fraction gradient of the form

$$\frac{d\tilde{C}}{dx'} = \text{R}\left[\frac{dC}{dx'}\exp\left(-i\omega t'\right)\right], \tag{6.2}$$

where R denotes the real part of a complex expression, $i = \sqrt{-1}$, t' is the time independent variable, ω is the oscillation (cyclic) frequency and dP/dx' and dC/dx' denote the amplitude of the oscillating pressure and molar fraction gradient respectively.

The binary gas mixture consists of two monoatomic species of molecular masses m_α, with the index "$\alpha = 1, 2$", always referring, without loss of generality, to the light and heavy species of the mixture respectively. The corresponding local number densities of the mixture components, defined by $\tilde{n}_\alpha(t')$, oscillate harmonically as

$$\tilde{n}_\alpha(t') = \mathrm{R}\left[n_\alpha \exp\left(-i\omega t'\right)\right], \tag{6.3}$$

where n_α, $a = 1, 2$ is the local amplitude of the oscillating number density of each species. The number density of the mixture is $\tilde{n}(t') = \tilde{n}_1(t') + \tilde{n}_2(t')$, while the molar fraction of the mixture is the ratio of the number density of the light species over the mixture number density, given by

$$\tilde{C}(t') = \mathrm{R}\left[C \exp\left(-i\omega t'\right)\right], \tag{6.4}$$

with

$$C = \frac{n_1}{n} = \frac{n_1}{n_1 + n_2} \tag{6.5}$$

being the local amplitude of the molar fraction. The molar fraction amplitude of the heavy species is $1 - C$. The mean molecular mass of the mixture is given by $m = Cm_1 + (1 - C)m_2$. The number densities of the species and the mixture are related to the corresponding pressures with the equation of states as $\tilde{P}_\alpha = \tilde{n}_\alpha kT$ and $\tilde{P}_\alpha = \tilde{n}_\alpha kT$ respectively, where $\tilde{P}_\alpha$ are the partial pressures, $\tilde{P} = \tilde{P}_1 + \tilde{P}_2$ is the total pressure, T is the reference temperature and k is the Boltzmann constant. The mass densities of the species and the mixture are defined as $\rho_\alpha = m_\alpha n_\alpha$ and $\rho = mn$ respectively.

Then, the deduced time-dependent flow quantities of practical interest include the bulk velocity $\tilde{U}_{a,i}(t', y')$, shear stress $\tilde{\Pi}_{a,i}(t', y')$ and heat flow $\tilde{Q}_{a,i}(t', y')$ of the two species $\alpha = 1, 2$, which depend on y', the space independent variable vertical to the plates and vary harmonically with time t' as

$$\tilde{Z}_{a,i}(t, y) = \mathrm{R}\left[Z_{a,i}(y) \exp\left(-i\omega t'\right)\right] \tag{6.6}$$

where $\tilde{Z}_{a,i}(t, y) = \left[\tilde{U}_{a,i}(t, y), \tilde{\Pi}_{a,i}(t, y), \tilde{Q}_{a,i}(t, y)\right]$, while $Z_{a,i}(y) = \left[U_{a,i}(y), \Pi_{a,i}(y), Q_{a,i}(y)\right]$ is a vector of the corresponding complex functions. Also, the subscripts $i = P$ and $i = C$ denote the flow due to the pressure and molar fraction gradient respectively. By combining $U_{a,i}(y)$ and $\Pi_{a,i}(y)$ the hydrodynamic velocity and shear stress of the gas

mixture are obtained as

$$U_i(y) = \frac{1}{\rho}\left[\rho_1 U_{1,i}(y) + \rho_2 U_{2,i}(y)\right] = \frac{m_1}{m}C U_{1,i}(y) + \frac{m_2}{m}(1-C)U_{2,i}(y) \qquad (6.7)$$

and

$$\Pi_i(y) = \frac{1}{n}\left[n_1 \Pi_{1,i}(y) + n_2 \Pi_{2,i}(y)\right] = C\Pi_{1,i}(y) + (1-C)\Pi_{2,i}(y) \qquad (6.8)$$

respectively. The shear stress at the wall is denoted by Π_W.

In addition, of major theoretical and technological importance are the deduced oscillatory particle flow rates of the two species

$$\tilde{J}'_{a,i}(t') = \mathrm{R}\left[J'_{a,i}\exp(-i\omega t')\right], \qquad (6.9)$$

where $J_{a,i}$ are complex functions, given by

$$J'_{a,i} = n_\alpha \int_{-H/2}^{H/2} U_{a,i}\, dy', \qquad (6.10)$$

as well as the corresponding mixture particle flow rate

$$\tilde{J}'_i = \tilde{J}'_{1,i} + \tilde{J}'_{2,i} \qquad (6.11)$$

and the molar fraction flow rate

$$\tilde{J}'_i = n_1 \int_{-H/2}^{H/2}\left(\tilde{U}_{1,i} - \tilde{U}_{2,i}\right) dy' \qquad (6.12)$$

Another overall quantity of practical interest is the pumping power needed to drive the oscillatory mixture flow, given by the product of the acting pressure force times the average hydrodynamic velocity of the mixture $\bar{U}'^{(P)}(t')$ over the cross section, written as [128, 72]

$$\tilde{E}'(t') = Hd\tilde{P}(t')\bar{U}'_{(P)}(t') = HdP\cos(\omega t')\,\mathrm{R}\left[\bar{U}_{(P)}\exp(-i\omega t')\right], \qquad (6.13)$$

where $\bar{U}_P{}' = \int_{-H/2}^{H/2} U_P\, dy'$. It is noted that the pumping power is applied only in the pressure driven oscillatory flow. The particle flow rates and the pumping power are given in particles per second per meter and in Watt per meter respectively.

Furthermore, based on the average hydrodynamic velocity and the wall shear stress of the mixture, the inertia (or acceleration) and viscous forces respectively, acting on a

144

fluid element may be defined. At any time over a cycle, the net sum of these two forces, which may add or subtract to each other at different times within the oscillatory cycle, must be equal to the pressure force driving the oscillatory flow. The detailed analysis is presented in Appendix B.2, where the time-dependent force balance expression (B.18), to be used for benchmarking purposes, is derived.

At this stage it is convenient to introduce the dimensionless independent variables

$$x = x'/H, y = y'/H, t = t'\omega, \tag{6.14}$$

the dimensionless amplitude of the local pressure gradient as well as of the local molar fraction gradient

$$X_P = \frac{H}{P}\frac{dP}{dx'} = \frac{1}{P}\frac{dP}{dx} << 1, \quad X_C = \frac{H}{C}\frac{dC}{dx'} = \frac{1}{C}\frac{dC}{dx} << 1 \tag{6.15}$$

and the characteristic speed of the mixture $v = \sqrt{2kT/m}$. The condition of both $X_P << 1$ and $X_C << 1$ is due to the fully developed flow assumption. Then, the bulk velocity, shear stress and heat flow in Eq. (6.6) are non-dimensionalized by (v), $(2P)$ and (vP) respectively to yield:

$$\tilde{u}_{a,i}(t,y) = \mathrm{R}\left[u_{a,i}(y)\exp(-it)\right] =$$

$$= \mathrm{R}\left[u_{\alpha,i}^{(A)}(y)\exp\left[i\left(u_{a,i}^{(P)}(y) - t\right)\right]\right] = u_{\alpha,i}^{(A)}(y)\cos\left[t - u_{a,i}^{(P)}(y)\right] \tag{6.16}$$

$$\tilde{\varpi}_{a,i}(t,y) = \mathrm{R}\left[\varpi_{a,i}(y)\exp(-it)\right] =$$

$$= \mathrm{R}\left[\varpi_{\alpha,i}^{(A)}(y)\exp\left[i\left(\varpi_{a,i}^{(P)}(y) - t\right)\right]\right] = \varpi_{\alpha,i}^{(A)}(y)\cos\left[t - \varpi_{a,i}^{(P)}(y)\right] \tag{6.17}$$

$$\tilde{q}_{a,i}(t,y) = \mathrm{R}\left[q_{a,i}(y)\exp(-it)\right] =$$

$$= \mathrm{R}\left[q_{\alpha,i}^{(A)}(y)\exp\left[i\left(q_{\alpha,i}^{(P)}(y) - t\right)\right]\right] = q_{\alpha,i}^{(A)}(y)\cos\left[t - q_{\alpha,i}^{(P)}(y)\right] \tag{6.18}$$

In Eqs. (6.16)-(6.18) the superscripts (A) and (P) refer to the amplitude and the phase angle respectively of each complex quantity while the subscripts $i = P$ and $i = C$ denote the flow due to the pressure and molar fraction gradient respectively. Obviously, the dimensionless time-dependent bulk velocity $\tilde{u}_{a,i}(t,y)$, shear stress $\tilde{\varpi}_{a,i}(t,y)$ and heat flow $\tilde{q}_{a,i}(t,y)$ of the two species are not necessarily in phase to each other and more importantly to either the oscillating pressure gradient in Eq. (6.1) or the oscillating molar fraction gradient in (6.2). The dimensionless velocity and shear stress of the mixture (see Eqs. (6.7) and (6.8)) are denoted by $u_i(y)$ and $\varpi_i(y)$ respectively.

Furthermore, the flow rates in Eqs. (6.9) and (6.10) are non-dimensionalized by $(PH/m\upsilon)$ to obtain the dimensionless oscillatory particle flow rates of each species

$$\tilde{G}_{a,i}\left(t'\right) = \mathrm{R}\left[G_{a,i}\exp\left(-it\right)\right] = \mathrm{R}\left[G_{\alpha,i}^{(A)}\exp\left[i\left(G_{\alpha,i}^{(P)} - t\right)\right]\right] = G_{\alpha,i}^{(A)}\cos\left[t - G_{\alpha,i}^{(P)}\right],$$
(6.19)

where

$$G_{a,i} = G_{\alpha,i}^{(A)}\exp\left(iG_{\alpha,i}^{(P)}\right) = 2\int_{-1/2}^{1/2}u_{a,i}dy.$$
(6.20)

In order to study the dimensionless flow rates of the mixture, it is necessary to introduce the so-called kinetic coefficients which are given in [48]. They are non-dimensionalized by $(PH/m\upsilon)$ and the dimensionless kinetic coefficients $\tilde{\Lambda}_{PP}$, $\tilde{\Lambda}_{CP}$, $\tilde{\Lambda}_{PC}$ and $\tilde{\Lambda}_{CC}$ are written as

$$\tilde{\Lambda}_{Pi}\left(t\right) = \mathrm{R}\left[\Lambda_{Pi}\exp\left(-it\right)\right] = \Lambda_{Pi}^{(A)}\cos\left[t - \Lambda_{Pi}^{(P)}\right],$$
(6.21)

$$\tilde{\Lambda}_{Ci}\left(t\right) = \mathrm{R}\left[\Lambda_{Ci}\exp\left(-it\right)\right] = \Lambda_{Ci}^{(A)}\cos\left[t - \Lambda_{Ci}^{(P)}\right],$$
(6.22)

where $i = P, C$ (with P denoting the flow due to pressure gradient and C the flow due to molar fraction gradient) and the superscripts (A) and (P), always referring to amplitudes and phase angles respectively. The complex dimensionless kinetic coefficients Λ_{Pi} and Λ_{Ci} are given by

$$\Lambda_{Pi} = CG_{1,i} + (1 - C)G_{2,i},$$
(6.23)

$$\Lambda_{Ci} = C\left(G_{1,i} - G_{2,i}\right).$$
(6.24)

It is also noted that the cross kinetic coefficients are identical $(\tilde{\Lambda}_{CP} = \tilde{\Lambda}_{PC})$ via the Onsager-Casimir equations [203]. In addition, the pumping power in Eq. (6.13) is non-dimensionalized by $(\upsilon H X_P P)$ to find the dimensionless oscillatory pumping power

$$\tilde{E}\left(t\right) = dx\cos\left(t\right)\mathrm{R}\left[\bar{u}_P\exp\left(-it\right)\right] = \frac{1}{2}dx\cos\left(t\right)\mathrm{R}\left[\left[\frac{m_1}{m}CG_{1,P} + \frac{m_2}{m}\left(1 - C\right)G_{2,P}\right]\exp\left(-it\right)\right].$$
(6.25)

Here, the dimensionless mean velocity has been substituted by the dimensionless flow rate, since it is readily seen that $G_{\alpha i} = 2\bar{u}_{\alpha i}$. By integrating Eq. (6.25) over one oscillation cycle, the average pumping power over the cycle is derived as

$$\bar{E} = \frac{1}{2\pi}\int_0^{2\pi}\tilde{E}\left(t\right)dt = \frac{1}{4}dx\left[\frac{m_1}{m}CG_{1,P}^{(A)}\cos G_{1,P}^{(P)} + \frac{m_2}{m}\left(1 - C\right)G_{2,P}^{(A)}\cos G_{2,P}^{(P)}\right].$$
(6.26)

It is pointed out that although the net flow rate over one cycle is zero, a nonzero cycle-average pumping power is required to maintain the oscillatory flow. In the low frequency regime, where the imaginary part of all macroscopic quantities is gradually diminished and the phase angles tend to zero the steady-state solution is approached.

The objectives of the present Chapter include the computation of the macroscopic distributions of the velocity and shear stress in Eqs. (6.16) and (6.17), the particle flow rates of the species and the kinetic coefficients of the mixture in Eqs. (6.19)-(6.24) and the pumping powers in Eqs. (6.25) and (6.26), in terms of the parameters characterizing the flow. As in the case of oscillatory single gas flow, the oscillatory binary gas mixture flow between parallel plates is also characterized by the gas rarefaction and oscillation parameters. The gas rarefaction parameter is proportional to the inverse Knudsen number, defined as

$$\delta = \frac{PH}{\upsilon\mu},\tag{6.27}$$

where P is a reference pressure, H is the distance between the plates, υ is the characteristic speed of the mixture and μ is the viscosity coefficient of the mixture at reference temperature T. The oscillation parameter is the ratio of the intermolecular collision frequency defined as $\nu = P/\mu$ over the oscillation frequency ω, given by

$$\theta = \frac{P}{\mu\omega}.\tag{6.28}$$

The steady-state conditions are reached as $\theta \to \infty$ ($\omega \to 0$). In addition to δ and θ, the composition of the binary gas mixture, i.e., the molecular masses m_1 and m_2 of the two monoatomic components, as well as the amplitude of the molar fraction C, must be specified.

Once the parameters δ, θ, m_1, m_2 and C are defined, the input data are complete and the flow behavior and characteristics for any binary gas mixture in the whole range of the gas rarefaction and oscillation frequencies may be investigated. The solution is obtained based on the infinite capillary theory via linear kinetic modeling described in the next section.

6.3 Kinetic formulation and modeling

The steady-state fully-developed binary gas mixture flow between parallel plates, driven by pressure, temperature and molar fraction gradients, in the whole range of

gas rarefaction, has been considered in [48]. Modeling has been based on McCormack kinetic model [44], which has been proven to be a very reliable model, fulfilling all associated requirements (satisfies the conservation laws, the H-theorem and provides correct values for all transport coefficients). Here, the work follows the formulation in [48] related only to the pressure and molar fraction gradient part and it is accordingly extended to include the oscillatory flow behavior.

Due to the condition of small local gradients ($X_P \ll 1$ and $X_C \ll 1$) the unknown time-dependent distribution function of each species can be linearized in a standard manner as

$$f_\alpha (t, x, y, c_\alpha) = f_\alpha^0 (c_\alpha) \left[1 + \tilde{h}_\alpha (t, y, c_\alpha) \right], \tag{6.29}$$

where

$$f_\alpha^0 (c_\alpha) = n_\alpha \left(\frac{m}{2\pi kT} \right)^{3/2} \exp \left[-c_\alpha^2 \right] \tag{6.30}$$

is the absolute Maxwellian of each species, $\tilde{h}_\alpha (t, y, c_\alpha)$ are the unknown perturbed distribution functions and $c_\alpha = [c_{\alpha x}, c_{\alpha y}, c_{\alpha z}]$ is the dimensionless molecular velocity vector, with $\alpha = 1, 2$ always denoting the light and heavy species respectively. Furthermore, taking advantage of the harmonic motion, the complex distribution function $h_\alpha (y, c_\alpha)$ is also introduced so that

$$\tilde{h}_\alpha (t, y, c_\alpha) = \mathrm{R} \left[h_\alpha (y, c_\alpha) \exp (-it) \right]. \tag{6.31}$$

Based on Eqs. (6.29) and (6.31), the problem under consideration may by formulated in terms of $h_\alpha (y, c_\alpha)$ by the following system of two linearized Boltzmann equations:

$$-i\frac{\delta}{\theta} \sqrt{\frac{m_\alpha}{m}} h_\alpha + c_{\alpha y} \frac{\partial h_\alpha}{\partial y} = \omega_\alpha \sum_{\beta=1}^{2} L_{\alpha\beta} h_\alpha - c_{\alpha x} (X_P + \eta_\alpha X_C), \quad a = 1, 2 \tag{6.32}$$

where $\eta_1 = 1$ and $\eta_2 = -C/ (1 - C)$. In Eq. (6.32), $\omega_\alpha = \delta \left(C/\gamma_1 + (1 - C)/\gamma_2 \right) \sqrt{m_\alpha/m}$, while $L_{\alpha\beta}$ is the linearized McCormack collision term and γ_α $(a = 1, 2)$ are the collision frequencies of each species, both given in detail in Appendix B.1. Comparing Eq. (6.32) with the corresponding steady-state one in [48], it is readily seen that the only difference is the first term at the left hand side of Eq. (6.32) plus the fact that here, the unknown distributions and the associated macroscopic quantities in the collision term are complex. Obviously, as $\theta \to \infty$ ($\omega \to 0$) Eq. (6.32) tends to the steady-state

one. It is also noted that since Eq. (6.32) is linear its solution can be decomposed as

$$h_\alpha = h_{a,P} X_P + h_{a,C} X_C \tag{6.33}$$

and accordingly, the moments of distribution function are written as

$$u_\alpha = u_{a,P} X_P + u_{a,C} X_C, \, q_\alpha = q_{a,P} X_P + q_{a,C} X_C, \, \varpi_\alpha = \varpi_{a,P} X_P + \varpi_{a,C} X_C. \tag{6.34}$$

As it is well-known, the $z-$ and $x-$components of the molecular velocity vector may be eliminated, greatly reducing the computation effort of solving Eq. (6.32), by applying the so-called projection procedure and introducing the following reduced distribution functions:

$$\Phi_\alpha \left(y, c_{ay} \right) = \frac{1}{\pi} \sqrt{\frac{m}{m_\alpha}} \int_{-\infty}^{\infty} \int_{-\infty}^{\infty} h_\alpha \left(y, c_\alpha \right) c_{ax} \exp \left[-c_{ax}{}^2 - c_{az}{}^2 \right] dc_{ax} dc_{az}, \tag{6.35}$$

$$\Psi_\alpha \left(y, c_{ay} \right) = \frac{1}{\pi} \sqrt{\frac{m}{m_\alpha}} \int_{-\infty}^{\infty} \int_{-\infty}^{\infty} h_\alpha \left(y, c_\alpha \right) c_{ax} \left(c_{ax}^2 + c_{az}^2 - 2 \right) \exp \left[-c_{ax}^2 - c_{az}^2 \right] dc_{ax} dc_{az}. \tag{6.36}$$

Then, Eq. (6.32) is multiplied successively by the functions $\sqrt{m/m_\alpha} c_{ax} \exp \left(-c_{ax}^2 - c_{az}^2 \right)/\pi$ and $\sqrt{m/m_\alpha} c_{ax} \left(c_{ax}^2 + c_{az}^2 - 2 \right) \exp \left(-c_{ax}^2 - c_{az}^2 \right)/\pi$ and the resulting equations are integrated over c_{ax} and c_{az} to deduce the following four coupled equations for the four unknown reduced complex distribution functions:

$$-i \frac{\delta}{\theta} \sqrt{\frac{m_\alpha}{m}} \Phi_\alpha + c_{\alpha y} \frac{\partial \Phi_\alpha}{\partial y} + \omega_\alpha \gamma_\alpha \Phi_\alpha =$$

$$-\frac{1}{2} \sqrt{\frac{m}{m_\alpha}} \left(X_P + \eta_\alpha X_C \right) + \omega_\alpha \left\{ \gamma_\alpha u_\alpha - v_{\alpha\beta}^{(1)} \left(u_\alpha - u_\beta \right) - \frac{1}{2} v_{\alpha\beta}^{(2)} \left(q_\alpha - \frac{m_\alpha}{m_\beta} q_\beta \right) + \right.$$

$$+ 2 \sqrt{\frac{m}{m_\alpha}} \left[\left(\gamma_\alpha - v_{\alpha\alpha}^{(3)} + v_{\alpha\alpha}^{(4)} - v_{\alpha\beta}^{(3)} \right) \varpi_\alpha + v_{\alpha\alpha}^{(4)} \varpi_\beta \right] c_{ay} +$$

$$+ \frac{2}{5} \left[\left(\gamma_\alpha - v_{\alpha\alpha}^{(5)} + v_{\alpha\alpha}^{(6)} - v_{\alpha\beta}^{(5)} \right) q_\alpha + v_{\alpha\beta}^{(6)} \sqrt{\frac{m_\beta}{m_\alpha}} q_\beta - \frac{5}{4} v_{\alpha\beta}^{(2)} \left(u_\alpha - u_\beta \right) \right] \left(c_{ay}^2 - \frac{1}{2} \right) \right\} \tag{6.37}$$

$$-i \sqrt{\frac{m_\alpha}{m}} \frac{\delta}{\theta} \Psi_\alpha + c_{\alpha y} \frac{\partial \Psi_\alpha}{\partial y} + \omega_\alpha \gamma_\alpha \Psi_\alpha =$$

$$\frac{4}{5} \omega_\alpha \left[\left(\gamma_\alpha - v_{\alpha\alpha}^{(5)} + v_{\alpha\alpha}^{(6)} - v_{\alpha\beta}^{(5)} \right) q_\alpha + v_{\alpha\beta}^{(6)} \sqrt{\frac{m_\beta}{m_\alpha}} q_\beta - \frac{5}{4} v_{\alpha\beta}^{(2)} \left(u_\alpha - u_\beta \right) \right] \tag{6.38}$$

149

In Eqs. (6.37) and (6.38) $\alpha, \beta = 1, 2$, with $\alpha \neq \beta$, while the expressions for the quantities $v_{\alpha\beta}^{(k)}$ are given in terms of the Chapman-Cowling integrals [25]. The macroscopic quantities u_α, ϖ_α and q_α at the right hand side of Eqs. (6.37) and (6.38) are defined in Eqs. (6.16), (6.17), (6.18) and (6.34) respectively and after applying the linearization and projection procedures, they are obtained as moments of Φ_α and Ψ_α as follows:

$$u_\alpha (y) = \frac{1}{\sqrt{\pi}} \int_{-\infty}^{\infty} \Phi_\alpha \exp\left(-c_{ay}^2\right) dc_{ay}, \tag{6.39}$$

$$\varpi_\alpha (y) = \frac{1}{\sqrt{\pi}} \sqrt{\frac{m_\alpha}{m}} \int_{-\infty}^{\infty} \Phi_\alpha c_{ay} \exp\left(-c_{ay}^2\right) dc_{ay}, \tag{6.40}$$

$$q_\alpha (y) = \frac{1}{\sqrt{\pi}} \int_{-\infty}^{\infty} \left[\Psi_\alpha + \left(c_{ay}^2 - \frac{1}{2}\right) \Phi_\alpha\right] \exp\left(-c_{ay}^2\right) dc_{ay}. \tag{6.41}$$

In the present work purely diffuse reflection at the walls is assumed. It is readily deduced that the outgoing reduced distribution functions at the two walls are identically equal to zero, i.e.

$$\Phi_\alpha (\pm 1/2, c_{\alpha y}) = \Psi_\alpha (\pm 1/2, c_{\alpha y}) = 0, c_{\alpha y} \gtrless 0. \tag{6.42}$$

Thus, the kinetic formulation of the problem is properly defined by the system of Eqs. (6.37) and (6.38), subject to the boundary conditions (6.42), along with the associated moments (6.39)-(6.41).

It is interesting to comment on the behavior of the flow and of Eqs. (6.37) and (6.38) at limiting values of the involved parameters. The flow is in the hydrodynamic regime when both $\delta >> 1$ and $\theta >> 1$. Also, as $\theta \to \infty$, Eqs. (6.37) and (6.38) are reduced to the corresponding ones describing steady-state binary gas flow between parallel plates [48]. At the other end, as $\theta \to 0$, the flow is in the very high oscillation frequency regime, with the amplitude of the distribution functions Φ_α and Ψ_α diminishing due to fluid inertia, while as $\delta \to 0$, with $\theta > 0$, the kinetic equations for steady-state binary gas flow in the free molecular limit are recovered [48]. Furthermore, $C = 0$ or for binary gas mixtures with species having the same molecular mass $m_1 = m_2$, Eqs. (6.37) and (6.38) are reduced to the corresponding ones for oscillatory single gas flow that has been presented in Chapter 4.

The above set of equations is computationally solved based on the discrete velocity method [63] in the c_y-space and on the second-order diamond finite difference scheme [49] in the $y-$space. The continuum spectrum of $c_y \in (-\infty, \infty)$ is properly transferred to $[0, \infty)$ and then, it is replaced by a set of discrete velocities $m = 1, 2, ..., M$, which are

taken to be the roots of the Hermite polynomial of order M, accordingly mapped from $(-\infty, \infty)$ to $[0, \infty)$. The macroscopic distributions are numerically integrated by the Gauss-Hermite quadrature scheme. The specific set of discrete molecular velocities has been found to be very effective in the whole range of gas rarefaction. The discretized equations are solved in an iterative manner between the kinetic equations (6.37) and (6.38) and the moment equations (6.39)-(6.41). Since the computed quantities are complex their real and imaginary parts are obtained. The iteration map is concluded when the following criterion in terms of the bulk velocity and the heat flow of the species is fulfilled:

$$\varepsilon_j^{(\kappa)} = \max_i \left\{ \left| u_{1,j,i}^{(\kappa)} - u_{1,j,i}^{(\kappa-1)} \right| + \left| u_{2,j,i}^{(\kappa)} - u_{2,j,i}^{(\kappa-1)} \right| + \left| q_{1,j,i}^{(\kappa)} - q_{1,j,i}^{(\kappa-1)} \right| + \left| q_{2,j,i}^{(\kappa)} - q_{2,j,i}^{(\kappa-1)} \right| \right\} < \varepsilon \tag{6.43}$$

Here, ε is the tolerance parameter, the superscript (κ) is the iteration index, the subscript $j = \mathrm{R}, \Im$ refers to the real and imaginary part of the macroscopic quantity and the subscript $i = 1, 2, ..., I$ refers to the node number in $y \in [-1/2, 1/2]$. The numerical parameters have been gradually refined to ensure grid independent results up to at least three significant figures with $M = 128$ and $I = 10^4$. The implemented computational scheme has been previously successfully applied to steady-state binary gas mixture and oscillatory single gas flows [48, 49, 197, 127, 128].

Once the real and imaginary part of the macroscopic distributions and of the overall quantities (e.g. flow rates) are obtained, it is straightforward to compute their amplitudes and phase angles, as well as the corresponding time-dependent quantities, presented and discussed in the next section.

6.4 Results and discussion

Computational results of the oscillatory pressure- and molar fraction driven flows are presented in this Section. Results for the pressure-driven velocity distributions and flow rates, the kinetic coefficient $\tilde{\Lambda}_{PP}$ and some complimentary quantities (wall shear stress and pumping power) are presented in Sections 6.5.1, 6.5.2 and 6.5.3 respectively, in a wide range of the gas rarefaction and oscillation parameters δ and θ, as well as of the molar fraction $C \in [0, 1]$ and the molecular mass ratio of the heavy over the light species m_2/m_1. In addition, results for the molar fraction-driven velocity distributions and the kinetic coefficients Λ_{CC} and Λ_{PC} are presented in Section 6.5.4. Although several binary gas mixtures have been considered, the effect of m_2/m_1 is

demonstrated by presenting results mostly for He–Xe, with $m_2/m_1 = 32.8$ and Ne–Ar, with $m_2/m_1 = 1.98$. To better demonstrate the flow characteristics in oscillatory pressure-driven binary gas mixture flow, comparisons between the present results and the corresponding ones for steady-state binary gas flow in [48] and oscillatory single gas flow in Section 4.4.2 (or in [128]) are performed. The accuracy of the computational scheme and the presented results has been accordingly validated by grid refinement, by always fulfilling the benchmark balance expression (B.18) and by systematic comparisons with previous works at limiting values of the involved parameters (e.g. $C = 0$, $\theta \to \infty$, $\delta, \theta \gg 1$). It is noted that the results of the molar fraction-driven flow are compared with the corresponding ones for steady-state binary gas flow in [48]. All results are in dimensionless form.

6.4.1 Pressure-driven velocity distributions

The amplitudes and the phase angle of the complex macroscopic velocity distributions $u_{\alpha,P} = u_{\alpha,P}^{(A)} \exp\left(i u_{\alpha,P}^{(P)}\right)$ of the two species are reported in Figs. 6.1, 6.2 and 6.3 for various values of δ, θ and C. Most of the results are for He–Xe, while some results for Ne–Ar are also presented.

In Fig. 6.1, the distributions of the velocity amplitude $u_{\alpha,P}^{(A)}(y)$ and the phase angle $u_{a,P}^{(P)}(y)$ of each species of the He–Xe gas mixture, with $C = 0.5$, are provided for $\delta = [0.1, 1, 10]$ and $\theta = [0.1, 1, 10]$. It is evident that both He and Xe present the same qualitatively behavior in terms of the gas rarefaction and oscillation parameters. Also, as expected, there is a close qualitative resemblance with corresponding results, presented in [127, 128], for oscillatory flows of single gases. Very briefly, it is observed that as θ is decreased, the amplitude $u_{\alpha,P}^{(A)}$ is decreased, while the phase angle $u_{a,P}^{(P)}$ is increased. It is also seen that at small δ and large θ (e.g., $\delta = 0.1$ and $\theta \geq 1$) the velocity amplitudes have the expected shape with their maximum appearing at the center of the flow field, while at large δ and small θ (e.g., $\delta = 10$ and $\theta \leq 1$) the velocity amplitudes are flattening in the core of the flow and the maximum amplitudes are appearing in thin layers adjacent to the walls. The corresponding phase angles in the former case are small, while in the latter one are large close to the limiting value of $\pi/2$. This is the so-called "velocity overshooting" or "Richardson effect", well-known for long time in oscillatory viscous flows [78, 72] and recently reported in gas rarefied flows [127, 128]. In the present Chapter, the investigation is focused in comparing the above described flow patterns and characteristics between the light and heavy species of the mixture.

It is readily seen, in Fig. 6.1 that the velocity amplitudes of He are always about one order of magnitude larger than the corresponding ones of Xe. It is well-known from investigations in steady-state binary gas mixture flows, that lighter species travel faster than heavier ones, resulting to gas separation, which is increased as the gas flow becomes more rarefied [48, 49]. Therefore, the present results are expected. However, it is interesting to note that as θ is decreased, i.e., as the oscillation frequency is increased, the relative difference between the velocity amplitudes of the light and heavy species is increased. This becomes more evident at $\delta = 10$, where the amplitudes of He and Xe for $\theta = 10$ are relatively close to each other, since the flow is in the hydrodynamic regime, while for $\theta = 1$ and 0.1 the difference between them is gradually increased. On the contrary, the velocity phase angles of He are always smaller than the corresponding ones of Xe. In general, the velocity phase angles are increased as θ is decreased. It may be stated that as the oscillation frequency is increased the velocity amplitude and phase angle of both species is decreased and increased respectively. Clearly however, the difference between the velocity amplitudes of the light and heavy species is increased with the oscillation frequency, not only for small but also for large values of the gas rarefaction parameter. This is a first indication that in oscillatory gas mixture flows, gas separation may be intensified as the oscillation frequency is increased due to inertia forces, which affect differently the light and heavy species.

In Fig. 6.2, the distributions of the velocity amplitude $u_{\alpha,P}^{(A)}(y)$ and the phase angle $u_{a,P}^{(P)}(y)$ of each species of the He–Xe gas mixture, with $C = [0, 0.1, 0.5, 0.9]$, are provided for $\delta = [0.1, 1, 10]$ and $\theta = 1$. Here, the effect of the molar fraction on the velocity amplitude and the phase angle is investigated for typical values of the gas rarefaction and oscillation parameters. The case of $C = 0$ corresponds to oscillatory single gas flow. As C is increased from zero to 0.9, i.e., the molar fraction of the light species (He) is increased, the velocity amplitudes and phase angles of both species are decreased and increased respectively. Of course, as $C \to 1$, the single gas flow results ($C = 0$) are recovered [48, 49]. It is noted that the changes in $u_{1,P}^{(A)}(y)$ and $u_{1,P}^{(P)}(y)$ of He in terms of C, compared to the corresponding ones $u_{2,P}^{(A)}(y)$ and $u_{2,P}^{(P)}(y)$ of Xe, both qualitatively and quantitatively, on a relative base, are about the same. This behavior remains the same in the whole range of gas rarefaction and oscillation parameters.

In Fig. 6.3, the distributions of the velocity amplitude $u_{\alpha,P}^{(A)}(y)$ of each species of the binary gas mixtures of He–Xe, He-Ar and Ne–Ar, with $C = [0.1, 0.4, 0.7, 0.9]$, are provided for $\delta = 10$ and $\theta = 0.1$. The specific values of the gas rarefaction and oscillation parameters, associated with high frequency oscillatory flow between the

transition and slip flow regimes, are suitable for investigating the velocity overshooting phenomenon in the components of the two mixtures. Observing the velocity amplitudes of He, Ne, Ar and Xe, it is evident that for these flow parameters, velocity overshooting is always present. More importantly, it is seen that as the gas becomes heavier, the velocity overshooting becomes sharper appearing, along with its maximum value, closer to the wall in a layer which is gradually becoming thinner. This description remains valid for all molar fractions tested. Comparing the behavior of the velocity amplitudes of the species, it is seen that the shape of the profiles of He and Xe as well as of He and Ar is quite different, while of Ne and Ar is similar, since the difference in the molecular masses of the species is much larger in the former than in the latter case. Overall, it is clear that the Richardson effect becomes more dominant as the molecular mass of the gas species is increased.

Having obtained a description of the dependency of the velocity distribution of each species of the binary gas mixture on the molecular masses and molar fraction in a wide range of the flow parameters, in the next section the corresponding behavior of the flow rates is investigated.

6.4.2 Pressure-driven kinetic coefficients and flow rates

The reported results include the complex kinetic coefficient $\Lambda_{PP} = \Lambda_{PP}^{(A)} \exp\left(i\Lambda_{PP}^{(P)}\right)$ (Figs. 6.4, 6.5 and 6.6) and the complex flow rates of the species $G_{\alpha,P} = G_{\alpha,P}^{(A)} \exp\left(iG_{\alpha,P}^{(P)}\right)$ (Figs. 6.7, 6.8, 6.9 and 6.10) as well as of the time-dependent kinetic coefficient $\tilde{\Lambda}_{PP}(t) = \Lambda_{PP}^{(A)} \cos\left[t - \Lambda_{PP}^{(P)}\right]$ (Fig. 6.11). The effect of the oscillation frequency on the gas separation phenomenon is investigating by computing the amplitude ratio $G_{1,P}^{(A)}/G_{2,P}^{(A)}$ and the phase angle difference $G_{2,P}^{(P)} - G_{1,P}^{(P)}$ of the two species.

In Fig. 6.4, the He–Xe kinetic coefficient amplitude $\Lambda_{PP}^{(A)}$ and phase angle $\Lambda_{PP}^{(P)}$ are provided in terms of $\delta \in \left[10^{-4}, 10^2\right]$, with $\theta = \left[1, 10, 10^2\right]$ and $C = [0, 0.25, 0.5, 0.75, 0.9]$. The results for oscillatory single gas flow ($C = 0$), previously reported in [128], are also included here for comparison purposes. It is seen that the flow rate amplitudes and phase angles of the mixture ($C \neq 0$) depend on the flow parameters very similarly to the corresponding single gas ones ($C = 0$). The behavior of the single gas flow rate in terms of the flow parameters has been analyzed in detail in [127] and it remains the same in the binary gas mixture flow and therefore is not repeated here. It is only pointed out that as θ is decreased (the oscillation frequency is increased), the kinetic coefficient amplitude is decreased and the phase angle is increased. Focusing on the

154

effect of the molar fraction, it is seen that always the kinetic coefficient amplitude is larger and the phase angle is smaller than the corresponding ones of the single gas. Also, $\Lambda_{PP}^{(A)}$ and $\Lambda_{PP}^{(P)}$ vary non-monotonically with C. More specifically, as C is increased, $\Lambda_{PP}^{(A)}$ is initially increased until the molar fraction is in the range of $C \in [0.5, 0.75]$ and then it is decreased to reach the single gas one, while $\Lambda_{PP}^{(P)}$ varies in the opposite way, i.e., it is first decreased and then increased. It is noted that the effect of C on $\Lambda_{PP}^{(A)}$ remains significant in all oscillation regimes, while its effect on $\Lambda_{PP}^{(P)}$ is important only in high and moderate frequencies and becomes negligible at low frequencies. At large values of the gas rarefaction parameter ($\delta \geq 10$) the effect of C is gradually diminished.

A more detailed view of the effect of the molar fraction on the kinetic coefficient is shown in Fig. 6.15, where its amplitude $\Lambda_{PP}^{(A)}$ and phase angle $\Lambda_{PP}^{(P)}$ are provided in terms of C for many values of $\theta = [0.1, 1, 10, 50, 10^2]$ and the typical value of $\delta = [0.1, 1, 10]$. The non-monotonic behavior of $\Lambda_{PP}^{(A)}$ and $\Lambda_{PP}^{(P)}$ in terms of C, along with its dependency on θ, are clearly demonstrated. It is seen that the amplitude $\Lambda_{PP}^{(A)}$ strongly depends on C for all θ, but it varies more significantly as the oscillation parameter is increased. The phase angle $\Lambda_{PP}^{(P)}$ depends on C for small values of θ, while it is practically independent of C for $\theta \geq 10$. This behavior remains qualitative the same in the whole range of gas rarefaction, with the general observation that the effect of the molar fraction is more pronounced as δ is decreased and the flow becomes more rarefied. Also, as δ is increased the maximum kinetic coefficient amplitude appears at larger molar fractions. Similar to Fig. 6.15, the amplitude $\Lambda_{PP}^{(A)}$ and phase angle $\Lambda_{PP}^{(P)}$ of Ne-Ar are presented in Fig. 6.16. It is readily seen that the kinetic coefficient amplitude $\Lambda_{PP}^{(A)}$ and the phase angle $\Lambda_{PP}^{(P)}$ of the mixture in terms of C, are becoming flat completely independent of the molar fraction due to the small difference in the molecular masses of the species.

Next, the investigation is continued by considering the amplitudes and the phase angles of the mixture components in terms of C and m_2/m_1, which are of particular interest in investigating the gas separation phenomenon for various values of δ, θ. As reported in [194], gas separation in rarefied steady-state pressure-driven binary gas flows though capillaries may be analyzed by computing the ratio of the particle flow rates J_1/J_2. It has been shown that the ratio J_1/J_2, independently of C, is monotonically increased as δ is decreased, varying from one in the hydrodynamic limit ($\delta \to \infty$), where there is no separation, up to its maximum value, equal to $\sqrt{m_2/m_1}\,(1-C)\,/C$, in the free molecular limit ($\delta \to 0$), where the flow of each species is independent [194]. Therefore, in the present work dealing with complex quantities, instead of explicitly

providing the species flow rate amplitudes and phase angles, the amplitude ratio $G_{1,P}^{(A)}/G_{2,P}^{(A)}$ and the phase angle difference $G_{2,P}^{(P)} - G_{1,P}^{(P)}$ of the two species are reported.

In Fig. 6.7, the ratio of flow rate amplitudes $G_{1,P}^{(A)}/G_{2,P}^{(A)}$ is provided in terms of $\delta \in [10^{-4}, 10^2]$ for the He–Xe gas mixture, with $C = [0.05, 0.35, 0.65, 0.95]$ and $\theta = [10^{-2}, 0.1, 1, 10, 10^2]$. At $\theta = 10$ the ratio $G_{1,P}^{(A)}/G_{2,P}^{(A)}$ varies qualitatively similarly as in the steady-state binary gas flow setup. It is about constant or slightly reduced in the free molecular regime, then it is rapidly decreased in the transition regime and finally, in the slip and hydrodynamic regime goes asymptotically to one. However, at $\theta = 1$ and $\theta = 0.1$ the behavior of $G_{1,P}^{(A)}/G_{2,P}^{(A)}$ is completely different. It remains about constant in free molecular regime, but then, it is rapidly increased in the transition regime and finally, as δ is further increased, it keeps asymptotically increasing to some constant value. This behavior, with the minimum and maximum values of $G_{1,P}^{(A)}/G_{2,P}^{(A)}$ appearing at the free molecular and hydrodynamic limits respectively and the rapid increase in the transition regime (completely reversed compared to the steady-state behavior) becomes more pronounced as θ is decreased. It is evident that the oscillation parameter θ has a dominant effect on the amplitude ratio of He over Xe, which is significantly increased as θ is decreased (at $\theta = 0.1$ the flow rate amplitude of He is about thirty times larger than of Xe). This behavior is due to the corresponding behavior of the velocity amplitudes commented in Fig. 6.1 and it is contributed to inertia forces, which are increased with the oscillation frequency and they influence the bulk velocity amplitude of the heavy species much more than of the light one. Therefore, as θ is decreased, the flow rate amplitude of the heavy species decreases much more significantly than the light one and although both amplitudes are decreased the velocity amplitude ratio of the light over the heavy species is increased. This effect is magnified in the transition regime, as the flow becomes less rarefied overcoming diffusion effects due to increased intermolecular collisions and therefore, as δ is increased the amplitude ratio keeps increasing. It is seen that the effect of C with regard to these flow characteristics is rather small and becomes even smaller as the oscillation frequency is increased (θ is decreased). In general, the amplitude ratio is slightly increased with the molar fraction.

In Fig. 6.8, the ratio of flow rate amplitudes $G_{1,P}^{(A)}/G_{2,P}^{(A)}$ is provided in terms of $\delta \in [10^{-4}, 10^2]$ for the Ne-Ar gas mixture, with $C = [0.05, 0.35, 0.65, 0.95]$ and $\theta = [10^{-2}, 0.1, 1, 10, 10^2]$. The behavior is qualitatively the same with the corresponding one of the He-Xe mixture for all values of the oscillation parameter θ. However due to the small difference in the molecular masses of the species the dependency of the ratio

on C is negligible. The only noteworthy variation in terms of C is observed for $\theta = 1$ and for large values of δ (e.g., $\delta \geq 1$). It is noted that the maximum value of the ratio is much smaller than in Fig. 6.7.

The ratio of flow rate amplitudes $G_{1,P}^{(A)}/G_{2,P}^{(A)}$ is presented again in Fig. 6.9, in terms of $\theta \in [10^{-4}, 10^2]$ for the He-Xe and Ne-Ar gas mixtures, with $C = 0.5$ and $\delta = [0.1, 1, 10]$. At high oscillation frequencies ($\theta \leq 10^{-2}$), although the flow rate amplitude of each species is decreased, the ratios of the species amplitudes take their highest values, which are almost constant independent of the gas rarefaction parameter δ and equal, as it is numerically found, with the molecular mass ratio of the heavy over the light species m_2/m_1 ($G_{He,P}^{(A)}/G_{Xe,P}^{(A)} = 32.8, G_{Ne,P}^{(A)}/G_{Ar,P}^{(A)} = 1.98$). Then, at moderate oscillation frequencies ($10^{-2} < \theta < 10$) the amplitude ratio is rapidly decreased in all gas rarefaction regimes. Finally, at small oscillation frequencies ($\theta \geq 10$) the corresponding steady-state results are asymptotically recovered. Obviously, the effect of the molecular mass ratio m_2/m_1 on the ratio of the flow rate amplitude of the light over the heavy species is dominant.

In Fig. 6.10, the difference of the flow rate phase angles $G_{2,P}^{(P)} - G_{1,P}^{(P)}$ is provided in terms of $\delta \in [10^{-4}, 10^2]$ for the He–Xe gas mixture, with $C = [0.05, 0.35, 0.65, 0.95]$ and $\theta = [0.1, 1, 10]$. At $\theta = 10$, as well as at $\theta = 1$, the difference of the flow rate phase angles $G_{2,P}^{(P)} - G_{1,P}^{(P)}$ is monotonically increased with δ, with a rapid increase occurring at intermediate values of δ in the transition regime. This is not the case at $\theta = 0.1$, where the difference $G_{2,P}^{(P)} - G_{1,P}^{(P)}$ is first increased, reaching some maximum value in the transition regime and then it is decreased reaching asymptotically some constant value. This behavior is also present at $\theta < 0.1$ (not shown here), with the maximum value appearing at lower δ, as θ is decreased. In general, it is demonstrated that there is phase angle difference between the flow rates of the two species of the mixture.

In Figure 6.11, the phase lag between the oscillatory pressure gradient, the flow rates of each species and kinetic coefficient $\tilde{\Lambda}_{PP}$ is demonstrated, by plotting the time-dependent flow rates $\tilde{G}_{1,P}(t)$ of He, $\tilde{G}_{2,P}(t)$ of Xe, as well as $\tilde{\Lambda}_{PP}(t) = C\tilde{G}_{1,P}(t) + (1 - C)\tilde{G}_{2,P}(t)$ of the He–Xe gas mixture with $C = 0.5$, over one cycle $t \in [0, 2\pi]$ for $\delta = [0.1, 1, 10]$ and $\theta = [0.1, 10]$. It is noted that the dimensionless time-dependent pressure gradient is equal to $\cos(t)$. In the case $\theta = 10$ (low oscillation frequency), all quantities when $\delta = [0.1, 1]$ are in phase to each other, while when $\delta = 10$ they are out of phase, with $\tilde{G}_{2,P}(t)$ having a larger phase lag, compared to $\tilde{G}_{1,P}(t)$, with respect to the pressure gradient. In the case $\theta = 0.1$ (high oscillation frequency), when $\delta = 0.1$ all quantities are almost in phase to each other, while when $\delta = [1, 10]$ they

are out of phase. For $\theta = 0.1$ and $\delta = 10$, the maximum phase angle lag, almost equal to $\pi/2$, is observed. Again the phase angle lag of the flow rate of Xe is larger than the one of He. The phase lag of the $\tilde{\Lambda}_{PP}$ is, as expected, between the phase lags of the two species. Also, the amplitudes of the oscillatory He flow rate are much larger than the corresponding ones of Xe. All these remarks are in agreement with the discussion presented in terms of the amplitudes and the phase angles of the species flow rates in Figs. (6.7, 6.9 and 6.10). Overall, it may be stated that the oscillatory flow rates and pressure gradient are in phase when $\delta << \theta$ and completely out of phase when $\theta << \delta$, with the heavier species have larger phase angle lags compared to the lighter ones.

Closing this subsection on the flow rates it is noted that the flow rates of other mixtures (e.g. He-Ar), as well as of their species, have been computed, in the whole range of the molar fraction and for various values of the flow parameters. The flow rate amplitude ratio $G_{1,P}^{(A)}/G_{2,P}^{(A)}$ and phase angle difference $G_{2,P}^{(P)} - G_{1,P}^{(P)}$ of the species of all binary gas mixtures tested have a close resemblance with the corresponding ones for He and Xe. However, quantitatively the results are different with the values of $G_{1,P}^{(A)}/G_{2,P}^{(A)}$ and $G_{2,P}^{(P)} - G_{1,P}^{(P)}$ becoming much smaller and gradually independent of C, as the molecular mass ratio m_2/m_1 is decreased, recovering the oscillatory single gas behavior as $m_2/m_1 \rightarrow 1$. This remark, well-known in steady-state flows, remains valid also in oscillatory gas mixture flows. The results for He–Ar and other mixtures of monoatomic gases are not reported here because it is believed that they do not provide any additional important information concerning the understanding of the oscillatory binary gas flow properties and characteristics.

The most interesting finding concerning the flow rates is that, independent of the molar fraction and the gas rarefaction regime, the amplitude ratio of the oscillatory flow rates of the light over the heavy species is significantly increased as the oscillation frequency is increased. Clearly, these results may be of major technological importance in developing gas separation apparatus in the whole range of the Knudsen number.

6.4.3 Pressure-driven wall shear stress and pumping power

Complementary quantities of the oscillatory binary gas mixture of practical interest, namely the wall shear stress $\varpi_{W,P} = \varpi_{W,P}^{(A)} \exp\left(i\varpi_{W,P}^{(P)}\right)$ (Fig. 6.12), as well as the oscillatory pumping power $\tilde{E}(t)$ (Fig. 6.13) and cycle-average pumping power $\bar{E}$ (Fig. 6.14), given by Eqs. (6.25) and (6.26) respectively, are here considered.

In Fig. 6.12, the wall shear stress amplitude $\varpi_{W,P}^{(A)}$ and phase angle $\varpi_{W,P}^{(P)}$ are provided in terms of $C \in [0,1]$ for $\theta = [0.1, 1, 10, 50, 10^2]$ and the typical value of

$\delta = [0.1, 1, 10]$. It is readily seen that as the molar fraction varies between zero and one, both the wall shear stress amplitude and phase angle remain constant for $\theta = [10, 50, 10^2]$ and vary slightly for $\theta = [0.1, 1]$. It is evident that the dependency of the shear stress on the molar fraction is very weak and this behavior remains the same in the whole range of gas rarefaction. As expected $\varpi_{W,P}^{(A)}$ is decreased and $\varpi_{W,P}^{(P)}$ is increased as θ is decreased. Actually, $\varpi_{W,P}^{(A)}$ almost diminishes at very high oscillation frequencies. Furthermore, as θ is increased and the oscillation frequency tends to zero, the shear stress amplitude $\varpi_{W,P}^{(A)}$ approaches the limiting value of 0.25, which is the steady-state dimensionless wall shear stress, independent of δ [204], while the shear stress phase angle $\varpi_{W,P}^{(P)}$ approaches zero. These results further validate the accuracy of the present oscillatory binary gas mixture computational approach.

In Fig. 6.13, the time-dependent pumping power $\tilde{E}(t)$ of the He–Xe gas mixture with $C = 0.5$, over one cycle $t \in [0, 2\pi]$ is plotted for $\delta = [0.1, 1, 10]$ and $\theta = [0.1, 10]$. More specifically, instead of $\tilde{E}(t)$, the results correspond to the normalized time-dependent pumping power $\tilde{E}(t)/dx$. Obviously, the pumping power has two peaks within each oscillatory cycle because it consists of the product of the oscillatory flow times the oscillatory pressure gradient and its integral over one cycle is not zero in order to drive the mixture flow, although the oscillatory net flow is zero. The dependency of the mixture pumping power on the flow parameters is similar to the one observed in oscillatory single gas flow [164, 128]. In general, as θ is decreased its amplitude is decreased and its phase angle lag is increased and this behavior becomes more dominant as δ is increased. As it has already been seen in [128], the oscillatory pumping power, at certain times within the time period $t \in [0, 2\pi]$, may become negative due to the pressure gradient which becomes negative when the flow is reversed. At the same time the sign of the flow rate, due to the phase angle lag, remains positive leading to a negative pumping power. This is mainly occurring when the flow rate is out of phase. These remarks remain valid in the whole range of the molar fraction. Furthermore, the effect of C on the amplitude of the mixture pumping power is negligible in most cases and becomes more important as both δ and θ are decreased, where the amplitude of the mixture pumping power is decreased as C is increased. Also, the effect of the molar fraction on the phase angle of the mixture pumping power is very small.

In Fig. 6.14, the normalized cycle-average pumping power $\bar{E}/dx$ for the binary gas mixtures of He–Xe and Ne–Ar in terms of C is plotted for various values of $\theta = [0.1, 1, 10, 10^2]$ and the typical values of $\delta = [0.1, 1, 10]$. The corresponding steady-state pumping power $\bar{E}_S$ of the binary gas mixture flow of He–Xe and Ne–Ar are

also plotted for comparison purposes. In general, as θ is decreased the cycle-average pumping power is decreased, which is expected since as the oscillation frequency is increased the flow rate amplitude is decreased. At large values of the oscillation parameter ($\theta \geq 10$), as the flow becomes stationary the cycle-average pumping power becomes half of the corresponding steady-state one. The same trend has been observed in oscillatory single gas flows [164, 128]. Furthermore, the effect of the molar fraction on the cycle-average pumping powers of He–Xe and Ne–Ar is very weak.

6.4.4 Molar fraction-driven flow: velocity distributions and kinetic coefficients

The binary gas mixture flow due to oscillating molar fraction is studied in this Section. The results include the velocity of each species as well as the kinetic coefficients $\tilde{\Lambda}_{PP}$ and $\tilde{\Lambda}_{PC}$. The differences between the pressure-driven flow and molar fraction-driven flow are also commented.

In Fig. 6.15, the distributions of the velocity amplitude $u_{\alpha,C}^{(A)}(y)$ and the phase angle $u_{a,C}^{(P)}(y)$ of each species of the He–Xe gas mixture, with $C = 0.5$, are provided for $\delta = [0.1, 1, 10]$ and $\theta = [0.1, 1, 10]$. It is evident that behavior of the velocity amplitude and the phase angle of both species is similar to the corresponding one in Fig. 6.1. The velocity amplitudes of He are always than the corresponding ones of Xe. On the contrary, the velocity phase angles of He are always smaller than the corresponding ones of Xe. However, it is evident that when $\delta \gg \theta$ (e.g., $\delta = 10$ and $\theta = 0.1$) the difference between the phase angles of the two species is diminished. This isn't seen in Fig. 6.1 where there is a phase angle difference between the velocities of the two species of the mixture even in small oscillation parameters. It is also interesting to note that the so-called "velocity overshooting" or "Richardson effect", already seen in oscillatory pressure-driven flows, is observed here in flows due to oscillating molar fraction gradient. In general, the velocity distributions of the molar fraction-driven flow are quite similar to the corresponding ones of the pressure-driven flow.

In Fig. 6.16, the amplitudes of the kinetic coefficients $\Lambda_{CC}^{(A)}$ and $\Lambda_{PC}^{(A)}$ are provided in terms of $\delta \in [10^{-4}, 10^2]$, with $\theta = [1, 10, 10^2]$ and $C = [0.05, 0.25, 0.5, 0.75, 0.9]$. It is seen that both amplitudes $\Lambda_{CC}^{(A)}$ and $\Lambda_{PC}^{(A)}$ are decreased monotonically as the rarefaction parameter is increased. This trend is observed for all values of the molar fraction C. Focusing on the effect of the molar fraction, the amplitude $\Lambda_{CC}^{(A)}$ is increased monotonically as the molar fraction is increased or as the mixture becomes lighter.

160

The amplitude of the coefficient $\Lambda_{CC}^{(A)}$ is the one with the strongest dependency on C. Furthermore, the amplitude of the coefficient $\Lambda_{CP}^{(A)}$ varies non-monotonically with the molar fraction C. More specifically, as C is increased, $\Lambda_{PC}^{(A)}$ is initially increased until the molar fraction is $C = 0.75$ and then it is decreased to reach the single gas one. Of course, since $\Lambda_{PC}^{(A)}$ is a cross effect, it is diminished for either $C = 0$ or $C \to 1$. Another noteworthy remark is that for $C = 0.5$ and $\theta = 10$, $\Lambda_{PC}^{(A)}$ is rapidly decreased while for all the other parameters it is gradually reduced. The effect of C is gradually reduced at large values of the rarefaction parameter ($\delta \geq 10$).

A more detailed view of the effect of the molar fraction on the complex kinetic coefficient Λ_{CC} is shown in Fig. 6.17, where its amplitude $\Lambda_{CC}^{(A)}$ and phase angle $\Lambda_{CC}^{(P)}$ are provided in terms of C for many values of $\theta = [0.1, 1, 10, 50, 10^2]$ and the typical values of $\delta = [0.1, 1, 10]$. It is evident that as the molar fraction is increased both the amplitude $\Lambda_{CC}^{(A)}$ and the phase angle $\Lambda_{CC}^{(P)}$ are increased. However, it is interesting to note that this behavior isn't encountered for all values of the oscillation parameter. More specifically, the amplitude $\Lambda_{CC}^{(A)}$ varies non-monotonically with C when $\delta > \theta$. As C is increased it is initially increased, until the molar fraction is in the range of $C \in [0.5, 0.8]$ and then it is decreased. Therefore, the kinetic coefficient Λ_{CC} depends strongly on the oscillation parameter and it is decreased as θ is decreased even when the mixture becomes very light. It is also noted that the phase angle $\Lambda_{CC}^{(P)}$ is increased monotonically as the oscillation parameter is decreased, following the behavior of the kinetic coefficient $\Lambda_{PP}^{(P)}$. The largest value of phase angle $\Lambda_{CC}^{(P)}$ is always observed for very light mixtures and small oscillation parameters.

In Fig. 6.18, the amplitude $\Lambda_{PC}^{(A)}$ and phase angle $\Lambda_{PC}^{(P)}$ are provided in terms of the molar fraction C for $\theta = [0.1, 1, 10, 50, 10^2]$ and with $\delta = [0.1, 1, 10]$. It is seen that the amplitude $\Lambda_{PC}^{(A)}$ presents a non-monotonic behavior. As C is increased, $\Lambda_{PC}^{(A)}$ is initially increased until the molar fraction is in the range of $C \in [0.7, 0.9]$ and then it is decreased to reach the single gas one where it is diminished. This behavior is seen for all values of the oscillation and rarefaction parameters. In terms of the oscillation parameter, it is interesting to note that the amplitude $\Lambda_{PC}^{(A)}$ varies non-monotonically. As θ is decreased it reaches a maximum for $\theta = 1$ and then it is decreased for $\theta = 0.1$. For large values of δ, this maximum is seen for $\theta = 10$. Thus, the amplitude of the kinetic coefficient $\Lambda_{PC}^{(A)}$ has a resonant behavior in terms of θ which hasn't been seen in the other kinetic coefficients. Furthermore, the phase angle $\Lambda_{PC}^{(P)}$ is increased as the molar fraction C is increased for all values of the rarefaction parameter. Also, as the

oscillation parameter is decreased the phase angle is always increased except for $\delta = 10$ where it varies non- monotonically.

Finally, the investigation is ended by considering the effect of the intermolecular potential on the kinetic coefficients. Since it has been seen in [48] that the effect of the intermolecular interaction potential is more important in the kinetic coefficients Λ_{CP} and Λ_{CC}, a similar comparison is made here for the amplitudes of the two kinetic coefficients. In Tables 6.1 and 6.2 the amplitudes of the kinetic coefficients $\Lambda_{CC}^{(A)}$ and $\Lambda_{PC}^{(A)}$ are presented respectively for two molecular models: the rigid spheres and a realistic potential of the intermolecular interaction. The details of the potentials are presented in [48]. The amplitudes are provided for several values of the rarefaction parameter $\delta = [10^{-2}, 10^{-1}, 1, 10, 10^2]$ and the molar fraction $C = [0.1, 0.25, 0.5, 0.75, 0.9]$ with the oscillating parameter being $\theta = [0.1, 1, 10]$. At first, it is seen that the impact of the potential on both amplitudes, $\Lambda_{CC}^{(A)}$ and $\Lambda_{PC}^{(A)}$, is significant for large values of θ and δ (e.g., $\theta, \delta \geq 1$). Actually, the largest differences are always seen for $\theta = 10$ and $\delta = 100$. On the contrary, the smallest ones are seen for small values of the oscillation parameter. It seems that in high frequency oscillation flows the effect of the intermolecular potential is diminished. Furthermore, as the molar fraction is increased the differences between the intermolecular potentials are slightly reduced even though it isn't directly seen in Tables 6.1 and 6.2. It is also noted that the resonant behavior of the amplitude $\Lambda_{PC}^{(A)}$ is seen for both potentials (e.g., $C = 0.5$ and $\delta = 1$). In general, the intermolecular potential has a significant effect on the kinetic coefficients Λ_{CP} and Λ_{CC} for larger values of θ and δ or as the flow tends to the hydrodynamic regime.

6.5 Concluding remarks

The rarefied oscillatory pressure- and molar fraction driven fully-developed isothermal binary gas mixture flow between parallel plates is computationally investigated in terms of the mixture molar fraction $C \in [0, 1]$ and the molecular mass ratio m_2/m_1 of the heavy over the light species, in a wide range of the gas rarefaction parameter δ and oscillation parameter θ, which are inversely proportional to the Knudsen number and the oscillation frequency respectively. Modeling is based on the McCormack kinetic model equation, subject to diffuse boundary conditions. The computed output quantities are in dimensionless form and include macroscopic quantities of theoretical and technological importance. More specifically, the amplitude and phase angle of the velocity distributions and flow rates of the two species, as well as of the kinetic

coefficients and wall shear stress of the mixture are reported. In addition, the time evolution of the kinetic coefficient $\tilde{\Lambda}_{PP}$ and the pumping power, as well as the cycle-average pumping power due to the pressure gradient are provided. The results refer to the binary gas mixtures of He–Xe, He-Ar and Ne–Ar. The numerical work has been successfully validated in various ways, including grid refinement, fulfillment of a derived force balance benchmark expression and systematic comparisons with corresponding works, available in the literature, at limiting conditions, such as steady-state binary gas flow as $\theta \to \infty$ [48] and oscillatory single gas flow when $C = 0$ or $m_1/m_2 = 1$ [128].

The flow rate, wall shear stress and pumping power of the binary gas mixture flow due oscillating pressure gradient have qualitative resemblance with the corresponding ones in oscillatory single gas flow, in terms of δ and θ, but there are quantitative deviations particularly in the flow rates depending on C and m_2/m_1. As in the case of single gases, as θ is decreased (the oscillation frequency is increased), always the amplitude of all quantities is decreased, while their phase angle is increased. The effect of the mixture components and its molar fraction is very important on the velocities and the corresponding flow rates of the species of the mixture, as well as the ratio of their flow rate amplitudes.

Concerning the mixture quantities, it has been found that as m_2/m_1 is increased, the kinetic coefficient amplitude $\Lambda_{PP}^{(A)}$ becomes larger and the phase angle $\Lambda_{PP}^{(P)}$ becomes smaller than the corresponding ones of the single gas. The variation with respect to C is non-monotonic, taking the maximum and minimum values for the amplitude and the phase angle respectively at intermediate values of the molar fraction. The variation of the amplitude $\Lambda_{PP}^{(A)}$ and the phase angle $\Lambda_{PP}^{(P)}$ is more significant at small and large frequencies respectively. The time evolution of the $\tilde{\Lambda}_{PP}$ is in phase with the oscillatory pressure gradient when $\delta << \theta$ and completely out of phase when $\theta << \delta$. On the contrary, it has been found that the mixture wall shear stress and pumping power depend very weakly on C and m_2/m_1 in the whole range of δ and θ.

Concerning the species quantities and starting with the velocity distributions, it has been found that as the oscillation frequency is increased, although the velocity amplitudes of both species are decreased, the relative difference between the velocity amplitudes of the light and heavy species is increased. This behavior is observed at small δ and it becomes more pronounced as δ is increased, which is not expected, since as it is well-known gas separation effects are decreased as the flow becomes less rarefied and is dominated by intermolecular collisions. In parallel, the velocity phase angles of both species are increased, without observing a specific pattern with regard

163

to their phase angle difference. Obviously, a similar behavior has been observed in the corresponding flow rates, which has been systematically investigated in terms of the ratio of the flow rate amplitude of the light over the heavy species. In small oscillation frequencies (large θ), the variation of the ratio of the flow rate amplitude is the expected one, i.e., it is decreased as the flow becomes less rarefied. However, at moderate and high oscillation frequencies the behavior is reversed and the ratio of the flow rate amplitude is increased as the flow becomes less rarefied. It has been found that as θ is decreased, the flow rate amplitude of the heavy species is decreased much more significantly than of the light one and therefore, the ratio of the flow rate amplitude of the light over the heavy species is increased. It is believed that this is due to inertia effects, which are increased with the oscillation frequency and they influence the velocity (and flow rate) amplitude of the heavy species much more than of the light one. This effect is further amplified as δ is increased and the flow becomes less rarefied, overcoming diffusion effects due to intermolecular collisions, provided that θ is sufficiently small. This behavior depends weakly on C but very strongly on m_2/m_1. It has been confirmed that at high frequencies the flow rate amplitude ratio of the light over the heavy species, independent of δ, tends to the molecular mass ratio of the heavy over the light species m_2/m_1. Furthermore, it is worthwhile to note that the phase lag of the velocity and the flow rate of the heavy species are always larger than the corresponding ones of the light one, while the velocity overshooting effect, well-known in oscillatory flows, becomes more dominant as the molecular mass of the gas species is increased. These observations are in agreement with previous remarks concerning the inertia effect on the flow rate amplitudes of the two species.

Next, it has been seen that the kinetic coefficients $\Lambda_{CC}^{(A)}$ and $\Lambda_{CP}^{(A)}$ decrease monotonically as δ is increased for a constant value of the oscillation parameter. The amplitude $\Lambda_{CC}^{(A)}$ varies non-monotonically in terms of the molar fraction C only for small values of θ while the amplitude $\Lambda_{CP}^{(A)}$ varies in the whole range of the oscillation parameter. In addition, the variation of amplitude $\Lambda_{CP}^{(A)}$ with respect to θ is non-monotonic, taking the maximum for the amplitude at an intermediate value of the oscillation parameter. This isn't seen in the other kinetic coefficients, $\Lambda_{PP}^{(A)}$ and $\Lambda_{CC}^{(A)}$, which are increased monotonically as the oscillation parameter is increased. Furthermore, the phase angles of the kinetic coefficients, $\Lambda_{CC}^{(A)}$ and $\Lambda_{CP}^{(A)}$, are increased as the mixture becomes lighter.

Finally, the effect of the intermolecular potential is also investigated for the oscillatory molar fraction driven flow. It has been seen that the molecular model affects the kinetic coefficient amplitudes, $\Lambda_{CC}^{(A)}$ and $\Lambda_{CP}^{(A)}$, significantly for large values of the

rarefaction and oscillation parameters. On the contrary, for small values of θ the effect of the potential is diminished.

Table 6.1 Amplitude of the kinetic coefficient $\Lambda_{CC}^{(A)}$ in terms of C and δ for rigid spheres and realistic potential of the He–Xe mixture with $\theta = [0.1, 1, 10]$.

C	δ	Rigid spheres			Realistic potential		
		$\theta = 0.1$	$\theta = 1$	$\theta = 10$	$\theta = 0.1$	$\theta = 1$	$\theta = 10$
0.1	0.01	1.477	1.760	1.771	1.485	1.799	1.813
	0.1	8.119(-1)	1.076	1.087	8.231(-1)	1.120	1.134
	1	2.448(-1)	4.640(-1)	4.752(-1)	2.536(-1)	5.126(-1)	5.280(-1)
	10	2.788(-2)	8.710(-2)	9.189(-2)	2.862(-2)	1.053(-1)	1.133(-1)
	100	2.812(-3)	9.395(-3)	1.000(-2)	2.882(-3)	1.154(-2)	1.262(-2)
0.25	0.01	3.421	4.177	4.220	3.436	4.252	4.301
	0.1	1.850	2.556	2.599	1.871	2.645	2.695
	1	5.382(-1)	1.108	1.152	5.541(-1)	1.211	1.268
	10	5.983(-2)	2.112(-1)	2.268(-1)	6.099(-2)	2.508(-1)	2.760(-1)
	100	6.025(-3)	2.283(-2)	2.481(-2)	6.133(-3)	2.751(-2)	3.088(-2)
0.5	0.01	5.854	7.560	7.743	5.869	7.631	7.820
	0.1	3.023	4.610	4.798	3.048	4.716	4.916
	1	8.014(-1)	1.999	2.180	8.162(-1)	2.141	2.361
	10	8.496(-2)	3.904(-1)	4.448(-1)	8.575(-2)	4.470(-1)	5.275(-1)
	100	8.533(-3)	4.223(-2)	4.922(-2)	8.604(-3)	4.884(-2)	5.967(-2)
0.75	0.01	7.171	1.022(+1)	1.092(+1)	7.179	1.023(+1)	1.093(+1)
	0.1	3.305	6.092	6.798	3.322	6.155	6.884
	1	7.214(-1)	2.540	3.170	7.266(-1)	2.657	3.377
	10	7.271(-2)	4.867(-1)	6.738(-1)	7.289(-2)	5.282(-1)	7.797(-1)
	100	7.284(-3)	5.201(-2)	7.617(-2)	7.300(-3)	5.655(-2)	9.010(-2)
0.9	0.01	7.913	1.284(+1)	1.487(+1)	7.919	1.283(+1)	1.496(+1)
	0.1	2.921	7.211	9.232	2.931	7.252	9.391
	1	4.821(-1)	2.590	4.304	4.829(-1)	2.667	4.584
	10	4.786(-2)	4.202(-1)	9.227(-1)	4.789(-2)	4.342(-1)	1.069
	100	4.789(-3)	4.354(-2)	1.069(-1)	4.791(-3)	4.487(-2)	1.269(-1)

Table 6.2 Amplitude of the kinetic coefficient $\Lambda_{CP}^{(A)}$ in terms of C and δ for rigid spheres and realistic potential of the He–Xe mixture with $\theta = [0.1, 1, 10]$.

C	δ	Rigid spheres			Realistic potential		
		$\theta = 0.1$	$\theta = 1$	$\theta = 10$	$\theta = 0.1$	$\theta = 1$	$\theta = 10$
0.1	0.01	1.289	1.464	1.453	1.297	1.503	1.494
	0.1	7.474(-1)	9.106(-1)	8.940(-1)	7.574(-1)	9.513(-1)	9.373(-1)
	1	2.365(-1)	4.290(-1)	3.907(-1)	2.450(-1)	4.736(-1)	4.338(-1)
	10	2.694(-2)	8.406(-2)	8.679(-2)	2.766(-2)	1.016(-1)	1.069(-1)
	100	2.717(-3)	9.076(-3)	9.644(-3)	2.785(-3)	1.115(-2)	1.217(-2)
0.25	0.01	2.917	3.370	3.341	2.930	3.442	3.420
	0.1	1.681	2.108	2.064	1.700	2.187	2.150
	1	5.166(-1)	1.014	9.157(-1)	5.319(-1)	1.107	1.007
	10	5.742(-2)	2.025(-1)	2.124(-1)	5.853(-2)	2.405(-1)	2.582(-1)
	100	5.782(-3)	2.191(-2)	2.376(-2)	5.886(-3)	2.640(-2)	2.958(-2)
0.5	0.01	4.672	5.598	5.538	4.684	5.664	5.614
	0.1	2.650	3.541	3.448	2.671	3.628	3.544
	1	7.546(-1)	1.778	1.580	7.687(-1)	1.904	1.706
	10	7.993(-2)	3.667(-1)	4.064(-1)	8.067(-2)	4.200(-1)	4.817(-1)
	100	8.028(-3)	3.973(-2)	4.619(-2)	8.095(-3)	4.595(-2)	5.600(-2)
0.75	0.01	4.827	6.115	6.040	4.833	6.117	6.039
	0.1	2.646	3.924	3.792	2.659	3.960	3.829
	1	6.428(-1)	2.095	1.829	6.475(-1)	2.191	1.937
	10	6.458(-2)	4.315(-1)	5.762(-1)	6.475(-2)	4.684(-1)	6.669(-1)
	100	6.470(-3)	4.619(-2)	6.742(-2)	6.484(-3)	5.022(-2)	7.977(-2)
0.9	0.01	3.676	4.933	4.883	3.679	4.911	4.838
	0.1	1.902	3.195	3.079	1.909	3.207	3.076
	1	3.687(-1)	1.773	1.583	3.692(-1)	1.826	1.670
	10	3.641(-2)	3.188(-1)	6.669(-1)	3.643(-2)	3.293(-1)	7.731(-1)
	100	3.643(-3)	3.311(-2)	8.091(-2)	3.645(-3)	3.412(-2)	9.608(-2)
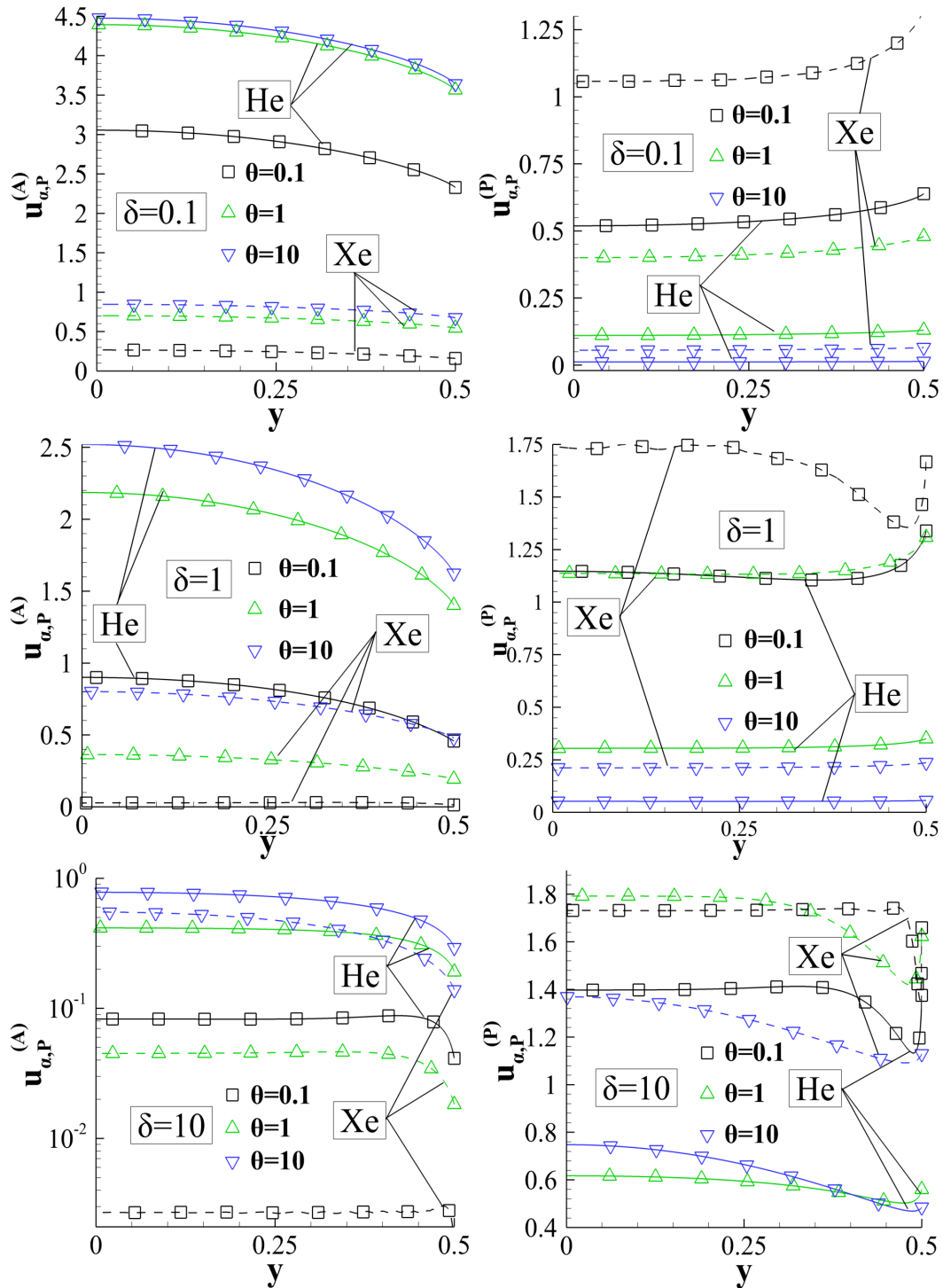
Figure 6.1 Velocity amplitude $u_{a,P}^{(A)}(y)$ and phase angle $u_{a,P}^{(P)}(y)$ of each species of He–Xe, with $C = 0.5$, for $\delta = [0.1, 1, 10]$ and $\theta = [0.1, 1, 10]$ (He: solid lines, Xe: dashed lines).

168
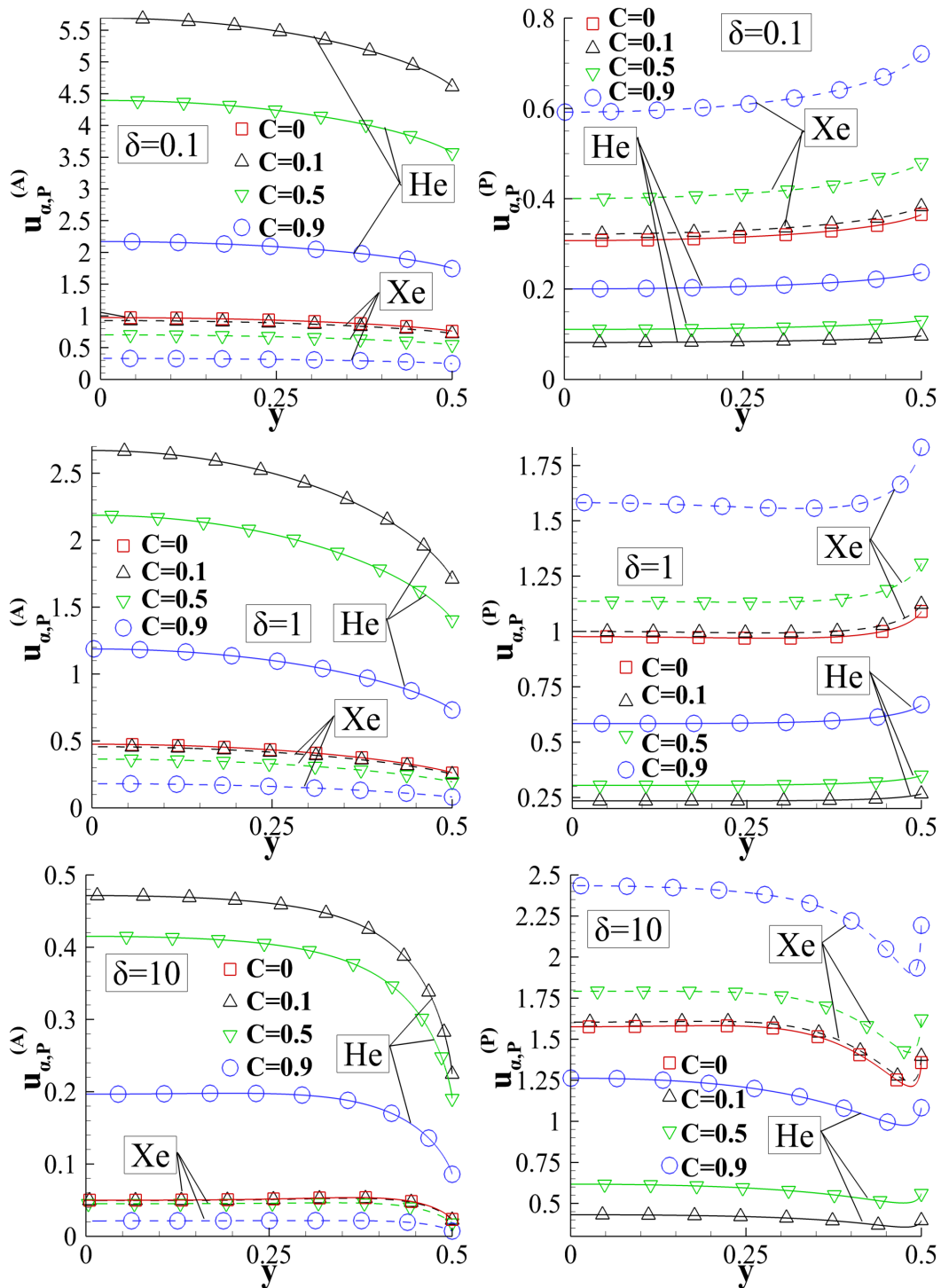
Figure 6.2 Velocity amplitude $u^{(A)}_{\alpha,P}(y)$ and the phase angle $u^{(P)}_{a,P}(y)$ of each species of He–Xe, with $C = [0, 0.1, 0.5, 0.9]$, for $\delta = [0.1, 1, 10]$ and $\theta = 1$ (He: solid lines, Xe: dashed lines).

169
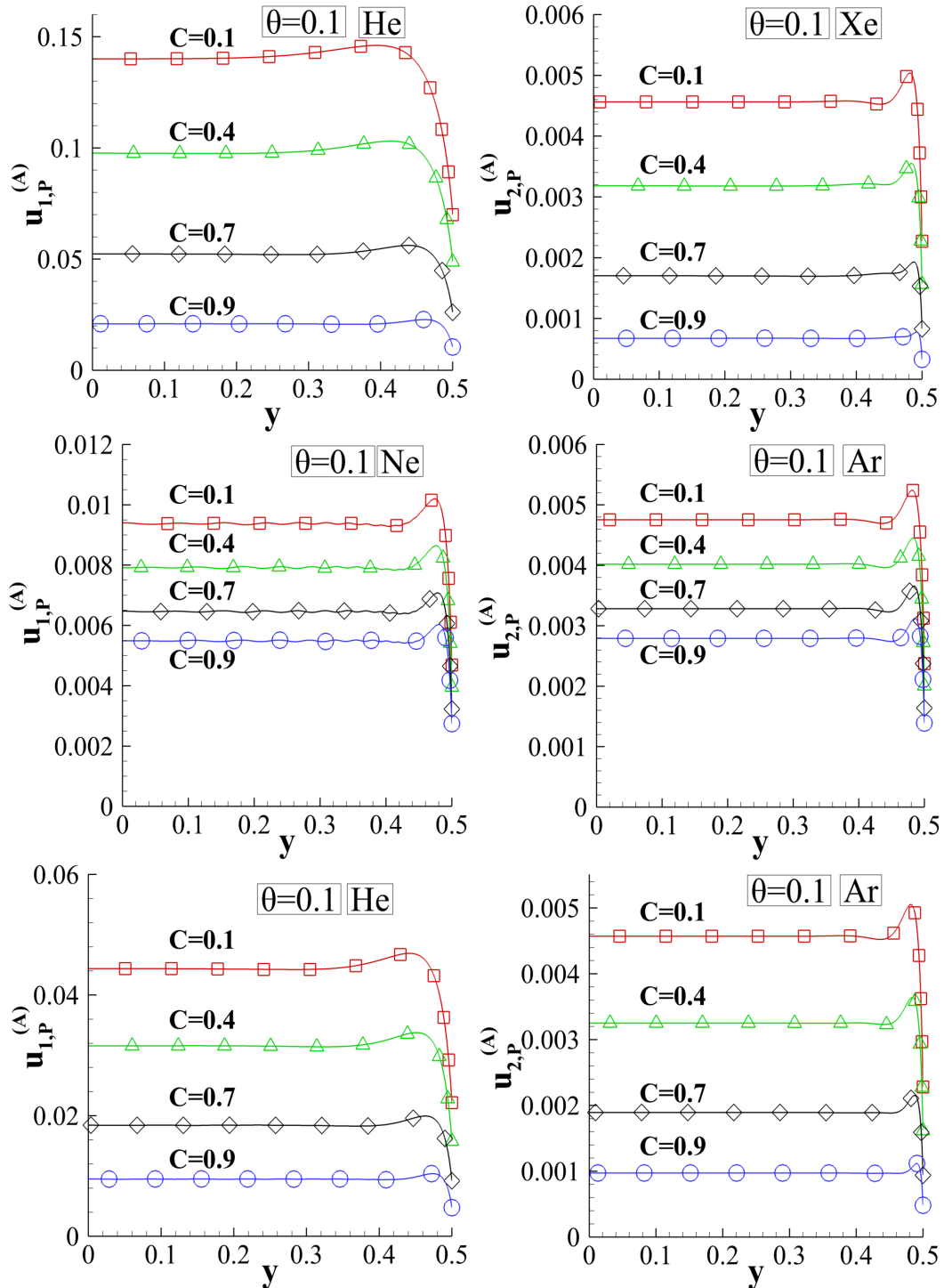
Figure 6.3 Velocity amplitude $u_{\alpha,P}^{(A)}(y)$ of each species of He–Xe, He-Ar and Ne–Ar, with $C = [0.1, 0.4, 0.7, 0.9]$, for $\delta = 10$ and $\theta = 0.1$.

170
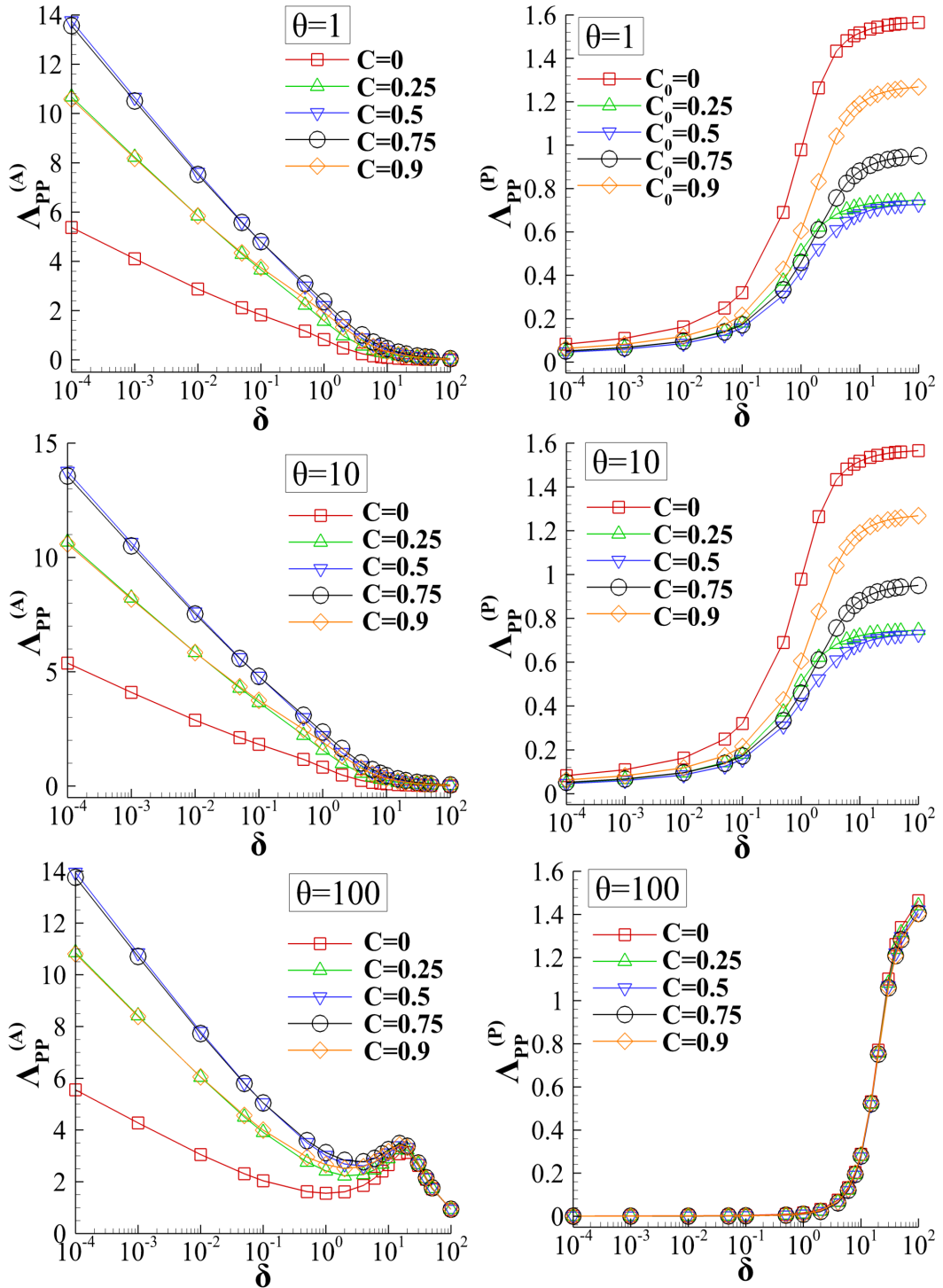
Figure 6.4 Kinetic coefficient amplitude $\Lambda_{PP}^{(A)}$ and phase angle $\Lambda_{PP}^{(P)}$ of He-Xe in terms of $\delta \in [10^{-4}, 10^2]$, with $C = [0, 0.25, 0.5, 0.75, 0.9]$ and $\theta = [1, 10, 10^2]$.

171
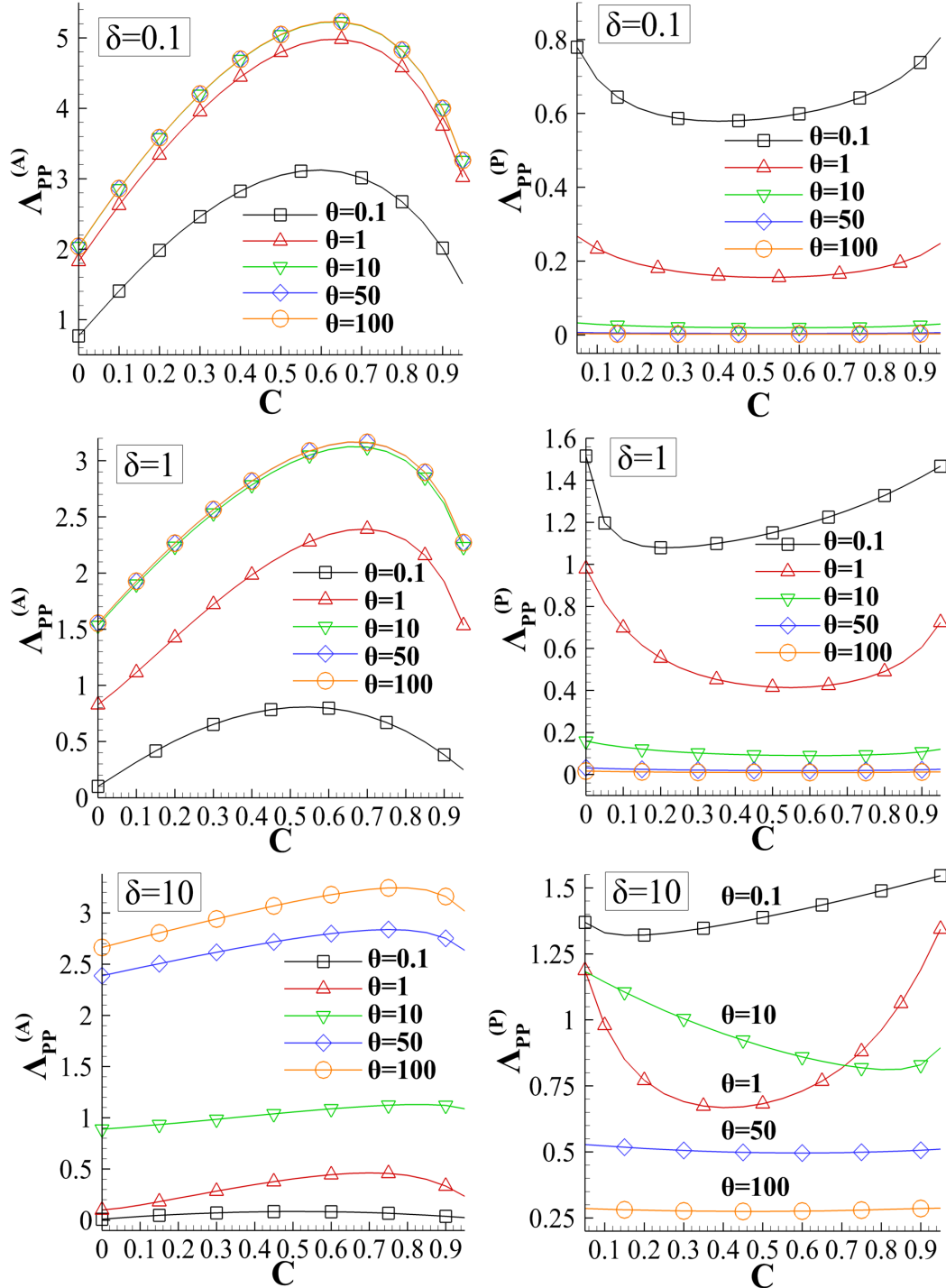
Figure 6.5 Kinetic coefficient amplitude $\Lambda_{PP}^{(A)}$ and phase angle $\Lambda_{PP}^{(P)}$ of He-Xe in terms of the molar fraction C for $\delta = [0.1, 1, 10]$ and $\theta = [10^{-1}, 1, 10, 50, 10^{2}]$.

172
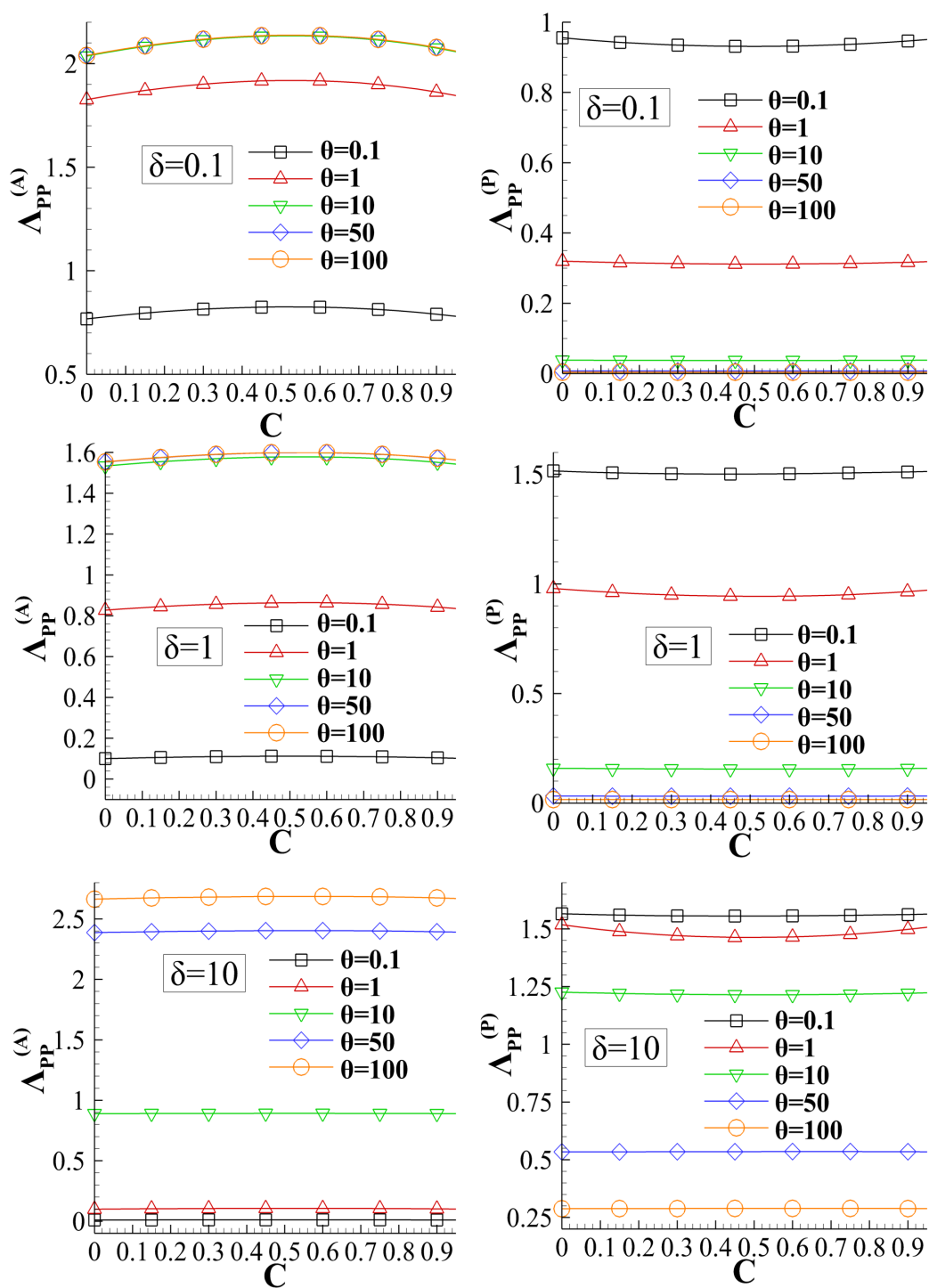
Figure 6.6 Kinetic coefficient amplitude $\Lambda_{PP}^{(A)}$ and phase angle $\Lambda_{PP}^{(P)}$ of Ne-Ar in terms of the molar fraction C for $\delta = [0.1, 1, 10]$ and $\theta = [10^{-1}, 1, 10, 50, 10^2]$.

173
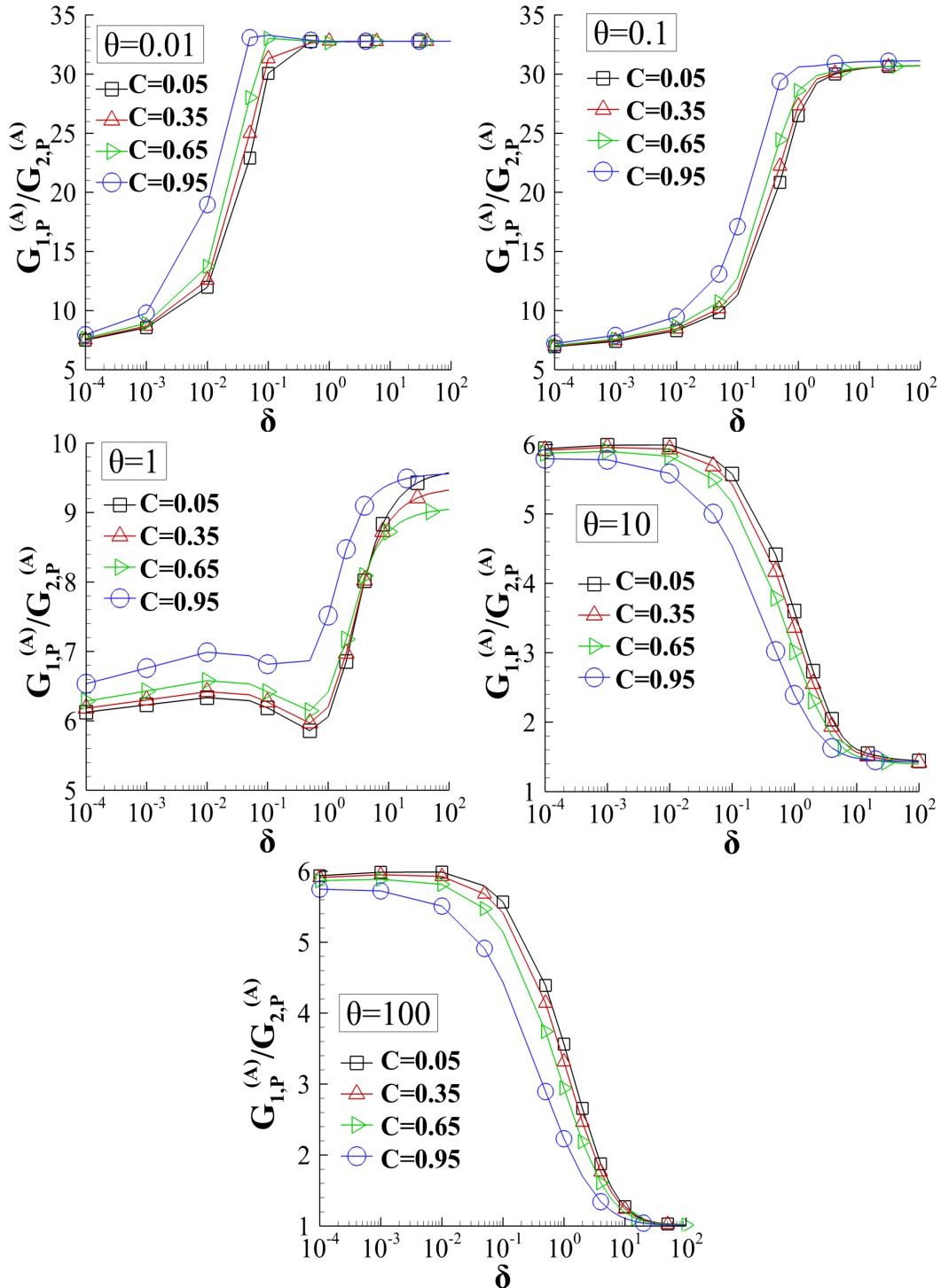
Figure 6.7 Ratio of flow rate amplitudes $G_{1,P}^{(A)}/G_{2,P}^{(A)}$ of the species of He-Xe in terms of $\delta \in [10^{-4}, 10^2]$, with $C = [0, 05, 0.35, 0.65, 0.95]$ and $\theta = [10^{-2}, 0.1, 1, 10, 10^2]$.

174
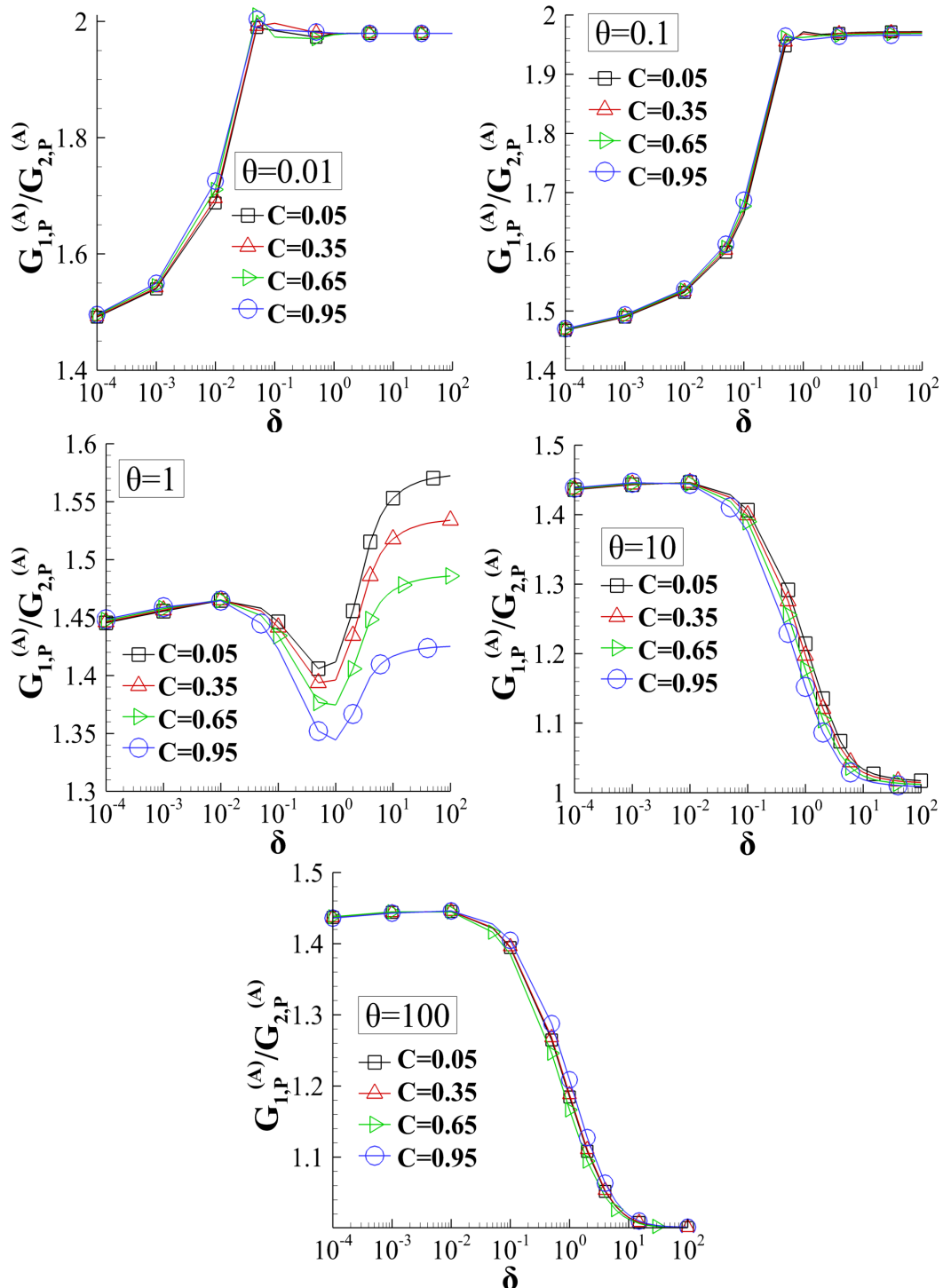
Figure 6.8 Ratio of flow rate amplitudes $G_{1,P}^{(A)}/G_{2,P}^{(A)}$ of the species of Ne-Ar in terms of $\delta \in [10^{-4}, 10^2]$, with $C = [0, 05, 0.35, 0.65, 0.95]$ and $\theta = [10^{-2}, 0.1, 1, 10, 10^2]$.
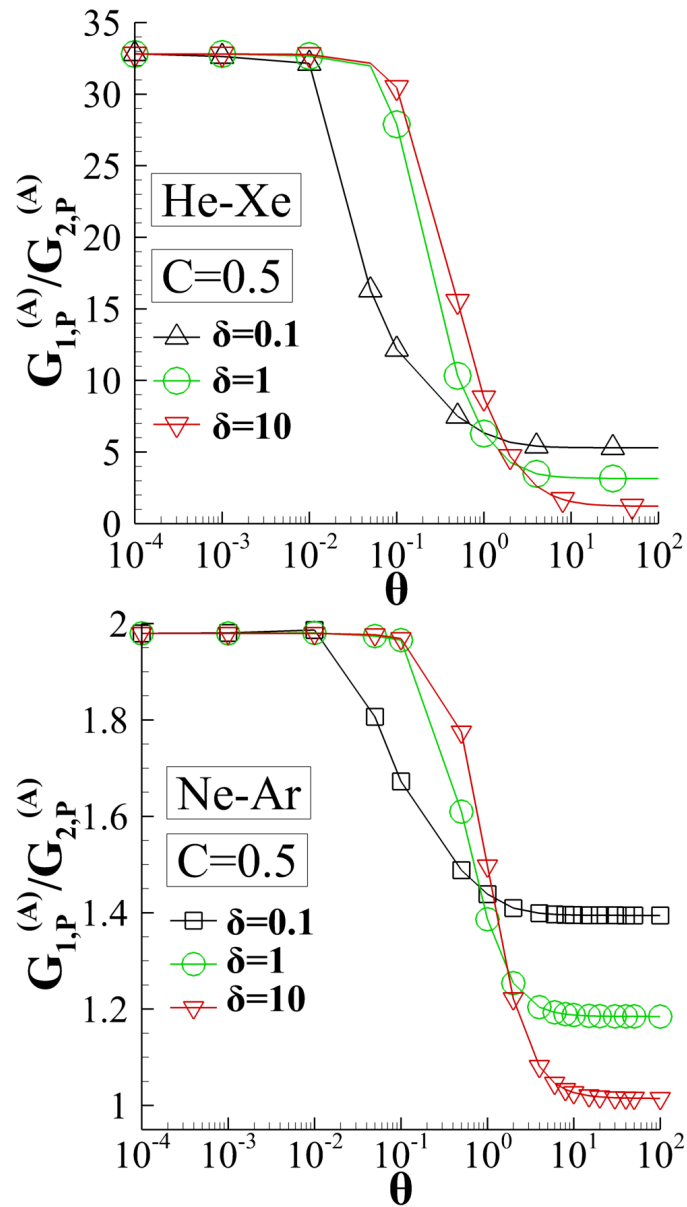
Figure 6.9 Ratio of flow rate amplitudes $G_{1,P}^{(A)}/G_{2,P}^{(A)}$ of the species of He-Xe and Ne-Ar, with $C = 0.5$, in terms of $\theta \in [10^{-4}, 10^2]$ for $\delta = [0.1, 1, 10]$.
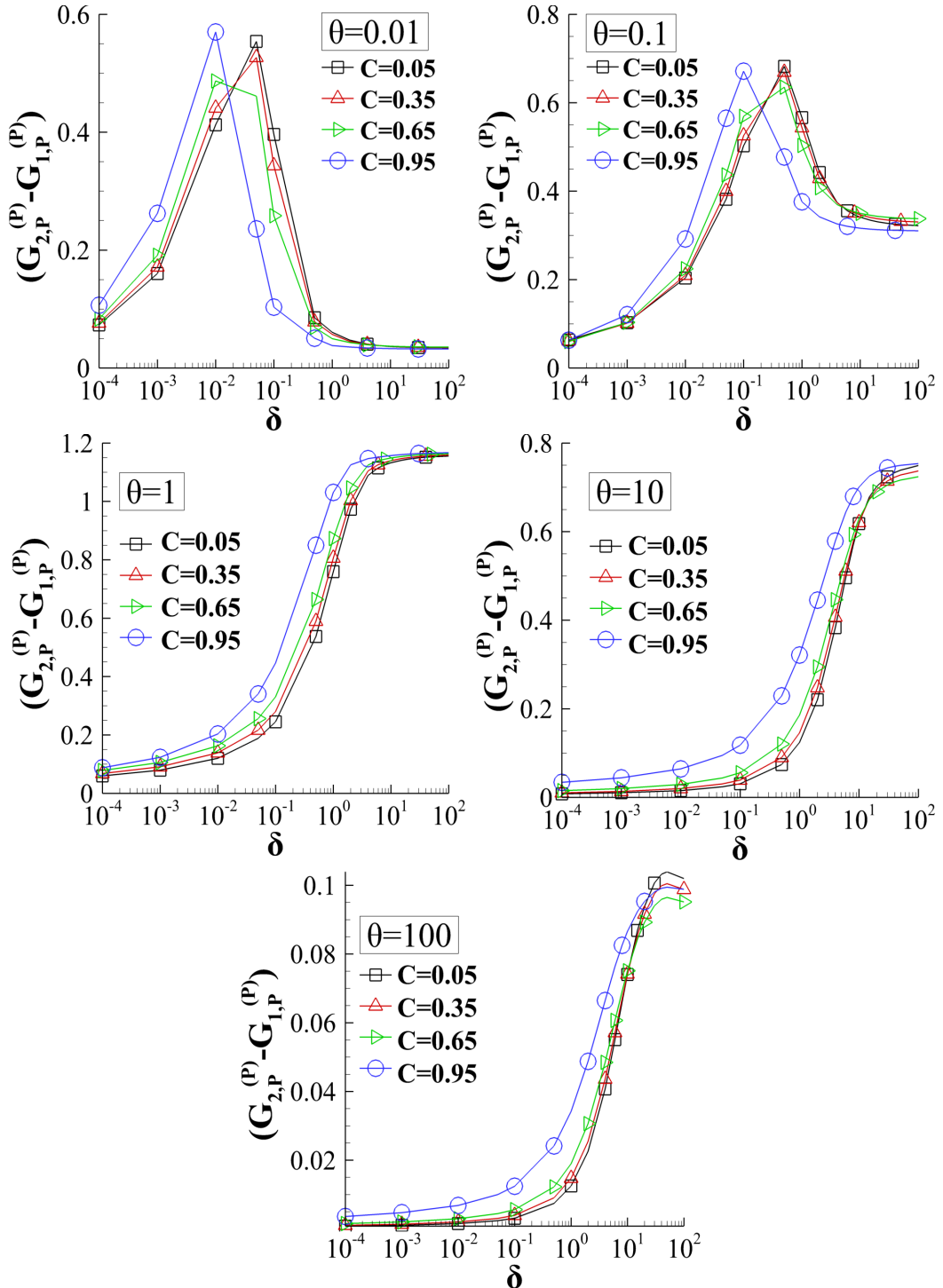
Figure 6.10 Difference of the flow rate phase angles $G_{2,P}^{(P)} - G_{1,P}^{(P)}$ of the species of He-Xe in terms of $\delta \in [10^{-4}, 10^2]$, with $C = [0.05, 0.35, 0.65, 0.95]$ and $\theta = [10^{-2}, 0.1, 1, 10, 10^2]$.

177
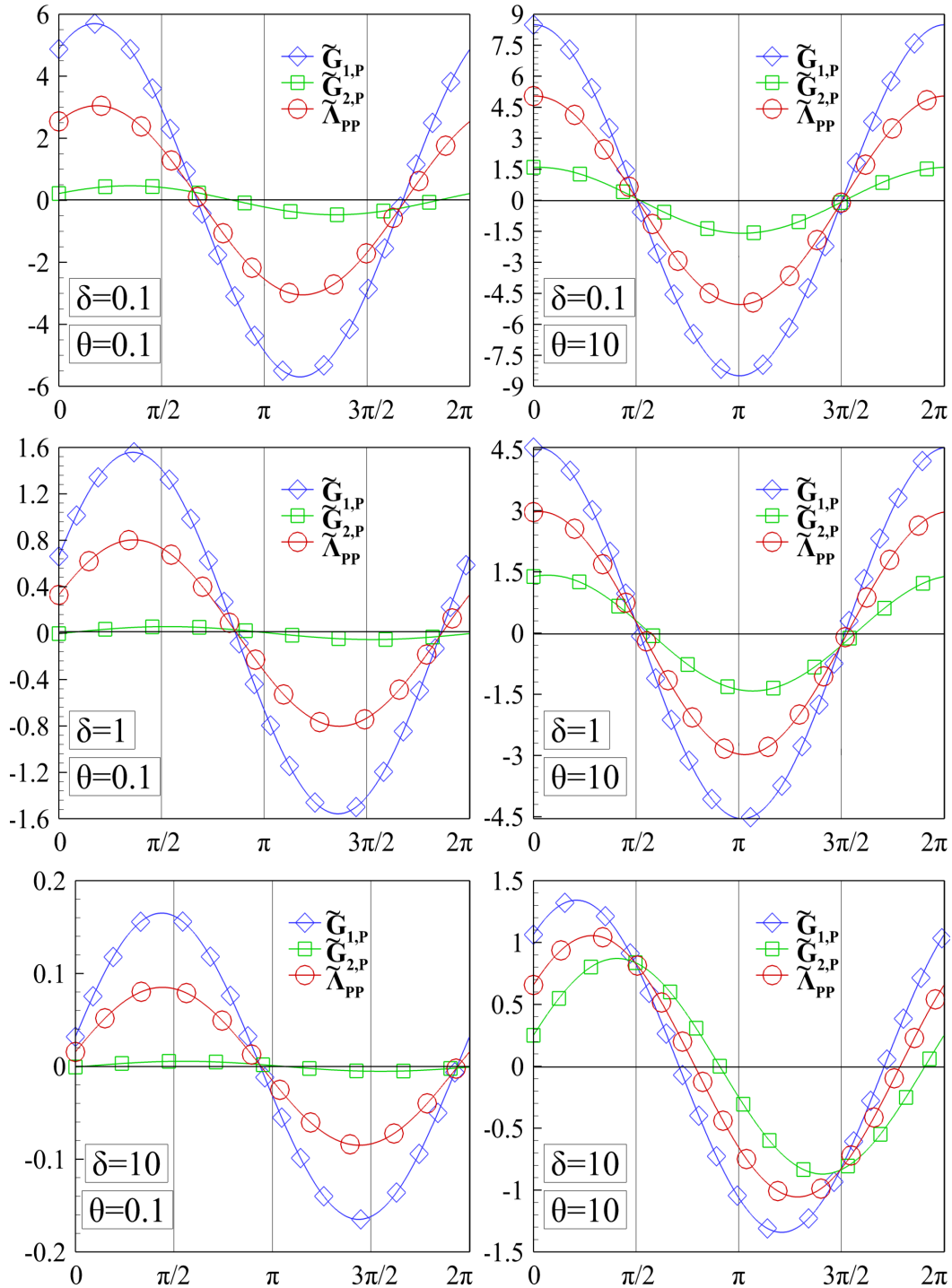
Figure 6.11 Time-dependent flow rates $\tilde{G}_{1,P}(t)$ of He, $\tilde{G}_{2,P}(t)$ of Xe and $\tilde{\Lambda}_{PP}(t)$ of He–Xe, with $C = 0.5$, over one cycle $t \in [0, 2\pi]$ for $\delta = [0.1, 1, 10]$ and $\theta = [0.1, 10]$.

178
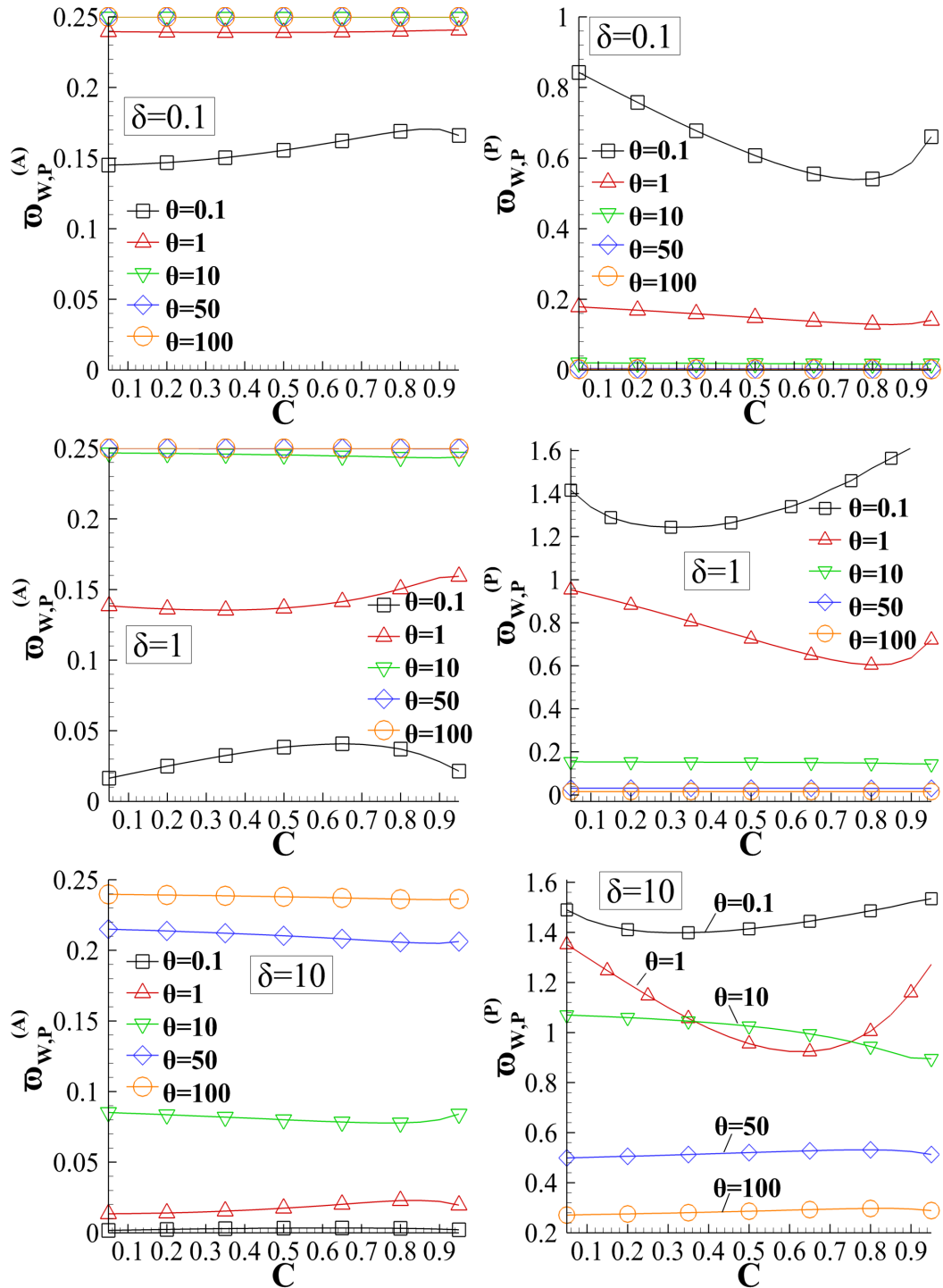
Figure 6.12 Wall shear stress amplitude $\varpi_{W,P}^{(A)}$ and phase angle $\varpi_{W,P}^{(P)}$ of He-Xe in terms of C for $\theta = [0.1, 1, 10, 50, 10^2]$ and $\delta = [0.1, 1, 10]$.

179
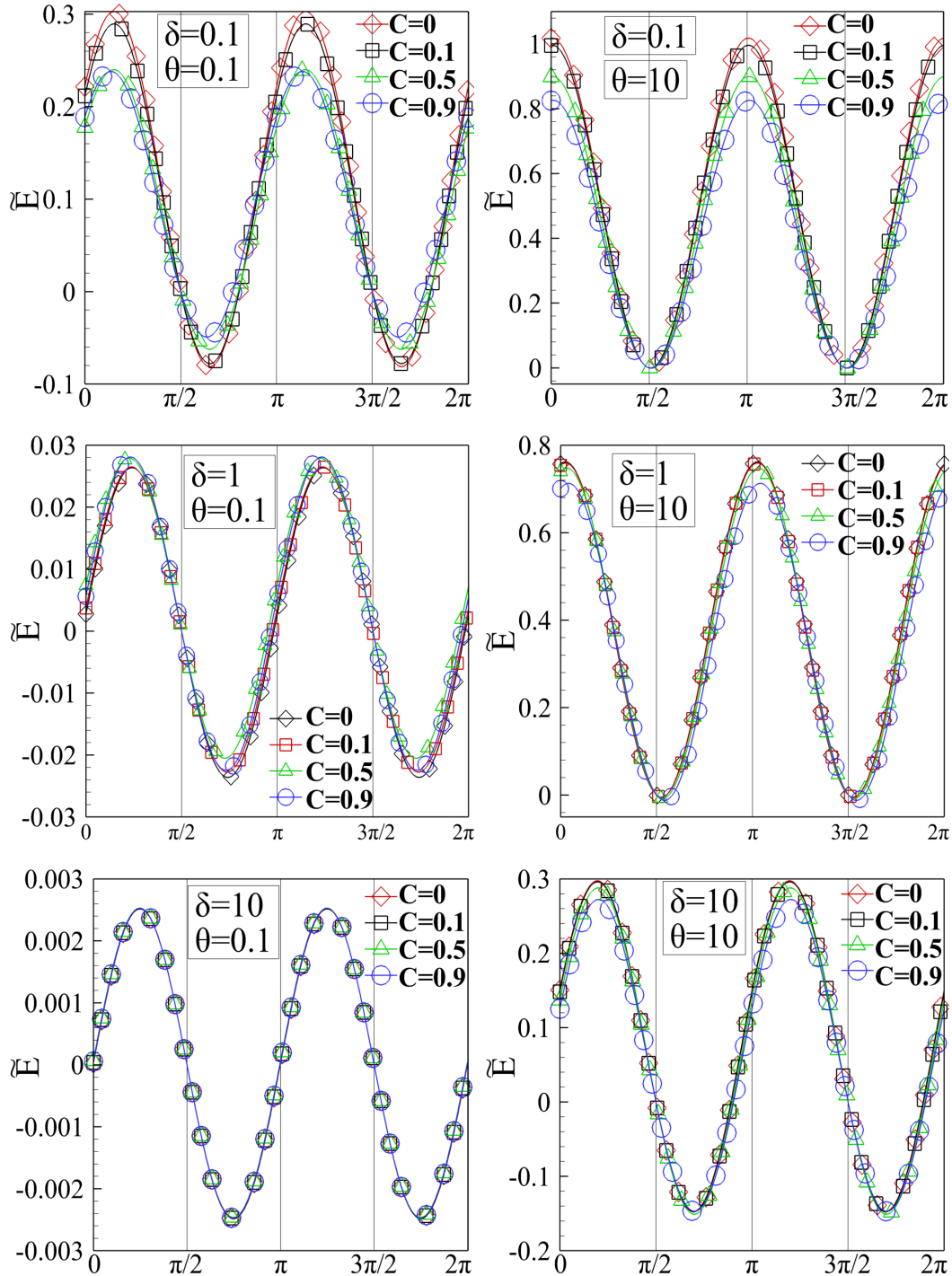
Figure 6.13 Normalized time-dependent pumping power $\tilde{E}\left(t\right)/dx$ of He–Xe, with $C = [0, 0.1, 0, 5, 0.9]$, over one cycle $t \in [0, 2\pi]$ for $\delta = [0.1, 1, 10]$ and $\theta = [0.1, 10]$.

180
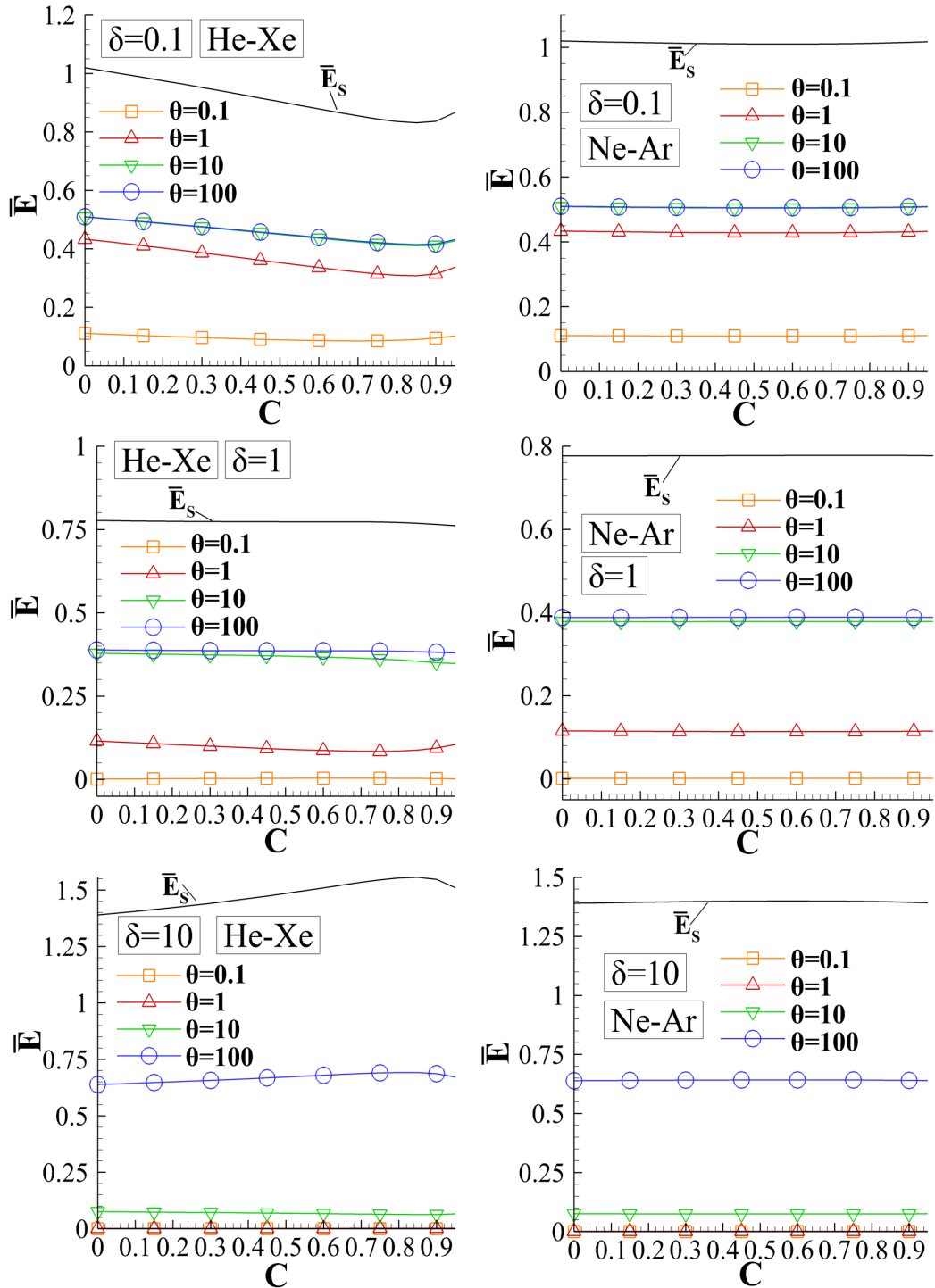
Figure 6.14 Normalized cycle-average pumping power $\bar{E}/dx$ of He–Xe and Ne–Ar in terms of C for $\delta = [0.1, 1, 10]$ and $\theta = [0.1, 1, 10, 10^2]$ ($\bar{E}_S$ is the steady-state pumping power).
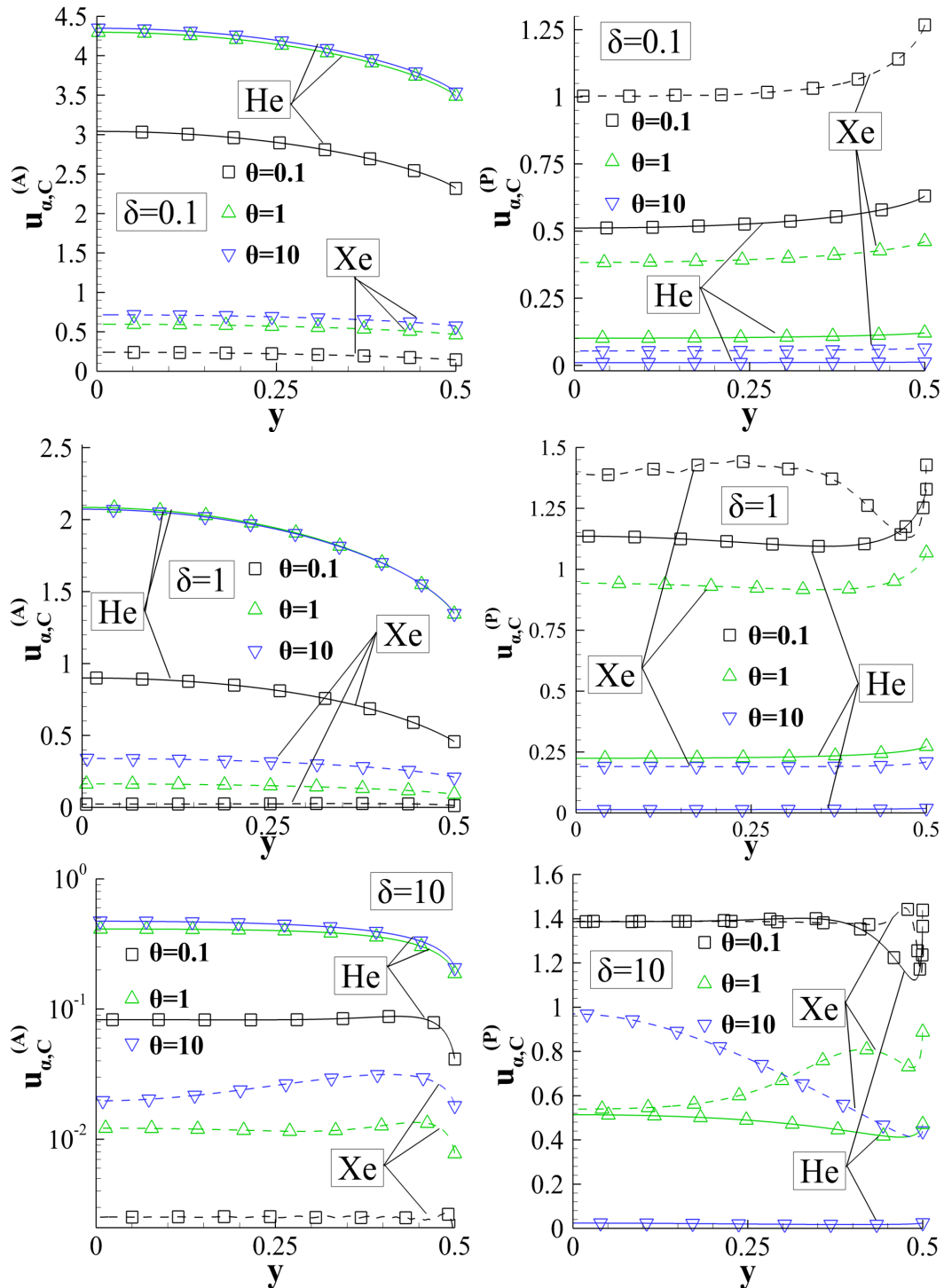
Figure 6.15 Velocity amplitude $u_{a,C}^{(A)}(y)$ and phase angle $u_{a,C}^{(P)}(y)$ of each species of He–Xe, with $C = 0.5$, for $\delta = [0.1, 1, 10]$ and $\theta = [0.1, 1, 10]$ (He: solid lines, Xe: dashed lines).
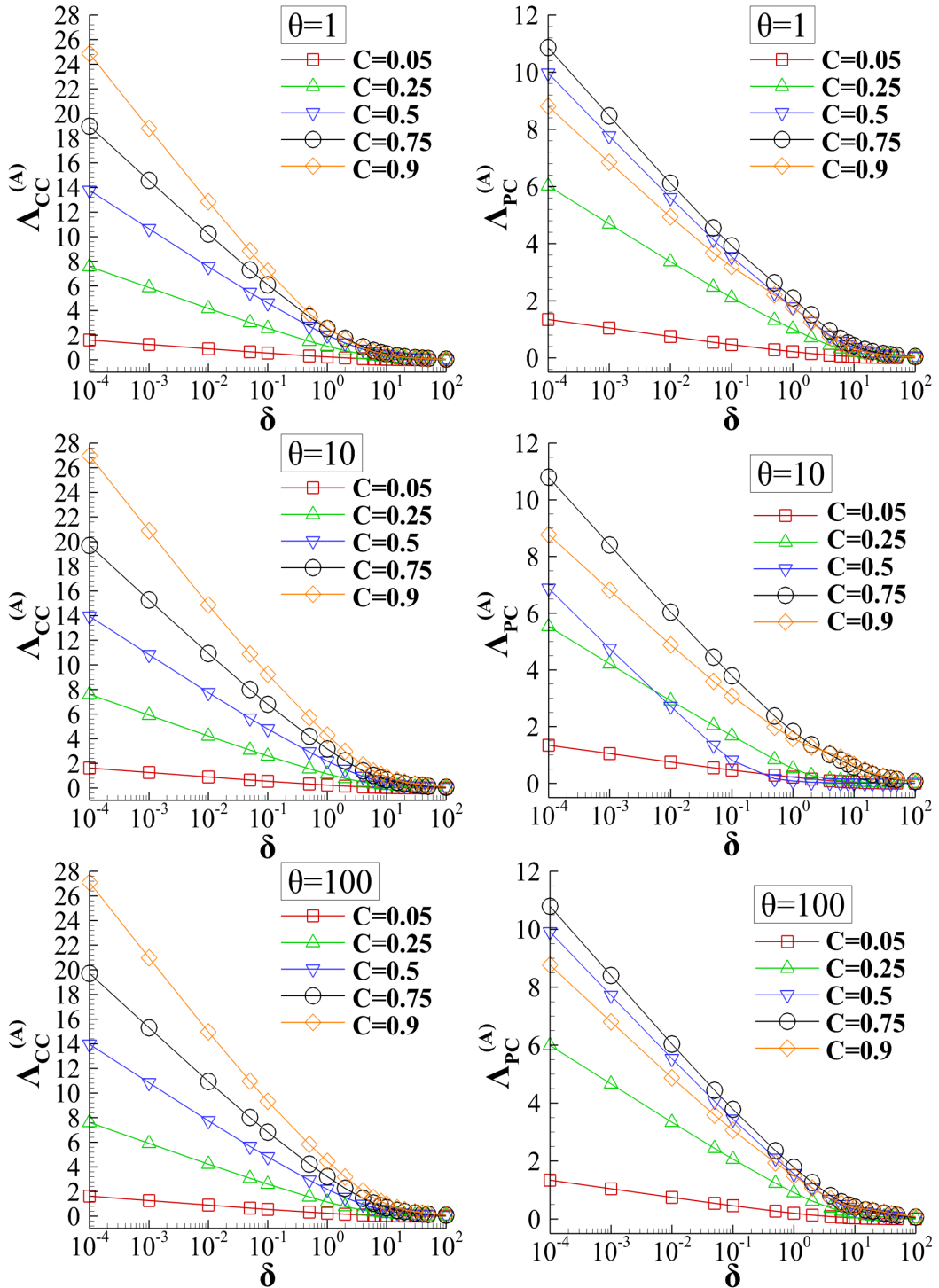
Figure 6.16 Kinetic coefficient amplitudes $\Lambda_{CC}^{(A)}$ and $\Lambda_{PC}^{(A)}$ of He-Xe in terms of $\delta \in [10^{-4}, 10^2]$, with $C = [0, 0.25, 0.5, 0.75, 0.9]$ and $\theta = [1, 10, 10^2]$.

183
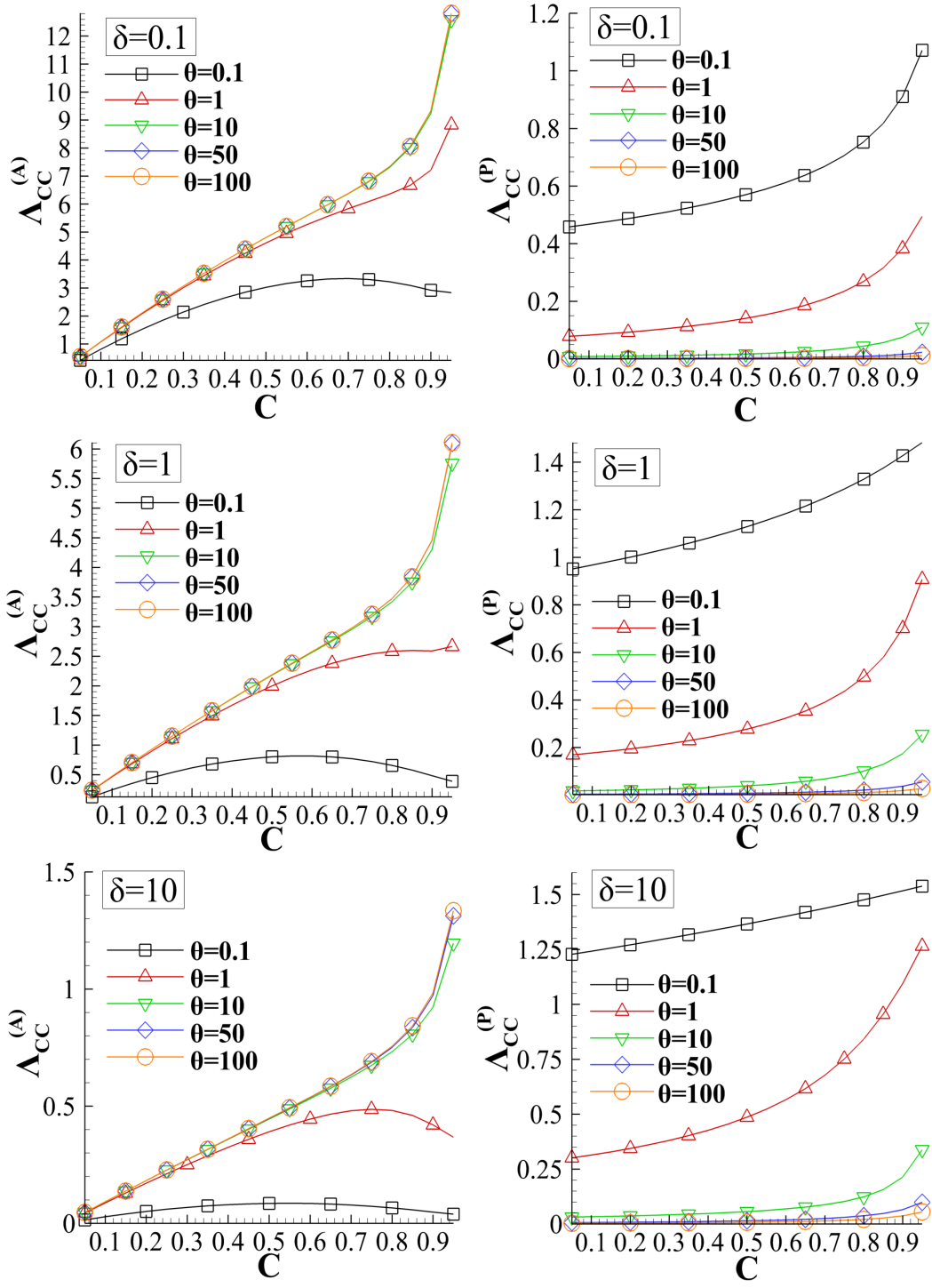
Figure 6.17 Kinetic coefficient amplitude $\Lambda_{CC}^{(A)}$ and phase angles $\Lambda_{CC}^{(P)}$ of He-Xe in terms of the molar fraction C for $\delta = [0.1, 1, 10]$ and $\theta = [10^{-1}, 1, 10, 50, 10^2]$.
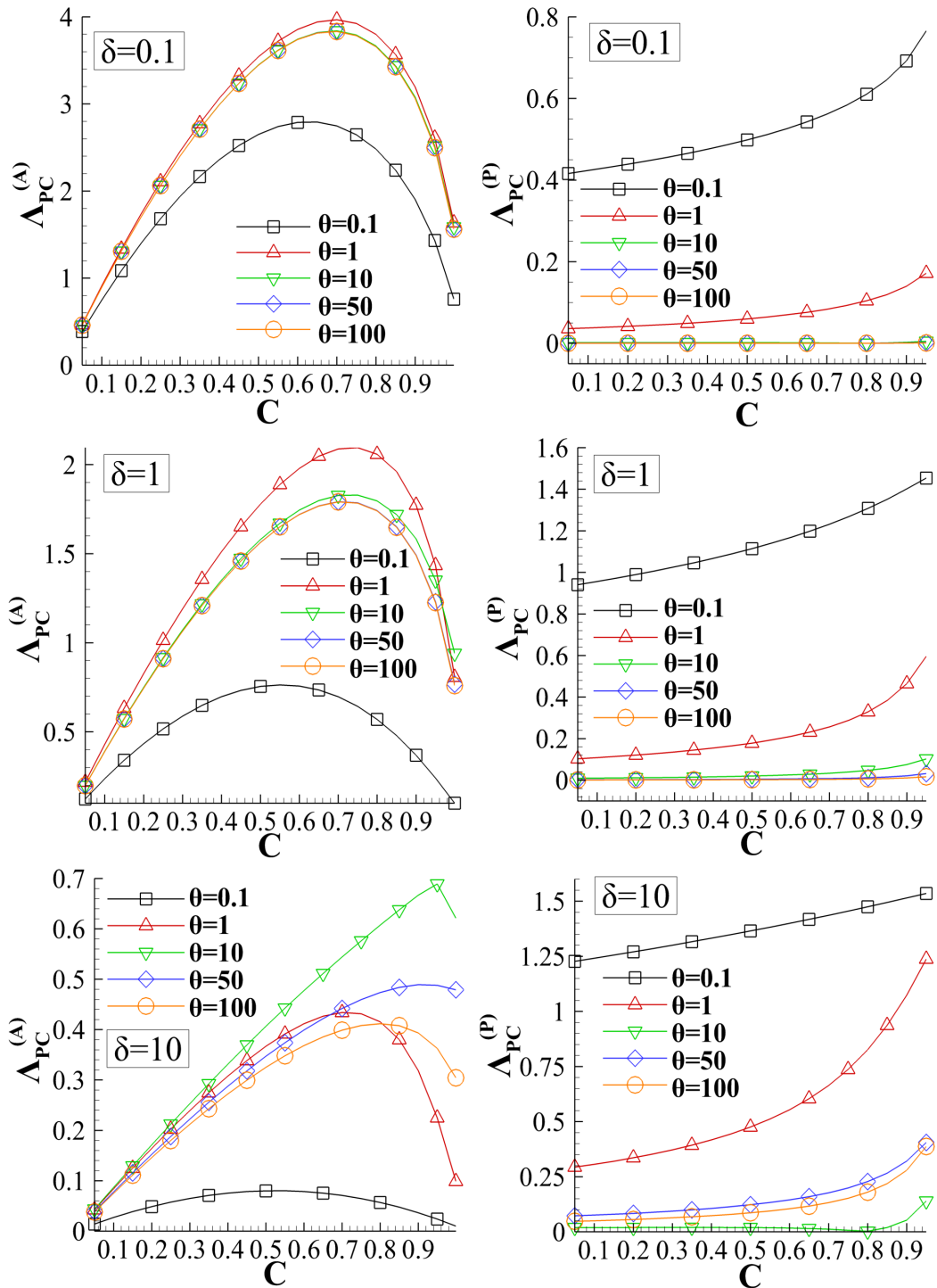
Figure 6.18 Kinetic coefficient amplitude $\Lambda_{PC}^{(A)}$ and phase angle $\Lambda_{PC}^{(P)}$ of He-Xe in terms of the molar fraction C for $\delta = [0.1, 1, 10]$ and $\theta = [10^{-1}, 1, 10, 50, 10^2]$.

Chapter 7

Oscillatory boundary driven rarefied gas flow between parallel plates

7.1 Introduction

Oscillatory boundary-driven flows have been widely investigated in the whole range of the Knudsen number and the oscillation frequency. More specifically, the oscillatory shear driven rarefied gas flow (or the oscillatory Couette flow) has been solved with deterministic modelling in [144, 28, 147] and stochastic modelling in [145, 146]. Even though this flow configuration has already been studied, it is added in the current Thesis since it was used in order to test the complex kinetic codes before the other flow configurations were investigated. The oscillatory shear-driven flow is computed with the linearized unsteady BGK kinetic model equation and the solution is benchmarked with the corresponding results in [28]. The flow is characterized by the gas rarefaction and the oscillation parameter. Furthermore, two parallelization strategies based on Open Multi-Processing (OpenMP) [205] and OpenACC® [206] directives are proposed and tested. Both techniques use a set of directives to specify code and data that can be parallelized. The OpenMP of shared memory model uses multiple threads to express the parallelism however it can be used only in a single computing node. The OpenACC directives supports offloading of both computation and data from a host device (typically a CPU host) to an accelerator device (typically a GPU).

7.2 Flow configuration

Consider the rarefied oscillatory fully-developed isothermal monatomic gas flow between two infinite long parallel plates. The flow is in the $x'-$direction normal to the plates, which are fixed at $y' = \pm H/2$. The flow is caused by the oscillating lower plate at $y' = -H/2$ and the velocity of the plate is written as

$$\tilde{U}_W = \mathrm{R}\left[U_W \exp\left(-i\omega t'\right)\right], \tag{7.1}$$

where R denotes the real part of a complex expression, $i = \sqrt{-1}$, t' is the time independent variable, ω is the oscillation (cyclic) frequency and U_W denotes the amplitude of the oscillating plate. The oscillating plate yields an unsteady gas flow in the $y'-$direction, which depends harmonically on time and it is characterized by its bulk velocity given by

$$\tilde{U}\left(t', x'\right) = \mathrm{R}\left[U\left(x'\right)\exp\left(-i\omega t'\right)\right], \tag{7.2}$$

and its shear stress given by

$$\tilde{P}_{xy}\left(t', x'\right) = \mathrm{R}\left[P_{xy}\left(x'\right)\exp\left(-i\omega t'\right)\right]. \tag{7.3}$$

The functions $\left[U\left(x'\right), P_{xy}\left(x'\right)\right]$ are complex ones and they aren't in phase neither with each other nor with the oscillating plate.

The flow parameters defining the problem are the gas rarefaction parameter δ and the oscillation parameter θ. The first one is given by

$$\delta = \frac{PH}{\mu \upsilon} \tag{7.4}$$

where μ is the gas viscosity at some reference temperature T and $\upsilon = \sqrt{2RT}$ is the most probable molecular speed ($R = k/m$, with k denoting the Boltzmann constant and m the molecular mass, is the gas constant). The second one is the oscillation parameter θ which is written as

$$\theta = \frac{P}{\mu \omega}. \tag{7.5}$$

Next, it is suitable to introduce the dimensionless independent variables

$$x = x'/H, y = y'/H, t = t'\omega. \tag{7.6}$$

188

Then, the bulk velocity and shear stress in Eqs. (7.2)-(7.3) are non-dimensionalized by (U_W) and $(v/(2U_W P))$ respectively to yield:

$$\tilde{u}(t, x) = \mathrm{R}\left[u(x)\exp(-it)\right] =$$

$$= \mathrm{R}\left[u^{(A)}(x)\exp\left[i\left(u^{(P)}(x) - t\right)\right]\right] = u^{(A)}(x)\cos\left[t - u^{(P)}(x)\right] \qquad (7.7)$$

$$\tilde{p}_{xy}(t, x) = \mathrm{R}\left[p_{xy}(x)\exp(-it)\right] =$$

$$= \mathrm{R}\left[p_{xy}^{(A)}(x)\exp\left[i\left(p_{xy}^{(P)}(x) - t\right)\right]\right] = p_{xy}^{(A)}(x)\cos\left[t - p_{xy}^{(P)}(x)\right]. \qquad (7.8)$$

In Eqs. (7.7)-(7.8) the superscripts (A) and (P) refer to the amplitude and the phase angle respectively of each complex quantity. The amplitude and the phase of both quantities are computed in a wide range of the rarefaction and oscillation parameters. The shear stress at the wall is denoted by P_W.

7.3 Kinetic formulation and numerical scheme

The flow is simulated at the kinetic level by the time-dependent BGK kinetic model equation [33], which is written as

$$\frac{\partial \tilde{f}}{\partial t'} + \xi_x \frac{\partial \tilde{f}}{\partial x'} = \frac{P}{\mu}\left(f^M - \tilde{f}\right). \qquad (7.9)$$

Here, $f = f(t', x', \boldsymbol{\xi})$ is the unknown distribution function which is a function of time t', position x' and molecular velocity vector $\boldsymbol{\xi} = (\xi_x, \xi_y, \xi_z)$. The local Maxwellian distribution is written as

$$f^M = n\left(\frac{m}{2\pi kT}\right)^{3/2}\exp\left[-m\left[\boldsymbol{\xi} - \tilde{U}(t', x')\right]^2 \Big/ (2kT)\right], \qquad (7.10)$$

where the number density n and the temperature T are constant due to the isothermal fully developed flow assumption. The velocity and shear stress (defined in Eqs. (7.2)-(7.3)) may be obtained by the first and second moments of f according to

$$\tilde{U}(t', x') = \frac{1}{n}\int \xi_x \tilde{f}(t', x', \boldsymbol{\xi})\,d\boldsymbol{\xi} \qquad (7.11)$$

and

$$\tilde{P}_{xy}(t', x') = m\int \xi_x\left(\xi_y - \tilde{U}\right)\tilde{f}(t', x', \boldsymbol{\xi})\,d\boldsymbol{\xi}, \qquad (7.12)$$

189

respectively.

Next, the condition of small velocity amplitude of the oscillating wall ($U_W \ll 1$) allows the linearization of Eq. (7.9) by representing the unknown distribution function as

$$f\left(t', x', \boldsymbol{\xi}\right) = f_0 \left[1 + \tilde{h}\left(t, x, \boldsymbol{c}\right) \frac{U_W}{\upsilon}\right], \tag{7.13}$$

where $\boldsymbol{c} = \boldsymbol{\xi}/\upsilon$, $f_0 = \frac{n}{\pi^{3/2}\upsilon^3} \exp\left[-\boldsymbol{c}^2\right]$ is the absolute Maxwellian and $\tilde{h}\left(t, x, \boldsymbol{c}\right)$ is the unknown perturbed distribution function. Substituting expressions (7.13) into Eq. (7.9) and introducing the dimensionless variables, yields the following linearized BGK kinetic model equation:

$$\frac{\delta}{\theta} \frac{\partial \tilde{h}}{\partial t} + c_x \frac{\partial \tilde{h}}{\partial x} = \delta \left[2c_y \tilde{u}\left(t, x\right) - \tilde{h}\left(t, x, \boldsymbol{c}\right)\right]. \tag{7.14}$$

Since Eq. (7.14) is linear, it is convenient to introduce the complex distribution function $h\left(x, \boldsymbol{c}\right)$ so that

$$\tilde{h}\left(t, x, \boldsymbol{c}\right) = \mathrm{R}\left[h\left(x, \boldsymbol{c}\right) \exp\left(-it\right)\right]. \tag{7.15}$$

Then, Eq. (7.14) is rewritten in terms of h as

$$h\left(\delta - \frac{\delta}{\theta}i\right) + c_x \frac{\partial h}{\partial x} = 2\delta c_y u\left(x\right). \tag{7.16}$$

The non-dimensionalization and linearization procedures are also applied to the velocity and the shear stress given by Eqs. (7.11) and (7.12) to obtain:

$$u\left(x\right) = \frac{1}{\pi^{3/2}} \int_{-\infty}^{\infty} \int_{-\infty}^{\infty} \int_{-\infty}^{\infty} c_y h e^{-c^2} dc_x dc_y dc_z, \tag{7.17}$$

$$p_{xy}\left(x\right) = \frac{1}{\pi^{3/2}} \int_{-\infty}^{\infty} \int_{-\infty}^{\infty} \int_{-\infty}^{\infty} c_x c_y h e^{-c^2} dc_x dc_y dc_z. \tag{7.18}$$

At this stage the components c_y and c_z of the molecular velocity vector may be eliminated by applying the projection procedure and introducing the reduced perturbed distribution function

$$Y\left(x, c_x\right) = \frac{1}{\pi} \int_{-\infty}^{\infty} \int_{-\infty}^{\infty} c_y h\left(x, c_x, c_y, c_z\right) \exp\left[-c_y^2 - c_z^2\right] dc_y dc_z. \tag{7.19}$$

Equation (7.19) is multiplied by $c_y \exp\left(-c_y^2 - c_z^2\right)/\pi$ and the resulting equation is integrated over c_y and c_z to deduce

$$\left(\delta - i\frac{\delta}{\theta}\right) Y + c_x \frac{\partial Y}{\partial x} = \delta u. \tag{7.20}$$

Operating similarly on the moments of h, given by Eqs. (7.17)-(7.18), yields:

$$u\left(x\right) = \frac{1}{\sqrt{\pi}} \int_{-\infty}^{\infty} Y e^{-c_x^2} dc_x, \tag{7.21}$$

$$p_{xy}\left(x\right) = \frac{1}{\sqrt{\pi}} \int_{-\infty}^{\infty} c_x Y e^{-c_x^2} dc_x. \tag{7.22}$$

It is noted that the distribution function Y as well as the velocity u and the shear stress p_{xy} are complex quantities.

Next, the same non-dimensionalization and linearization procedures are also applied in the boundary conditions. The Maxwell diffuse boundary conditions supplementing the governing equation (7.20) are written as

$$Y\left(-1/2, c_x\right) = 1, c_x > 0 \tag{7.23}$$

$$Y\left(1/2, c_x\right) = 0, c_x < 0. \tag{7.24}$$

The kinetic formulation of the oscillatory Couette flow is defined by Eq. (7.20) with the associated moments (7.21)-(7.22) subject to boundary conditions (7.23)-(7.24). The numerical solution is based on the DVM method which substitutes the continuum spectrum $c_x \in [0, \infty)$ a discrete set $c_{x,m}$, $m = 1, 2...M$, which is taken to be the roots of the Legendre polynomial of order M, accordingly mapped from $[-1, 1]$ to $[0, \infty)$. The discretization in the physical space is based on a second order central difference scheme. The discretized equations are solved in an iterative manner and the iteration map is concluded when the criteria

$$\left|u_{Re,i}^{(k+1)} - u_{Re,i}^{(k)}\right| < \varepsilon \quad \text{and} \quad \left|u_{Im,i}^{(k+1)} - u_{Im,i}^{(k)}\right| < \varepsilon \tag{7.25}$$

is fulfilled. Here, ε is the tolerance parameter, the superscript k denotes the iteration index, $i = 1, 2...L + 1$ are the nodes in the physical space, while $u_{Re,i}$ and $u_{Im,i}$ are the real and imaginary part of macroscopic velocity respectively at each node (i).

Here it is interesting to note that if the complex notation is directly applied in a computer code then the discretization in the physical space is similar to the corresponding one of the steady-state kinetic equations. However, if the governing equation (7.20) is separated into real and imaginary parts then specific attention should be given in the discretization process. At first, the complex distribution function is written as $Y = Y_{Re} + iY_{Im}$ then it is inserted into Eq. (7.20) and finally the real and imaginary parts are given in the discretized form:

$$c_{x,m} \left.\frac{\partial Y_{Re}^{(k+1/2)}}{\partial x}\right|_{i,m} + \delta \left. Y_{Re}^{(k+1/2)}\right|_{i,m} + \frac{\delta}{\theta} \left. Y_{Im}^{(k+1/2)}\right|_{i,m} = \delta \left. u_{Re}^{(k)}\right|_i, \qquad (7.26)$$

$$c_{x,m} \left.\frac{\partial Y_{Im}^{(k+1/2)}}{\partial x}\right|_{i,m} + \delta \left. Y_{Im}^{(k+1/2)}\right|_{i,m} - \frac{\delta}{\theta} \left. Y_{Re}^{(k+1/2)}\right|_{i,m} = \delta \left. u_{Im}^{(k)}\right|_i. \qquad (7.27)$$

Eqs. (7.26)-(7.27) are rewritten as

$$c_{x,m} \frac{Y_{Re,i+\frac{1}{2},m}^{(k+1/2)} - Y_{Re,i-\frac{1}{2},m}^{(k+1/2)}}{h} + \frac{\delta}{2}\left(Y_{Re,i+\frac{1}{2},m}^{(k+1/2)} + Y_{Re,i-\frac{1}{2},m}^{(k+1/2)}\right)$$
$$+ \frac{\delta}{2\theta}\left(Y_{Im,i+\frac{1}{2},m}^{(k+1/2)} + Y_{Im,i-\frac{1}{2},m}^{(k+1/2)}\right) = \frac{\delta}{2}\left(u_{Re,i+\frac{1}{2}} + u_{Re,i-\frac{1}{2}}\right)^{(k)}, \qquad (7.28)$$

$$c_{x,m} \frac{Y_{Im,i+\frac{1}{2},m}^{(k+1/2)} - Y_{Im,,i-\frac{1}{2},m}^{(k+1/2)}}{h} + \frac{\delta}{2}\left(Y_{Im,i+\frac{1}{2},m}^{(k+1/2)} + Y_{Im,,i-\frac{1}{2},m}^{(k+1/2)}\right)$$
$$- \frac{\delta}{2\theta}\left(Y_{Re,i+\frac{1}{2},m}^{(k+1/2)} + Y_{Re,i-\frac{1}{2},m}^{(k+1/2)}\right) = \frac{\delta}{2}\left(u_{Im,i+\frac{1}{2}} + u_{Im,,i-\frac{1}{2}}\right)^{(k)}, \qquad (7.29)$$

where h is the distance between adjacent nodes in the physical space. It is seen that the two equations are coupled and the term $Y_{Im,i+\frac{1}{2},m}^{(k+1/2)}$ is in the Eq. (7.28) even though it is computed from Eq. (7.29). Therefore, Eq. (7.29) is solved in terms of $Y_{Im,i+\frac{1}{2},m}^{(k+1/2)}$ and then the solution is inserted into Eq. (7.28) which is given by

$$Y_{Re,i+\frac{1}{2},m}^{(k+1/2)} = \left[1 + T0 + \frac{T0^2}{\theta^2\left(1+T0\right)}\right]^{-1} \left\{ \begin{array}{l} \left(1 - T0 - \frac{T0^2}{\theta^2(1+T0)}\right) Y_{Re,i-\frac{1}{2},m}^{(k+1/2)} \\ - \frac{T0(1-T0)}{\theta(1+T0)} Y_{Im,i-\frac{1}{2},m}^{(k+1/2)} \\ + T0\left(u_{Re,i+\frac{1}{2}} + u_{Re,i-\frac{1}{2}}\right)^{(k)} \\ + \frac{T0^2}{\theta(1+T0)}\left(u_{Im,i+\frac{1}{2}} + u_{Im,i-\frac{1}{2}}\right)^{(k)} \end{array} \right\}, \quad (7.30)$$

where $T0 = h\delta/2c_{x,m}$. The imaginary part is given by Eq. (7.29) since the real part of the distribution function has been already computed by Eq.(7.30). It is noted that Eq.

(7.30) is derived for positive values of the molecular velocity $c_{x,m}$. In conclusion, the use of Eqs. (7.28)-(7.29) isn't encouraged since the complex solution of Eq. (7.20) is more easily solved.

7.4 Parallelization techniques

In all the deterministic kinetic solvers the computational cost is high since the investigated problems can be from 2D up to 5D. In the current flow configuration, the cost is the minimum since the problem is 1D in the physical space and 1D in the molecular velocity space. In DVM the continuum molecular velocity spectrum is replaced by a discrete set of molecular velocities, and thus the partial integrodifferential kinetic equation (7.20) is reduced to a set of differential equations. Each of these differential equations corresponds to one discrete velocity and can be solved separately. Therefore, the main strategy for parallelization is to assign each molecular velocity in a different processor. The estimates of the distribution functions at each processor are summed to estimate the updated macroscopic quantities [207]. The solution is performed in an iterative manner and the update data are exchanged between different molecular velocities one time per iteration. In the present Section, the aforementioned remarks are applied into two parallel versions of the kinetic solver, the first one is based on OpenMP directives while the second one is based on OpenACC directives.

7.4.1 Kinetic solver with OpenMP directives

Usually each CPU can solve independently a number of equations by using MPI processes or by employing OpenMP threads. With the OpenMP directive "*!\$omp parallel do*", the iterations of a do-loop are divided into the threads of the CPU and therefore the lop can be executed in parallel. This is also called loop-level parallelism [208] and it usually involves making small changes to the source code where the performances bottlenecks are seen. However, there is a more generalized parallel region construct to express parallel execution where multiple loops could be inside this region. This practice has the benefit that it can reduce the overhead of emerging threads and synchronization that is necessary when each parallel loop or region is created [208].

A parallel region is created with the directive "*!\$omp parallel clause*" and it includes the kinetic iteration algorithm. The term "*clause*" refers to the data that can be "*private*", "*shared*", "*default*", "*reduction*", and "*if*". In the kinetic solver, the

clause "*private*" is used to identify variables that are used as temporary within the parallel region such as the indexes of the loops or some coefficients necessary for the marching scheme. Also, if the distribution function isn't stored for all the nodes in the molecular velocity space, then it should also be declared as "*private*" in order to avoid race conditions. The race condition is explained in the next Section. Moreover, the "*shared*" variables typically include the roots and weights of the quadrature integration scheme and the macroscopic quantities from the previous iterations. Actually, these variables don't change their values in the parallel region. If it is necessary, only a single thread can update them in order to avoid race conditions. The "*reduction*" variables include the new macroscopic quantities which are computed with a reduction process from the new distribution functions.

Next, inside the parallel region the available OpenMP threads are mapped to the iterations of the loop with the molecular velocities. Each OpenMP thread executes a part of the loop. The new distribution functions are computed serially in the inner loops with the marching scheme. It is noted that since the OpenMP threads have already been assigned with work they can't be redeployed to acquire new computational load. Also, if the distribution functions are kept only for the nodes in the physical space then the distribution functions must be declared private. Then, the macroscopic quantities are computed and finally the relative error is computed. This procedure terminates the current iteration and then the error is checked in order to either finish or continue the computations. If the computations are continued, then the OpenMP threads are assigned with new computational work without having to be recreated.

7.4.2 Kinetic solver with OpenACC directives

The parallelism in a GPU is expressed differently. OpenACC defines three levels of parallelism: gang, worker, and vector. Additional execution may be marked as being sequential. This structure is also the same for CUDA where the equivalent to gang is the block, the equivalent to worker is the warp and the equivalent to vector is the thread. Vector parallelism is applied with vector operations that are performed with a particular vector length, indicating how many data elements may be operated on with the same instruction. Gang parallelism applied with gangs that work independently of each other and may not synchronize. Worker parallelism is between vector and gang levels. Using these three levels of parallelism, plus sequential, a programmer can map the parallelism in the code to any device. The more explicitly this mapping is done the less portable the code is even though it maximizes efficiency [209].

The changes in the kinetic iteration algorithm are shown in Fig. 7.1 where the typical flow chart has been introduced with the OpenACC additions. The data region will be explained later. At the first the attention is focused inside the iteration map where the computations are made. The do-loops where the values of the previous iterations are stored, are parallelized with the gang clause before each do-loop ("*!\$acc parallel loop gang*"). This accounts for the 1st acc parallel loop that is seen in Fig. 7.1.

Next, the molecular velocities are mapped to the gangs of the GPU. A single gang solves each molecular velocity. The number of gangs depends on the GPU however it can be around hundreds or even thousands. Here, the strategy is divided into two cases depending on whether the distribution function is stored at the memory for all molecular velocities. If it is stored then the parallel region is enabled with the directive "*!\$acc parallel loop gang*". This is the first strategy and it is usually applied in 1D problems where the spatial nodes are limited. However, in the second strategy, where the distribution function is stored at the memory only for spatial nodes, the distribution function needs to be declared "*private*". This means that each gang has a private copy of the distribution function in its memory. This is necessary only when the distribution function of the current molecular velocity is kept in the memory. Thus, when several gangs are employed, they need to compute their copy of the distribution function for a certain molecular velocity. By making private the distribution function, each gang computes a certain distribution function and therefore it works only on certain part of data. Otherwise if the distribution function isn't made private, the gang one could affect the distribution function of the gang two and then a data race is encountered leading to incorrect results. Of course, by keeping Y private for each gang this increases the memory in the GPU since the gangs are usually several hundred. Hence, the number of gangs is going to be limited depending on how many variables are being made private. After each loops ends the directive "*!\$acc end parallel loop*" is needed.

The next level of parallelism is introduced in the following do-loops which compute the new distribution functions and the macroscopic quantities and it is shown with the color green in Fig. 7.1. In this part of the solver a severe bottleneck is encountered. In the serial and parallel versions, a data dependency exists when the new distribution function is computed which leads to slower computations. In the OpenACC version, due to the data dependency, this part of the code is executed sequentially with the following command: "*!\$acc loop seq*". Eliminating the data dependency will decrease the computation time.

The computation of the macroscopic quantities is a reduction process and it is different in the two strategies. It is noted that OpenACC does not support array reduction while OpenMP does. When one or more loop iterations need to access an element in memory at the same time data races can occur. For instance, if one loop iteration is modifying the value contained in a variable and another is trying to read from the same variable in parallel, different results may occur depending on which iteration occurs first. In serial programs, the sequential loops ensure that the variable will be modified and read in a predictable order, but parallel programs don't make guarantees that a particular loop iteration will happen before another.

In the first strategy, the gangs are mapped to the spatial nodes and the vectors to the velocity nodes. The macroscopic quantities are reduced to temporary values and then each vector adds its partial sum to the general one that is assigned to a gang. In the second strategy, the clause "*atomic*" is needed since each gang has a private copy of the distribution function. The "*atomic*" directive will ensure that two vectors will not attempt to perform the update in the macroscopic quantity simultaneously. Finally, the calculations for the convergence criterion are parallelized with the directive "*!\$acc parallel loop gang*" as it is shown in Fig. 7.1. The error is checked in the host (or the CPU) and if an extra iteration is needed the same processes are repeated.

Even after applying all the aforementioned remarks there is a high chance that the solver is much slower than the serial CPU version. It is critical to understand that the main optimization in GPU's is done by handing efficiently the memory access. Since there is a separate memory in a GPU it is better to copy all data in the GPU with a single transfer instead of copying continuously data from the host memory to the GPU. In CUDA the memory optimization is of major importance since the programmer can handle all the available types of memory, the global, the shared and the texture memory. In OpenACC the main difference with CUDA is that the parallel loops will run in the GPU even if there aren't any data declared in the GPU while in CUDA the data have to be declared before the computations. Therefore, in OpenACC the computations are made in the GPU however the constant transfer of data is maximizing the overall time. All of the above point to the fact that each host code needs a region where the data are defined in the GPU. Thus the directive "*!\$acc data*" is applied which ensures that all the variables used in the computations are declared in the GPU and they are stored there for as long as the computations continue. After convergence has been reached then the data region ceases to exist. Each variable is defined differently in the directive and a complete analysis is given in [209]. Here for the kinetic solver, the clause "*copyin*"

196

is used for variables such as the roots and the weights of the integration method, the clause "*copy*" for variables such as the macroscopic quantities and the clause "*create*" for variables such as the arrays where the previous values of the macroscopic quantities are stored. It is mentioned that the size of all variables must be declared explicitly.

After optimizing data transfer the next step is to optimize the compute kernel. There are two tuning choices: changing the number of vectors per gang or changing the total number of gangs used. The parallel or kernel directives are extended in order to add the "*vector_length*" which the default value is 32 and can change to 1, 32, 64, 128, 256, 512, 1024. The "*num_gangs*" changes the number of gangs to the value that is the most efficient. It is noted that all these optimizations need to be verified with a profiler which is usually the PGPROF [210] for OpenACC and CUDA FORTRAN.

7.5   Results and discussion

Computational results include the amplitude and the phase angle of the shear stress at the walls p_W. The results are benchmarked with the Tables 2 and 3 from [28]. Different grids in the physical and velocity spaces have been applied and very good agreement between the present results and [28] is achieved with $M = 300$ and $N = 10000$. In addition, the parallelization strategies are benchmarked and the corresponding computational times and the speed-up are presented for different grids in the physical and velocity spaces.

In Table 7.1, the wall shear stress amplitude $p_W^{(A)}(\mp 1/2)$ is presented in terms of the gas rarefaction $\delta \in [10^{-2}, 50]$ and the oscillation parameter $\theta = [0.1, 1, 10, 50]$. For any given δ, $p_W^{(A)}(-1/2)$ is monotonically decreased as θ is increased while $p_W^{(A)}(1/2)$ is monotonically increased. In addition, for any given θ, as δ is increased, $p_W^{(A)}(1/2)$ is monotonically decreased. The dependency of $p_W^{(A)}(-1/2)$ on δ is more complex. At first, it is decreased until a certain value in the interval $0.1\theta \leq \delta \leq \theta$, where a local minimum is observed, then it is increased up to some δ, which depends on θ, and finally as δ is further increased it becomes constant. It is noted that for all θ, as $\delta \to 0$, the well-known analytical steady-state free molecular flow rate equal to $1/(2\sqrt{\pi}) = 0.282$ [28], is properly recovered. Also, for small values of θ and adequately dense atmosphere (large values of δ), $p_W^{(A)}(1/2)$ tends to diminish while the value of $p_W^{(A)}(-1/2)$ becomes constant. This behavior, which appears in high oscillation frequencies (small θ) is due to inertia forces and the fluid is rapidly reduced as it propagates in the physical space.

197

In Table 7.2, the wall shear stress phase angle $p_W^{(P)}(\mp 1/2)$ is presented in terms of the gas rarefaction $\delta \in [10^{-2}, 50]$ and the oscillation parameter $\theta = [0.1, 1, 10, 50]$. For any given θ, as δ is increased, i.e., as the oscillation frequency is increased, the phase angle $p_W^{(P)}(-1/2)$ is decreased until a certain value and then it is slightly increased. As δ is further increased it becomes constant. On the other hand, the phase angle $p_W^{(P)}(1/2)$ is monotonically increased as δ is increased. It is noted that for all θ, as $\delta \to 0$, the phase angle at both walls becomes zero since the steady-state flow is recovered. Furthermore, in terms of a constant value of δ the behavior is more complex. For $\delta \leq 0.1$, as θ is increased, $p_W^{(P)}(-1/2)$ is monotonically increased, while for $0.1 < \delta < 8$ it is initially decreased until some value of θ, where a local minimum is observed, and then it is increased. For $\delta > 8$, the phase angle $p_W^{(P)}(-1/2)$ is monotonically decreased as θ is increased. It is also noted that the phase angle $p_W^{(P)}(1/2)$ is monotonically decreased as θ is increased. Finally, the aforementioned remarks for both the amplitude and the phase angle of the wall shear stress are in agreement with the corresponding ones in [28].

Next, the computational time for three versions of the kinetic solver are presented in Table 7.3. The versions are: serial, parallelized with the OpenMP directives (4 and 8 threads) and parallelized with the OpenACC directives. Here, since the flow is 1D, the OpenACC version is the first of the cases mentioned in Section 7.4.2. The tested CPU is the INTEL® Core i7-7700K @4.2 GHz with a maximum number of 8 threads and the tested GPU is the NVIDIA® TITAN Xp. The results have been obtained for $M = 80, 300, 1000$ and $N = 10^3, 10^4, 10^5$. The execution time of all versions has been measured for 389 iterations (simulation case for $\delta = \theta = 10$). The computational time of the serial version is always the largest and it is considered as the reference case.

At first, it is seen that the OpenACC version always needs the least time except for $M = 80$ and $N = 10^4, 10^5$ where the OpenMP version with 8 threads exceeds it. It seems that the increased number of spatial nodes affects the time and since the molecular velocities aren't enough, the GPU isn't fully used. Both OpenMP versions decrease the computational time however it seems that the one with the 8-threads isn't as efficient as the one with the 4-threads. The decrease in computational time isn't equivalent to the employed threads. However, the additional threads aren't fully employed since the current tests are made on the operating system Windows®. It is noted that the parallelized versions haven't been optimized. The loop scheduling is the default one and it is done by the PGI® compiler. A more detailed analysis on the

scheduling of the OpenMP threads and more importantly on the gangs and the vector length of the GPU could further decrease the computational time.

Finally, the speed-up between the serial and the parallelized versions is defined as $S = T_{serial}/T_{par}$ where par denotes each parallelized version, the one with 4 OpenMP threads, the other one with 8 OpenMP threads and the final one with the OpenACC directives. In Table 7.4, the speed-up S is presented in terms of several values of the velocity and physical space grids for the three parallelized versions. It is seen that the OpenACC version has the largest speed-up in comparison with the OpenMP versions. The speed-up of the OpenACC version is increased as the velocity grid is increased. As the spatial nodes are increased the speed-up is also increased. However, the increase is larger when the molecular velocities are increased. This behavior is expected since they are directly connected to the gangs of the GPU. On the contrary, the spatial nodes are executed sequentially as the marching scheme is applied and therefore this stalls the computations leading to smaller speed-up. It is noted that the achieved occupancy is only 10% out of 100% when no loop scheduling is applied. It is possible that the speed-up will become larger if optimization techniques are applied.

Furthermore, the ideal speed-up in CPUs is linear which means that for 4 threads the ideal speed-up is 4. From Table 7.4, it is seen that the OpenMP version with the 4-threads presents a close to ideal behavior for most velocity and spatial grids. However, the OpenMP version with the 8-threads presents a worse behavior. While it increases the speed-up, the increase isn't equivalent to the more employed threads. It is mentioned before that a more appropriate operating system is needed for the current tests. If the same OpenMP version runs in the HPC facility GRNET-ARIS, which uses the processor Intel XEON E5-2680v2 with 20 cores, the speed-up increases to 18.5 and it is considered sufficient.

7.6 Concluding remarks

The time-dependent isothermal fully developed rarefied gas flow between parallel plates driven by harmonically oscillating plate is benchmarked with the corresponding results in [28]. The solution is based on the linearized unsteady BGK kinetic model equation. The two parameters characterizing the flow are the gas rarefaction and the oscillation parameters. The results are in very good agreement with [28] and a brief discussion about the amplitude and the phase angle of both walls is included.

Next, two parallelization strategies based on the OpenMP and OpenACC directives are presented. In the OpenMP version, the molecular velocities are executed in parallel while in the OpenACC version the parallel execution includes both molecular velocities and spatial nodes. It has been seen that both versions decrease computational time and increase the speed-up between them and the serial version. Between the two parallel versions, the faster one is the OpenACC version, which runs on a GPU, and it presents a speed-up of 15.5 for the denser grids. In addition, the parallel versions aren't optimized and the loop scheduling is based on the compiler. Optimizing the loops could decrease further the computational time. It is noted that the directives provide a reasonable speed-up without changing significantly the original FORTRAN code and this is their most significant advantage. The main disadvantage of the OpenMP method is that it is restricted to a single computing node. The main disadvantage of the OpenACC method is that it doesn't achieve the maximum efficiency in a parallel code. In order to achieve it, the CUDA programming model must be used. A recent example of the capabilities of modelling based on CUDA is presented in [211] where a program based on a single GPU outcomes a MPI parallelized CPU program running on 96 CPU cores.

Finally, the parallelization strategies reported in this Chapter are mostly used for two dimensional flows such as the rarefied gas flow in a comb-type assembly which is presented in the next Chapter.

Table 7.1 Wall shear stress amplitude $p_W^{(A)}$ in terms of gas rarefaction parameter δ and oscillation parameter θ.

δ	$p_W^{(A)}$							
	$\theta = 0.1$		$\theta = 1$		$\theta = 10$		$\theta = 50$	
	$y = -1/2$	$y = 1/2$	$y = -1/2$	$y = 1/2$	$y = -1/2$	$y = 1/2$	$y = -1/2$	$y = 1/2$
0	2.82(-1)	2.82(-1)	2.82(-1)	2.82(-1)	2.82(-1)	2.82(-1)	2.82(-1)	2.82(-1)
0.01	2.80(-1)	2.75(-1)	2.80(-1)	2.80(-1)	2.80(-1)	2.80(-1)	2.80(-1)	2.80(-1)
0.05	2.79(-1)	2.35(-1)	2.71(-1)	2.70(-1)	2.71(-1)	2.71(-1)	2.71(-1)	2.71(-1)
0.1	2.81(-1)	1.89(-1)	2.63(-1)	2.58(-1)	2.61(-1)	2.61(-1)	2.61(-1)	2.61(-1)
0.5	2.82(-1)	3.84(-2)	2.52(-1)	1.80(-1)	2.09(-1)	2.08(-1)	2.08(-1)	2.08(-1)
1	2.82(-1)	7.33(-3)	2.66(-1)	1.11(-1)	1.74(-1)	1.68(-1)	1.70(-1)	1.69(-1)
2	2.82(-1)	4.99(-4)	2.70(-1)	4.19(-2)	1.47(-1)	1.20(-1)	1.26(-1)	1.25(-1)
4	2.82(-1)	6.77(-6)	2.69(-1)	5.91(-3)	1.53(-1)	6.53(-2)	8.88(-2)	8.21(-2)
6			2.69(-1)	9.37(-4)	1.62(-1)	3.45(-2)	7.74(-2)	6.00(-2)
8					1.63(-1)	1.78(-2)	7.70(-2)	4.57(-2)
10					1.63(-1)	9.14(-3)	8.03(-2)	3.51(-2)
15					1.62(-1)	1.72(-3)	8.65(-2)	1.77(-2)
20					1.62(-1)	3.24(-4)	8.70(-2)	8.69(-3)
30							8.66(-2)	2.08(-3)
40							8.66(-2)	4.98(-4)
50							8.66(-2)	1.19(-4)

Table 7.2 Wall shear stress phase $p_W^{(P)}$ in terms of gas rarefaction parameter δ and oscillation parameter θ.

δ	$p_W^{(P)}$							
	$\theta = 0.1$		$\theta = 1$		$\theta = 10$		$\theta = 50$	
	$y = -1/2$	$y = 1/2$	$y = -1/2$	$y = 1/2$	$y = -1/2$	$y = 1/2$	$y = -1/2$	$y = 1/2$
0.01	-2.58(-3)	1.65(-1)	-4.49(-4)	1.74(-2)	0	1.74(-3)	0	3.48(-4)
0.05	-1.92(-2)	7.03(-1)	-7.25(-3)	8.31(-2)	-8.09(-4)	8.42(-3)	-1.62(-4)	1.68(-3)
0.1	-2.49(-2)	1.25	-2.22(-2)	1.61(-1)	-2.64(-3)	1.65(-2)	-5.30(-4)	3.30(-3)
0.5	-1.90(-2)	4.28	-1.59(-1)	7.14(-1)	-3.81(-2)	8.12(-2)	-7.72(-3)	1.63(-2)
1	-1.88(-2)	6.97	-1.87(-1)	1.31	-1.16(-1)	1.72(-1)	-2.44(-2)	3.46(-2)
2	-1.88(-2)	1.12(+1)	-1.66(-1)	2.28	-3.12(-1)	3.93(-1)	-7.83(-2)	8.05(-2)
4	-1.88(-2)	1.80(+1)	-1.66(-1)	3.73	-5.20(-1)	9.56(-1)	-2.50(-1)	2.11(-1)
6			-1.66(-1)	4.63	-5.23(-1)	1.57	-4.45(-1)	3.92(-1)
8					-5.08(-1)	2.18	-5.87(-1)	6.16(-1)
10					-5.06(-1)	2.79	-6.56(-1)	8.71(-1)
15					-5.06(-1)	4.30	-6.69(-1)	1.57
20					-5.06(-1)	5.83	-6.52(-1)	2.28
30							-6.50(-1)	3.68
40							-6.51(-1)	5.08
50							-6.51(-1)	6.48

Table 7.3 Computational time in seconds for different versions of the kinetic solver with several grids $M = 80, 300, 1000$ and $N = 10^3, 10^4, 10^5$

M	N	Serial	OpenMP-4 threads	OpenMP-8 threads	OpenACC
80	10^3	1.3	0.4	0.7	0.6
	10^4	13.5	4.5	2.5	3.9
	10^5	135.5	40.3	24.8	36.8
300	10^3	4.9	1.5	1.1	0.8
	10^4	50.9	15.1	9.0	5.1
	10^5	512.8	141.9	88.4	49.5
1000	10^3	17.1	5.5	4.0	1.4
	10^4	186.9	55.2	42.3	11.8
	10^5	1857.3	540.6	411.5	119.9

Table 7.4 Speed-up S for different versions of the kinetic solver with several grids $M = 80, 300, 1000$ and $N = 10^3, 10^4, 10^5$

M	N	OpenMP-4 threads	OpenMP-8 threads	OpenACC
80	10^3	3.1	1.7	2.1
	10^4	3.0	5.4	3.5
	10^5	3.4	5.5	3.7
300	10^3	3.4	4.4	6.4
	10^4	3.4	5.7	9.9
	10^5	3.6	5.8	10.4
1000	10^3	3.1	4.3	12.6
	10^4	3.4	4.4	15.9
	10^5	3.4	4.5	15.5
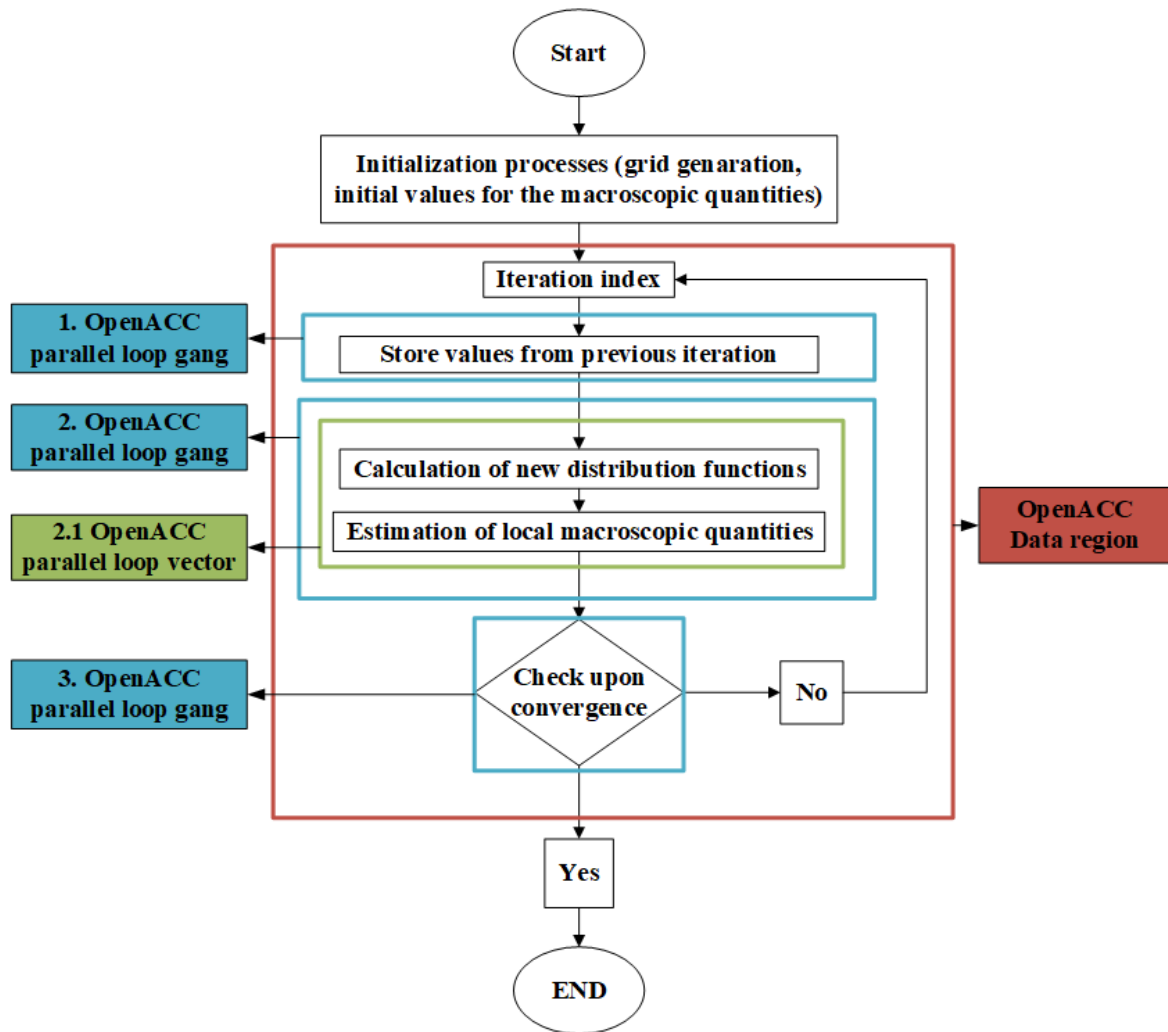
Figure 7.1 Flow diagram of the typical iteration algorithm with OpenACC directives

Chapter 8

Oscillatory rarefied gas flow in vertically/laterally driven comb-type assemblies

8.1 Introduction

Damping forces on solid structures are caused by the collisions of the gas molecules impinging on the structure's surface. Squeeze flow damping (SFD) [212] refers to the energy that must be dissipated to displace the air in the plate to substrate gap as it oscillates vertically. If the plate oscillates laterally then the major source of energy dissipation is the viscous drag through the relative fluid-structure sliding and this is usually referred as slide flow damping. In the hydrodynamic regime, when the inertial forces are neglected, squeeze flow damping in air gaps of oscillating structures may be modelled with the Reynolds equation [213] which considers the viscous and compressibility effects. However, the Reynolds equation is usable only up to a certain frequency, from there on the inertia forces must be considered leading to wave propagation models [110]. Similarly, the slide flow is modelled as either a Couette or a Stokes flow [112]. In the slip regime, continuum-based solutions, that include rarefaction effects, have also been reported [214, 116]. In the transition regime, the squeeze flow has been simulated with DSMC [215] as well as with the steady-state ES-BGK model [216] while the slide flow has been widely investigated with kinetic models [2].

205

A typical structure that combines both types of damping, squeeze and slide flow, is the two-dimensional configuration of a comb type structure. This flow configuration is common [217, 112, 218] and it has been reported in [5, 219] where a steady-state kinetic type approach has been implemented for the steady-state flow. These comb structures are normally operated at very low pressure (usually from 0.01 to 1000 Pa [220]) in order to reduce gas damping. However, it is interesting to note that gas damping may also be reduced if the device is operated close to the corresponding frequency of an antiresonance [154]. Furthermore, while the typical range of frequencies is around 3-5 kHz for accelerometers and 18-20 kHz for gyroscopes, there is need for extended sensing bandwidths for the next generation of inertial MEMS which will lead to higher operation frequencies [221]. Also, the plates in resonators are often driven at high frequencies on the order of MHz [7] which leads to small values of the oscillation parameter (see Table 2.1). Therefore, as the range of frequencies is increased, inertial forces must be included and a time-dependent kinetic formulation needs to be considered.

In this context, the present work is devoted to the kinetic solution of the time dependent rarefied gas flow in a comb type structure due to oscillating inner walls. The periodic flow is investigated by numerically solving the time-dependent linearized Shakhov kinetic equation subject to diffuse boundary conditions. The motion of the comb type structure is analyzed in order to provide insights in the flow characteristics such as the squeeze flow damping, the slide damping and the sound waves that appear at high frequencies. Detailed results of the dimensionless amplitude and the phase of all the average normal and shear stresses at the moving walls are provided in terms of the reference gas rarefaction and oscillation parameter as well as the different sets of geometries for the comb type structure. Other dimensionless output quantities include the amplitudes of the number density, velocity and temperature.

The remaining of the Chapter is structured as follows: In Section 8.2, the flow configuration is presented and the dimensionless parameters defining the flow are prescribed. The details of the kinetic modeling and the numerical scheme are presented in Sections 8.3 and 8.4 respectively. The numerical results and the discussion are presented in Section 8.5, which is divided into four Subsections. The concluding remarks are outlined in Section 8.6.

8.2 Flow configuration

The geometry of the periodically comb type structure to be considered, with the coordinate system and its origin, is shown in Figure 8.1. The fixed parameters are d_1, d_2, d_3, d_4, L_1 and L_2. It is assumed that the geometry repeats itself with a period L. Next, consider the flow of a rarefied gas between the two parts of the structure, where the outer part is stationary while the inner one is moving with constant velocity. The flow is considered as unbounded in the z direction and it depends on both x and y. Due to the imposed periodicity, only one section with length L of the comb structure may be considered. The flow domain under investigation is bounded by the flow inlet and outlet boundaries at $y = -L_2/2 - d_1 - d_3/2$ and $y = L_2/2 + d_1 + d_3/2$, respectively, and by the top and bottom walls. All the walls are considered isothermal with temperature T_0. Depending on the moving part movement, there are two distinct cases: a) the inner movable part moves with velocity $\tilde{U}_W = \mathrm{R}\left[U_W \exp\left(-i\omega t'\right)\right]$ in the y direction while the external stationary part is fixed and b) the inner movable part moves with velocity $\tilde{U}_W = \mathrm{R}\left[U_W \exp\left(-i\omega t'\right)\right]$ in the x direction. The first case is a vertically driven comb type structure while the second one is a laterally driven comb type structure. Also, R denotes the real part of a complex expression, $i = \sqrt{-1}$, t' is the time independent variable, U_W is the amplitude of the oscillating wall and ω is the oscillation (cyclic) frequency. According to Figure 8.1, if the moving wall oscillates vertically the squeeze flow is seen at the walls 1 and 2 of the comb and the slide flow at the wall 3. On the contrary, in the case of lateral motion, the squeeze flow is seen at the wall 3 and the slide flow at the walls 1 and 3.

Both flows, squeeze and slide, are generated by the oscillating plate either in the x or the y direction and they are characterized by the bulk velocity $\tilde{U}_x$, $\tilde{U}_y$, number density $\tilde{n}$, temperature $\tilde{T}$, heat flux $\tilde{Q}_x$, $\tilde{Q}_y$, and stress tensor $\tilde{\boldsymbol{P}}$. When the oscillation frequency is high enough then sound waves are generated in the direction normal to moving part and their properties are given by the same macroscopic quantities. All of the quantities depend harmonically on time and are given by

$$\tilde{n}\left(t', x', y'\right) = \mathrm{R}\left[n\left(x', y'\right)\exp\left(-i\omega t\right)\right] + n_0 \tag{8.1}$$

$$\tilde{U}_x\left(t', x', y'\right) = \mathrm{R}\left[U_x\left(x', y'\right)\exp\left(-i\omega t\right)\right] \tag{8.2}$$

$$\tilde{U}_y\left(t', x', y'\right) = \mathrm{R}\left[U_y\left(x', y'\right)\exp\left(-i\omega t\right)\right] \tag{8.3}$$

$$\tilde{T}\left(t', x', y'\right) = \mathrm{R}\left[T\left(x', y'\right)\exp\left(-i\omega t\right)\right] + T_0 \tag{8.4}$$

$$\tilde{Q}_x\left(t', x', y'\right) = \mathrm{R}\left[Q_x\left(x', y'\right)\exp\left(-i\omega t\right)\right] \tag{8.5}$$

$$\tilde{Q}_y\left(t', x', y'\right) = \mathrm{R}\left[Q_y\left(x', y'\right)\exp\left(-i\omega t\right)\right] \tag{8.6}$$

$$\tilde{P}_{ij}\left(t', x', y'\right) = \mathrm{R}\left[P_{ij}\left(x', y'\right)\exp\left(-i\omega t\right)\right], i = x, y, z, j = x, y, z, i \neq j \tag{8.7}$$

$$\tilde{P}_{ij}\left(t', x', y'\right) = \mathrm{R}\left[P_{ij}\left(x', y'\right)\exp\left(-i\omega t\right)\right] + P_0, i = x, y, z, j = x, y, z, i = j \tag{8.8}$$

where $n\left(x', y'\right)$, $U_x\left(x', y'\right)$, $U_x\left(x', y'\right)$, $T\left(x', y'\right)$, $Q_x\left(x', y'\right)$, $Q_y\left(x', y'\right)$ and $P_{ij}\left(x', y'\right)$ are complex functions and P_0 is the equilibrium pressure while $n_0 = P_0/k_B T_0$ is the equilibrium number density. For $\omega = 0$ the squeeze and slide flows are simplified due to the drop of the time dependent term.

The flow parameters defining the problem are the gas rarefaction parameter δ and the dimensionless oscillation frequency θ. The first one is the same as in steady-state configurations and it is given by

$$\delta = \frac{P_0 d_1'}{\mu \upsilon} \tag{8.9}$$

where μ is the gas viscosity at some reference temperature T_0 and $\upsilon = \sqrt{2R_g T_0}$ is the most probable molecular speed ($R_g = k_B/m$, with k_B denoting the Boltzmann constant and m the molecular mass, is the gas constant). The second one is the ratio of the intermolecular collision frequency $\nu = P_0/\mu$, over the oscillation frequency ω:

$$\theta = \frac{P_0}{\mu \omega}. \tag{8.10}$$

Next, by taking the distance d_1 as the characteristic length of the problem it is convenient to introduce the dimensionless independent variables along with the non-dimensional distances of the moving part and stationary part

$$x = x'/d_1', y = y'/d_1', t = t'\omega, \tag{8.11}$$

$$L_1 = L_1'/d_1', L_2 = L_2'/d_1', d_2 = d_2'/d_1', d_3 = d_3'/d_1', d_4 = d_4'/d_1' \tag{8.12}$$

as well as the macroscopic quantities in dimensionless form defined as

$$u = U/U_W, \rho = \left(n\,\upsilon\right)/\left(n_0\,U_W\right), \tau = \left(T_0\,\upsilon\right)/\left(n_0\,U_W\right), \Pi_{ij} = \left(P_{ij}\,\upsilon\right)/\left(2P_0\,U_W\right). \tag{8.13}$$

208

Each dimensionless time-dependent complex macroscopic quantity may be written as

$$\tilde{a}\left(t,x,y\right) = \mathrm{R}\left[a\left(x,y\right)\exp\left(-it\right)\right] = \mathrm{R}\left[a_A\left(x,y\right)\exp\left(ia_P\left(x,y\right)\right)\exp\left(-it\right)\right] = a_A\cos\left[t-a_P\right]$$
(8.14)

where $a = \left[u_x, u_y, \rho, \Pi_{ij}, q_x, q_y, \tau\right]$ and the subscripts A and P denote the amplitude and the phase of each complex quantity. It is evident that both $\alpha_A\left(t,x,y\right)$ and $\alpha_P\left(t,x,y\right)$ are of main importance in determining the flow behavior and they will be computed in terms of the two main parameters, δ and θ, fully defining the flow. It is also expected that as $\omega \to 0$ (or $\theta \to \infty$), the imaginary parts of the macroscopic quantities are gradually diminishing and the solution tends towards the steady-state one.

In addition, the average gas stresses are also of major practical importance since they are needed in order to evaluate the damping forces in squeeze and slide flow. The average normal stress is denoted as $\bar{\Pi}_{yy}$ in the y direction for a vertically driven comb structure while as $\bar{\Pi}_{xx}$ in the x direction for a laterally driven one. In both cases the average shear stress is denoted as $\bar{\Pi}_{xy}$. Thus, the time dependent average gas stress over the length is defined as

$$\tilde{\bar{\Pi}}_{ij}\left(t,x,y\right) = \mathrm{R}\left[\bar{\Pi}_{ij}\exp\left(-it\right)\right],$$
(8.15)

where

$$\bar{\Pi}_{ij}\left(y\right) = \int_0^{L_1} \Pi_{ij}\left(x,y\right)dx \Big/ L_1, \bar{\Pi}_{ij}\left(x\right) = \int_0^{L_2} \bar{\Pi}_{ij}\left(x,y\right)dy \Big/ L_2$$
(8.16)

with $ij = xx, yy, xy$.

8.3 Kinetic formulation

For arbitrary values of the parameters δ and θ the flow may be simulated at the kinetic level by the time-dependent Shakhov kinetic model equation written as

$$\frac{\partial \tilde{f}}{\partial t'} + \xi_x \frac{\partial \tilde{f}}{\partial x'} + \xi_y \frac{\partial \tilde{f}}{\partial y'} = \frac{P_0}{\mu}\left(f^S - \tilde{f}\right)$$
(8.17)

where

$$f^S = f^M \left(1 + \frac{2m}{15n\left(kT\right)^2}\tilde{\boldsymbol{Q}}\left(\boldsymbol{\xi}-\tilde{\boldsymbol{U}}\right)\left[\frac{\left(\boldsymbol{\xi}-\tilde{\boldsymbol{U}}\right)^2}{2kT} - \frac{5}{2}\right]\right)$$
(8.18)

with

$$f^M = n \left(\frac{m}{2\pi kT} \right)^{3/2} \exp \left[-m \frac{\left[\boldsymbol{\xi} - \tilde{U}\left(t', x', y'\right) \right]^2}{(2kT)} \right] \tag{8.19}$$

being the local Maxwellian distribution. Here, $\tilde{f} = \tilde{f}\left(t', x', y', \boldsymbol{\xi}\right)$ is the unknown distribution function and $\boldsymbol{\xi} = (\xi_x, \xi_y, \xi_z)$ is the molecular velocity vector. Also, $\tilde{n}$, $\tilde{\boldsymbol{U}}$, $\tilde{T}$, $\tilde{\boldsymbol{Q}}$, $\tilde{P}_{ij}$ and $\tilde{P}$ are the macroscopic distributions of number density, velocity, temperature, heat flow and stress respectively, which may be obtained by the moments of the distribution function according to

$$\tilde{n}\left(t', x', y'\right) = \int_{-\infty}^{+\infty} \tilde{f}\left(t', x', y', \boldsymbol{\xi}\right) d\boldsymbol{\xi}, \tag{8.20}$$

$$\tilde{U}\left(t', x', y'\right) = \frac{1}{n} \int_{-\infty}^{+\infty} \boldsymbol{\xi} \tilde{f}\left(t', x', y', \boldsymbol{\xi}\right) d\boldsymbol{\xi}, \tag{8.21}$$

$$\tilde{T}\left(t', x', y'\right) = \frac{m}{3nk_B} \int_{-\infty}^{+\infty} \left(\xi - \tilde{U}\right)^2 \tilde{f}\left(t', x', y', \boldsymbol{\xi}\right) d\boldsymbol{\xi}, \tag{8.22}$$

$$\tilde{Q}\left(t', x', y'\right) = \frac{m}{2} \int_{-\infty}^{+\infty} \left(\xi - \tilde{U}\right) \left(\xi - \tilde{U}\right) \tilde{f}\left(t', x', y', \boldsymbol{\xi}\right) d\boldsymbol{\xi}, \tag{8.23}$$

$$\tilde{P}_{ij}\left(t', x', y'\right) = m \int_{-\infty}^{+\infty} \left(\xi_i - \tilde{U}_i\right) \left(\xi_j - \tilde{U}_j\right) \tilde{f}\left(t', x', y', \boldsymbol{\xi}\right) d\boldsymbol{\xi}. \tag{8.24}$$

Due to the condition of the much smaller velocity amplitude of the moving part than the most probable molecular velocity $(U_W \ll \upsilon)$ the unknown distribution function is linearized as

$$\tilde{f}\left(t', x', y', \boldsymbol{c}\right) = f^0 \left[1 + \frac{U_W}{\upsilon} \tilde{h}\left(t', x', y', \boldsymbol{c}\right) \right], \tag{8.25}$$

where $\boldsymbol{c} = \boldsymbol{\xi}/\upsilon$, $f_0 = \frac{n}{\pi^{3/2}\upsilon^3} \exp\left[-\boldsymbol{c}^2\right]$ is the absolute Maxwellian and $\tilde{h}\left(t, x, y, \boldsymbol{c}\right)$ is unknown perturbed distribution function. Substituting expression (8.25) into Eq. (8.17) and introducing the dimensionless variables as defined in Eqs. (8.11) and (8.13), yields the time-dependent linearized Shakhov kinetic model equation

$$\frac{\delta}{\theta} \frac{\partial \tilde{h}}{\partial t} + c_x \frac{\partial \tilde{h}}{\partial x} + c_y \frac{\partial \tilde{h}}{\partial y} = \delta \left(\mathrm{R} \left(\tilde{\rho} + 2c_x \tilde{u}_x + 2c_y \tilde{u}_y + \tilde{\tau} \left(\boldsymbol{c}^2 - \frac{3}{2} \right) + \frac{4}{15} \left(c_x \tilde{q}_x + c_y \tilde{q}_y \right) \left(\boldsymbol{c}^2 - \frac{5}{2} \right) \right) - \tilde{h} \right). \tag{8.26}$$

Here, δ and θ are defined by Eqs. (8.9) and (8.10) respectively, while $\tilde{\rho}\left(t, x, y\right)$, $\tilde{u}_x\left(t, x, y\right)$, $\tilde{u}_y\left(t, x, y\right)$, $\tilde{\tau}\left(t, x, y\right)$, $\tilde{q}_x\left(t, x, y\right)$ and $\tilde{q}_x\left(t, x, y\right)$ are time-dependent macroscopic quantities given in Eqs. (8.1)-(8.8) after introducing the dimensionless variables defined in Eq. (8.13).

Next, it is convenient to introduce the complex distribution function $h(x, y, \boldsymbol{c})$ so that

$$\tilde{h}(t, x, y, \boldsymbol{c}) = \mathrm{R}\left[h(x, y, \boldsymbol{c}) \exp(-it)\right]. \tag{8.27}$$

Also, the molecular velocity vector $\boldsymbol{c} = (c_x, c_y, c_z)$ is transformed as $\boldsymbol{c} = (\zeta, \varphi, c_z)$, where $c_r = \zeta \cos\varphi$ and $c_\varphi = \zeta \sin\varphi$. Then, Eq. (8.27) is rewritten in terms of h as

$$c_r \frac{\partial h}{\partial x} + c_\varphi \frac{\partial h}{\partial y} + h\left(\delta - \frac{\delta}{\theta} i\right) = \delta\left(\rho + 2c_r u_x + 2c_\varphi u_y + \tau\left(\boldsymbol{c}^2 - \frac{3}{2}\right) + \frac{4}{15}(c_r q_x + c_\varphi q_y)\left(\boldsymbol{c}^2 - \frac{5}{2}\right)\right). \tag{8.28}$$

At this stage the $z-$component of the molecular velocity vector may be eliminated by applying the so-called projection procedure and introducing the reduced distribution functions

$$Y(x, y, c_r, c_\varphi) = \frac{1}{\sqrt{\pi}} \int_{-\infty}^{\infty} h(x, y, c_r, c_\varphi, c_z) \exp\left[-c_z^2\right] dc_z, \tag{8.29}$$

$$X(x, y, c_r, c_\varphi) = \frac{1}{\sqrt{\pi}} \int_{-\infty}^{\infty} h(x, y, c_r, c_\varphi, c_z)\left(c_z^2 - \frac{1}{2}\right) \exp\left[-c_z^2\right] dc_z. \tag{8.30}$$

Equation (8.28) is multiplied by $c_z \exp(-c_z^2)/\sqrt{\pi}$ and $\left(c_z^2 - \frac{1}{2}\right) \frac{1}{\sqrt{\pi}} \exp(-c_z^2)$ and the resulting equations are integrated over c_z to deduce

$$\left(\delta - i\frac{\delta}{\theta}\right) Y + c_r \frac{\partial Y}{\partial x} + c_\varphi \frac{\partial Y}{\partial y} = \delta\left(\rho + 2u_x c_r + 2u_y c_\varphi + \tau\left(c^2 - 1\right) + \frac{4}{15}(c_r q_x + c_\varphi q_y)\left(c^2 - 2\right)\right), \tag{8.31}$$

$$\left(\delta - i\frac{\delta}{\theta}\right) X + c_r \frac{\partial X}{\partial x} + c_\varphi \frac{\partial X}{\partial y} = \delta\left(\frac{\tau}{2} + \frac{2}{15}(c_r q_x + c_\varphi q_y)\right), \tag{8.32}$$

where the macroscopic quantities are defined by Eqs. (8.1)-(8.8) and they are computed from the reduced distribution function according to

$$\rho(x, y) = \frac{1}{\pi} \int_0^{2\pi} \int_0^{+\infty} Y e^{-\zeta^2} \zeta d\zeta d\varphi, \tag{8.33}$$

$$u_x(x, y) = \frac{1}{\pi} \int_0^{2\pi} \int_0^{+\infty} Y e^{-\zeta^2} \zeta^2 \cos\varphi d\zeta d\varphi, \tag{8.34}$$

$$u_y(x, y) = \frac{1}{\pi} \int_0^{2\pi} \int_0^{+\infty} Y e^{-\zeta^2} \zeta^2 \sin\varphi d\zeta d\varphi, \tag{8.35}$$

$$\tau(x, y) = \frac{1}{\pi} \int_0^{2\pi} \int_0^{+\infty} \frac{2}{3}\left[Y\left(\zeta^2 - 1\right) + X\right] \zeta e^{-\zeta^2} d\zeta d\varphi, \tag{8.36}$$

$$q_x(x, y) = \frac{1}{\pi} \int_0^{2\pi} \int_0^{+\infty} \left[Y\left(c^2 - 2\right) + X\right] e^{-\zeta^2} \zeta^2 \cos\varphi d\zeta d\varphi, \tag{8.37}$$

$$q_y(x, y) = \frac{1}{\pi} \int_0^{2\pi} \int_0^{+\infty} \left[Y\left(c^2 - 2\right) + X \right] e^{-\zeta^2} \zeta^2 \sin \varphi d\zeta d\varphi, \qquad (8.38)$$

$$\Pi_{xy}(x, y) = \frac{1}{\pi} \int_0^{2\pi} \int_0^{+\infty} Y e^{-\zeta^2} \zeta^3 \sin \varphi \cos \varphi d\zeta d\varphi, \qquad (8.39)$$

$$\Pi_{xx}(x, y) = \frac{1}{\pi} \int_0^{2\pi} \int_0^{+\infty} Y e^{-\zeta^2} \zeta^3 \left(\cos \varphi\right)^2 d\zeta d\varphi, \qquad (8.40)$$

$$\Pi_{yy}(x, y) = \frac{1}{\pi} \int_0^{2\pi} \int_0^{+\infty} Y e^{-\zeta^2} \zeta^3 \left(\sin \varphi\right)^2 d\zeta d\varphi. \qquad (8.41)$$

Equations (8.31)-(8.32) are the governing kinetic equations with their associated moments (8.33)-(8.41) and they are valid in the whole range of δ and θ. It is noted that as $\theta \to \infty$ ($\omega = 0$) and $\delta << \theta$ Eqs. (8.31)-(8.32) are reduced to the steady-state rarefied gas flows in a comb type-structure. At the other end, as $\theta \to 0$ ($\omega \to \infty$), the solution tends to be constant at very high frequencies indicating a fully trapped gas situation [154].

Turning now to the boundary conditions it is noted that purely diffuse scattering is assumed at the wall, i.e., $f^+ = f_w^M$, where the superscript $(+)$ denotes particles departing from the wall and f_w^M is the Maxwellian distribution defined by the wall conditions. Based on the above and following the linearization and non-dimensionalization procedures it is readily deduced that

$$\tilde{h}^+ = \tilde{\rho}_w + 2\, c \cdot \tilde{U}_W + \tilde{\tau}_w \left(c^2 - \frac{3}{2}\right) \Rightarrow h^+ = \rho_W + 2\, c \cdot U_W + \tau_w \left(c^2 - \frac{3}{2}\right) \qquad (8.42)$$

where τ_W denotes the non-dimensional temperature of the boundary. The non-dimensional quantity ρ_W can be estimated by the usual impermeability condition, which states that the normal component of the gas velocity on the wall vanishes. Next, the projection procedure as well as the mapping in the polar coordinate system are applied in order to reduce Eq. (8.42) to

$$\text{Vertical motion:} \quad Y^+ = \rho_W + 2\zeta \sin \varphi + \tau_w \left(\zeta^2 - 1\right) \qquad (8.43)$$

$$\text{Lateral motion:} \quad Y^+ = \rho_W + 2\zeta \cos \varphi + \tau_w \left(\zeta^2 - 1\right) \qquad (8.44)$$

$$X^+ = \tau_w/2. \qquad (8.45)$$

In the vertical motion, the movable part is moving in the y direction while in the lateral motion in the x direction. It is noted that the two motions are independent of each other. The boundary conditions for Eq. (8.31) are given in Tables 8.1 and 8.2 for

vertical and lateral motion respectively and for the walls (1-10) according to Figure 8.1.

Table 8.1 Boundary conditions for comb type structures under vertical motion

Wall	Angle	Y^+	ρ_w	Eq.
1	$0 < \varphi < \pi$	$\rho_w + 2\zeta \sin\varphi$	$\sqrt{\pi} - \dfrac{2}{\sqrt{\pi}} \displaystyle\int_0^\pi \int_0^\infty Y^- e^{-\zeta^2} \zeta^2 \sin\varphi \, d\zeta \, d\varphi$	(8.46)
2	$\pi < \varphi < 2\pi$	$\rho_w + 2\zeta \sin\varphi$	$-\sqrt{\pi} + \dfrac{2}{\sqrt{\pi}} \displaystyle\int_\pi^{2\pi} \int_0^\infty Y^- e^{-\zeta^2} \zeta^2 \sin\varphi \, d\zeta \, d\varphi$	(8.47)
3, 4, 5	$-\dfrac{\pi}{2} < \varphi < \dfrac{\pi}{2}$	$\rho_w + 2\zeta \sin\varphi$	$-\dfrac{2}{\sqrt{\pi}} \displaystyle\int_{-\frac{\pi}{2}}^{\frac{\pi}{2}} \int_0^\infty Y^- e^{-\zeta^2} \zeta^2 \cos\varphi \, d\zeta \, d\varphi$	(8.48)
6, 7, 10	$\dfrac{\pi}{2} < \varphi < \dfrac{3\pi}{2}$	ρ_w	$\dfrac{2}{\sqrt{\pi}} \displaystyle\int_{\frac{\pi}{2}}^{\frac{3\pi}{2}} \int_0^\infty Y^- e^{-\zeta^2} \zeta^2 \cos\varphi \, d\zeta \, d\varphi$	(8.49)
8	$\pi < \varphi < 2\pi$	ρ_w	$\dfrac{2}{\sqrt{\pi}} \displaystyle\int_\pi^{2\pi} \int_0^\infty Y^- e^{-\zeta^2} \zeta^2 \sin\varphi \, d\zeta \, d\varphi$	(8.50)
9	$0 < \varphi < \pi$	ρ_w	$-\dfrac{2}{\sqrt{\pi}} \displaystyle\int_0^\pi \int_0^\infty Y^- e^{-\zeta^2} \zeta^2 \sin\varphi \, d\zeta \, d\varphi$	(8.51)

Table 8.2 Boundary conditions for comb type structures under lateral motion

Wall	Angle	Y^+	ρ_w	Eq.
1	$0 < \varphi < \pi$	$\rho_w + 2\zeta \cos\varphi$	$-\dfrac{2}{\sqrt{\pi}} \displaystyle\int_0^\pi \int_0^\infty Y^- e^{-\zeta^2} \zeta^2 \sin\varphi \, d\zeta \, d\varphi$	(8.52)
2	$\pi < \varphi < 2\pi$	$\rho_w + 2\zeta \cos\varphi$	$\dfrac{2}{\sqrt{\pi}} \displaystyle\int_\pi^{2\pi} \int_0^\infty Y^- e^{-\zeta^2} \zeta^2 \sin\varphi \, d\zeta \, d\varphi$	(8.53)
3, 4, 5	$-\dfrac{\pi}{2} < \varphi < \dfrac{\pi}{2}$	$\rho_w + 2\zeta \cos\varphi$	$\sqrt{\pi} - \dfrac{2}{\sqrt{\pi}} \displaystyle\int_{-\frac{\pi}{2}}^{\frac{\pi}{2}} \int_0^\infty Y^- e^{-\zeta^2} \zeta^2 \cos\varphi \, d\zeta \, d\varphi$	(8.54)
6-10			See Eqs. (8.49)-(8.51)	

The boundary conditions for Eq. (8.31) at the walls (6-10) are the same for both cases. In all walls the boundary condition for Eq. (8.32) is the same, $X^+ = 0$ since all the walls of the comb type structure are at isothermal conditions $\tau_w = 0$. The flow field is periodic in the x direction with period L. Then, the periodic boundary conditions

at the inlet and the outlet of the flow field imply that

$$Y\left(0, -L_2/2 - d_1 - d_3/2, c_r, c_\varphi\right) = Y\left(0, L_2/2 + d_1 + d_3/2, c_r, c_\varphi\right), \tag{8.55}$$

$$X\left(0, -L_2/2 - d_1 - d_3/2, c_r, c_\varphi\right) = X\left(0, L_2/2 + d_1 + d_3/2, c_r, c_\varphi\right). \tag{8.56}$$

Finally, the flow setup is now properly defined by Eqs. (8.31)-(8.32) with the associated conditions (8.33)-(8.41) subject to boundary conditions (8.46)-(8.56). It is noted that the displacement in the y or the x direction of the moving wall isn't taken into account due to the small wall velocity amplitude hypothesis that has been made in Eq. (8.25).

8.4   Numerical scheme

The numerical solution is deterministic. The discretization in the molecular velocity space is performed using the discrete velocity method. The continuum spectrum $\zeta \in [0, \infty)$ is substituted by a discrete set ζ_m, $m = 1, 2 ... M$, which is taken to be the roots of the Legendre polynomial of order M, accordingly mapped from $[-1, 1]$ to $[0, \infty)$. Also, a set of discrete angles φ_n, $n = 1, 2 ... N$ equally spaced in $[0, 2\pi]$ is defined. The discretization in the physical space is based on a second order central difference scheme by the flow domain in rectangular elements denoted by (i, j), with $i = 1, 2, ..., I$ and $j = 1, 2, ..., J$. The discretized equations are solved in an iterative manner. The iteration map is concluded when the following criteria are fulfilled:

$$\varepsilon_{Re}^{(k)} = \max_{i,j} \left\{ \begin{array}{l} \left|u_{x,Re,i,j}^{(k)} - u_{x,Re,i,j}^{(k-1)}\right| + \left|u_{y,Re,i,j}^{(k)} - u_{y,Re,i,j}^{(k-1)}\right| + \left|\rho_{Re,i,j}^{(k)} - \rho_{Re,i,j}^{(k-1)}\right| \\ + \left|q_{x,Re,i,j}^{(k)} - q_{x,Re,i,j}^{(k-1)}\right| + \left|q_{y,Re,i,j}^{(k)} - q_{y,Re,i,j}^{(k-1)}\right| + \left|\tau_{Re,i,j}^{(k)} - \tau_{Re,i,j}^{(k-1)}\right| \end{array} \right\} < 10^{-7}, \tag{8.57}$$

$$\varepsilon_{Im}^{(k)} = \max_{i,j} \left\{ \begin{array}{l} \left|u_{x,Im,i,j}^{(k)} - u_{x,Im,i,j}^{(k-1)}\right| + \left|u_{y,Im,i,j}^{(k)} - u_{y,Im,i,j}^{(k-1)}\right| + \left|\rho_{Im,i,j}^{(k)} - \rho_{Im,i,j}^{(k-1)}\right| \\ + \left|q_{x,Im,i,j}^{(k)} - q_{x,Im,i,j}^{(k-1)}\right| + \left|q_{y,Im,i,j}^{(k)} - q_{y,Im,i,j}^{(k-1)}\right| + \left|\tau_{Im,i,j}^{(k)} - \tau_{Im,i,j}^{(k-1)}\right| \end{array} \right\} < 10^{-7}. \tag{8.58}$$

Here, the superscript k denotes the iteration index, subscripts Re and Im are the real and imaginary part of each macroscopic quantity respectively at each node (i, j) and $\varepsilon^{(k)}$ is the error after k iterations. This numerical scheme has been extensively applied in steady-state and time-dependent flow configurations with considerable success [222, 223, 127]. In general, the number of iterations required for convergence is increased as either θ or δ are increased. The most computationally intensive cases are when both flow parameters are large and the flow is in the slip and hydrodynamic regimes. The

214

numerical parameters have been gradually refined to ensure grid independent results up to at least two significant figures with $M = 16$, $N = 100$ and $I = J = 301$. It is noted that the OpenMP parallelization strategy, presented in Section 7.4.1, is applied in this two-dimensional flow and the molecular angles are assigned into the available threads.

8.5 Results and discussion

The rarefied gas flow in a comb type structure due to an imposed oscillatory wall has been simulated in a wide range of the gas rarefaction and oscillation parameters. The computed dimensionless complex density, velocity, temperature distributions and average stress distributions are based on the kinetic formulation. The results include the amplitude and the phase angle. A detailed investigation and parametrization of the average stress distributions, in terms of all involved geometric and flow parameters, is performed. Simulations based on the present methodology have been performed for $L_1 = 5.68$, $L_2 = 0.8$, $d_2 = 1.3$ and $d_1 = d_3/2 = d_4$. In the 2D flow configuration reported in [219] the geometrical characteristics are $L_1' = 15$ μm, $L_2' = 2.56$ μm, $d_1' = 3.2$ μm and $d_2' = 4.2$ μm and they are considered in the present work as the typical length scales from which the non-dimensional lengths are deduced.

The results are organized into four Subsections. In Section 8.5.1, the average normal and shear stress at the moving walls are presented in terms of the rarefaction and oscillation parameter. Section 8.5.2 includes the average stresses in terms of the different lengths of the comb type structure. Two dimensional contours as well as a comparison with literature results are discussed in Section 8.5.3. Finally, Section 8.5.4 describes the oscillatory rarefied gas flow due to the lateral motion of the inner part.

8.5.1 Average stresses on the moving walls

In Figure 8.2, the average normal stress amplitude $\bar{\Pi}_{yy,A}\left(L_2/2\right)$ and phase $\bar{\Pi}_{yy,P}\left(L_2/2\right)$ at the surface 1 are presented in terms of the gas rarefaction $\delta \in [10^{-4}, 10^2]$ and the oscillation parameter $\theta = [0.1, 1, 10]$. It is clearly seen that the amplitude of the average stress $\bar{\Pi}_{yy,A}\left(L_2/2\right)$ depends non-monotonically on δ. For $\theta = [0.1, 1]$ and at small values of δ (free molecular regime), it remains constant. Then, as δ is increased, it is decreased until $\delta = \theta$, where a minimum is observed. Next, as δ is further increased, it oscillates until it reaches a constant value ($\bar{\Pi}_{yy,A} = 1.005$) for $\delta \gg \theta$ which corresponds to the

high frequency regime. This limiting value is almost the same as in 1-D oscillatory flow configurations [27]. For $\theta = 10$, the $\bar{\Pi}_{yy,A}(L_2/2)$ has a more intense oscillatory behavior in comparison with the corresponding ones for the smaller values of θ. Therefore, it is seen that a minimum value is presented in the interval $\theta < \delta < 2\theta$ which has also been reported in 1-D oscillatory flow configurations [27]. This minimum $\delta/\theta \approx 1.43$ has also been seen in [149] even though this work is focused on a thermoacoustic wave. The minimum here is appeared at the same oscillation parameter as in [149]. The minimums that are appeared in the amplitude of the average normal stress are very important since they indicate the existence of an antiresonance in which the damping force is minimized. In the continuum regime (large value of δ and θ) the number of maximum (resonances) and minimum (anti-resonances) are increased (e.g. for $\theta = 10$, $\delta > 10$). On the contrary in the transition regime only a single minimum is observed (e.g. for $\delta \approx \theta$). Furthermore, the dependency of $\bar{\Pi}_{yy,A}(L_2/2)$ on θ is more complex. Until $\delta < 0.5$ the amplitude $\bar{\Pi}_{yy,A}(L_2/2)$ is increased as θ is increased. As δ is increased, the pattern isn't clear enough to draw definitive remarks. Finally, it is noted that these values of θ are indicative and the behavior of $\bar{\Pi}_{yy,A}(L_2/2)$ may include more minimum and maximum values.

The discussion on Figure 8.2 is continued by analyzing the behavior of the average normal stress phase $\bar{\Pi}_{yy,P}(L_2/2)$ in the whole range of δ and θ. For $\theta = [0.1, 1]$, the phase difference $\bar{\Pi}_{yy,P}(L_2/2)$ depends non-monotonically on δ. At first, as δ is increased it is increased and then it is decreased until it reaches a negative constant value. The behavior of $\bar{\Pi}_{yy,P}(L_2/2)$ for $\theta = 10$ is more resonant as δ is increased. Moreover, the dependency on δ is quite complex and the phase changes significantly in an oscillatory manner. This behavior is expected to include more complex phenomena when the values of θ are increased. In addition, it seems that the phase lag tends to zero when a resonance or an antiresonance occurs. It is also seen that after a minimum is presented (e.g. for $\theta = 10$, $\delta = 15$) the phase $\bar{\Pi}_{yy,P}(L_2/2)$ becomes negative and as δ is increased and a maximum is appeared, then $\bar{\Pi}_{yy,P}(L_2/2)$ becomes positive (e.g. for $\theta = 10$, $\delta = 100$).

In Figure 8.3, the shear stress amplitude $\bar{\Pi}_{xy,A}(L_1)$ and phase $\bar{\Pi}_{xy,P}(L_1)$ at the surface 3 are presented in terms of the gas rarefaction $\delta \in [10^{-4}, 10^2]$ and the oscillation parameter $\theta = [0.1, 1, 10, 10^2]$. A similar qualitative behavior to $\bar{\Pi}_{yy,A}(L_2/2, \delta, \theta)$ is seen for $\bar{\Pi}_{xy,A}(L_1, \delta, \theta)$ although the amplitudes of the shear stress along surface 3 is one order of magnitude smaller than the amplitudes of the normal stress on surface. As δ is increased $\bar{\Pi}_{xy,A}(L_1, \delta, \theta)$ is reduced and it oscillates until it reaches a constant

216

value ($\bar{\Pi}_{xy,A} = 0.2803$) for $\delta \gg \theta$. As δ becomes much larger than θ the difference between the normal and the shear stress is reduced. Also, as with the normal stress amplitude, the shear stress amplitude (e.g. for $\theta = 0.1$, $\delta = 2$) is also very close to the limiting value as in 1-D oscillatory Couette flow configuration [28] even if there the flow is considered as incompressible. In addition, even though the two quantities present the same qualitatively behavior, the attributes of the flow here are different. The sound waves that are generated in the top part of the flow configuration aren't present here and instead transversal waves are generated from the wall 3. The analytical behavior of the flow will be discussed further in the Section 8.5.3 where the contours of all the macroscopic quantities will be presented.

The phase $\bar{\Pi}_{xy,P}(L_1)$ also presents the same qualitatively behavior as the normal stress phase $\bar{\Pi}_{yy,P}(L_2/2)$. However, by comparing Figures 8.2 and 8.3, it is seen that there are some small differences between the two stresses. For $\theta = [0.1, 1, 10]$ the minimum of the $\bar{\Pi}_{xy,A}(L_1)$ is achieved for $\delta = \theta$. On the contrary, for $\theta = 10$, the minimum of the $\bar{\Pi}_{yy,A}(L_2/2)$ is achieved for $\delta = 15$, a slightly larger rarefaction parameter. The comparison between the phases of the two stresses reveals a different behavior near each minimum. The average normal shear stress phase $\bar{\Pi}_{xy,P}(L_1)$ changes its sign and becomes negative sooner than the corresponding phase $\bar{\Pi}_{yy,P}(L_2/2)$.

A more detailed analysis about the effect of θ is given in Figure 8.4 where the normal stress amplitude $\bar{\Pi}_{yy,A}(L_2/2)$ and phase $\bar{\Pi}_{yy,P}(L_2/2)$ are presented in terms of the oscillation parameter θ and for $\delta = [0.1, 1, 10]$. For $\delta \leq 1$, as θ is increased, $\bar{\Pi}_{yy,A}$ is monotonically increased until a local maximum is observed, then it is decreased up to some θ, which depends on δ, and a minimum is seen. Finally, as θ is further increased it is again increased until it reaches a constant value at the steady-state regime as it has been seen in Fig. 8.2. However, for $\delta = 10$ before the local maximum there is a small decrease and a local minimum is observed. As θ is increased the trend is the same as for $\delta \leq 1$. It is noted that the minimum seen in Fig. 8.2 it is also seen here for $\delta/\theta \approx 1.43$. It is also interesting to check the scaling law derived in [154] in the current 2D analysis. According to [154], a resonance is seen when $\theta \approx 0.33\delta$ and an anti-resonance when $\theta \approx 0.75\delta$. From Fig. 8.4 it seems that the scaling law captures all the major resonance and anti-resonance states. Moreover, from the corresponding Figure for the phase it is seen that the trend is qualitatively the same as with the amplitude however for very large values of θ the phase $\bar{\Pi}_{yy,P}$ is decreased to zero. This is expected since the flow is headed to the steady-state regime. Also, as in Fig. 8.2, it

seems that the corresponding phase is equal to zero for certain values of θ in which the maximum and the minimum of the amplitude are appeared.

Similarly with Figure 8.4, in Figure 8.5 the shear stress amplitude $\bar{\Pi}_{xy,A}(L_1)$ and phase $\bar{\Pi}_{xy,P}(L_1)$ are presented in terms of the oscillation parameter θ and for $\delta = [0.1, 1, 10]$. As it has been observed in Fig. 8.3 the results are qualitatively the same with the normal stress amplitude. The trends are the same however here the minimums and the maximums are not as intensive as the ones seen for the normal stress amplitude. Accordingly, with the shear stress amplitude, the trend of the phase $\bar{\Pi}_{xy,P}$ is the same as the trend in the normal stress phase. Here, it is also seen that the phase is very close to zero as θ is deceased.

Closing this section the data contained in the previous Figures are shown here in terms of the ratio of the gas rarefaction parameter δ over the oscillation parameter θ or the Strouhal number defined as $St = \delta/\theta$. As it has been already pointed out in [127], the Strouhal number is not adequate, only by itself, to characterize the flow. Both parameters, δ and θ, are need in order to accurately compute the forces. In Figure 8.6, the normal stress amplitude $\bar{\Pi}_{yy,A}(L_2/2)$ and the shear stress amplitude $\bar{\Pi}_{xy,A}(L_1)$ are given for $\theta = [0.1, 1, 10]$ with the dashed lines and for $\delta = [0.1, 1, 10]$ with the solid lines. In the first case the gas rarefaction parameter δ is varied with the oscillation parameter θ being constant while exactly the opposite is applied for the second case. The comparison is made between $\theta = 10$ and $\delta = 10$, etc. It is clear that near $\delta/\theta \approx 1.4$ the minimum is the same for both lines, dashed and solid and for all three distinct cases. Therefore, the same result is achieved when $\delta = 14.3$ and $\theta = 10$ but also when $\delta = 10$ and $\theta = 6.97$. This leads to two different sets of parameters that they achieve this minimum in the normal stress amplitude. For example, this could be useful in the design of an application, knowing that changing the oscillation frequency but also the distance (not simultaneously) could lead to the same results.

As the ratio δ/θ is increased it is seen that behavior is almost the same for $\theta = 0.1$ and $\delta = 0.1$ however for $\theta = 10$ and $\delta = 10$ it is not the same. For example, near $\delta/\theta \approx 2.8$ a maximum (resonance) is observed and it is different between $\theta = 10$ and $\delta = 10$. As δ/θ is further increased the trends are different for each case even though the ratio is the same. Thus, depending on the application the optimal solution isn't trivial. It depends on its structural and operational restrictions (e.g. due to the limitation of the oscillation frequency ω, the oscillation parameter θ is larger leading to a larger resonance for $\delta/\theta \approx 2.8$). Similar trends are observed for the shear stress amplitude $\bar{\Pi}_{xy,A}$. Therefore, the effect of θ on the stress amplitude for a constant δ

and similarly the effect of δ on the stress amplitude for a constant θ are quite different and extensive computations or scaling laws such as the ones reported in [154, 148] are needed in order to investigate all possible solutions. Also, the use of dimensionless kinetic databases should be applied with carefulness due to the resonant behavior of the flow.

8.5.2 Effect of geometrical parameters

Typical examples of the parametric analysis that can easily be performed by the proposed kinetic approach are given in this section. More specifically, the effect on the stresses of the length L_1 dimension is shown in Table 8.3, of the width L_2 dimension in Table 8.4 and of the gap d_2 dimension in Table 8.5. In all cases, the flow configuration with $L_1 = 5.68$, $L_2 = 0.8$, $d_2 = 1.3$ and $d_1 = d_3/2 = d_4$ is considered as the reference operation scenario. The influence of each parameter is studied in terms of the amplitude of the normal stress $\bar{\Pi}_{yy,A}(L_2/2)$ and the shear stress $\bar{\Pi}_{yy,A}(L_2/2)$ by varying this parameter and keeping the remaining ones unchanged. All the results are given in terms of the gas rarefaction $\delta = [0.1, 1, 10]$ and the oscillation parameter $\theta = [0.1, 1, 10]$. It is useful to divide the results into three frequency regimes: the low frequency one ($\theta = 10$,$\delta = [0.1, 1]$ and $\theta = 1$,$\delta = 0.1$), the moderate frequency one ($\delta \approx \theta$) and the high frequency one ($\theta = 0.1$,$\delta = [1, 10]$ and $\theta = 1$, $\delta = 10$).

In Table 8.3, the average normal stress amplitude $\bar{\Pi}_{yy,A}(L_2/2)$ and shear stress amplitude $\bar{\Pi}_{xy,A}(L_1)$ are presented for different dimensions $L_1 = [3.4, 9]$ along with their relative differences with the original one $L_1 = 5.68$. The primary goal here is to comment based on the increase or decrease of the L_1 dimension. In the low frequency regime, as L_1 is increased $\bar{\Pi}_{yy,A}(L_2/2)$ and $\bar{\Pi}_{xy,A}(L_1)$ are also increased. In the moderate frequency regime, this behavior is reversed and $\bar{\Pi}_{yy,A}(L_2/2)$ is decreased as L_1 is increased while $\bar{\Pi}_{xy,A}(L_1)$ continues to increase. In the high frequency regime, as L_1 is increased both amplitudes remain almost constant. As a general remark, while in all other cases, increasing the L_1 dimension leads to smaller average distribution $\bar{\Pi}_{yy,A}(L_2/2)$ for $\theta = 10$ and $\delta = 0.1$ it leads to larger stress distribution. It is also seen that as the gas regime becomes more dense (e.g. for $\theta = \delta = 10$), the relative differences are increased by the change in the dimension while they aren't so easily affected in a more rarefied regime (e.g. for $\theta = \delta = 0.1$). Overall, the differences in the shear stress amplitude are smaller than the corresponding ones in the normal stress amplitude. This is expected since the computation of $\bar{\Pi}_{yy,A}(L_2/2)$ depends strongly

on L_1 dimension. $\bar{\Pi}_{xy,A}(L_1)$ is affected mainly for $\theta = 10$ and when the L_1 dimension is decreased to $L_1 = 2.4$.

In Table 8.4, the average normal stress amplitude $\bar{\Pi}_{yy,A}(L_2/2)$ and shear stress amplitude $\bar{\Pi}_{xy,A}(L_1)$ are presented for different dimensions $L_2 = [0.4, 2]$ along with their relative differences with the original one $L_2 = 0.8$. It seems that the change in the L_2 dimension doesn't affect much the normal stress amplitude $\bar{\Pi}_{yy,A}(L_2/2)$. It remains almost constant as L_2 is increased or decreased and the only large difference is presented in the low frequency regime. Regarding now the shear stress amplitude $\bar{\Pi}_{xy,A}(L_1)$, in the low frequency regime, as L_2 is increased $\bar{\Pi}_{xy,A}(L_1)$ is also increased while in the high frequency regime it remains constant. For $L_2 = 0.4$ it is seen that the relative differences are smaller than the corresponding ones for $L_2 = 2$. It is also noted that for $\delta = \theta$, the relative difference is increased for $L_2 = 2$, especially for $\delta = \theta = 10$ where the largest difference is observed. Therefore, it is seen that as L_2 is decreased to $L_2 = 0.4$ the effect of L_2 becomes smaller and only for larger values of L_2 the $\bar{\Pi}_{xy,A}(L_1)$ is increased due to the direct connection of the L_2 dimension to the slide damping.

In Table 8.5, the average normal stress amplitude $\bar{\Pi}_{yy,A}(L_2/2)$ and shear stress amplitude $\bar{\Pi}_{xy,A}(L_1)$ are presented for different dimensions $d_2 = [0.6, 2.6]$ along with their relative differences with the original one $d_2 = 1.3$. It is seen that the normal stress amplitude $\bar{\Pi}_{yy,A}(L_2/2)$ isn't greatly affected by the increase or decrease in the d_2 dimension. In the low frequency regime, as d_2 is increased $\bar{\Pi}_{yy,A}(L_2/2)$ is decreased while in the high frequency regime it remains almost constant. In addition, $\bar{\Pi}_{xy,A}(L_1)$ is also decreased as d_2 is increased however the difference is largest than the corresponding one for $\bar{\Pi}_{yy,A}(L_2/2)$. As d_2 is decreased the gap is also decreased leading to the fact that the gas is further compressed. This affects directly and strongly the $\bar{\Pi}_{xy,A}(L_1)$ and in a smaller level the $\bar{\Pi}_{yy,A}(L_2/2)$. It is noted that for $\delta = \theta = 0.1$, the relative difference is larger for the larger dimension $d_2 = 2.6$ while for $\delta = \theta = 10$ it is larger for the smaller dimension $d_2 = 0.6$. Thus, it seems that the d_2 dimension affects differently the damping forces $\bar{\Pi}_{xy,A}(L_1)$ in each frequency regime.

8.5.3 Flow characteristics and range of validity of 1-D equations analysis

In Figure 8.7, the velocity amplitude $u_{y,A}$ and the normal stress amplitude $\Pi_{yy,A}$ are presented for $\delta = [0.1, 1, 10]$ and $\theta = 1$ in two dimensional contours. It is useful to recall Fig. 8.1 and its notation in order to discuss the current Figure. It is obvious

that the movement of the moving part affects significantly the flow field in all cases and the damping mechanism changes as δ is increased. The analysis is focused in the upper part of the comb type structure since the amplitudes are symmetrical between the top and the bottom part. For $\delta = 0.1$, the velocity amplitude $u_{y,A}$ is large between the walls 3 and 10. It is also large above the wall 1 and below the wall 3. Similarly, the corresponding normal amplitude $\Pi_{yy,A}$ is also large and it extends in the whole area between the walls 1 and 8 and between the walls 2 and 9. As δ is increased the amplitude $u_{y,A}$ remains large in the area confined by the walls 4,6,1 and 8. However, the behavior of the normal stress amplitude is changed. Not only it is reduced but also its maximum value is now appeared at the wall 8 and not at the moving wall 1. This is related to the propagation of the acoustic waves and particularly the formation of standing-waves. When the oscillation parameter is close to the standing-wave frequencies the normal stress is minimized at the wall 1 while the velocity remains large. This minimum has been seen in Fig. 8.2. It is also observed that between the walls 4 and 6 the amplitude $\Pi_{yy,A}$ is close to zero since the movement of the moving part is in the $y-$ direction. For $\delta = 10$, the amplitudes are changed again. Here, the behavior of $\Pi_{yy,A}$ is qualitatively the same as with the velocity amplitude and the maximum of the amplitude is appeared at the wall 1. It is also seen that the flow field is reduced near the moving part.

This confinement is more clearly observed in Fig. 8.8 where the density amplitude ρ_A and the temperature amplitude τ_A are presented for $\delta = [0.1, 1, 10]$ and $\theta = 0.1$ in two dimensional contours. Here, the oscillation parameter θ is equal to 0.1 which leads to oscillation of higher frequency. For $\delta = 0.1$, it seems that both amplitudes are large in the whole area between walls 1, 4 and 8. As δ is increased the confinement of the gas is more visible for ρ_A while the amplitude of the temperature τ_A still extends in a large area between the walls 1 and 8. As δ is further increased the phenomenon known as full trapped gas situation [154] is clearly seen. Both amplitudes (ρ_A and τ_A) are reduced in a tiny layer near the moving part and in the rest of the flow field they are almost zero. Therefore, the complete computation of the whole flow domain by using two dimensional equations may not be necessary. The solution given by the equivalent 1-D flow configurations, the oscillatory rarefied shear driven flow and the sound wave propagation, might be the same as the 2-D flow configuration for certain values of δ and θ.

It has been observed before that for a constant value of θ as δ is increased the gas is confined in a very small area near the moving wall. Therefore, due to the large

computational effort that is required to solve the 2-D geometry it would be useful to check the range of the validity of the equivalent 1-D problems. In Table 8.6, the average normal stress amplitude $\bar{\bar{\Pi}}_{yy,A}(L_2/2)$ from the current work and the one in [27] in terms of gas rarefaction parameter δ for $\theta = [0.1, 1, 10]$ are presented. It is deduced that for $\theta = 0.1$, even for $\delta = 0.1$ the comparison is good and the relative error is around 3% and becomes smaller as δ is increased. For $\theta = 1$ the error between the approaches diminishes after $\delta \gg 10$. As θ is increased the error is very large for the present values of δ however it is expected that as δ is increased the relative error is going to be reduced. Furthermore, in Table 8.7, the average shear stress amplitude $\bar{\bar{\Pi}}_{xy,A}(L_1)$ from the current work and the one in [28] in terms of gas rarefaction parameter δ and for $\theta = [0.1, 1, 10]$ are presented. The same qualitatively behavior for the error of $\bar{\bar{\Pi}}_{xy,A}$ as for the error of $\bar{\bar{\Pi}}_{yy,A}$ is observed here even though there are small quantitatively deviations. Closing this section, it is concluded that the 1-D equations can be applied when δ is much larger than θ ($\delta \gg \theta$).

8.5.4 Rarefied gas flow in lateral driven comb type assemblies

The oscillatory rarefied gas flow in a comb-type structure driven by the lateral harmonic motion of the moving surface is defined by Eqs. (8.31)-(8.32) with the associated conditions (8.33)-(8.41) subject to boundary conditions (8.52)-(8.56). Also, the geometrical parameters are the same as the ones in the vertically driven comb type assembly. The amplitudes of the average normal and shear stresses as well as the amplitudes of the velocity in the x-direction, the normal stress in the x-direction, the density and the temperature are included in this subsection. It is noted that the presented components of the velocity and the stress are in the x-direction since the motion of the movable part is in this direction.

In Fig. 8.9, the average normal stress amplitude $\bar{\bar{\Pi}}_{xx,A}(L_1, \delta, \theta)$ at the surface 3 and the shear stress amplitude $\bar{\bar{\Pi}}_{xy,A}(L_2/2, \delta, \theta)$ at the surface 1 are presented in terms of gas rarefaction parameter δ and for oscillation parameter $\theta = [0.1, 1]$. It is seen that the amplitude of the average normal stress has a similar behavior with the corresponding normal stress in Fig. 8.2 for both values of θ. Furthermore, the amplitude of the average shear stress is qualitatively different in comparison with the corresponding shear stress in Fig. 8.3 for both values of θ. It is increased as the rarefaction parameter is increased and it reaches a constant value as $\delta \gg \theta$. The minimums seen in the vertically driven comb aren't shown here since the movement of the inner part is in

the x-direction and the wall 4 seems to affect the shear stress at the wall 1. Of course more simulations are needed in order to justify this assumption.

In Figure 8.10, the velocity amplitude $u_{x,A}$ and the normal stress amplitude $\Pi_{xx,A}$ are presented for $\delta = [0.1, 1, 10]$ and $\theta = 1$ in two dimensional contours. The flow characteristics are different here due to the lateral movement of the inner part. More specifically, the values of both quantities are increased between the walls 1, 4 and 8 and 3 and 10. This behavior is expected since they are close to the moving walls. The velocity amplitude is decreased near the corner of the walls 8 and 10 where the initial oscillation dampens due to the increased distance L_1. On the other hand, the normal stress is significant in the whole computational domain and the largest values are seen near the moving walls and the inlet and outlet of the flow. As δ is increased the gas moves more closely towards the moving walls and its velocity and normal stress are decreased as it departs from them. As δ is further increased this phenomenon becomes even more significant and the gas trapping, already mentioned in vertically driven combs, is seen.

In Figure 8.11, the density amplitude ρ_A and the temperature amplitude τ_A are presented for $\delta = [0.1, 1, 10]$ and $\theta = 1$. At first, it is evident that the behavior of the density and temperature is similar to the aforementioned one in Fig. 8.10. As δ is increased the values of the quantities are reduced in the computational domain and they remain large near the moving walls. It is also seen that the largest values are near the inflow and outflow of the domain and between the walls 3 and 10. In conclusion, the decreased gas rarefaction combined with high oscillation frequency leads to gas trapping which is more significant in the laterally-driven comb type assembly due to the small length of the moving walls. Therefore, as $\delta \gg \theta$ the one-dimensional models should be used whether the movable part moves in the y- or x-direction.

8.6 Concluding remarks

The oscillatory flow of a monoatomic gas in a comb type assembly due to the vertical/lateral harmonic motion of the moving surface is numerically investigated in a wide range of the gas rarefaction parameter δ and of the oscillation parameter θ for several sets of geometric parameters corresponding to small, moderate and large lengths. Modeling and simulations are based on the linearized unsteady Shakhov kinetic model equation. The results are in dimensionless form and include the macroscopic distributions of velocity in the y- and x-direction, density, temperature and stress

vector, as well as space-averaged macroscopic variables to deduce overall quantities such as the average normal and the shear stresses. The movement of the inner part is either in the x- or in the y- direction leading to gas flow in a vertically- or in a laterally-driven comb type assembly.

A complete visualization of the flow characteristics is shown with the amplitude of the velocity, normal stress, density and temperature. They are presented in the whole computational domain for several gas rarefaction and oscillation parameters. It is seen that all quantities are significantly affected by the oscillatory motion and the gas rarefaction. As the rarefaction parameter is increased and the oscillation frequency is high the gas trapping phenomenon becomes apparent. Also, as the rarefaction parameter is increased the damping mechanism is changed leading to different normal stress distributions which are visible in the whole computational domain. It is noted that the aforementioned behavior is seen in both comb type assemblies, the vertically- and laterally-driven one.

In order to study the damping forces, the average normal stress and the shear stress are computed in the moving walls. The normal stress is connected with the oscillatory squeeze flow and the shear stress with the oscillatory slide (or shear) flow. It is found that in terms of the gas rarefaction and oscillation parameters the dependency of both quantities is not monotonic. The local minimums and maximums in the amplitudes correspond to certain anti-resonance and resonance states which are triggered by the increasing oscillation frequency as well as the other dimensional parameters, such as the pressure and the characteristic distance. It is also seen that in many cases there are two different sets of rarefaction and oscillation parameters that can create an anti-resonance state which may be useful in the design of a comb type assembly. Moreover, the phases of the shear stress and the normal stress are equal to zero in these states and they also depend non-monotonically on the rarefaction and oscillation parameters. After an anti-resonance is seen the phases become negative and as the gas rarefaction is decreased and a resonance is seen, then they become positive. Furthermore, as $\delta \gg \theta$ the amplitude and the phase of the shear and normal stress tend to constant values. Also, in this regime due to gas trapping the macroscopic quantities may be evaluated by one-dimensional kinetic equations since the agreement between the two-dimensional and one-dimensional flow results is very good.

In terms of the dimensions, the shear and the normal stress depend heavily on the dimensions in the low frequency regime while for high frequencies they remain constant despite any change in the dimensions. More specifically, the dimension L_1

affects mostly the normal stress at the wall 1 and as it is increased the normal stress is also increased. It is worthwhile to note that near the anti-resonance states the previous trend is reversed and the normal stress is reduced. In addition, the shear stress is mostly affected by the variation in the dimension d_2. As d_2 is reduced the shear stress is increased. In the anti-resonance states the trend is reversed and the shear stress is reduced. In terms of the dimension L_2, the shear stress is reduced as the L_2 is reduced.

Overall, it may be concluded that the two-dimensional geometry is always needed in the low frequency regime while in the high frequency it may be omitted and simpler one-dimensional flows can be used.

Table 8.3 Average stress amplitude $\bar{\Pi}_{yy,A}(L_2/2,\delta,\theta)$ and $\bar{\Pi}_{xy,A}(L_1,\delta,\theta)$ in terms of gas rarefaction parameter δ and oscillation parameter θ for comb type structures under vertical motion for different dimensions $L_1=[3.4,9]$ along with their relative differences (%) with the reference one $L_1=[5.68]$.

θ	δ	$\bar{\Pi}_{yy,A}(L_2/2,\delta,\theta)$					$\bar{\Pi}_{xy,A}(L_1,\delta,\theta)$				
		$L_1=3.4$	$L_1=5.68$	$L_1=9$	$\lvert\Delta_{3.4}\rvert$	$\lvert\Delta_9\rvert$	$L_1=3.4$	$L_1=5.68$	$L_1=9$	$\lvert\Delta_{3.4}\rvert$	$\lvert\Delta_9\rvert$
0.1	0.1	6.965(-1)	6.498(-1)	6.350(-1)	6.70	2.28	2.139(-1)	2.163(-1)	2.154(-1)	1.1	0.4
	1	1.012	1.010	1.009	0.20	0.11	2.799(-1)	2.799(-1)	2.799(-1)	0.0	0.0
	10	1.004	1.005	1.005	0.05	0.03	2.804(-1)	2.804(-1)	2.804(-1)	0.0	0.0
1	0.1	2.478	3.838	4.573	54.90	19.15	4.783(-1)	5.086(-1)	4.762(-1)	6.3	6.4
	1	6.293(-1)	5.739(-1)	5.544(-1)	8.80	3.41	1.829(-1)	1.874(-1)	1.866(-1)	2.5	0.4
	10	9.591(-1)	9.599(-1)	9.603(-1)	0.08	0.04	2.638(-1)	2.638(-1)	2.638(-1)	0.0	0.0
10	0.1	2.849	5.922	1.119(+1)	107.84	88.95	5.410(-1)	7.585(-1)	1.075	40.2	41.8
	1	2.138	3.436	4.282	60.67	24.63	4.678(-1)	5.242(-1)	5.040(-1)	12.1	3.9
	10	5.354(-1)	4.494(-1)	4.320(-1)	16.05	3.87	7.881(-2)	9.600(-2)	8.882(-2)	21.8	7.5

Table 8.4 Average stress amplitude $\bar{\Pi}_{yy,A}(L_2/2,\delta,\theta)$ and $\bar{\Pi}_{xy,A}(L_1,\delta,\theta)$ in terms of gas rarefaction parameter δ and oscillation parameter θ for comb type structures under vertical motion for different dimensions $L_2=[0.4,2]$ along with their relative differences (%) with the reference one $L_2=[0.8]$.

θ	δ	$\bar{\Pi}_{yy,A}(L_2/2,\delta,\theta)$					$\bar{\Pi}_{xy,A}(L_1,\delta,\theta)$				
		$L_2=0.4$	$L_2=0.8$	$L_2=2$	$\lvert\Delta_{0.4}\rvert$	$\lvert\Delta_2\rvert$	$L_2=0.4$	$L_2=0.8$	$L_2=2$	$\lvert\Delta_{0.4}\rvert$	$\lvert\Delta_2\rvert$
0.1	0.1	6.516(-1)	6.498(-1)	6.491(-1)	0.27	0.10	2.243(-1)	2.163(-1)	2.324(-1)	3.6	7.4
	1	1.010	1.010	1.010	0.00	0.00	2.776(-1)	2.799(-1)	2.809(-1)	0.8	0.4
	10	1.005	1.005	1.005	0.00	0.00	2.792(-1)	2.804(-1)	2.811(-1)	0.4	0.3
1	0.1	3.814	3.838	3.900	0.65	1.60	4.650(-1)	5.086(-1)	5.531(-1)	9.4	8.7
	1	5.759(-1)	5.739(-1)	5.747(-1)	0.34	0.12	1.931(-1)	1.874(-1)	2.157(-1)	3.0	15.1
	10	9.599(-1)	9.599(-1)	9.599(-1)	0.00	0.00	2.577(-1)	2.638(-1)	2.663(-1)	2.4	0.9
10	0.1	5.768	5.922	6.353	2.67	7.29	6.670(-1)	7.585(-1)	8.847(-1)	13.7	16.6
	1	3.396	3.436	3.539	1.16	3.01	4.830(-1)	5.242(-1)	5.620(-1)	8.5	7.2
	10	4.589(-1)	4.494(-1)	4.503(-1)	2.07	0.20	1.042(-1)	9.600(-2)	1.390(-1)	7.9	44.8

226

Table 8.5 Average stress amplitude $\bar{\Pi}_{yy,A}\left(L_2/2,\delta,\theta\right)$ and $\bar{\Pi}_{xy,A}\left(L_1,\delta,\theta\right)$ in terms of gas rarefaction parameter δ and oscillation parameter θ for comb type structures under vertical motion for different dimensions $d_2=[0.6,2.6]$ along with their relative differences (%) with the reference one $d_2=[1.3]$.

θ	δ	$\bar{\Pi}_{yy,A,top}\left(\delta,\theta\right)$					$\bar{\Pi}_{xy,A,m}\left(\delta,\theta\right)$				
		$d_2=0.6$	$d_2=1.3$	$d_2=2.6$	$|\Delta_{0.6}|$	$|\Delta_{2.6}|$	$d_2=0.6$	$d_2=1.3$	$d_2=2.6$	$|\Delta_{0.6}|$	$|\Delta_{2.6}|$
0.1	0.1	6.437(-1)	6.498(-1)	6.512(-1)	0.94	0.22	2.175(-1)	2.163(-1)	2.369(-1)	0.5	9.5
	1	1.010	1.010	1.010	0.00	0.00	2.793(-1)	2.799(-1)	2.799(-1)	0.2	0.0
	10	1.005	1.005	1.005	0.00	0.00	2.804(-1)	2.804(-1)	2.804(-1)	0.0	0.0
1	0.1	4.027	3.838	3.800	4.68	0.99	7.879(-1)	5.086(-1)	3.643(-1)	35.4	28.4
	1	5.649(-1)	5.739(-1)	5.756(-1)	1.60	0.30	1.749(-1)	1.874(-1)	2.100(-1)	7.1	12.1
	10	9.599(-1)	9.599(-1)	9.599(-1)	0.00	0.00	2.641(-1)	2.638(-1)	2.638(-1)	0.1	0.0
10	0.1	7.368	5.922	5.609	19.63	5.29	1.448	7.585(-1)	4.426(-1)	47.6	41.7
	1	3.737	3.436	3.350	8.06	2.50	8.394(-1)	5.242(-1)	3.646(-1)	37.5	30.5
	10	4.375(-1)	4.494(-1)	4.579(-1)	2.72	1.89	6.212(-2)	9.600(-2)	1.083(-1)	54.5	12.8

Table 8.6 Extend of validity of 1D-solution in [27] by comparison with the present 2D-analysis for the average normal stress amplitude $\bar{\Pi}_{yy,A}\left(L_2/2,\delta,\theta\right)$ in terms of gas rarefaction parameter δ for $\theta=[0.1,1,10]$.

δ	$\bar{\Pi}_{yy,A}\left(L_2/2,\delta,\theta\right)$			$\bar{\Pi}_{yy,A}\left(\delta,\theta\right)$ [27]		
	$\theta=0.1$	$\theta=1$	$\theta=10$	$\theta=0.1$	$\theta=1$	$\theta=10$
0.01	3.923	6.129	6.153	5.392	48.85	789.4
0.1	0.649	3.838	5.922	0.6255	5.234	47.59
0.5	0.975	1.085	4.666	0.9709	1.176	10.04
1	1.010	0.5739	3.436	1.008	0.5337	5.039
2	1.004	0.7949	2.168	1.006	0.7686	2.456
4	1.005	0.9606	1.302	1.007	0.9645	1.313
6	1.005	0.9667	0.9359	1.007	0.9695	0.8822
8	1.005	0.9543	0.6649	1.007	0.9553	0.6156
10	1.005	0.9599	0.4494	1.007	0.9617	0.4045
15	1.005	0.9584	0.3173	1.007	0.96	0.2242
20	1.005	0.9583	0.8022	1.007	0.9599	0.7795

227

Table 8.7 Extend of validity of 1D-solution in [28] by comparison with the present 2D-analysis for the average shear stress amplitude $\bar{\Pi}_{xy,A}\left(L_1,\delta,\theta\right)$ in terms of gas rarefaction parameter δ for $\theta=[0.1,1,10]$.

| δ	$\bar{\Pi}_{xy,A}\left(L_1,\delta,\theta\right)$			$\bar{\Pi}_{xy,A}\left(\delta,\theta\right)$ [28]		
	$\theta=0.1$	$\theta=1$	$\theta=10$	$\theta=0.1$	$\theta=1$	$\theta=10$
0.01	0.4983	0.7581	0.7639	0.2821	0.2821	0.2821
0.1	0.2163	0.5086	0.7585	0.2801	0.2797	0.2797
0.5	0.2768	0.2329	0.6551	0.2788	0.2714	0.2709
1	0.2799	0.1874	0.5254	0.2813	0.2634	0.2612
2	0.2802	0.2748	0.3717	0.2819	0.2521	0.2093
4	0.2803	0.2506	0.2253	0.2819	0.2665	0.1741
6	0.2803	0.2616	0.1289	0.2819	0.2696	0.1465
8	0.2803	0.2627	0.0848	0.2819	0.2688	0.1531
10	0.2804	0.2638	0.0959	0.2819	0.2688	0.1622
15	0.2804	0.2647	0.1615	0.2819	0.2688	0.1632
20	0.2804	0.2653	0.1801	0.2819	0.2688	0.1627
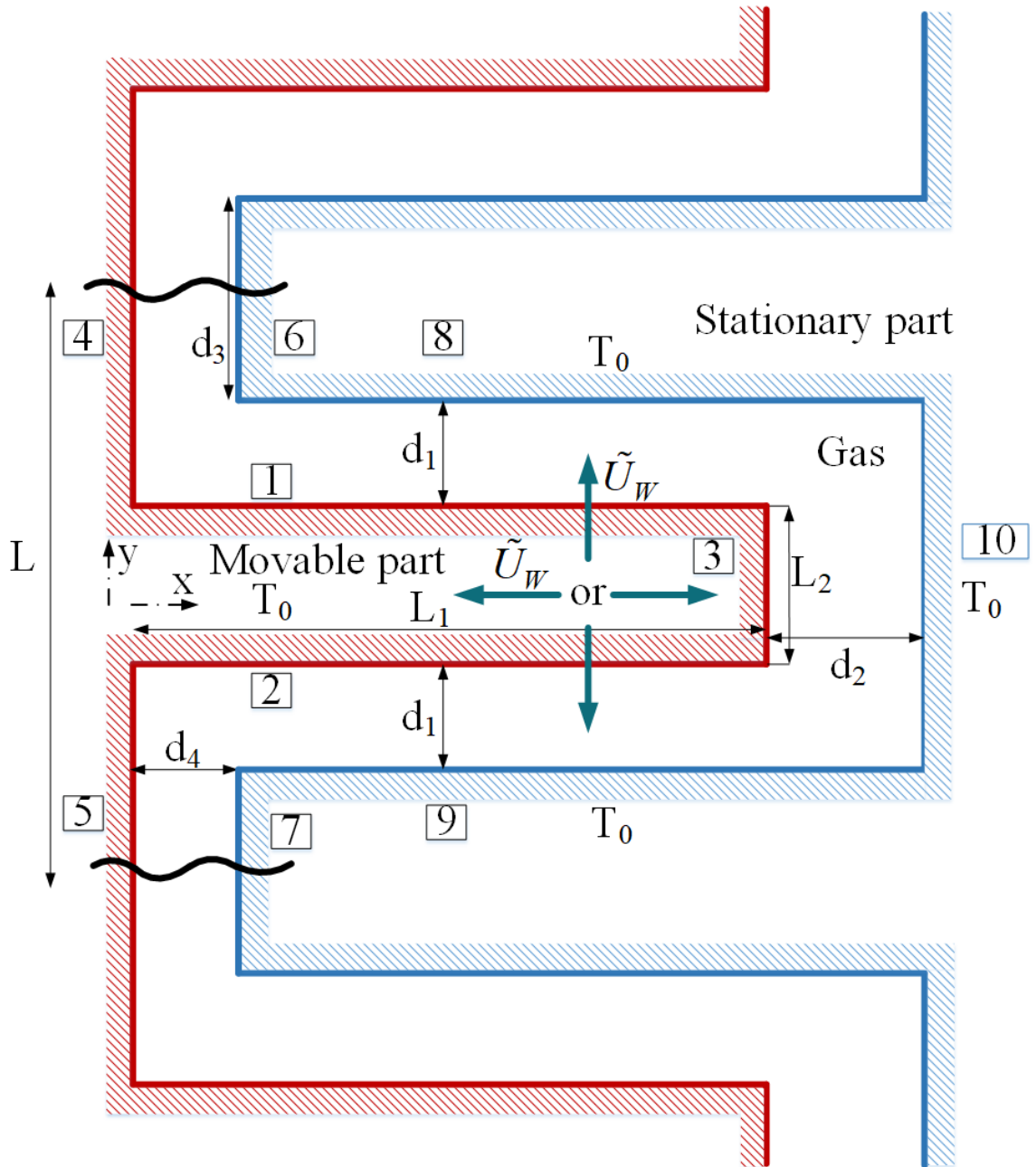
Figure 8.1 Flow configuration in a comb-type structure

229
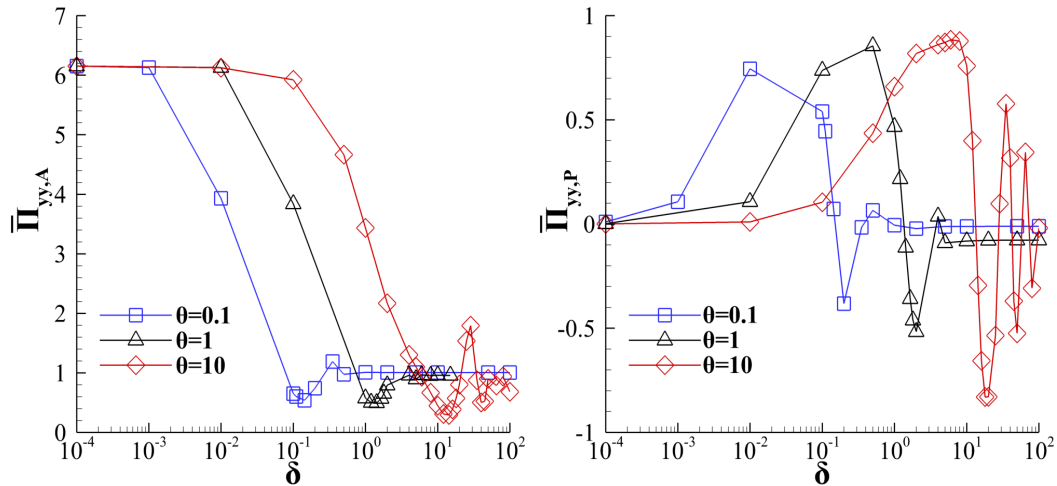
Figure 8.2 Average normal stress amplitude $\bar{\Pi}_{yy,A}\left(L_2/2, \delta, \theta\right)$ and phase $\bar{\Pi}_{yy,P}\left(L_2/2, \delta, \theta\right)$ at surface 1 in terms of gas rarefaction parameter δ and for oscillation parameter $\theta = [0.1, 1, 10]$.
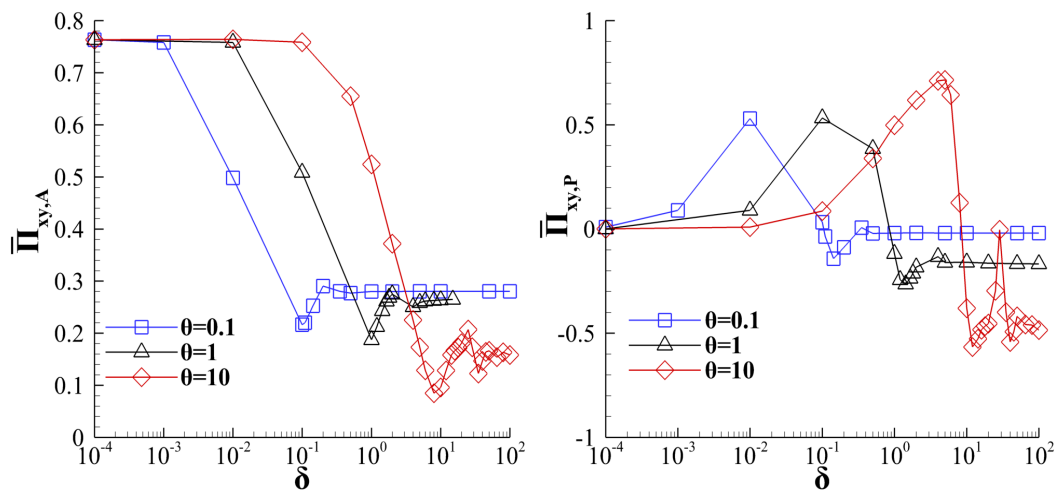
Figure 8.3 Average shear stress amplitude $\bar{\Pi}_{xy,A}\left(L_1, \delta, \theta\right)$ and phase $\bar{\Pi}_{xy,P}\left(L_1, \delta, \theta\right)$ at surface 3 in terms of gas rarefaction parameter δ and for oscillation parameter $\theta = [0.1, 1, 10]$.

230
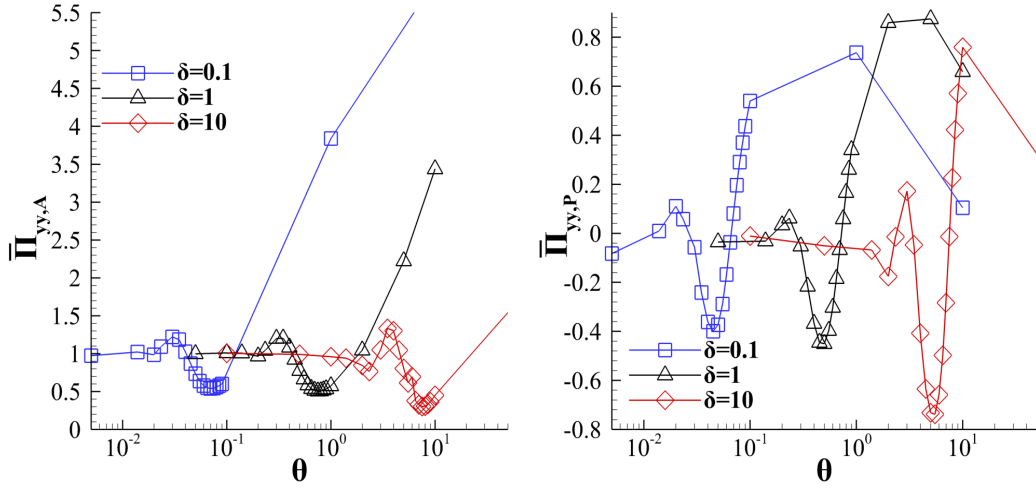
Figure 8.4 Average normal stress amplitude $\bar{\bar{\Pi}}_{yy,A}\left(L_2/2,\delta,\theta\right)$ and phase $\bar{\bar{\Pi}}_{yy,P}\left(L_2/2,\delta,\theta\right)$ at surface 1 in terms of the oscillation parameter θ and for gas rarefaction parameter $\delta=[0.1,1,10]$.
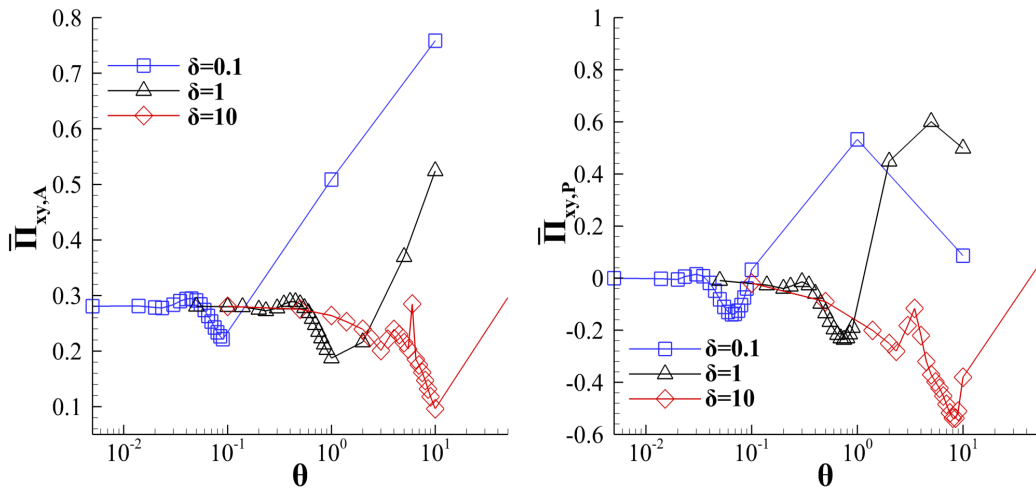
Figure 8.5 Average shear stress amplitude $\bar{\bar{\Pi}}_{xy,A}\left(L_1,\delta,\theta\right)$ and phase $\bar{\bar{\Pi}}_{xy,P}\left(L_1,\delta,\theta\right)$ at surface 3 in terms of the oscillation parameter θ and for gas rarefaction parameter $\delta=[0.1,1,10]$.

231
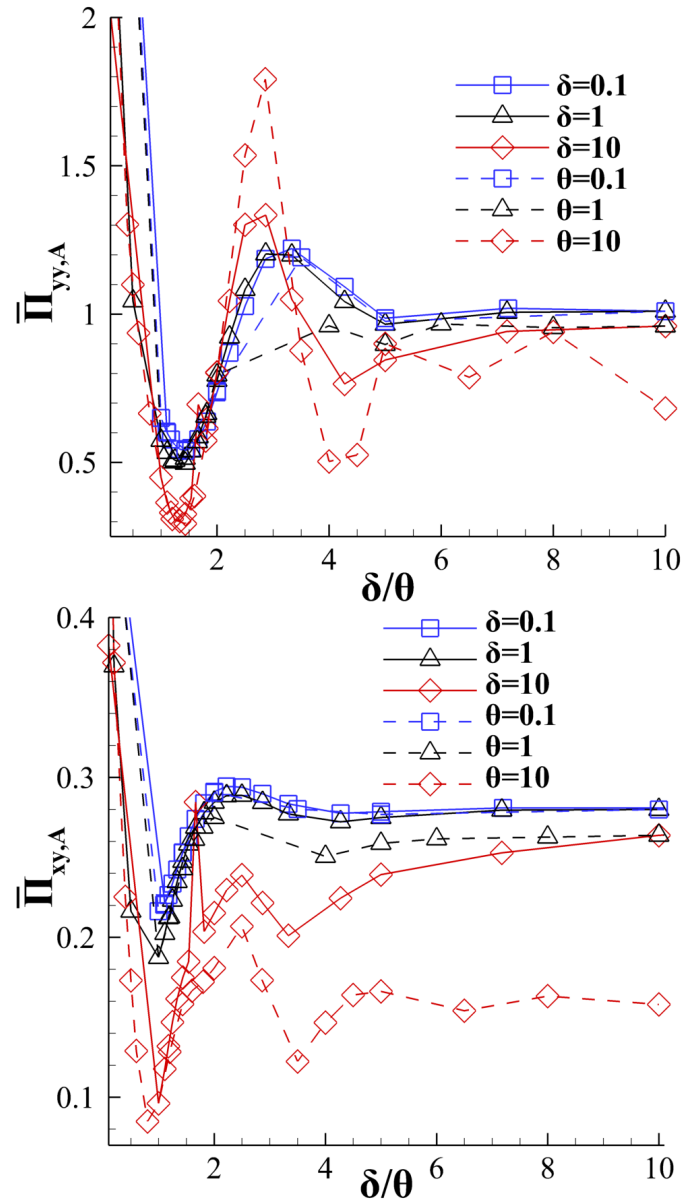
Figure 8.6 Average normal stress amplitude $\bar{\Pi}_{yy,A}\left(L_2/2, \delta, \theta\right)$ and shear stress amplitude $\bar{\Pi}_{xy,A}\left(L_1, \delta, \theta\right)$ in terms of δ/θ, for gas rarefaction parameter $\delta = [0.1, 1, 10]$ and oscillation parameter $\theta = [0.1, 1, 10]$.
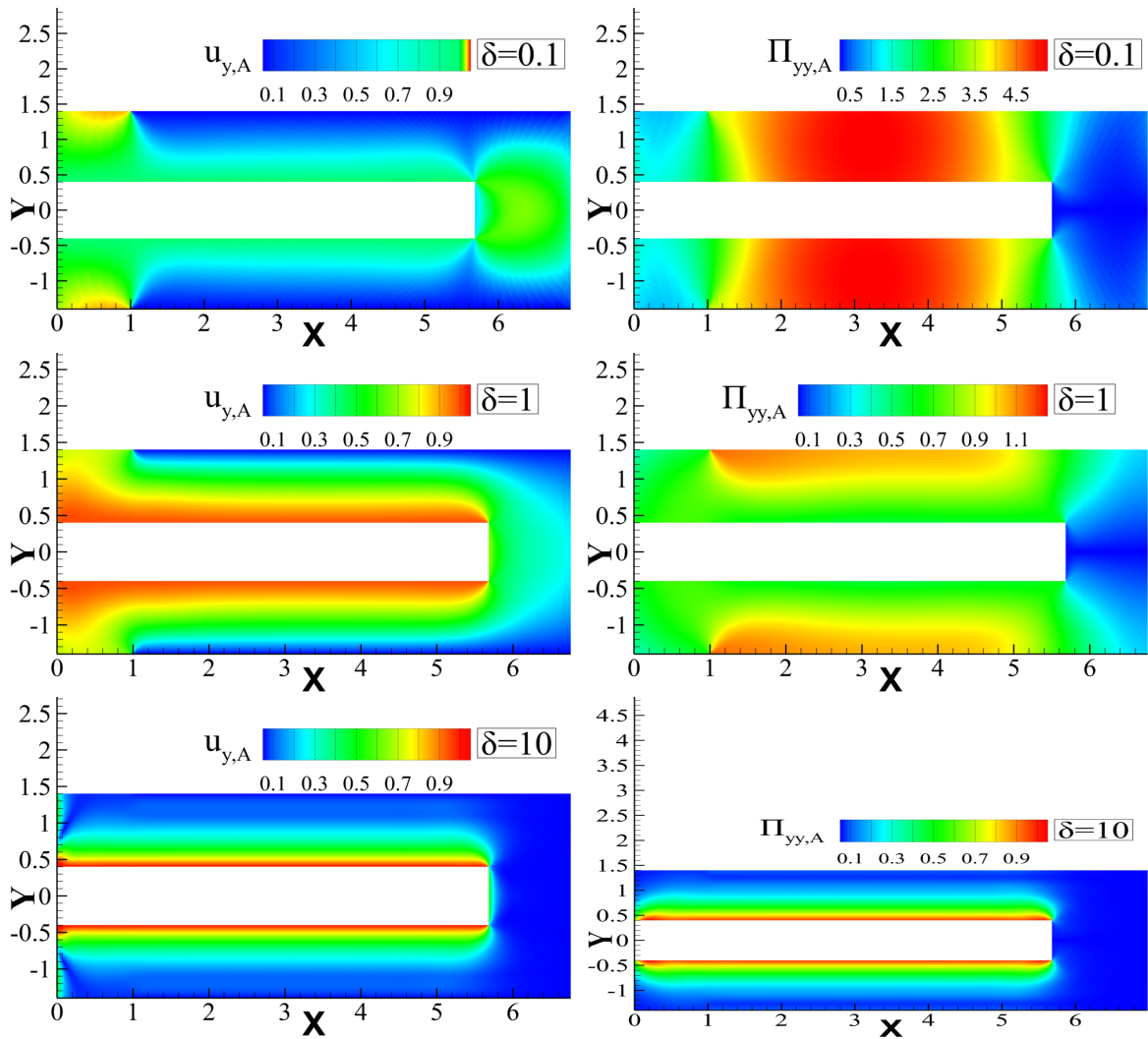
Figure 8.7 Contours of velocity $u_{y,A}(\delta, \theta)$ and normal stress amplitude $\Pi_{yy,A}(\delta, \theta)$ for comb type structures under vertical motion with $\delta = [0.1, 1, 10]$ and $\theta = 1$.

Figure 8.8 Contours of density $\rho_A(\delta, \theta)$ and temperature amplitude $\tau_A(\delta, \theta)$ for comb type structures under vertical motion with $\delta = [0.1, 1, 10]$ and $\theta = 0.1$.

234

Figure 8.9 Average normal stress amplitude $\bar{\Pi}_{xx,A}\left(L_1, \delta, \theta\right)$ and shear stress amplitude $\bar{\Pi}_{xy,A}\left(L_2/2, \delta, \theta\right)$ in terms of gas rarefaction parameter δ and for oscillation parameter $\theta = [0.1, 1]$.
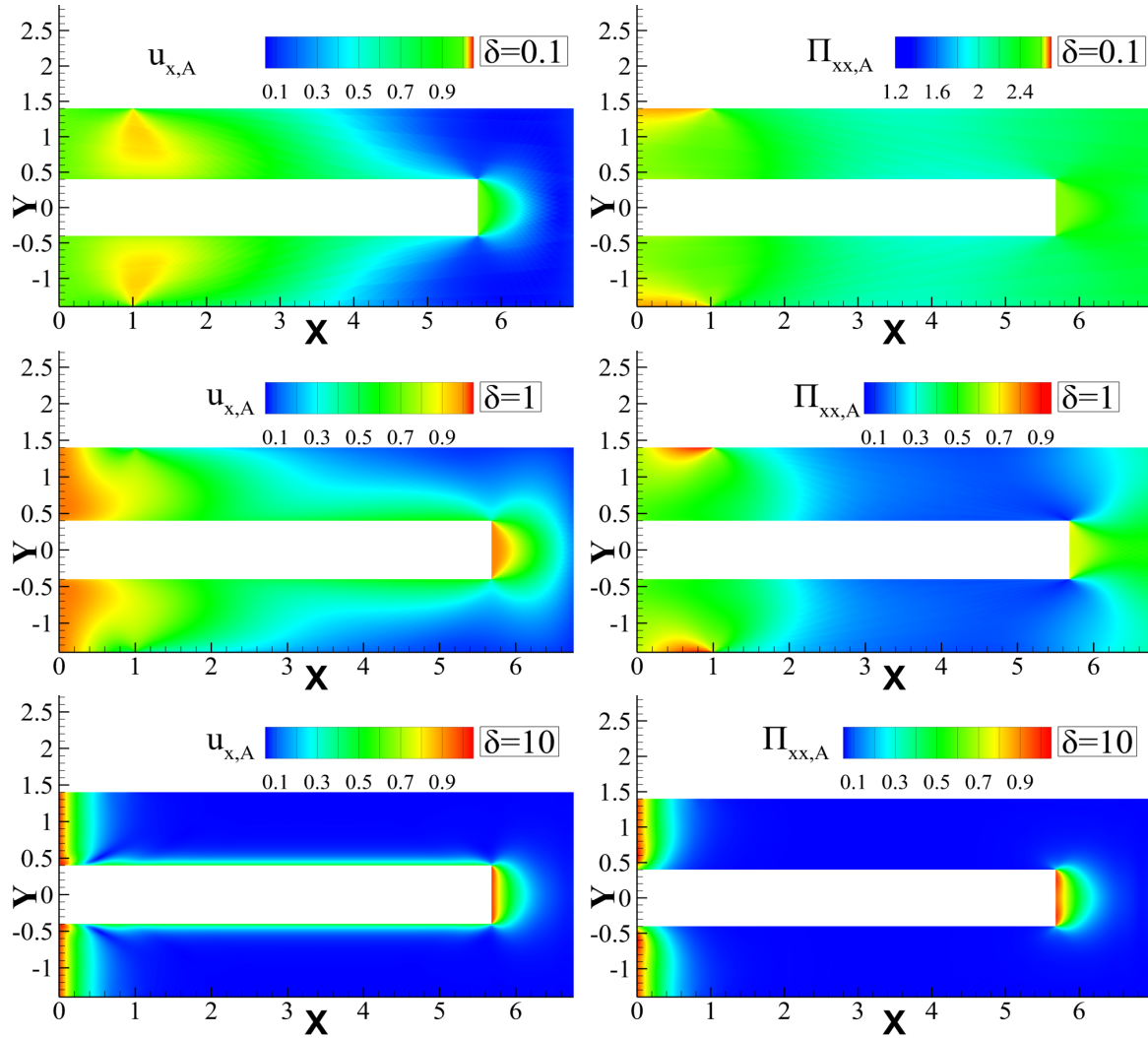
Figure 8.10 Contours of velocity $u_{x,A}(\delta, \theta)$ and normal stress amplitude $\Pi_{xx,A}(\delta, \theta)$ for comb type structures under lateral motion with $\delta = [0.1, 1, 10]$ and $\theta = 1$.
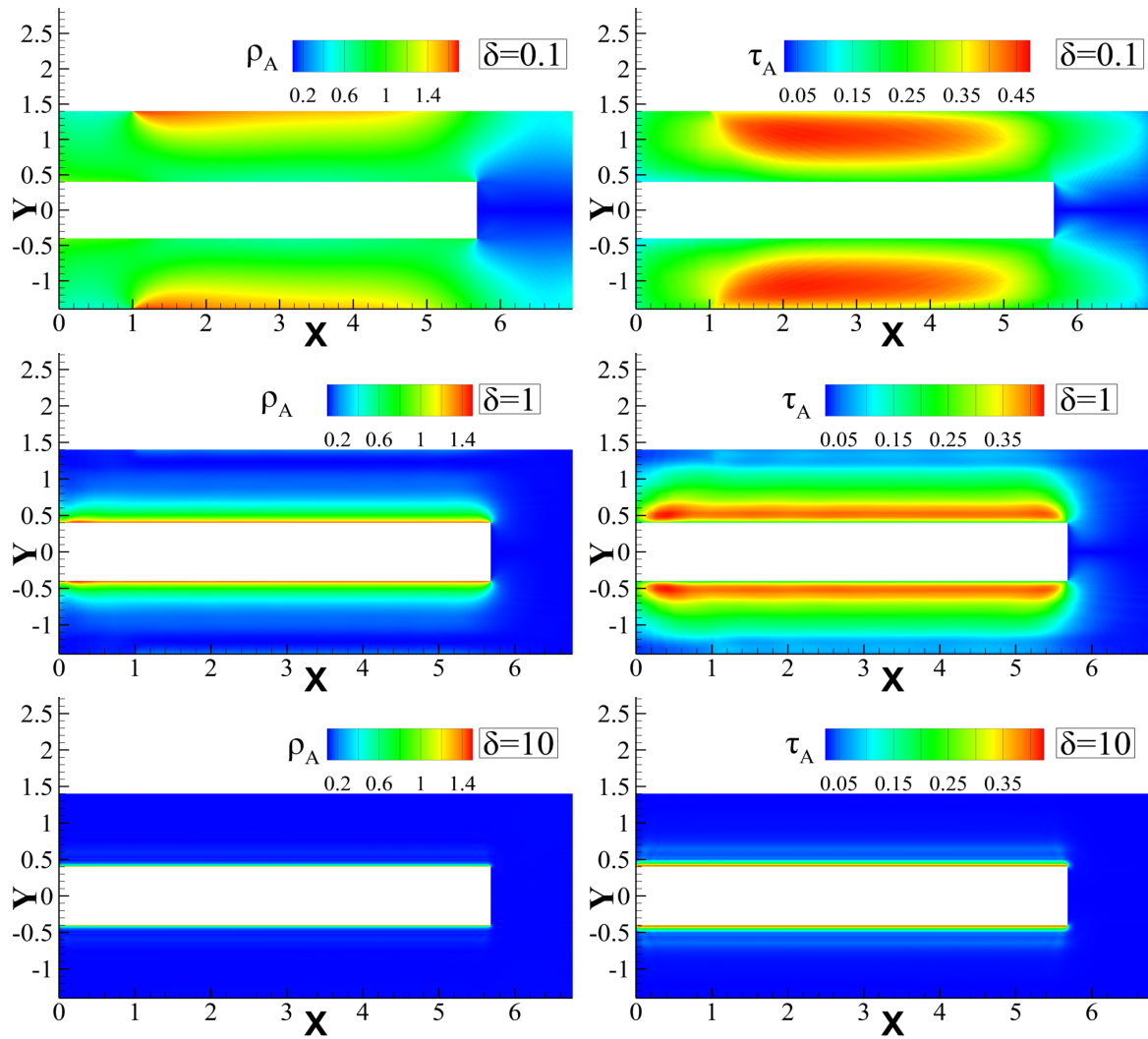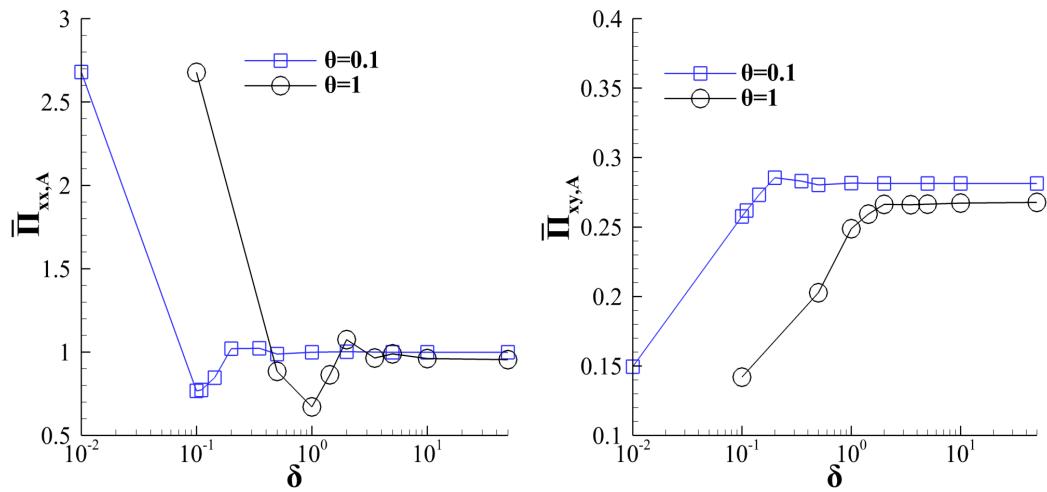
236

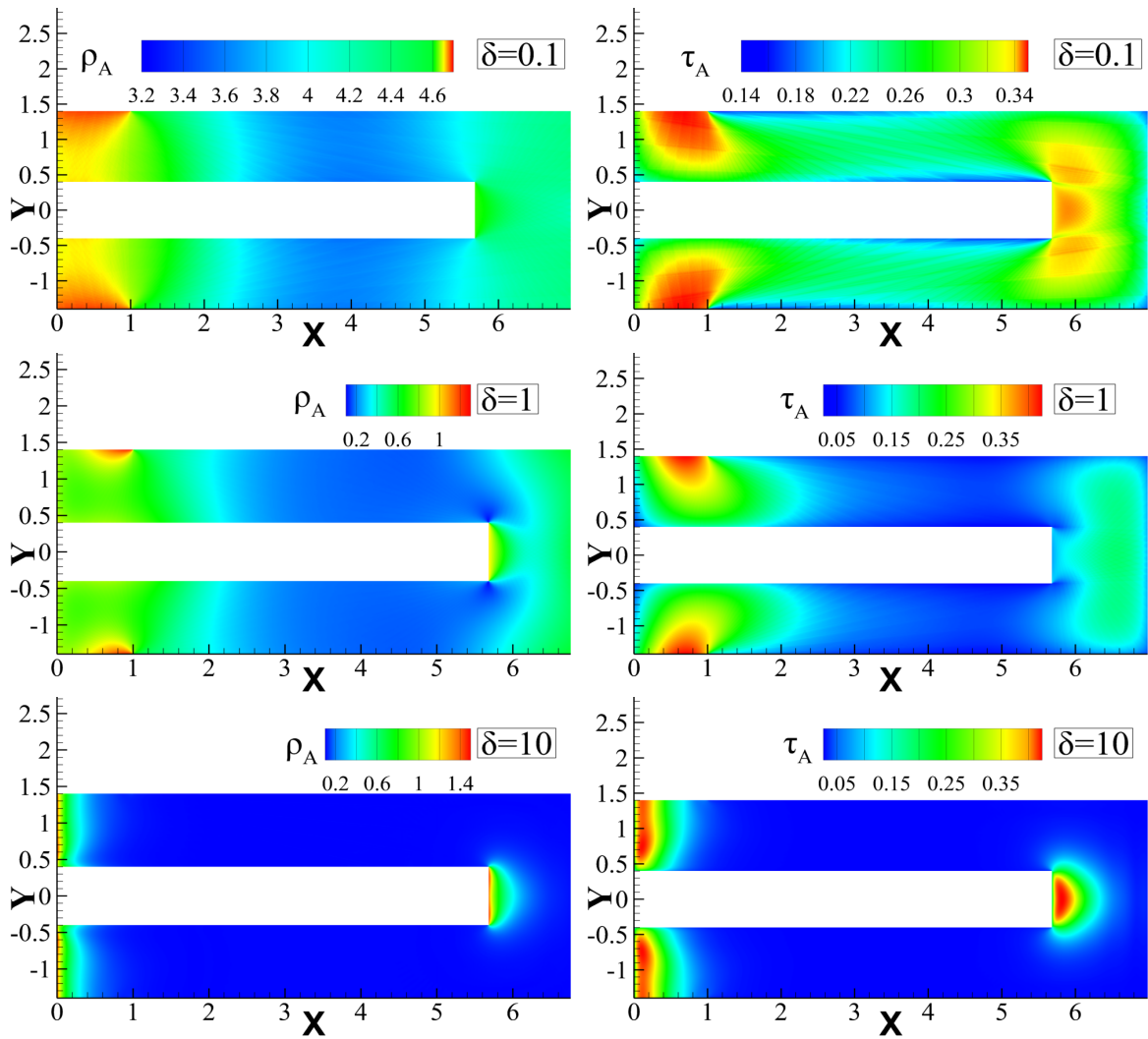Figure 8.11 Contours of density $\rho_A\left(\delta,\theta\right)$ and temperature amplitude $\tau_A\left(\delta,\theta\right)$ for comb type structures under lateral motion with $\delta=\left[0.1,1,10\right]$ and $\theta=1$.

Chapter 9

Concluding remarks

9.1 Summary and contributions

In the present dissertation, oscillatory rarefied gas flows in capillaries and enclosures have been investigated. The oscillatory motion is always considered as harmonic and it may be induced by an oscillating pressure gradient, external force, molar fraction or boundary wall. Modelling is based on kinetic theory by implementing suitable kinetic models and the DSMC method. The kinetic solution is valid in the whole range of the gas rarefaction parameter (or Knudsen number) and the oscillation frequency, which may be as high or even higher than the intermolecular collision frequencies. The amplitude of the oscillatory motion is considered as either small or arbitrary large, leading to linearized or nonlinear kinetic equations respectively. The simulations are based on monoatomic single gases and binary gas mixtures. The flow configurations include flows between parallel plates, in circular tubes, in rectangular ducts and in comb-type assemblies. Oscillatory and pulsatile rarefied gas flows may be applied in several technological devices including sensors, controllers, resonators, pumps, cooling setups, gas separators and mixers. Since the emerging technologies in vacuum technology and MEMS require low pressures and/or reduced dimensions, as well as high resonance frequencies, kinetic type approaches are needed to properly compute the flow characteristics in a wide range of space and time scales. A brief recap of the flow configurations modeled and simulated with kinetic modeling in the present work is reviewed in the next paragraphs.

In Chapter 3, the oscillatory pressure driven fully-developed rarefied gas flow in a circular tube is investigated, based on the linearized time-dependent BGK kinetic model equation. Computational results of the amplitude and the phase angle of the

flow rates and the velocity distributions, as well as of the periodic time evolution of these macroscopic quantities, are provided. The limiting flow rates in the slip and free molecular regimes for very low and high frequency oscillations are properly recovered by the kinetic solution. It is seen that at low oscillation frequencies, the flow rate and velocity distribution are in phase with the pressure gradient, while as the frequency is increased the amplitude of the macroscopic quantities is decreased and the phase angle lag is increased. In terms of the gas rarefaction, there is a non-monotonic behavior and the maximum flow rate amplitude may be observed at some intermediate value of the gas rarefaction parameter depending upon the oscillation parameter. At high frequencies, the flow consists of the core oscillating in a plug-flow mode and the Stokes layer with the velocity overshoot. These effects, which are well known in classical hydrodynamics, are also present in oscillatory rarefied flows even though higher oscillation frequencies are needed to trigger these phenomena.

In Chapter 4, the pulsatile pressure driven fully-developed flow of a rarefied gas through an orthogonal duct is investigated by decomposing the flow into its steady and oscillatory parts. The investigation is focused on the oscillatory part, which is numerically solved, based on the time-dependent linear BGK equation, in a wide range of the gas rarefaction parameter and the oscillation parameter, as well as for various values of the duct aspect ratio and the tangential momentum accommodation coefficient. Numerical results are provided for the amplitude, phase angle and time evolution of the velocity distribution, the flow rate, the mean wall shear stress, the acting inertial and viscous forces, the pumping power and the time average pumping power. Always as the oscillation frequency is increased, the amplitude of all macroscopic quantities is decreased and their phase angle lag with respect to the pressure gradient is increased. It is also observed that at small and moderate frequencies there is a critical degree of gas rarefaction in the transition regime, where a maximum flow rate is obtained. Concerning the duct aspect ratio, it has been found that as the aspect ratio is decreased and tends to zero, which corresponds to pulsatile flow between parallel plates, the flow rate and mean wall shear stress amplitudes are increased, while their phase lags are slightly affected. Similarly, the accommodation coefficient has a significant effect on the amplitudes and a very weak one on the phases of the macroscopic quantities. Furthermore, the detailed computation of the inertia and viscous forces in terms of the gas rarefaction and oscillation parameters, clarifies when the flow consists of the inviscid piston flow in the core and the oscillating Stokes layer at the wall with the velocity overshooting. Finally, the oscillatory pumping power has two peaks within

240

each oscillatory cycle and its integral over one cycle is not zero. The time average pumping power is increased as the oscillation frequency is reduced and its maximum value is one half of the corresponding steady one.

In Chapter 5, the nonlinear oscillatory fully-developed rarefied gas flow between parallel isothermal and nonisothermal plates due to an external harmonic force is investigated by the DSMC method and kinetic models. The parameters include the gas rarefaction and oscillation parameters, the force amplitude and the temperature ratio between the plates. The results are in dimensionless form and include the axial velocity, temperature, pressure, wall shear stress and heat flow vector, as well as the flow rate, cycle-averaged wall shear stress, space-averaged axial heat flow and pumping power. In terms of the mass flow rate amplitude, the DSMC results have been compared with nonlinear oscillatory kinetic model (BGK and Shakhov) results and the agreement is very good. However, there are significant discrepancies in the axial and normal heat flows. The DSMC results have been also compared with linear oscillatory results to find out that the largest deviation in the flow rate amplitude reaches about 25% at large external forces. Furthermore, all macroscopic distributions have sinusoidal pattern with its fundamental frequency being the same with the driving frequency of the external force without the appearance of other harmonics, except of the axial heat flow where the nonlinearities are responsible for generating oscillatory motion containing several harmonics. Nonlinear effects are becoming more significant in highly rarefied flows and low oscillation frequencies. Furthermore, in the nonlinear oscillatory flow with nonisothermal plates, it is seen that the space-average normal heat flow presents a periodic behavior only for low force oscillation frequencies and its magnitude is affected only by the temperature ratio.

In Chapter 6, the rarefied, oscillatory, pressure-and molar fraction driven binary gas mixture flow between parallel plates is investigated. The extra parameters here include the mixture molar fraction and the molecular mass ratio of the species, increasing significantly the computational effort. Modeling is based on the McCormack kinetic model. The output quantities are in dimensionless form and include the velocity distributions and flow rates of the species, as well as the kinetic coefficients, wall shear stress and pumping power of the mixture. Due to inertia forces, the heavier species are affected more drastically than the lighter ones resulting to large differences between the flow rate amplitudes of the species, which are increased as the flow becomes less rarefied, provided that the oscillation frequency is adequately high. At very high frequencies the ratio of the flow rate amplitudes of the light over the heavy species is approximately

241

equal to the inverse of their molecular mass ratio in the whole range of gas rarefaction. It is seen that independent of the molar fraction and the gas rarefaction regime, the amplitude ratio of the oscillatory flow rates of the light over the heavy species is significantly increased as the oscillation frequency is increased. The present results may be of major technological importance in developing and designing gas separation apparatus in the whole range of the Knudsen number that operate at moderate and high frequencies.

In Chapter 7, the oscillatory fully-developed shear driven rarefied gas flow between parallel plates is computationally investigated in terms of the gas rarefaction and oscillation parameter. This problem has been considered mainly for benchmarking purposes, as well as for optimizing the computer codes. It is pointed out that when the real and imaginary parts of the kinetic equation are solved separately, a specific treatment of the marching scheme is required. It is also seen that a suitable speed-up is achieved when two parallelization strategies based on OpenMP and OpenACC directives are applied.

In Chapter 8, the oscillatory rarefied gas flow in comb-type structures driven by the vertical/lateral harmonic motion of the moving surface is investigated. Modelling is based on the linearized unsteady Shakhov kinetic model equation. Computational results are presented mainly for the average normal pressure and shear stress of the moving walls in terms of the oscillation frequency, the gas rarefaction and the geometry of the structure. As the rarefaction parameter is increased, the amplitudes of both quantities are initially reduced, reaching some minimum values (anti-resonance state). Then, they are slightly increased and start to oscillate until they remain constant. Also, two-dimensional plots of the velocity, normal pressure, density and temperature amplitude are presented in order to visualize the whole flow domain. In addition, the gas trapping phenomenon is seen for low gas rarefaction and high oscillation frequencies. In the high frequency regime, the flow may be treated as one-dimensional. Finally, for low frequencies the stresses depend heavily on the comb dimensions, while for high frequencies they remain constant despite any changes in dimensions.

It is hoped that the theoretical findings and the computational results reported here will support, at some extend, the detailed design and optimization of various technological devices.

9.2 Future work

The work of the present Ph.D. thesis may be further extended to more complex time-dependent flow configurations. In this framework some research topics that can be implemented in the future are presented.

In oscillatory and pulsatile pressure-driven flows, the fluid displacement may be taken into account in an effort to simulate flows in more complex geometries. The effect of the piston displacement can be also considered. Although the computational effort will be significantly increased, the obtained results will be tailor-made directly connected to technological applications.

Furthermore, taking into consideration that in the hydrodynamic regime the axial heat diffusion between two containers of different temperature may be enhanced due to some axial oscillatory fluid motion, it may be interesting to investigate the corresponding problem in the transition regime. In this effort it is required in order to couple the pressure and temperature effects to solve the nonlinear problem and to investigate if the increased heat transfer rate will be maintained as the gas rarefaction is increased.

Extending the work on oscillatory binary gas mixture flows, the gas separation effect may be investigated by considering gas expansion of long capillaries into vacuum. In this setup the pressure gradient amplitude in the inlet may vary in the whole range of the Knudsen number at the entrance, while at the outlet is always set equal to zero. The profiles of the amplitude of the pressure and concentration along the capillary may be obtained and then the conductances of the two species may be deduced in order to explore if and how much the oscillatory motion increases gas separation. Obviously the work may be repeated for mixtures with more than two species.

The comb type structure may be further investigated as a part of an accelerometer or a resonator taking into account other sources of damping in addition to fluid damping. Also, the effect of the displacement of the moving parts of the comb assembly may be considered to have a more complete and probably accurate description.

In all proposed work a common factor is the increased computational cost. Therefore, it is necessary that the parallelization techniques must be extended. A first scenario is to couple the OpenMP/MPI with the OpenACC directives in order to exploit more GPUs. A second one is to couple the OpenACC directives with CUDA. When the maximum efficiency is reached with the OpenACC directives, the CUDA programming model is employed in certain kernels to gain speed-up that OpenACC cannot deliver.

The work of the present Ph.D. thesis is strictly computational. The development of suitable experimental rigs close to the flow configurations considered here and the comparison with the present numerical results will be obviously very useful.

Bibliography

[1] C. Cercignani. *Rarefied Gas Dynamics: From Basic Concepts To Actual Calculations.* Cambridge University Press, Cambridge, 2000.

[2] F. Sharipov. *Rarefied Gas Dynamics.* Wiley-VCH Verlag GmbH & Co. KGaA, Weinheim, Germany, 2016.

[3] C.-m. Ho and Y.-c. Tai. Micro-electro-mechanical-systems (MEMS) and fluid flows. *Annual Review of Fluid Mechanics*, 30(1):579–612, 1998.

[4] S. Colin. Chapter 2 - Single-phase gas flow in microchannels. In S. G. Kandlikar, S. Garimella, D. Li, S. Colin, and M. R. King, editors, *Heat Transfer and Fluid Flow in Minichannels and Microchannels*, pages 9–86. Elsevier Science Ltd, Oxford, 2006.

[5] A. Frangi, A. Frezzotti, and S. Lorenzani. On the application of the BGK kinetic model to the analysis of gas-structure interactions in MEMS. *Computers and Structures*, 85(11-14):810–817, 2007.

[6] T. Veijola and T. Mattila. Modeling of nonlinear micromechanical resonators and their simulation with the harmonic-balance method. *International Journal of RF and Microwave Computer-Aided Engineering*, 11(5):310–321, 2001.

[7] V. Kempe. *Inertial MEMS.* Cambridge University Press, Cambridge, 2011.

[8] P. Cheng and T. S. Zhao. Heat transfer in oscillatory flows. *Annual Review of Heat Transfer*, 9(9):359–420, 1998.

[9] R. Blythman, S. Alimohammadi, T. Persoons, N. Jeffers, and D. B. Murray. Parametric analysis of laminar pulsating flow in a rectangular channel. *Heat and Mass Transfer*, 54(8):2177–2186, 2018.

[10] S. Colin, C. Aubert, and R. Caen. Unsteady gaseous flows in rectangular microchannels: frequency response of one or two pneumatic lines connected in series. *European Journal of Mechanics - B/Fluids*, 17(1):79–104, 1998.

[11] H. Ma. *Oscillating Heat Pipes.* Springer New York, New York, NY, 2015.

[12] A. Batikh, L. Baldas, R. Caen, W. Ghozlani, and A. Kourta. Experimental characterization of sub-millimetric fluidic actuators: Application to boundary layer separation control. *Experimental Heat Transfer*, 23(1):4–26, 2010.

[13] A. M. Thomas. Unusual effects of oscillating flows in an annulus on mass transfer and separation. *Advances in Space Research*, 32(2):279–285, 2003.

[14] T. Zhao and P. Cheng. A numerical solution of laminar forced convection in a heated pipe subjected to a reciprocating flow. *International Journal of Heat and Mass Transfer*, 38(16):3011–3022, 1995.

[15] A. Hacioglu and R. Narayanan. Oscillating flow and separation of species in rectangular channels. *Physics of Fluids*, 28(7):073602, 2016.

[16] V. Kovalev, A. Yakunchikov, and V. Kosiantchouk. Study of gas separation by the means of high-frequency membrane oscillations. *Acta Astronautica*, 116:282–285, 2015.

[17] R. A. Abreu, A. P. Troup, and M. K. Sahm. Causes of anomalous solid formation in the exhaust systems of low-pressure chemical vapor deposition and plasma enhanced chemical vapor deposition semiconductor processes. 12:2763–2767, 1994.

[18] N. Vasileiadis, G. Tatsios, S. Misdanitis, and D. Valougeorgis. Modeling of complex gas distribution systems operating under any vacuum conditions: Simulations of the ITER divertor pumping system. *Fusion Engineering and Design*, 103:125–135, 2016.

[19] K. B. Heraty, J. G. Laffey, and N. J. Quinlan. Fluid Dynamics of Gas Exchange in High-Frequency Oscillatory Ventilation: In Vitro Investigations in Idealized and Anatomically Realistic Airway Bifurcation Models. *Annals of Biomedical Engineering*, 36(11):1856–1869, 2008.

[20] S. Chakraborty and A. P. S. Bhalla. Controlling microchannel gas flow rates through time-modulated pressure pulsation. *Journal of Applied Physics*, 102(11):114910, 2007.

[21] R. Richardson and B. Evans. A review of pulse tube refrigeration. *International Journal of Refrigeration*, 20(5):367–373, 1997.

[22] K. Jousten, editor. *Handbook of Vacuum Technology.* Wiley-VCH Verlag GmbH & Co. KGaA, Weinheim, Germany, 2016.

[23] J. Moss, C. Glass, and F. Greene. DSMC Simulations of Apollo Capsule Aerodynamics for Hypersonic Rarefied Conditions. In *9th AIAA/ASME Joint Thermophysics and Heat Transfer Conference*, Reston, Viriginia, 2006. American Institute of Aeronautics and Astronautics.

[24] M. Knudsen. Die Gesetze der Molekularströmung und der inneren Reibungsströmung der Gase durch Röhren. *Annalen der Physik*, 333(1):75–130, 1909.

[25] J. H. Ferziger and H. G. Kaper. *Mathematical theory of transport processes in gases.* North-Holland Pub. Co., Amsterdam, 1972.

[26] F. Sharipov and D. Kalempa. Gas flow around a longitudinally oscillating plate at arbitrary ratio of collision frequency to oscillation frequency. *Rarefied Gas Dynamics*, (2):1140–1145, 2007.

[27] D. Kalempa and F. Sharipov. Sound propagation through a rarefied gas confined between source and receptor at arbitrary Knudsen number and sound frequency. *Physics of Fluids*, 21(10):1–15, 2009.

[28] F. Sharipov and D. Kalempa. Numerical modeling of the sound propagation through a rarefied gas in a semi-infinite space on the basis of linearized kinetic equation. *The Journal of the Acoustical Society of America*, 124(4):1993–2001, 2008.

[29] J. R. Womersley. Method for the calculation of velocity, rate of flow and viscous drag in arteries when the pressure gradient is known. *The Journal of Physiology*, 127(3):553–563, 1955.

[30] J. C. Maxwell. V. Illustrations of the dynamical theory of gases.—Part I. On the motions and collisions of perfectly elastic spheres. *The London, Edinburgh, and Dublin Philosophical Magazine and Journal of Science*, 19(124):19–32, 1860.

247

[31] J. C. Maxwell. IV. On the dynamical theory of gases. *Philosophical Transactions of the Royal Society of London*, 157:49–88, 1867.

[32] C. Shen. *Rarefied Gas Dynamics*. Heat and Mass Transfer. Springer Berlin Heidelberg, Berlin, Heidelberg, 2005.

[33] P. L. Bhatnagar, E. P. Gross, and M. Krook. A Model for Collision Processes in Gases. I. Small Amplitude Processes in Charged and Neutral One-Component Systems. *Physical Review*, 94(3):511–525, 1954.

[34] P. Welander. On the temperature jump in a rarefied gas. *Arkiv Fysik*.

[35] F. Sharipov and V. Seleznev. Data on internal rarefied gas flows. *Journal of Physical and Chemical Reference Data*, 27(3):657–706, 1998.

[36] E. M. Shakhov. Generalization of the Krook kinetic relaxation equation. *Fluid Dynamics*, 3(5):95–96, 1972.

[37] L. H. Holway. New Statistical Models for Kinetic Theory: Methods of Construction. *Physics of Fluids*, 9(9):1658, 1966.

[38] P. Andries, P. Le Tallec, J.-P. Perlat, and B. Perthame. The Gaussian-BGK model of Boltzmann equation with small Prandtl number. *European Journal of Mechanics - B/Fluids*, 19(6):813–830, 2000.

[39] A. Fernandes and W. Marques. Kinetic model analysis of time-dependent problems in polyatomic gases. *Physica A: Statistical Mechanics and its Applications*, 373:97–118, 2007.

[40] V. A. Rykov. A model kinetic equation for a gas with rotational degrees of freedom. *Fluid Dynamics*, 10(6):959–966, 1976.

[41] L. Sirovich. Kinetic Modeling of Gas Mixtures. *Physics of Fluids*, 5(8):908, 1962.

[42] T. F. Morse. Kinetic Model Equations for a Gas Mixture. *Physics of Fluids*, 7(12):2012, 1964.

[43] B. B. Hamel. Kinetic Model for Binary Gas Mixtures. *Physics of Fluids*, 8(3):418, 1965.

[44] F. J. McCormack. Construction of linearized kinetic models for gaseous mixtures and molecular gases. *Physics of Fluids*, 16(12):2095, 1973.

248

[45] P. Andries, K. Aoki, and B. Perthame. A consistent BGK-type model for gas mixtures. *Journal of Statistical Physics*, 106(5):993–1018, 2002.

[46] S. Kosuge. Model Boltzmann equation for gas mixtures: Construction and numerical comparison. *European Journal of Mechanics - B/Fluids*, 28(1):170–184, 2009.

[47] F. Sharipov. Gaseous mixtures in vacuum systems and microfluidics. *Journal of Vacuum Science & Technology A: Vacuum, Surfaces, and Films*, 31(5):050806, 2013.

[48] S. Naris, D. Valougeorgis, D. Kalempa, and F. Sharipov. Gaseous mixture flow between two parallel plates in the whole range of the gas rarefaction. *Physica A: Statistical Mechanics and its Applications*, 336(3-4):294–318, 2004.

[49] S. Naris, D. Valougeorgis, D. Kalempa, and F. Sharipov. Flow of gaseous mixtures through rectangular microchannels driven by pressure, temperature, and concentration gradients. *Physics of Fluids*, 17(10):1–12, 2005.

[50] S. Naris and D. Valougeorgis. Shear driven micro-flows of gaseous mixtures. *Sensor Letters*, 4(1):46–52, 2006.

[51] F. Sharipov and D. Kalempa. Gaseous mixture flow through a long tube at arbitrary Knudsen numbers. *Journal of Vacuum Science & Technology A: Vacuum, Surfaces, and Films*, 20(3):814–822, 2002.

[52] J. C. Maxwell. On Stresses in Rarified Gases arising from Inequalities of Temperature. In *The Scientific Papers of James Clerk Maxwell*. 2013.

[53] S. Pantazis and D. Valougeorgis. Rarefied gas flow through a cylindrical tube due to a small pressure difference. *European Journal of Mechanics, B/Fluids*, 38:114–127, 2013.

[54] J. Pitakarnnop, S. Varoutis, D. Valougeorgis, S. Geoffroy, L. Baldas, and S. Colin. A novel experimental setup for gas microflows. *Microfluidics and Nanofluidics*, 8(1):57–72, 2010.

[55] S. Varoutis, S. Naris, V. Hauer, C. Day, and D. Valougeorgis. Computational and experimental study of gas flows through long channels of various cross sections

in the whole range of the Knudsen number. *Journal of Vacuum Science & Technology A: Vacuum, Surfaces, and Films*, 27(1):89, 2009.

[56] M. Epstein. A model of the wall boundary condition in kinetic theory. *AIAA Journal*, 5(10):1797–1800, 1967.

[57] C. Cercignani and M. Lampis. Kinetic models for gas-surface interactions. *Transport Theory and Statistical Physics*, 1(2):101–114, 1971.

[58] S. Pantazis, S. Varoutis, V. Hauer, C. Day, and D. Valougeorgis. Gas-surface scattering effect on vacuum gas flows through rectangular channels. *Vacuum*, 85(12):1161–1164, 2011.

[59] H. Grad. On the kinetic theory of rarefied gases. *Communications on Pure and Applied Mathematics*, 2(4):331–407, 1949.

[60] H. Struchtrup. *Macroscopic Transport Equations for Rarefied Gas Flows*. Interaction of Mechanics and Mathematics. Springer Berlin Heidelberg, Berlin, Heidelberg, 2005.

[61] S. Varoutis, D. Valougeorgis, O. Sazhin, and F. Sharipov. Rarefied gas flow through short tubes into vacuum. *Journal of Vacuum Science & Technology A: Vacuum, Surfaces, and Films*, 26(2):228–238, 2008.

[62] R. Gatignol. *Théorie Cinétique des Gaz à Répartition Discrète de Vitesses*, volume 36 of *Lecture Notes in Physics*. Springer Berlin Heidelberg, Berlin, Heidelberg, 1975.

[63] A. B. Huang. Nonlinear Rarefied Couette Flow with Heat Transfer. *Physics of Fluids*, 11(6):1321, 1968.

[64] G. A. Bird. *Molecular Gas Dynamics and the Direct Simulation of Gas Flows*. The Oxford engineering science series. Clarendon Press, 1994.

[65] G. A. Bird. Direct simulation and the Boltzmann equation. *Physics of Fluids*, 1970.

[66] K. Koura and H. Matsumoto. Variable soft sphere molecular model for inverse-power-law or Lennard-Jones potential. *Physics of Fluids A: Fluid Dynamics*, 3(10):2459–2465, 1991.

[67] W. Wagner. A convergence proof for Bird's direct simulation Monte Carlo method for the Boltzmann equation. *Journal of Statistical Physics*, 66(3-4):1011–1044, 1992.

[68] P. M. Morse and K. U. Ingard. *Theoretical acoustics*. McGraw-Hill, New York, 1968.

[69] G. G. Stokes. On the effect of the Internal friction of fluids on the motion of pendulums - Section III. Technical report, 1850.

[70] H. Schlichting and K. Gersten. *Boundary-Layer Theory*. Springer Berlin Heidelberg, Berlin, Heidelberg, 2017.

[71] F. White. *Viscous Fluid Flow*. McGraw-Hill Education, 2005.

[72] M. Zamir. *The Physics of Pulsatile Flow*. Springer New York, New York, NY, 2000.

[73] E. G. Richardson and E. Tyler. The transverse velocity gradient near the mouths of pipes in which an alternating or continuous flow of air is established. *Proceedings of the Physical Society*, 42(1):1–15, 1929.

[74] T. Sexl. Über den von E. G. Richardson entdeckten "Annulareffekt". *Zeitschrift für Physik*, 1930.

[75] D. G. Drake. On the flow in a channel due to a periodic pressure gradient. *Quarterly Journal of Mechanics and Applied Mathematics*, 18(1):1–10, 1965.

[76] C. Fan and B.-T. Chao. Unsteady, laminar, incompressible flow through rectangular ducts. *Zeitschrift für angewandte Mathematik und Physik ZAMP*, 16(3):351–360, 1965.

[77] H. ITO. Theory of Laminar Flow through a Pipe with Non-Steady Pressure Gradients. *Transactions of the Japan Society of Mechanical Engineers*, 18(66):101–108, 1952.

[78] S. Uchida. The pulsating viscous flow superposed on the steady laminar motion of incompressible fluid in a circular pipe. *Zeitschrift für angewandte Mathematik und Physik ZAMP*, 7(5):403–422, 1956.

251

[79] C. Fan and B.-T. Chao. Unsteady, laminar, incompressible flow through rectangular ducts. *Zeitschrift für angewandte Mathematik und Physik ZAMP*, 16(3):351–360, 1965.

[80] N. Rott. Time-dependent solutions of the navier-stokes equations. In F. K. MOORE, editor, *Theory of Laminar Flows. (HSA-4)*, pages 395–411. Princeton University Press, 1964.

[81] R. Blythman, T. Persoons, N. Jeffers, K. Nolan, and D. Murray. Localised dynamics of laminar pulsatile flow in a rectangular channel. *International Journal of Heat and Fluid Flow*, 66:8–17, 2017.

[82] H. L. Ma and C. H. Kuo. Theoretical analysis of an oscillatory plane Poiseuille flow-A link to the design of vortex flow meter. *Physics of Fluids*, 29(5), 2017.

[83] J. Majdalani. Exact Navier-Stokes Solution for the Pulsatory Viscous Channel Flow with Arbitrary Pressure Gradient. *Journal of Propulsion and Power*, 24(6):1412–1423, 2008.

[84] S. Tsangaris and N. W. Vlachakis. Exact solution of the navier-stokes equations for the fully developed, pulsating flow in a rectangular duct with a constant cross-sectional velocity. *Journal of Fluids Engineering, Transactions of the ASME*, 125(2):382–384, 2003.

[85] H. Gordon Harris and S. L. Goren. Axial diffusion in a cylinder with pulsed flow. *Chemical Engineering Science*, 22(12):1571–1576, 1967.

[86] E. J. Watson. Diffusion in oscillatory pipe flow. *Journal of Fluid Mechanics*, 133:233–244, 1983.

[87] G. W. Howell. Separation of isotopes by oscillatory flow. *Physics of Fluids*, 31(6):1803, 1988.

[88] M. J. Jaeger, T. Soepardi, A. Maddahian, and U. Kurzweg. Diffusional Separation of Gases and Solutes in Oscillatory Flow. *Separation Science and Technology*, 26(4):503–514, 1991.

[89] U. H. Kurzweg and M. J. Jaeger. Diffusional separation of gases by sinusoidal oscillations. *Physics of Fluids*, 30(4):1023, 1987.

[90] R. G. Rice and L. C. Eagleton. Mass transfer produced by laminar flow oscillations. *The Canadian Journal of Chemical Engineering*, 48(1):46–51, 1970.

[91] A. M. Thomas and R. Narayanan. Physics of oscillatory flow and its effect on the mass transfer and separation of species. *Physics of Fluids*, 13(4):859–866, 2001.

[92] A. M. Thomas and R. Narayanan. A comparison between the enhanced mass transfer in boundary and pressure driven oscillatory flow. *International Journal of Heat and Mass Transfer*, 45(19):4057–4062, 2002.

[93] L. Kumar and S. Narayanan. Analysis of pulsatile flow and its role on particle removal from surfaces. *Chemical Engineering Science*, 65(20):5582–5587, 2010.

[94] U. H. Kurzweg, G. Howell, and M. J. Jaeger. Enhanced dispersion in oscillatory flows. *Physics of Fluids*, 27(5):1046, 1984.

[95] U. H. Kurzweg. Enhanced heat conduction in oscillating viscous flows within parallel-plate channels. *Journal of Fluid Mechanics*, 156(-1):291, 1985.

[96] M. Kaviany. Some aspects of enhanced heat diffusion in fluids by oscillation. *International Journal of Heat and Mass Transfer*, 29(12):2002–2006, 1986.

[97] I. Takahashi. Axial Heat-Transfer Characteristics Enhanced by Oscillating Fluid in a Thin Tube.A Newly Proposed Model and Expression for Effective Thermal Diffusivity. *Transactions of the Japan Society of Mechanical Engineers Series B*, 61(581):275–282, 1995.

[98] H. Cho and J. Hyun. Numerical solutions of pulsating flow and heat transfer characteristics in a pipe. *International Journal of Heat and Fluid Flow*, 11(4):321–330, 1990.

[99] M. Faghri, K. Javdani, and A. Faghri. Heat transfer with laminar pulsating flow in a pipe. *Letters in Heat and Mass Transfer*, 6(4):259–270, 1979.

[100] H. N. Hemida, M. N. Sabry, A. Abdel-Rahim, and H. Mansour. Theoretical analysis of heat transfer in laminar pulsating flow. *International Journal of Heat and Mass Transfer*, 2002.

[101] M. Mackley and P. Stonestreet. Heat transfer and associated energy dissipation for oscillatory flow in baffled tubes. *Chemical Engineering Science*, 50(14):2211–2224, 1995.

[102] V. V. Mamayev, V. S. Nosov, and N. I. Syromyatnikov. Investigation of heat transfer in pulsed flow of air in pipes. *Heat Transfer Sov Res*, 8:111–116, 1976.

[103] T. Moschandreou and M. Zamir. Heat transfer in a tube with pulsating flow and constant heat flux. *International Journal of Heat and Mass Transfer*, 40(10):2461–2466, 1997.

[104] J.-C. Yu, Z.-X. Li, and T. Zhao. An analytical study of pulsating laminar heat convection in a circular tube with constant heat flux. *International Journal of Heat and Mass Transfer*, 47(24):5297–5301, 2004.

[105] E. M. Benavides. Heat transfer enhancement by using pulsating flows. *Journal of Applied Physics*, 105(9):094907, 2009.

[106] T. Veijola. Chapter Fourteen - Gas Damping in Vibrating MEMS Structures. In V. Lindroos, M. Tilli, A. Lehto, T. B. T. H. o. S. B. M. M. Motooka, and Technologies, editors, *Micro and Nano Technologies*, pages 259–279. William Andrew Publishing, Boston, 2010.

[107] O. Reynolds. On the Theory of Lubrication and Its Application to Mr. Beauchamp Tower's Experiments, Including an Experimental Determination of the Viscosity of Olive Oil. *Philosophical Transactions of the Royal Society of London*, 177:157–234, 1886.

[108] R. M. Terrill. The Flow Between Two Parallel Circular Disks, One of Which is Subject to a Normal Sinusoidal Oscillation. *Journal of Lubrication Technology*, 91(1):126–131, 1969.

[109] M. Fox and P. Whitton. The damping of structural vibration by thin gas films. *Journal of Sound and Vibration*, 73(2):279–295, 1980.

[110] W. Beltman, P. van der Hoogt, R. Spiering, and H. Tijdeman. Air loads on a rigid plate oscillating normal to a fixed surface. *Journal of Sound and Vibration*, 206(2):217–242, 1997.

[111] Y.-H. Cho, B. M. Kwak, A. P. Pisano, and R. T. Howe. Slide film damping in laterally driven microstructures. *Sensors and Actuators A: Physical*, 40(1):31–39, 1994.

[112] Xia Zhang and W. Tang. Viscous air damping in laterally driven microresonators. In *Proceedings IEEE Micro Electro Mechanical Systems An Investigation of Micro Structures, Sensors, Actuators, Machines and Robotic Systems*, pages 199–204. IEEE, 1994.

[113] Y. J. J. Yang and P. C. Yen. An efficient macromodeling methodology for lateral air damping effects. *Journal of Microelectromechanical Systems*, 2005.

[114] T. Veijola, H. Kuisma, and J. Lahdenperä. The influence of gas-surface interaction on gas-film damping in a silicon accelerometer. *Sensors and Actuators A: Physical*, 66(1-3):83–92, 1998.

[115] T. Veijola, H. Kuisma, J. Lahdenperä, and T. Ryhänen. Equivalent-circuit model of the squeezed gas film in a silicon accelerometer. *Sensors and Actuators: A. Physical*, 48(3):239–248, 1995.

[116] T. Veijola. Compact model for a MEM perforation cell with viscous, spring, and inertial forces. *Microfluidics and Nanofluidics*, 6(2):203–219, 2009.

[117] T. Veijola. Compact models for squeezed-film dampers with inertial and rarefied gas effects. *Journal of Micromechanics and Microengineering*, 14(7):1109–1118, 2004.

[118] C. Cercignani. Variational Approach to Boundary-Value Problems in Kinetic Theory. *Physics of Fluids*, 9(6):1167, 1966.

[119] C. Cercignani and A. Daneri. Flow of a rarefied gas between two parallel plates. *Journal of Applied Physics*, 34(12):3509–3513, 1963.

[120] S. K. Loyalka and T. C. Cheng. Sound-wave propagation in a rarefied gas. *Physics of Fluids*, 22(5):830, 1979.

[121] C. E. Siewert, R. D. M. Garcia, and P. Grandjean. A concise and accurate solution for Poiseuille flow in a plane channel. *Journal of Mathematical Physics*, 21(12):2760–2763, 1980.

[122] I. A. Graur, A. P. Polikarpov, and F. Sharipov. Numerical modelling of rarefied gas flow through a slit at arbitrary pressure ratio based on the kinetic equation. *Zeitschrift für angewandte Mathematik und Physik*, 63(3):503–520, 2012.

255

[123] S. Pantazis, D. Valougeorgis, and F. Sharipov. End corrections for rarefied gas flows through capillaries of finite length. *Vacuum*, 97:26–29, 2013.

[124] F. SHARIPOV. Numerical simulation of rarefied gas flow through a thin orifice. *Journal of Fluid Mechanics*, 518:35–60, 2004.

[125] S. Varoutis, D. Valougeorgis, and F. Sharipov. Simulation of gas flow through tubes of finite length over the whole range of rarefaction for various pressure drop ratios. *Journal of Vacuum Science & Technology A: Vacuum, Surfaces, and Films*, 27(6):1377–1391, 2009.

[126] S. Pantazis, D. Valougeorgis, and F. Sharipov. End corrections for rarefied gas flows through circular tubes of finite length. *Vacuum*, 101:306–312, 2014.

[127] A. Tsimpoukis and D. Valougeorgis. Rarefied isothermal gas flow in a long circular tube due to oscillating pressure gradient. *Microfluidics and Nanofluidics*, 22(1):5, 2018.

[128] A. Tsimpoukis and D. Valougeorgis. Pulsatile pressure driven rarefied gas flow in long rectangular ducts. *Physics of Fluids*, 30(4):047104, 2018.

[129] T. Cheng and S. Loyalka. Sound wave propagation in a rarefied gas-II: Gross-Jackson model. *Progress in Nuclear Energy*, 8(2-3):263–268, 1981.

[130] S. K. Loyalka, N. Petrellis, and T. S. Storvick. Some exact numerical results for the BGK model: Couette, Poiseuille and thermal creep flow between parallel plates. *Zeitschrift für angewandte Mathematik und Physik ZAMP*, 1979.

[131] J. R. Thomas and C. E. Siewert. Sound-wave propagation in a rarefied gas. *Transport Theory and Statistical Physics*, 8(4):219–240, 1979.

[132] M. Greenspan. Propagation of Sound in Five Monatomic Gases. *The Journal of the Acoustical Society of America*, 28(4):644–648, 1956.

[133] C. Cercignani and A. Majorana. Analysis of thermal and shear waves according to BKG kinetic model. *ZAMP Zeitschrift fr angewandte Mathematik und Physik*, 36(5):699–711, 1985.

[134] R. D. M. Garcia and C. E. Siewert. The linearized Boltzmann equation: Sound-wave propagation in a rarefied gas. *Zeitschrift fur Angewandte Mathematik und Physik*, 57(1):94–122, 2005.

256

[135] N. G. Hadjiconstantinou and O. Simek. Constant-Wall-Temperature Nusselt Number in Micro and Nano-Channels. *Journal of Heat Transfer*, 124(2):356, 2002.

[136] N. G. Hadjiconstantinou and A. L. Garcia. Molecular simulations of sound wave propagation in simple gases. *Physics of Fluids*, 13(4):1040–1046, 2001.

[137] A. Manela and L. Pogorelyuk. Cloaking via heating: Approach to acoustic cloaking of an actuated boundary in a rarefied gas. *Physics of Fluids*, 26(6):062003, 2014.

[138] R.-J. Wang and K. Xu. The study of sound wave propagation in rarefied gases using unified gas-kinetic scheme. *Acta Mechanica Sinica*, 28(4):1022–1029, 2012.

[139] L. Wu. Sound propagation through a rarefied gas in rectangular channels. *Physical Review E*, 94(5):053110, 2016.

[140] Y. Ben Ami and A. Manela. Acoustic field of a pulsating cylinder in a rarefied gas: Thermoviscous and curvature effects. *Physical Review Fluids*, 2(9):093401, 2017.

[141] Y. Ben-Ami and A. Manela. The sound of a pulsating sphere in a rarefied gas: continuum breakdown at short length and time scales. *Journal of Fluid Mechanics*, 871:668–693, 2019.

[142] D. R. Emerson, X.-J. Gu, S. K. Stefanov, S. Yuhong, and R. W. Barber. Nonplanar oscillatory shear flow: From the continuum to the free-molecular regime. *Physics of Fluids*, 19(10):107105, 2007.

[143] Y. W. Yap and J. E. Sader. Sphere oscillating in a rarefied gas. *Journal of Fluid Mechanics*, 794:109–153, 2016.

[144] T. Doi. Numerical analysis of oscillatory Couette flow of a rarefied gas on the basis of the linearized Boltzmann equation for a hard sphere molecular gas. *Zeitschrift fur Angewandte Mathematik und Physik*, 61(5):811–822, 2010.

[145] N. G. Hadjiconstantinou. Oscillatory shear-driven gas flows in the transition and free-molecular-flow regimes. *Physics of Fluids*, 17(10):1–9, 2005.

[146] J. H. Park, P. Bahukudumbi, and A. Beskok. Rarefaction effects on shear driven oscillatory gas flows: A direct simulation Monte Carlo study in the entire Knudsen regime. *Physics of Fluids*, 16(2):317–330, 2004.

[147] Y. W. Yap and J. E. Sader. High accuracy numerical solutions of the Boltzmann Bhatnagar-Gross-Krook equation for steady and oscillatory Couette flows. *Physics of Fluids*, 24(3):0–18, 2012.

[148] L. Wu, J. M. Reese, and Y. Zhang. Oscillatory rarefied gas flow inside rectangular cavities. *Journal of Fluid Mechanics*, 748:350–367, 2014.

[149] T. Doi. Plane Poiseuille flow of a rarefied gas in the presence of strong gravitation. *Physical Review E - Statistical, Nonlinear, and Soft Matter Physics*, 83(2):1–10, 2011.

[150] A. Manela and N. G. Hadjiconstantinou. Gas-flow animation by unsteady heating in a microchannel. *Physics of Fluids*, 22(6):1–12, 2010.

[151] J. Nassios, Y. W. Yap, and J. E. Sader. Flow generated by oscillatory uniform heating of a rarefied gas in a channel. *Journal of Fluid Mechanics*, 800(2016):433–483, 2016.

[152] D. Kalempa and F. Sharipov. Numerical modelling of thermoacoustic waves in a rarefied gas confined between coaxial cylinders. *Vacuum*, 109:326–332, 2014.

[153] A. Manela, G. A. Radtke, and L. Pogorelyuk. On the damping effect of gas rarefaction on propagation of acoustic waves in a microchannel. *Physics of Fluids*, 26(3):032001, 2014.

[154] L. Desvillettes and S. Lorenzani. Sound wave resonances in micro-electro-mechanical systems devices vibrating at high frequencies according to the kinetic theory of gases. *Physics of Fluids*, 24(9):1–24, 2012.

[155] S. Lorenzani and L. Desvillettes. A kinetic approach for the evaluation of damping in micro-electro-mechanical systems devices vibrating at high frequencies. In *AIP Conference Proceedings 1501*, volume 808, pages 802–808, 2012.

[156] A. Manela and L. Pogorelyuk. Active noise control of a vibrating surface: Continuum and non-continuum investigations on vibroacoustic sound reduction

258

by a secondary heat-flux source. *Journal of Sound and Vibration*, 358:20–34, 2015.

[157] T. Ohwada and M. Kunihisa. Direct Simulation of a Flow Produced by a Plane Wall Oscillating in Its Normal Direction. *AIP Conference Proceedings*, 663(October):202–209, 2003.

[158] K. Aoki, S. Kosuge, T. Fujiwara, and T. Goudon. Unsteady motion of a slightly rarefied gas caused by a plate oscillating in its normal direction. *Physical Review Fluids*, 2(1):1–33, 2017.

[159] T. Tsuji and K. Aoki. Numerical analysis of nonlinear acoustic wave propagation in a rarefied gas. *28 th International Symposium on Rarefied Gas Dynamics RGD 28*, 1501:115–122, 2012.

[160] T. Tsuji and K. Aoki. Gas motion in a microgap between a stationary plate and a plate oscillating in its normal direction. *Microfluidics and Nanofluidics*, 16(6):1033–1045, 2014.

[161] Y. Ben-Ami and A. Manela. Nonlinear thermal effects in unsteady shear flows of a rarefied gas. *Physical Review E*, 98(3):033121, 2018.

[162] S. Wang, A. Batikh, L. Baldas, A. Kourta, N. Mazellier, S. Colin, and S. Orieux. On the modelling of the switching mechanisms of a Coanda fluidic oscillator. *Sensors and Actuators A: Physical*, page 111618, 2019.

[163] P. Wang, L. Zhu, W. Su, L. Wu, and Y. Zhang. Nonlinear oscillatory rarefied gas flow inside a rectangular cavity. *Physical Review E*, 97(4):43103, 2018.

[164] A. Tsimpoukis, N. Vasileiadis, G. Tatsios, and D. Valougeorgis. Nonlinear oscillatory fully-developed rarefied gas flow in plane geometry. *Physics of Fluids*, 31(6):067108, 2019.

[165] A. Fernandes and W. Marques. Sound propagation in binary gas mixtures from a kinetic model of the Boltzmann equation. *Physica A: Statistical Mechanics and its Applications*, 332:29–46, 2004.

[166] D. Kalempa and F. Sharipov. Sound propagation through a binary mixture of rarefied gases at arbitrary sound frequency. *European Journal of Mechanics, B/Fluids*, 57:50–63, 2016.

[167] D. Kalempa, F. Sharipov, and J. C. Silva. Sound waves in gaseous mixtures induced by vibro-thermal excitation at arbitrary rarefaction and sound frequency. *Vacuum*, 159:82–98, 2019.

[168] M. Bisi and S. Lorenzani. High-frequency sound wave propagation in binary gas mixtures flowing through microchannels. *Physics of Fluids*, 28(5):052003, 2016.

[169] M. Bisi and S. Lorenzani. Damping forces exerted by rarefied gas mixtures in micro-electro-mechanical system devices vibrating at high frequencies. *Interfacial Phenomena and Heat Transfer*, 2(3):253–263, 2014.

[170] R. Caen and S. Colin. Multidirectional Pneumatic Force Sensor For Grippers. In *Robotic Systems*, pages 551–558. Springer Netherlands, Dordrecht, 1992.

[171] A. Batikh, R. CAEN, S. COLIN, and L. BALDAS. Numerical and Experimental study of micro synthetic jets for flow control. *Heat and Technology*, (June):7, 2008.

[172] S. Wang, L. Baldas, S. Colin, N. Mazellier, and A. Kourta. Numerical and experimental characterization of a micro-oscillator for flow control. In *4th European Conference on Microfluidics (µFlu'14), Limerick, Ireland*, pages µFLU14–131:1–9, 2014.

[173] C. Morris and F. Forster. Low-order modeling of resonance for fixed-valve micropumps based on first principles. *Journal of Microelectromechanical Systems*, 12(3):325–334, 2003.

[174] O. Buchina and D. Valougeorgis. Oscillatory heating in a microchannel at arbitrary oscillation frequency in the whole range of the Knudsen number. *Journal of Physics: Conference Series*, 362(1), 2012.

[175] J. Lihnaropoulos and D. Valougeorgis. Unsteady vacuum gas flow in cylindrical tubes. *Fusion Engineering and Design*, 86(9-11):2139–2142, 2011.

[176] R. L. Panton. *Incompressible Flow*. John Wiley & Sons, Inc., Hoboken, NJ, USA, 2013.

[177] R. Blythman, T. Persoons, N. Jeffers, and D. B. Murray. Effect of oscillation frequency on wall shear stress and pressure drop in a rectangular channel for heat transfer applications. *Journal of Physics: Conference Series*, 745(3), 2016.

[178] J. Xiao. Thermoacoustic heat transportation and energy transformation Part 1: Formulation of the problem. *Cryogenics*, 35(1):15–19, 1995.

[179] F. Sharipov. Rarefied gas flow through a long rectangular channel. *Journal of Vacuum Science & Technology A: Vacuum, Surfaces, and Films*, 17(5):3062–3066, 1999.

[180] S. Naris and D. Valougeorgis. Rarefied gas flow in a triangular duct based on a boundary fitted lattice. *European Journal of Mechanics, B/Fluids*, 27(6):810–822, 2008.

[181] A. T. S. Varoutis, J. Lihnaropoulos, D. Valougeorgis, D. Mathioulakis. Estimation of the Poiseuille number and of the exact hydraulic diameter in rarefied gas flows through channels of various cross sections. In *Proceedings of the 1st European Conference on Microfluidics - Microfluidics*, Bologna, 2008.

[182] C. Cercignani. *The Boltzmann Equation and Its Applications*, volume 67 of *Applied Mathematical Sciences*. Springer New York, New York, NY, 1988.

[183] K. Aoki, S. Takata, and T. Nakanishi. Poiseuille-type flow of a rarefied gas between two parallel plates driven by a uniform external force. *Physical Review E - Statistical Physics, Plasmas, Fluids, and Related Interdisciplinary Topics*, 65(2), 2002.

[184] B. John, X.-J. Gu, and D. R. Emerson. Nonequilibrium gaseous heat transfer in pressure-driven plane Poiseuille flow. *Physical Review E*, 88(1):013018, 2013.

[185] M. Malek Mansour, F. Baras, and A. L. Garcia. On the validity of hydrodynamics in plane Poiseuille flows. *Physica A: Statistical Mechanics and its Applications*, 240(1-2):255–267, 1997.

[186] J. Meng, L. Wu, J. M. Reese, and Y. Zhang. Assessment of the ellipsoidal-statistical Bhatnagar–Gross–Krook model for force-driven Poiseuille flows. *Journal of Computational Physics*, 251:383–395, 2013.

[187] G. Tatsios, S. K. Stefanov, and D. Valougeorgis. Predicting the Knudsen paradox in long capillaries by decomposing the flow into ballistic and collision parts. *Physical Review E*, 91(6):061001, 2015.

[188] M. Tij, M. Sabbane, and A. Santos. Nonlinear Poiseuille flow in a gas. *Physics of Fluids*, 10(4):1021–1027, 1998.

[189] J. Meng, L. Wu, J. M. Reese, and Y. Zhang. Assessment of the ellipsoidal-statistical Bhatnagar–Gross–Krook model for force-driven Poiseuille flows. *Journal of Computational Physics*, 251:383–395, 2013.

[190] E. M. Shakhov. Generalization of the Krook kinetic relaxation equation. *Fluid Dynamics*, 3(5):95–96, 1968.

[191] S. Varoutis, D. Valougeorgis, and F. Sharipov. Application of the integro-moment method to steady-state two-dimensional rarefied gas flows subject to boundary induced discontinuities. *Journal of Computational Physics*, 227(12):6272–6287, 2008.

[192] D. Kalempa and F. Sharipov. Flows of rarefied gaseous mixtures with a low mole fraction. Separation phenomenon. *European Journal of Mechanics - B/Fluids*, 30(4):466–473, 2011.

[193] F. Sharipov and D. Kalempa. Separation phenomena for gaseous mixture flowing through a long tube into vacuum. *Physics of Fluids*, 17(12):127102, 2005.

[194] D. Valougeorgis, M. Vargas, and S. Naris. Analysis of gas separation, conductance and equivalent single gas approach for binary gas mixture flow expansion through tubes of various lengths into vacuum. *Vacuum*, 128:1–8, 2016.

[195] S. Meskos, S. Stefanov, and D. Valougeorgis. Gas Mixing and Final Mixture Composition Control in Simple Geometry Micro-mixers via DSMC Analysis. *Micromachines*, 10(3):178, 2019.

[196] F. Sharipov and D. Kalempa. Gaseous mixture flow through a long tube at arbitrary Knudsen numbers. *Journal of Vacuum Science & Technology A: Vacuum, Surfaces, and Films*, 20(3):814–822, 2002.

[197] L. Szalmas and D. Valougeorgis. Rarefied gas flow of binary mixtures through long channels with triangular and trapezoidal cross sections. *Microfluidics and Nanofluidics*, 9(2-3):471–487, 2010.

[198] L. Szalmas, J. Pitakarnnop, S. Geoffroy, S. Colin, and D. Valougeorgis. Comparative study between computational and experimental results for binary rarefied gas

flows through long microchannels. *Microfluidics and Nanofluidics*, 9(6):1103–1114, 2010.

[199] M. Vargas, S. Naris, D. Valougeorgis, S. Pantazis, and K. Jousten. Hybrid modeling of time-dependent rarefied gas expansion. *Journal of Vacuum Science & Technology A: Vacuum, Surfaces, and Films*, 32(2):021602, 2014.

[200] M. Vargas, S. Naris, D. Valougeorgis, S. Pantazis, and K. Jousten. Time-dependent rarefied gas flow of single gases and binary gas mixtures into vacuum. *Vacuum*, 109:385–396, 2014.

[201] V. V. Kosyanchuk, A. N. Yakunchikov, I. A. Bryukhanov, and S. A. Konakov. Numerical simulation of novel gas separation effect in microchannel with a series of oscillating barriers. *Microfluidics and Nanofluidics*, 21(7):116, 2017.

[202] V. V. Kosyanchuk and A. N. Yakunchikov. Simulation of gas separation effect in microchannel with moving walls. *Microfluidics and Nanofluidics*, 22(6):0, 2018.

[203] F. Sharipov. Reciprocal relations based on the non-stationary Boltzmann equation. *Physica A: Statistical Mechanics and its Applications*, 391(5):1972–1983, 2012.

[204] D. Valougeorgis. The friction factor of a rarefied gas flow in a circular tube. *Physics of Fluids*, 19(9):091702, 2007.

[205] A. R. B. OpenMP. OpenMP application program interface version 4.0, 2013.

[206] M. Wolfe. The OpenACC application programming interface, 2013.

[207] S. Misdanitis, S. Pantazis, and D. Valougeorgis. Pressure driven rarefied gas flow through a slit and an orifice. *Vacuum*, 86(11):1701–1708, 2012.

[208] R. Chandra, L. Dagum, D. Kohr, D. Maydan, J. McDonald, and R. Menon. *Parallel Programming in OpenMP*. Morgan Kaufmann Publishers Inc., San Francisco, CA, USA, 2001.

[209] OpenACC Programming and Best Practices Guide, 2015.

[210] The Portland Group (PGI). CUDA Fortran Programming Guide, 2018.

[211] L. Zhu, P. Wang, S. Chen, Z. Guo, and Y. Zhang. GPU acceleration of an iterative scheme for gas-kinetic model equations with memory reduction techniques. *Computer Physics Communications*, page 106861, 2019.

[212] M. Bao and H. Yang. Squeeze film air damping in MEMS. *Sensors and Actuators, A: Physical*, 136(1):3–27, 2007.

[213] J. J. Blech. On Isothermal Squeeze Films. *Journal of Lubrication Technology*, 105(4):615, 1983.

[214] T. Veijola and M. Turowski. Compact damping models for laterally moving microstructures with gas-rarefaction effects. *Journal of Microelectromechanical Systems*, 10(2):263–273, 2001.

[215] M. A. Gallis and J. R. Torczynski. An improved Reynolds-equation model for gas damping of microbeam motion. *Journal of Microelectromechanical Systems*, 13(4):653–659, 2004.

[216] X. Guo and A. Alexeenko. Compact model of squeeze-film damping based on rarefied flow simulations. *Journal of Micromechanics and Microengineering*, 19(4), 2009.

[217] W. Tang, T.-C. Nguyen, and R. Howe. Laterally driven polysilicon resonant microstructures. In *IEEE Micro Electro Mechanical Systems, , Proceedings, 'An Investigation of Micro Structures, Sensors, Actuators, Machines and Robots'*, volume 20, pages 53–59. IEEE, 1989.

[218] Young-Ho Cho, A. Pisano, and R. Howe. Viscous damping model for laterally oscillating microstructures. *Journal of Microelectromechanical Systems*, 3(2):81–87, 1994.

[219] S. Lorenzani, L. Gibelli, A. Frezzotti, A. Frangi, and C. Cercignani. Kinetic approach to gas flows in microchannels. *Nanoscale and Microscale Thermophysical Engineering*, 11(1-2):211–226, 2007.

[220] M. Dienel, M. Naumann, A. Sorger, D. Tenholte, S. Voigt, and J. Mehner. On the influence of vacuum on the design and characterization of MEMS. *Vacuum*, 86(5):536–546, 2012.

[221] A. Frangi, P. Fedeli, G. Langfelder, A. Chiesa, and G. Gattere. Fluid damping modeling for MEMS sensors operating in the 10 kHz-100 kHz range in near vacuum. *Proceedings of the IEEE International Conference on Micro Electro Mechanical Systems (MEMS)*, 2018-Janua(January):972–975, 2018.

[222] S. Naris and D. Valougeorgis. The driven cavity flow over the whole range of the Knudsen number. *Physics of Fluids*, 17(9):097106, 2005.

[223] S. Naris and D. Valougeorgis. Boundary-driven nonequilibrium gas flow in a grooved channel via kinetic theory. *Physics of Fluids*, 19(6):1–15, 2007.

[224] W. A. Ebert and E. M. Sparrow. Slip Flow in Rectangular and Annular Ducts. *Journal of Basic Engineering*, 87(4):1018–1024, 1965.

Appendix A

Solutions in the hydrodynamic and slip regimes

A.1 Analytical solution of the oscillatory flow in a rectangular duct

The hydrodynamic and slip regimes are characterized by large values of both flow parameters δ and θ. As $\delta \to \infty$ and $\theta \to \infty$, by retaining the fully-developed flow assumption the continuity equation is identically satisfied and the $z-$momentum equation becomes [10, 75, 72]

$$\rho \frac{\partial \hat{U}_{PUL}^{(m)}}{\partial t'} = -\frac{d\hat{P}_{PUL}}{dz'} + \mu \left(\frac{\partial^2 \hat{U}_{PUL}^{(m)}}{\partial x'^2} + \frac{\partial^2 \hat{U}_{PUL}^{(m)}}{\partial y'} \right), \tag{A.1}$$

where the pressure gradient $d\hat{P}_{PUL}\left(z', t'\right)/dz'$ and velocity $\hat{U}_{PUL}^{(m)}\left(t', x', y'\right)$, with $m = H, S$ denoting the hydrodynamic and slip solutions, are defined by Eqs. (4.1) and (4.2) respectively. The pressure gradient and the velocity are decomposed into the steady and oscillatory parts. The former one yields the steady Stokes equation and the latter one may be written in dimensionless form as

$$\frac{\partial^2 u^{(m)}}{\partial y^2} + \frac{\partial^2 u^{(m)}}{\partial x^2} + 2i\frac{\delta^2}{\theta} u^{(m)} = -\delta, \tag{A.2}$$

where $u^{(m)} = u^{(m)}\left(x, y\right)$, $m = H, S$, is the complex hydrodynamic or slip velocity. Equation (A.2) is also known as the unsteady Stokes equation. The steady and

Institutional Repository - Library & Information Centre - University of Thessaly
24/04/2024 08:10:15 EEST - 3.144.111.108

unsteady Stokes equations subject to no-slip and slip boundary conditions have been solved analytically in [224] and [10] respectively. Here, we are interested mainly to the oscillatory flow and therefore, the solution of Eq. (A.2) is provided in terms of the present notation without however describing the methodology.

In the hydrodynamic regime ($m = H$), Eq. (A.2) subject to the associated no-slip boundary conditions $u(x, \pm 1/2) = 0$ and $u(\pm H/2W, y) = 0$ is solved to yield

$$u^{(H)} = 4\delta \sum_{j=0}^{\infty} \frac{\sin(b_j/2)}{b_j p_j^2} \left[1 - \cosh(p_j x) \Big/ \cosh\left(\frac{W}{2H} p_j\right)\right] \cos(b_j y), \qquad (A.3)$$

where $b_j = (2j+1)\pi$, $j = 0, 1, 2, 3, ...$ and $p_j = \sqrt{b_j^2 - 2i\delta^2/\theta}$. The velocity field is integrated according to Eq. (4.22) to find the hydrodynamic flow rate

$$G^{(H)} = 8\delta \sum_{j=0}^{\infty} \frac{1 - \cos b_j}{b_j^2 p_j^2} \left[p_j - \frac{2H}{W} \tanh\left(\frac{W}{2H} p_j\right)\right]. \qquad (A.4)$$

Then, the velocity field is differentiated with respect to x and y to find the shear stresses

$$\tau_{xz}^{(H)} = -2 \sum_{j=0}^{\infty} \frac{\sin(b_j/2)}{b_j p_j} \left[1 - \sinh(p_j x) \Big/ \cosh\left(\frac{W}{2H} p_j\right)\right] \cos(b_j y) \qquad (A.5)$$

and

$$\tau_{yz}^{(H)} = -2 \sum_{j=0}^{\infty} \frac{\sin(b_j/2)}{p_j^2} \left[1 - \cosh(p_j x) \Big/ \cosh\left(\frac{W}{2H} p_j\right)\right] \sin(b_j y). \qquad (A.6)$$

In the slip regime ($m = S$), Eq. (A.2) subject to the associated slip boundary conditions [10]

$$u^{(S)}(x, \pm 1/2) = \mp \frac{\sigma_P}{\delta} \frac{du^{(S)}}{dy}\bigg|_{y=\pm 1/2} \quad and \quad u^{(S)}(\pm H/(2W), y) = \mp \frac{\sigma_P}{\delta} \frac{du^{(S)}}{dx}\bigg|_{x=H/(2W)} \tag{A.7}$$

where $\sigma_P = 1.016$ is the viscous slip coefficient is solved to yield

$$u^{(S)} = 4\delta \sum_{j=0}^{\infty} \frac{\sin(b_j/2)\cos(b_j y)}{b_j p_j^2 \left(1 + 2\frac{\sigma_P}{\delta} \sin^2(b_j/2)\right)} \left[1 - \frac{\cosh(p_j x)}{\cosh\left(\frac{W}{2H} p_j\right) + \frac{\sigma_P}{\delta} p_j \sinh\left(\frac{W}{2H} p_j\right)}\right] \tag{A.8}$$

268

In Eq. (A.8) $p_j = \sqrt{b_j^2 - 2i\delta^2/\theta}$, while the eigenvalues b_j are the roots of the transcendental equation $b_j \tan\left(b_j/2\right) = \delta/\sigma_P$. Then, the slip flow rate and shear stresses are

$$G^{(S)} = 8\delta \sum_{j=0}^{\infty} \frac{1 - \cos b_j}{b_j^2 p_j^3 \left(1 + 2\frac{\sigma_P}{\delta}\sin^2\left(b_j/2\right)\right)} \left(p_j - \frac{2H}{W} \frac{1}{\coth\left(\frac{W}{2H}p_j\right) + \frac{\sigma_P}{\delta}p_j}\right) \quad (A.9)$$

$$\tau_{xz}^{(S)} = -2 \sum_{j=0}^{\infty} \frac{\sin\left(b_j/2\right)\cos\left(b_j y\right)\sinh\left(p_j x\right)}{b_j p_j \left[1 + 2\frac{\sigma_P}{\delta}\sin^2\left(b_j/2\right)\right]\left[\cosh\left(\frac{W}{2H}p_j\right) + \frac{\sigma_P}{\delta}p_j\sinh\left(\frac{W}{2H}p_j\right)\right]} \quad (A.10)$$

$$\tau_{yz}^{(S)} = -2 \sum_{j=0}^{\infty} \frac{\sin\left(b_j/2\right)\cos\left(b_j y\right)}{p_j^2 \left(1 + 2\frac{\sigma_P}{\delta}\sin^2\left(b_j/2\right)\right)} \left[1 - \frac{\cosh\left(p_j x\right)}{\cosh\left(\frac{W}{2H}p_j\right) + \frac{\sigma_P}{\delta}p_j\sinh\left(\frac{W}{2H}p_j\right)}\right] \quad (A.11)$$

The closed form expressions (A.4)-(A.6) and (A.9)-(A.11) are implemented to validate the kinetic solution for large values of both δ and θ.

A.2 Numerical solution for nonlinear oscillatory flow between parallel plates

The hydrodynamic and slip regimes are characterized by large values of both the gas rarefaction and oscillation parameters. As $\delta \to \infty$ and $\theta \to \infty$, by retaining the fully developed flow assumption, the $x-$momentum incompressible equation becomes [185]

$$\rho \frac{\partial U^{(m)}}{\partial t'} = -\rho \hat{F}' + \mu \frac{\partial^2 U^{(m)}}{\partial y'^2}, \quad (A.12)$$

where, ρ is the mass density, μ is the viscosity and $U^{(m)}\left(t', y'\right)$ is the unknown macroscopic velocity, with $m = H, S$ denoting the hydrodynamic and slip solutions respectively. Introducing the dimensionless variables of Eqs. (5.9) and (5.10) into Eq. (A.12) yields the following conservation equations in dimensionless form:

$$\frac{\partial u^{(m)}}{\partial t} = -F \cos\left(\frac{\delta}{\theta} t\right) + \frac{1}{2\delta} \frac{\partial^2 u^{(m)}}{\partial y^2} \quad (A.13)$$

Equation (A.13) is subject in the hydrodynamic ($m = H$) and slip ($m = S$) regimes to the no-slip $u^{(H)}\left(\pm 1/2\right) = 0$ and slip

$$u^{(S)}\left(\pm 1/2\right) = \mp \frac{\sigma_P}{\delta} \frac{du^{(S)}}{dy}\bigg|_{y=\pm 1/2} \quad (A.14)$$

boundary conditions respectively. In Eq. (A.14), $\sigma_P = 1.016$ is the viscous slip coefficient [2].

Once the velocity distribution is found, the flow rate is readily deduced according to

$$M^{(S)}(t) = \int_{-1/2}^{1/2} u^{(S)}(t, y)\, dy. \tag{A.15}$$

Here Eq. (A.13) with boundary condition (A.14) is numerically solved using 2nd order finite difference schemes in time and space under the assumption of constant properties. The corresponding steady-state analytical solution [185] is properly recovered as $\theta \to \infty$. The present numerical results are used in Table 5.2 to check the range of validity of the slip regime and the accuracy of the DSMC solution in the slip regime.

Appendix B

McCormack kinetic model and momentum balance in binary gas mixture flows

B.1 Elements of the McCormack linearized collision term

The McCormack linearized collision term [44] for the flow between parallel plates is written as

$$L_{\alpha\beta}\tilde{h}_a = -\gamma_a\tilde{h}_a + 2\sqrt{\frac{m_a}{m}}\left\{\gamma_{\alpha\beta}\tilde{U}_a - v_{\alpha\beta}^{(1)}\left(\tilde{U}_a - \tilde{U}_\beta\right) - \frac{1}{2}v_{\alpha\beta}^{(2)}\left(\tilde{Q}_a - \frac{m_a}{m_\beta}\tilde{Q}_\beta\right)\right\}c_{ax}$$

$$+4\left[\left(\gamma_{\alpha\beta} - v_{\alpha\beta}^{(3)}\right)\tilde{\Pi}_a + v_{\alpha\alpha}^{(4)}\tilde{\Pi}_\beta\right]c_{ax}c_{ay}$$

$$+\frac{4}{5}\sqrt{\frac{m_a}{m}}\left\{\left(\gamma_{\alpha\beta} - v_{\alpha\beta}^{(5)}\right)\tilde{Q}_a + v_{\alpha\beta}^{(6)}\sqrt{\frac{m_\beta}{m_\alpha}}\tilde{Q}_\beta - \frac{5}{4}v_{\alpha\beta}^{(2)}\left(\tilde{U}_a - \tilde{U}_\beta\right)\right\}c_{ax}\left(c_a^2 - \frac{5}{2}\right). \quad \text{(B.1)}$$

The collision frequencies $\gamma_a = \gamma_{aa} + \gamma_{\alpha\beta}$ are expressed as

$$\gamma_\alpha = \frac{S_a S_\beta - v_{\alpha\beta}^{(4)}v_{\beta\alpha}^{(4)}}{S_\beta + v_{\alpha\beta}^{(4)}}, \quad \text{(B.2)}$$

271

where $S_a = v_{aa}^{(3)} - v_{aa}^{(4)} + v_{a\beta}^{(3)}$. In Eqs. (B.1) and (B.2), $\alpha = 1, 2$, $\beta \neq \alpha$ and the quantities $v_{\alpha\beta}^{(1-6)}$ are given by

$$v_{\alpha\beta}^{(1)} = \frac{16}{3} \frac{m_{\alpha\beta}}{m_a} n_\beta \Omega_{\alpha\beta}^{11}, \tag{B.3}$$

$$v_{\alpha\beta}^{(2)} = \frac{64}{15} \left(\frac{m_{\alpha\beta}}{m_a} \right)^2 n_\beta \left(\Omega_{\alpha\beta}^{12} - \frac{5}{2} \Omega_{\alpha\beta}^{22} \right), \tag{B.4}$$

$$v_{\alpha\beta}^{(3)} = \frac{16}{5} \frac{m_{\alpha\beta}^2}{m_a m_\beta} n_\beta \left(\frac{10}{3} \Omega_{\alpha\beta}^{11} + \frac{m_\beta}{m_a} \Omega_{\alpha\beta}^{22} \right), \tag{B.5}$$

$$v_{\alpha\beta}^{(4)} = \frac{16}{5} \frac{m_{\alpha\beta}^2}{m_a m_\beta} n_\beta \left(\frac{10}{3} \Omega_{\alpha\beta}^{11} - \Omega_{\alpha\beta}^{22} \right), \tag{B.6}$$

$$v_{\alpha\beta}^{(5)} = \frac{64}{15} \left(\frac{m_{\alpha\beta}}{m_\alpha} \right)^3 \frac{m_\alpha}{m_\beta} n_\beta \left(\Omega_{\alpha\beta}^{22} + \left(\frac{15}{4} \frac{m_\alpha}{m_\beta} + \frac{25}{8} \frac{m_\beta}{m_\alpha} \right) \Omega_{\alpha\beta}^{11} - \frac{1}{2} \frac{m_\beta}{m_\alpha} \left(5 \Omega_{\alpha\beta}^{22} - \Omega_{\alpha\beta}^{13} \right) \right), \tag{B.7}$$

$$v_{\alpha\beta}^{(6)} = \frac{64}{15} \left(\frac{m_{\alpha\beta}}{m_\alpha} \right)^3 \left(\frac{m_\alpha}{m_\beta} \right)^{3/2} n_\beta \left(-\Omega_{\alpha\beta}^{22} + \frac{55}{8} \Omega_{\alpha\beta}^{11} - \frac{5}{2} \Omega_{\alpha\beta}^{12} + \frac{1}{2} \Omega_{\alpha\beta}^{13} \right), \tag{B.8}$$

$$m_{\alpha\beta} = \frac{m_a m_\beta}{(m_a + m_\beta)}, \tag{B.9}$$

The Chapman-Cowling integrals $\Omega_{\alpha\beta}^{(ij)}$ [25] for the rigid sphere interaction are written as

$$\Omega_{\alpha\beta}^{(ij)} = \frac{(j+1)!}{8} \left[1 - \frac{1 + (-1)^i}{2(i+1)} \right] \left(\frac{\pi KT}{2 m_{\alpha\beta}} \right) (d_a + d_\beta)^2, \tag{B.10}$$

where d_a, $a = 1, 2$ is the diameter of the molecule of each species.

B.2 Formulation of the force balance expression

The inertia (or acceleration), viscous and pressure forces of the mixture acting on a fluid volume per unit length ($H dx'$) are given by

$$\tilde{F}_I(t') = H dx' \rho \frac{\partial \bar{U}'(t')}{\partial t'}, \tag{B.11}$$

$$\tilde{F}_V(t') = 2 dx' \tilde{\Pi}_W(t') \tag{B.12}$$

and

$$\tilde{F}_P(t') = H d\tilde{P}(t') \tag{B.13}$$

respectively, where $\rho = nm$ is the molecular mass density, $\bar{U}'(t')$ is the average hydrodynamic velocity of the mixture and $\tilde{\Pi}_W(t')$ is the wall shear stress of the mixture. All forces are divided by (HPX_P) to yield the corresponding dimensionless ones:

$$\tilde{f}_I(t') = 2dx\frac{\delta}{\theta}\frac{\partial \bar{u}'(t')}{\partial t} = dx\frac{\delta}{\theta}\left[\frac{m_1}{m}CG_1^{(A)}\sin\left(G_1^{(P)} - t\right) + \frac{m_2}{m}(1 - C)G_2^{(A)}\sin\left(G_2^{(P)} - t\right)\right]$$
(B.14)

$$\tilde{f}_V(t') = 4dx\tilde{\varpi}_W(t') = 4dx\varpi_W^{(A)}\cos\left(t - \varpi_W^{(P)}\right)$$
(B.15)

$$\tilde{f}_P(t') = dx\cos t$$
(B.16)

Since there is no net momentum flux, at any time during a time cycle, the pressure force is equal to the inertia plus the viscous forces:

$$\tilde{f}_P(t') = \tilde{f}_I(t') + \tilde{f}_V(t')$$
(B.17)

Substituting Eqs. (B.14)-(B.16) into Eq. (B.17) yields the force balance expression in dimensionless form:

$$\frac{\delta}{\theta}\left[\frac{m_1}{m}CG_1^{(A)}\sin\left(G_1^{(P)} - t\right) + \frac{m_2}{m}(1 - C)G_2^{(A)}\sin\left(G_2^{(P)} - t\right)\right] + 4\varpi_W^{(A)}\cos\left(t - \varpi_W^{(P)}\right) = \cos t$$
(B.18)

Equation (B.18) is used for confirming the accuracy of the computed amplitudes and angle phases of the flow rate and the shear stress.

Alexandros Tsimpoukis
Curriculum Vitae

🏠 Pedion Areos, Volos, Greece, 38334
📞 0030 24210 74297
✉ atsimpoukis@mie.uth.gr
in https://www.linkedin.com/in/alexandros-tsimpoukis-a0b58698/

EDUCATION

2016 – 2020	**Doctor of Philosophy (Defense Date: 13/3/2020)** Department of Mechanical Engineering *University of Thessaly*
2014 – 2015	**Master of Science (ECTS: 60)** GPA: 9.13 OUT OF 10 Department of Mechanical Engineering *University of Thessaly*
2008 – 2014	**Diploma (ECTS: 300)** GPA: 6.82 OUT OF 10 Department of Mechanical Engineering *Aristotle University of Thessaloniki*

ACADEMIC PROJECTS

4/2016-3/2020	**PhD Thesis** Rarefied oscillatory and pulsatile gas flows in capillaries and enclosures with applications in vacuum technology and microfluidics
SUPERVISOR	Prof. D. Valougeorgis
6/2015-10/2015	**MSc Thesis** Numerical investigation of the shock wave structure with kinetic and continuum models
SUPERVISOR	Prof. D. Valougeorgis
9/2013-3/2014	**Diploma Thesis** Calculation of Heating and Cooling Degree-days from records of meteorological stations in the greater metropolitan area of Thessaloniki
SUPERVISOR	Assoc. Prof. K. Papakostas

WORK EXPERIENCE

1/2016-	**PhD candidate** University of Thessaly
AREA OF STUDY	Rarefied gas flows, Kinetic modelling, Oscillatory flows Development of kinetic codes in FORTRAN
5/2014- 12/2015	**Mechanical Engineer** Small Engineering firm in Larissa
PROJECTS	Energy study and upgrading of buildings CAD Drawings (Sections, plans, views) HVAC applications

TEACHING EXPERIENCE

TEACHING ASSISTANT 2016, 2017, 2019	**University of Thessaly** Solar Thermal Systems
2018	Introduction to computer programming
2016	Numerical methods

INTERESTS

Volunteering in the local community association
Traveling and basketball

AWARDS

2019	**IUVSTA – Elsevier Student Award** *21st International Vacuum Congress*

COMPUTER SKILLS

PROGRAMMING	FORTRAN, MPI, OPENMP OPENACC, MATLAB MATHEMATICA, LaTeX
MICROSOFT OFFICE TOOLS	WORD, EXCEL, VISIO POWER POINT, PROJECT
APPLICATIONS	TECPLOT360, AutoCAD
SIMULATION	TRNSYS

LANGUAGES

GREEK	Native
ENGLISH	Very good (C1) IELTS 7.5 Advanced Level Certificate in English (ALCE)
FRENCH	Good (B2) Delf B2

PUBLICATIONS

Peer-reviewed journals: **3**, Conference proceedings: **4**

SCHOOLS AND WORKSHOPS

Introductory GPU Computing for Fluid Dynamics Applications, Introduction to parallel programming, 24th Summer School on Complexity, 1st and 2nd MIGRATE Summer School

ACADEMIC COURSES

UNDERGRADUATE	48 required for ME Diploma
GRADUATE	Kinetic theory of gases Advanced transport phenomena Advanced fluid mechanics Introduction to plasma phyics

REFERENCES

	Prof. Dimitris Valougeorgis
POSITION	Professor
EMPLOYER	*University of Thessaly*
EMAIL	diva@mie.uth.gr
PHONE	0030 24210 74058 (Work)

	Prof. Konstantinos Papakostas
POSITION	Associate Professor
EMPLOYER	*Aristotle University of Thessaloniki*
EMAIL	kpapakos@meng.auth.gr
PHONE	0030 2310 996025 (Work)

Publications in peer-reviewed journals

[1] A. Tsimpoukis, S. Naris and D. Valougeorgis, Oscillatory pressure-driven rarefied binary gas mixture flow between parallel plates, Submitted at Journal of Fluid Mechanics.

[2] A. Tsimpoukis, N. Vasileiadis, G. Tatsios, and D. Valougeorgis, Nonlinear oscillatory fully-developed rarefied gas flow in plane geometry, Physics of Fluids, 31, 067108, 2019.

[3] A. Tsimpoukis and D. Valougeorgis, Pulsatile pressure driven rarefied gas flow in long rectangular ducts, Physics of Fluids, 30, 047104, 2018.

[4] A. Tsimpoukis and D. Valougeorgis, Rarefied isothermal gas flow in a long circular tube due to oscillating pressure gradient, Microfluidics and Nanofluidics, 22, 5, 2018.

Publications in conference proceedings

[1] A. Tsimpoukis, and D. Valougeorgis. Oscillatory rarefied gas flow in a vertically driven comb-type assembly 11th FLOW, Kozani, Greece, 23-24/11, 2018. Available in Greek at: Link

[2] A. Tsimpoukis, and D. Valougeorgis, Rarefied pulsatile pressure-driven fully-developed gas flow in long circular tubes, 9th GRACM International Congress on Computational Mechanics, Chania, Greece, 04-06/06, 2018. Available at: Link

[3] A. Tsimpoukis, C. Tantos, and D. Valougeorgis, Time-dependent conductive heat transfer in rarefied polyatomic gases confined between parallel plates, Journal of Physics: Conference Series, 785, 012008, 2017.

[4] A. Tsimpoukis, G. Tatsios and D. Valougeorgis. Periodic oscillating Poiseuille flow in the whole range of the Knudsen number. 10th FLOW, Patra, Greece, 02-03/12, 2016. Available in Greek at: Link

Conferences

[1] A. Tsimpoukis and D. Valougeorgis, Oscillatory rarefied gas flow in comb-type assembly, 21st International Vacuum Congress, Malmo, Sweden, 01-05/07, 2019. (Poster)

[2] A. Tsimpoukis, and D. Valougeorgis. Oscillatory rarefied gas flow in a vertically driven comb-type assembly. 11th FLOW, Kozani, Greece, 23-24/11, 2018. (In Greek)

[3] A. Tsimpoukis, S. Naris and D. Valougeorgis, Oscillatory pressure driven flow of binary gas mixtures between parallel plates, 31st International Symposium on Rarefied Gas Dynamics, Glasgow, UK, 23-27/07, 2018.

[4] A. Tsimpoukis, S. Naris and D. Valougeorgis, Oscillatory pressure driven He-Xe gas mixture flow between parallel plates in the whole range of the Knudsen number, 3rd MIGRATE Workshop, Furiani, France, 27-29/06, 2018.

[5] A. Tsimpoukis and D. Valougeorgis, Rarefied pulsatile pressure-driven fully-developed gas flow in long circular tubes, 9th GRACM International Congress on Computational Mechanics, Chania, Greece, 04-06/06, 2018.

[6] A. Tsimpoukis and D. Valougeorgis, Rarefied gas flow in a comb-type assembly driven by the vertical harmonic motion of an element, 3rd Non-Equilibrium Gas Flows, Strasbourg, France, 28/02-02/03, 2018.

[7] A. Tsimpoukis, G. Tatsios and D. Valougeorgis. Rarefied cylindrical Poiseuille gas flow due to harmonically oscillating pressure gradient. 2nd MIGRATE Workshop, Sofia, Bulgaria, 29-30/06, 2017.

[8] A. Tsimpoukis, G. Tatsios and D. Valougeorgis. Periodic oscillating Poiseuille flow in the whole range of the Knudsen number. 10th FLOW, Patra, Greece, 02-03/12, 2016. (In Greek)

[9] A. Tsimpoukis, C. Tantos and D. Valougeorgis, Time-dependent conductive heat transfer in rarefied polyatomic gases confined between parallel plates, Nanoscale and Microscale Heat Transfer V, Santorini, Greece, 26-30/09, 2016.

[10] A. Tsimpoukis, G. Tatsios and D. Valougeorgis. Rarefied Poiseuille gas flow due to harmonically oscillating pressure gradient. 1st MIGRATE Workshop, Strasbourg, France, 30/06-01/07, 2016.

Summer schools and courses

[1] Introductory GPU Computing for Fluid Dynamics Applications, Politecnico di Milano, Milan, Italy, 02-05/10, 2018.

[2] Introduction to parallel programming, GRNET, Athens, Greece, 29/11-01/12, 2017.

[3] 24th Summer School on Complexity, University of Thessaly, Volos, Greece, 12-21/07, 2017.

[4] 2nd MIGRATE Summer School, Bulgarian Academy of Sciences, Sofia, Bulgaria, 27-28/06, 2017.

[5] 1st MIGRATE Summer School, University of Strasbourg, Strasbourg, France, 28-29/06, 2016.